eman ta zabal zazu

Universidad del País Vasco

Euskal Herriko Unibertsitatea

CHEMISTRY FACULTY OF DONOSTIA - SAN SEBASTIÁN

APPLIED CHEMISTRY DEPARTAMENT

COORDINATIONCHEMISTRY GROUP

DESIGN, SYNTHESIS AND CHARACTERIZATION OF MULTIFUNCTIONAL MOFs. FROM GAS ADSORPTION AND PHOTOCATALYSIS TO CISS EFFECT AND SPIN-CURRENTS.

DISSERTATION

to apply for the degree of Doctor in Chemistry

presented by

UXUA HUIZI RAYO

2020

Esker onak

Lehenik eta behin eskerrak eman nahi dizkiet Eider San Sebastian eta Javi Cepedari. Tesia bezalako etapa batean zuzendarien papera funtsezkoa dela esango nuke, eta zuek bikain bete duzue. Eskerrik asko zuen denborarengatik, formakuntzarengatik eta pazientziarengatik; baina bereziki, eskerrik asko emandako aukerengatik eta nigan jarritako konfiantza guztiarengatik. Espero dut etorkizunean elkarrekin ospakizun gehiago bizitzeko aukera izatea!

Vladimiro Mujica eta Jesus Ugalde aipatu nahi ditut. Zuekin lan egitea eta zuetaz ikastea oso aberasgarria izan da bai nire prestakuntzarako baita nire ezagutzarako ere. Agnieszka Tercjak eta Junkal Gutierrez ere garrantzitsuak izan dira, zuen lan aparta eta giro bikaina ezinbestekoak izan baitira tesiarentzako. Jose Seco ere eskertu nahi dut urte hauetan jarritako erraztasun guztiengatik, eta Ricardo Hernandez eta Roberto Ciganda ikerketaren munduan nire lehenengo pausuak ematen laguntzeagatik.

Eskerrik asko laborategiko lagunei! Gure arten sortutako harremana oso polita dela esango nuke. Oso ongi eta eroso sentitu naiz zuekin eta horrek asko lagundu dit, pertsona bikainez inguratuta egon naizelako. Momentu asko konpartitu ditugu, bai laborategian baita laborategitik kanpo, eta gehiago izatea espero dut. Plazer bat izan da etapa hau zuekin konpartitzea.

Ezin ditut ahaztu familia eta Jon Ander. Nire gaitasunaz inoiz ez duzue dudarik egin eta azken hiru urte hauetan, bereziki urduritasun eta lan gehieneko momentuetan, animoak soberan izan ditut oso gutxiren truke. Eskerrik asko beti nirekin egoteagatik.

Eta nire lagun Ainhoa eta Iosurekin bukatu nahi dut. Eskerrik asko zuei ere hainbestetan ni entzun eta lasaitzeagatik, edozer gauzaren alde ona ikusten laguntzeagatik eta ni hainbeste zaintzeagatik.

List of Abbreviations and Acronyms

Abbreviations

1, 2 and 3D: one-, two- and three-dimensional

A: acceptor8

***ac*:** alternating current

AFM: atomic force microscopy

ANG: adsorbed natural gas

BET: Brunauer–Emmett–Teller

Bio-MOF: Biological metal organic framework

BTPR: biaugmented trigonal prism

C-AFM: conductive atomic force microscopy

CB: conduction band

CCS: carbon capture and storage

CCW: counterclockwise

CD: circular dichroism

CISS: Chiral-Induced Spin Selectivity

CM-AFM: magnetically polarized conductive atomic force microscopy

CNG: compressed natural gas

cp: closed pore

CP: coordination polymer

CP: cross-polarization

CPL: circularly polarized luminescence

CPO: coordination polymer of Oslo

CSAPR: capped square antiprisms

CShMs: Continuous Shape Measurements

CT: charge tranfer

***cus*:** coordinative unsaturated sites

CW: clockwise

D: donor

dc: direct current

DET: Dexter electron transfer

DOS: density of states

FMMM: Functional Molecular Magnetic Materials

FR: fast relaxation

FRET: Förster resonance energy transfer

FTIR: Fourier transform infrared

HKUST: Hong Kong University of Science and Technology

HOMO: highest occupied molecular orbital

IC: internal conversions

MIL: Matériaux de l'Institut Lavoisier

IEA: International Energy Agency

IRMOF: Isoreticular Metal-organic Framework

ISC: intersystem crossing

ITHD: ith-d net topology

ITO: indium tin oxide

IUPAC: International Union of Pure and Applied Chemistry

LC: ligand-centered

LLCT: ligand-to-ligand charge transfer

LMCT: ligand-to-metal charge transfer

LMOF: luminescent metal-organic framework

Ln: lanthanides

LNG: liquefied natural

LnOF: lanthanide-organic framework

lp: large pore

LUMO: lowest unoccupied molecular orbital

MBB: molecular building blocks

M-BTT:

MC: metal-centered

MFF: muffins

MFU:

SIM: single-ion magnet

SMM: single-molecule magnet

MLCT: metal-to-ligand charge tranfer

MOF: metal-organic framework

NIR: Near-infrared

NMR: Nuclear Magnetic Resonance

np: narrow pore

NPEC: non-polarized electronic current

NU:

OLED: organic light-emitting diode

P: pressure

PL: photoluminescence

PSPBU: pseudo-square planar building unit

PTBU: pseudo- tetrahedral building unit

PXRD: Powder X-ray diffraction

QD: quantum dot

Q_{st}: isosteric heat

QTM: quantum tunneling of the magnetization

RISC: reverse intersystem crossing

RT: room temperature

SBU: secondary building unit

SC: semiconductor

SCXRD: Single-crystal X-ray diffraction

SNU: Seoul National University

SOC: spin-orbit coupling

SP: spin polarization

SPC: Soft porous crystals

SPEC: spin-polarized electron current

SR: slow relaxation

STM:

TBU: Tetrahedral building unit

TD-DFT: Time-dependent density-functional theory

TDX: Thermodiffraction

TGA: Thermogravimetric analysis

TM: transition metal

UiO: Universitetet i Oslo

UV: ultraviolet

VB: valence band

vis: visible light

VR: vibrational relaxation

ZIF: zeolitic imidazolate framework

ZMOF: zeolite-like metal-organic frameworks

Acronyms

$(OH)_2$-bdc / dobdc: 2,5-dihydroxy-1,4-bezenedicarboxylic acid

1,3,5-btc / btc: 1,3,5-bezenetricarboxylic acid

1,4-bdc / bdc: 1,4-bezenedicarboxylic acid, terephthalic acid

A_{ads}: adsorbed acceptor

adn: adenine

ata: 2-aminoterephthalate

***B*:** magnetic field

bdcppi: N,N'-bis(3,5-dicarboxyphenyl)pyromellitic diimide

bipy: 4,4'- bipyridine

bp-bdc: 2,5-bis(pentyloxy)-1,4-benzenedicarboxylic acid

bpdc: biphenyl-4,4'-dicarboxylic acid

br-bdc: 2-bromo-1,4-bezenedicarboxylic acid

brim: bromoimidazolate

btb: 4,4',4'',-benzene-1,3,5-triyl-tris(benzoic acid)

btdd: bis(1,2,3-triazolato-[4,5-b],[4',5'-i])dibenzo-[1,4]-dioxin

btt: 1,3,5-benzenetristetrazolate

cam: camphorate

CNip: 5-cyanoisophthalate

D*: exciter donor

***D*:** magnetic anisotropy

D_{ads}: adsorbed donor

dap: 2,7-diazapirene

dcim: dichloroimidazolate

DMF: dimethylformamide

dp-bdc: 2,5-dipropoxy-1,4-benzenedicarboxylic acid

e^-: electron

***E*°:** reduction potential

ghg: glycyl-L-histidylglycine

glum: dissymmetry factor

h^+: holes

H_2CNip: 5-cyanoisophthalic acid

H_2pmdc: 4,6-pyrimidinedicarboxylic acid

hcb-bdc: 1,2-dihydrocyclobutabenzene-3,6-dicarboxylic acid

hpdc: 4,5,9,10-tetrahydropyrene-2,7-dicarboxylic acid

***J*:** quantum number

L/D-tart: L/D-tartrate

Ln: lantanide

m-dobdc: 4,6-dioxide-1,3-benzenedicarboxylate

MeOH: methanol

mim: 2-methylimidazole

m_j

m_S

MS:

N3-bdc: 2-azide-1,4-bezenedicarboxylic acid

ndc: naphthalenedicarboxylate

NH2-bdc: 2-amino-1,4-bezenedicarboxylic acid

NH2-tpdc: 2'-amino-1,1':4,1''-terphenyl-4,4''-dicarboxylic acid

OH-bdc: 2-hydroxy-1,4-bezenedicarboxylic acid

pdc: 2,7-pyrenedicarboxylic acid

pdt: pyrazine-2,3-dithiolate

pmdc: 4,6-pyrimidinedicarboxylate

***S*:** ground state

S_0*:* singlet ground state

S_{BET}**:** specific surface area

S_n**:** excited singlet state

S_{total}**:** total surface area

T_B**:** blocking temperature

tcpb: 1,2,4,5-tetrakis(4-carboxyphenyl)benzene

TEOA: triethanolamine

T_n**:** excited triplet state

tpdc: [p-terphenyl]-4,4''-dicarboxylic acid

trz: 1,2,3-triazolate

***U*:** energy barrier

U_{eff}*:* energy barrier

v_m**:** vibrational state

Z: atomic number

μ_s**:** spin magnetic momento

Summary

The present work is focused on the design, synthesis and characterization of metal-organic frameworks (MOFs) for their study in the fields of gas adsorption, photocatalysis, luminescence, magnetism and spintronics. Three types of materials have been designed for this purpose depending on the final application of interest.

On the one hand, there is the family of heterometallic MOFs based on the pyrimidinedicarboxylate ligand (pmdc). This ligand is known for its rigidity because it forms chelated five-membered rings, in addition to the steric hydrance generated by the non-chelating oxygen atoms of the carboxylates that favour the coordination of solvent molecules with the metal. This enhances the adsorption properties that these materials may contain, as the removal of solvent molecules would generate coordination unsaturated sites that would facilitate the interactions of the adsorbates with the MOF surface. These MOFs have been constructed from the Sc(III) and Na(I) or Li(I) metals, as scandium provides greater stability to the structure while alkaline metals facilitate electrostatic interactions with the adsorbates due to their electropositive character. In this way, two MOFs synthesized by different methods have been obtained. This study has confirmed that the pmdc-MOFs have a three-dimensional and stable porous structure with coordination unsaturated sites, which makes them ideal materials for the storage of gases such as H_2, CO_2 and CH_4. Thus, the adsorption capacity of these MOFs has been confirmed in the adsorption experiments. Among these MOFs is the material with the highest CO_2 adsorption capacity among all the pmdc-based MOFs.

On the other hand, based on the ligand 5-cyanoisophthalate, a new three-dimensional MOF containing Ca(II) and Zn(II) metals has been synthesised and characterised for its subsequent use as catalyst in the photocatalytic reduction of CO_2. Its chemical stability has been studied using the solvent-exchange method, since it allows the exchange of coordinated solvents such as DMF for other more volatile ones, enabling the activation of the material. In this case, the DMF of the pristine MOF has been exchanged for MeOH or H_2O. In this way, it has been possible to characterise these two new materials and it has confirmed that the structure of the starting MOF remains stable. Furthermore, the removal of these coordinated solvents generates coordination unsaturated sites that increase interactions with CO_2 and facilitate its adsorption. Finally, the photocatalytic reduction of CO_2 in gas phase and under visible light has been carried out, obtaining CO as product from the reaction and degradation of the material. It is therefore concluded that these MOFs can transform CO_2 into CO thanks to the ligand-centred charge

transfers observed in the photoluminescence experiments, which allow the circulation of the charge carriers that will carry out the redox reactions.

This work also reports on the synthesis and characterization of five enantiomeric pairs of isostructural 3D metal–organic frameworks (MOFs) with the general formula {[Ln2(m4-tar)2(m-tar)(H2O)2]xH2O}n [where Ln(III) = Tb, Dy, Ho, Er and Tm; tar = tartrate (D- or L-) and x = 3 or 4 depending on the counterpart], which possess interesting luminescence and magnetic properties. These MOFs undergo progressive and reversible dehydration processes upon controlled heating yielding three crystalline phases. Alternating current magnetic measurements on Tb, Dy and Er-based compounds exhibit field induced single-molecule magnet behaviour dominated by QTM, which is partially suppressed when diluted on a Y-based matrix. Tartrate ligands show poor room temperature sensitization of Tb and Dy centers that is enhanced at low temperature (10 K), even enabling weak Tm-based emission. More interestingly, the dehydration modulates both magnetic and photoluminescence properties on the basis of both the distortions occurring in the coordination shells and a decrease of water molecules acting as quenchers, respectively, endowing these materials with potential humidity sensing capacity. Remarkably, the Tb-based MOF shows circularly polarized luminescence (CPL), being one of the examples of this very scarce family of CPL emitters reported so far.

Finally, the conductive and paramagnetic crystalline 3-D metal-organic framework (MOF), based on Dy(III) and the L-tartrate chiral ligand, is proved to behave as an almost ideal electron spin filtering material at room temperature, transmitting one spin component only, leading to a spin polarization (SP) power close to 100% in the ±2 V range, which is conserved over a long spatial range, larger than 1 μm in some cases. This impressive spin polarization capacity of this class of nano-structured materials is measured by means of magnetically polarized conductive atomic force microscopy, and is attributed to the Chirality-Induced Spin Selectivity (CISS) effect of the material arising from a multidimensional helicity pattern, the inherited chirality of the organic motive, and the enhancing influence of Dy(III) ions on the CISS effect, with large spin orbit coupling values. Our results represent the first example of a MOF-based and CISS-effect mediated spin filtering material that shows a nearly perfect SP. These striking results obtained with our robust and easy-to-synthesize chiral MOFs constitute an important step forward in to improve the performance of spin filtering materials for spintronic device fabrication.

Resumen

El presente trabajo esta enfocado al diseño, síntesis y caracterización de redes metalo-orgánicas (MOFs) para su estudio en los campos de la adsorción de gases, la fotocatálisis, la luminiscencia, el magnetismo y la espintrónica. Para ello se han diseñado tres tipos de materiales dependiendo de la aplicación final de interés.

Por un lado está la familia de MOFs heterometálicos basados en el ligando pirimidinadicarboxilato (pmdc). Este ligando es conocido por su rigidez debido a que forma anillos quelatos de cinco miembros, además de las repulsiones estéricas generadas por los átomos de oxígeno libres de los carboxilatos que favorecen la coordinación de moléculas de disolvente al metal. De esta manera se potencia las propiedades de adsorción que puedan contener dichos materiales, ya que la eliminación de esas moléculas de disolvente generaría vacantes coordinativas que facilitarían las interacciones de los adsorbatos con la superficie del MOF. Estos MOFs se han construido a partir de los metáles Sc(III) y Na(I) o Li(I), ya que el escandio aporta mayor estabilidad a la estructura mientras que los metales alcalinos facilitan las interacciones electrostáticas con los adsorbatos por su carácter electropositivo. De esta manera, se han obtenido dos MOFs preparados con métodos sintéticos diferentes, para su posterior caracterización mediante técnicas de rayos-X, termogravimetría y adsorción de N_2, entre otras. Este estudio ha confirmado que los pmdc-MOFs poseen una estructura porosa tridimensional y estable con vacantes coordinativas, lo cual los convierte en materiales idóneos para el almacenamiento de gases como el H_2, CO_2 y CH_4. Así, en los experimentos de adsorción se ha confirmado la capacidad de adsorción de estos MOFs, entre los cuales se encuentra el material con mayor capacidad de adsorción de CO_2 entre todos los MOFs basados en la pmdc.

Por otro lado, partido del ligando 5-cianoisoftalato, se ha sintetizado y caracterizado un nuevo MOF tridimensional basado en los metales Ca(II) y Zn(II) para su posterior uso como catalizador en la reducción fotocatalítica de CO_2, y se ha estudiado su estabilidad química mediante el método “solvent-exchange”, ya que permite el intercambio de disolventes coordinados como la DMF por otros más volátiles facilita la activación del material. En este caso, se ha intercambiado la DMF del MOF de partida por MeOH y H_2O. De esta manera se ha podido caracterizar estos dos nuevos materiales y se ha confirmado que la estructura del MOF de partida se mantiene estable. Además, la eliminación de dichos disolventes coordinados genera vacantes coordinativas que aumentan las interacciones con el CO_2 y facilita su adsorción. Finalmente, se ha llevado a cabo la reducción fotocatalítica de CO_2 en fase gas y bajo luz visible,

obteniendo como producto CO proveniente de la reacción y de la degradación del material. Por lo que se concluye que estos MOFs pueden transformar el CO2 en CO gracias a las transferencias de carga centradas en el ligando observadas en los experimentos de fotoluminiscencia, las cuales permiten la circulación de los portadores de carga que llevarán a cabo las reacciones redox.

Este trabajo también trata sobre la síntesis y caracterización de cinco pares enantioméricos de (MOFs) isoestructurales tridimensionales con la fórmula general $\{[Ln_2(m_4\text{-tart})_2(m\text{-tart})(H_2O)_2]\ xH_2O\}_n$ [donde Ln(III) = Tb, Dy, Ho, Er y Tm; tart = tartrato (D- o L-) y x = 3 o 4 dependiendo del compuesto], que poseen interesantes propiedades de luminiscencia y magnéticas. Estos MOF se someten a procesos de deshidratación progresiva y reversible mediante un calentamiento controlado que produce tres fases cristalinas. Las mediciones magnéticas de corriente alterna en compuestos basados en Tb, Dy y Er exhiben un comportamiento magnético de imanes moleculares inducido por el campo y dominado por el QTM, que se suprime parcialmente cuando se diluye en una matriz basada en Y. Los ligandos de tartrato muestran una pobre sensibilización a temperatura ambiente de los centros de Tb y Dy que se potencia a baja temperatura (10 K), permitiendo incluso una emisión débil basada en Tm. Lo más interesante es que la deshidratación modula las propiedades magnéticas y de fotoluminiscencia sobre la base de las distorsiones que se producen en las capas de coordinación y la disminución de las moléculas de agua que actúan como amortiguadores, respectivamente, lo que confiere a estos materiales una capacidad potencial de detección de la humedad. Cabe destacar que el MOF basado en Tb muestra una luminiscencia de polarización circular (CPL), siendo uno de los ejemplos de esta familia muy escasa de emisores de CPL de los que se ha informado hasta ahora.

Por último, se ha demostrado que el MOF cristalino conductivo y paramagnético tridimensional basado en Dy(III) y en el ligando quiral de L-tartrato, se comporta como un material filtrante de espín de electrones casi ideal a temperatura ambiente, transmitiendo un solo componente de espín, lo que da lugar a una potencia de polarización de espín (SP) cercana al 100% en el rango de ±2 V, que se conserva a lo largo de un largo alcance espacial, mayor que 1 µm en algunos casos. Esta impresionante capacidad de polarización de espín de esta clase de materiales nanoestructurados se mide por medio de la microscopía de fuerza atómica conductora polarizada magnéticamente, y se atribuye al efecto de selectividad de espín inducida por la quiralidad (CISS) del material que surge de un patrón de helicidad multidimensional, la quiralidad heredada del motivo orgánico y la influencia creciente de los iones Dy(III) en el efecto CISS, con grandes valores de acoplamiento de órbita de espín. Estos resultados representan el primer ejemplo de un material filtrante de espín basado en MOF y con efecto CISS que muestra un SP casi perfecto,

suponiendo estos resultados un importante paso adelante para mejorar el rendimiento de los materiales de filtrado de espín para la fabricación de dispositivos espintrónicos.

Table of Contents

List of Figures

List of Tables

Chapter 1

General Introduction to Metal-Organic Frameworks

1.1. Metal-organic frameworks: versatile and robust materials

Porous materials such as zeolites and silicates have always been of interest in the world of chemistry, since the pores and cavities of structures allow the diffusion of different types of fluid phases, facilitating both physical processes and chemical reactions.[1] Although the first porous materials to be used were porous carbon and clay-type minerals, zeolites have been considered the material of excellence for large-scale technological processes, specifically in the petrochemical industry.[2] In recent decades, the use of crystalline microporous materials has been spread to a wide variety of applications (optics, electronics and chemical sensing, among others), requiring the design and preparation of new materials with diverse structure types, compositions, size and morphology.[3]

In recent years, a new subclass of crystalline porous materials, called metal-organic frameworks (MOFs), has caught the attention of scientists working in chemistry and materials science research fields. Studies on MOFs began to rise in the '90s in view of their permanent large porosity that imbued with excellent gas adsorption capacity,[4] but the absence of a specific definition for such a general term and an adequate classification exposed MOF to an intense debate during many years.[5] In particular, the discussion derived from the overlap existing between the terms *coordination polymer* (CP) and *metal-organic framework*, since part of the scientific community held that both terms share the same meaning whereas others considered them different materials from each other. So, in 2009, the International Union of Pure and Applied Chemistry (IUPAC) started the project *Coordination Polymers and Metal-Organic Frameworks: terminology and nomenclature* with the aim of unifying both the language and the practice of the scientific community. In the latest recommendations published in 2013, the IUPAC specifies the following definitions:[6]

> ***Coordination polymer***
> *A coordination compound with repeating coordination entities extending in 1, 2, or 3 dimensions. Coordination polymers do not need to be crystalline; […].*
>
> ***Metal-organic framework***
> *A metal–organic framework, abbreviated to MOF, is a coordination network with organic ligands containing potential voids. This wording accounts for the fact that many systems are dynamic, and changes in structure and thus corresponding changes in potential porosity or solvent and/or guest filled voids may occur depending on temperature, pressure, or other external stimuli. For these reasons it is also not required that an MOF be crystalline. […].*

Based on these definitions, MOFs can be described according to the structural characteristics and physicochemical properties outlined in the following section.

1.1.1. General structural aspects of MOFs

Following the recommendations of the IUPAC, MOFs can be defined as a type of hybrid organic-inorganic coordination polymers with potential porosity, which are formed from the coordination between metal centers and multidentate organic ligands, generating functionalized and crystalline materials that can extend in various dimensions (Figure 1.1).

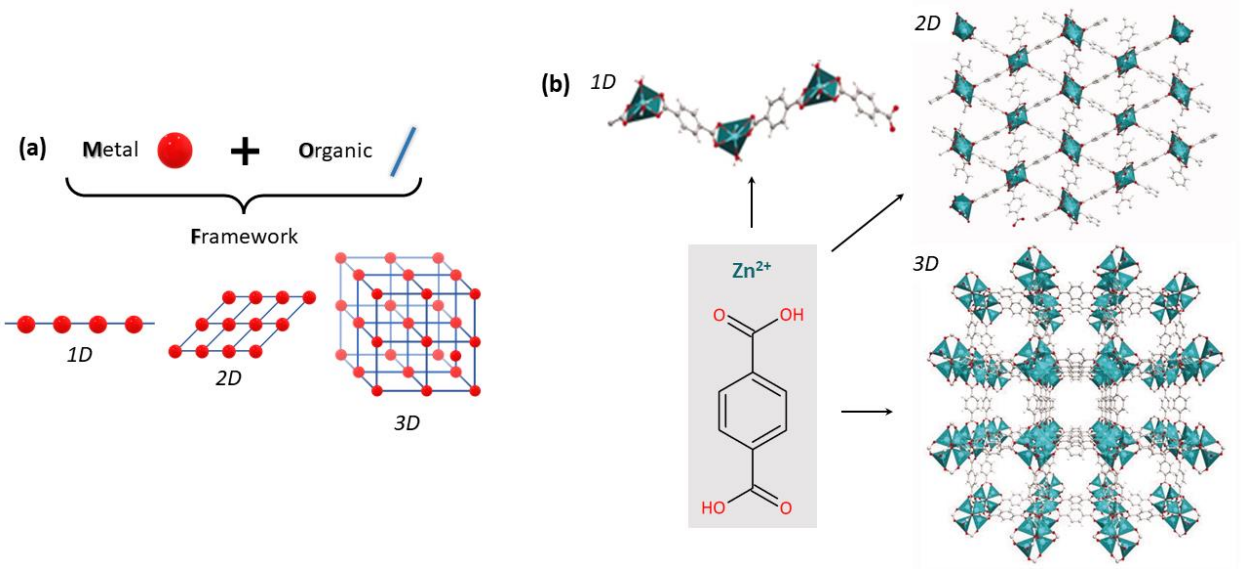

Figure 1.1. General structural aspects of MOFs. **(a)** Schematic representation of the components of a MOF and the types of possible architectures. **(b)** Dimensionalities adopted by crystalline framework structures constructed from 1,4-bezenedicarboxylic acid (1,4-bdc) and Zn^{2+} ions (MOF-5). Figure (b) is adapted from Reference 7.

Just as in zeolites, both structure and porosity of a MOF are determined by template molecules or structure-directing agents;[5] though the building principles of MOFs are multiple since there may be many factors involved in the self-assembling process of the organic ligands and metal centers/clusters construction units.[8] Even so, MOFs can also follow the synthetic method of zeolites based on structure-directing agents, obtaining structural properties determined by the different topologies formed by the arrangement of template molecules.[9] Accordingly, the structural and topological control of MOFs is based on reticular chemistry, which decomposes the framework into nodes and linkers according to the geometry and connectivity among metal centers and functional groups of ligands.[10] In the following pages, basic structural and compositional aspects of MOFs will be defined and discussed briefly.

Secondary building units

As depicted in Figure 1.1, typically, organic ligands that are used as building units contain aromatic moieties with carboxylic acids as coordinative groups (or N/S-donor ligands); so, the most common description is that of clusters formed by the combination of different metals with these functional groups. These metal-carboxylate clusters (also equivalent to those formed with organic anionic units such as phosphonate, sulfonate, and heterocyclic compounds like 1,4-dioxine or tetrazolate) compose the secondary building units (SBU) of MOFs, which guide the topology of the resulting network allowing the generation of materials with almost infinite architectures and compositions.[11] Figure 1.2 shows some representative SBUs and organic linkers for well-known MOFs, where the large diversity of organic linkers, metal cations, SBU and architectures can be observed.[12] For instance, the three-dimensional HKUST-1 (Figure 1.2a) is built up by the junction of paddlewheel SBUs, which are formed by dimeric units of two metals connected by four 1,3,5-benzenetricarboxylate ligands (1,3,5-btc).[13]

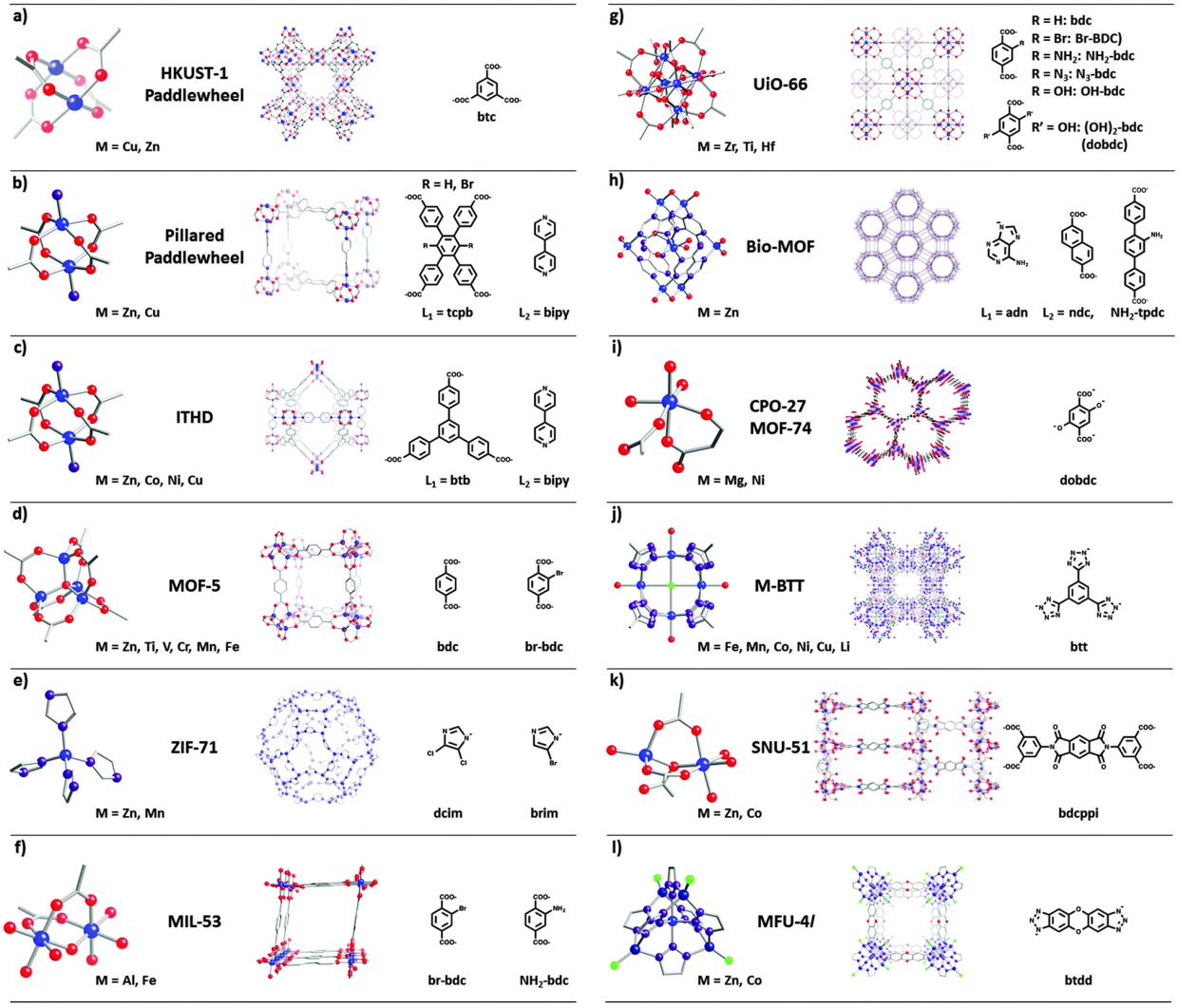

Figure 1.2. Examples of structural architecture of MOFs. Lattice structures and SBUs (metal nodes and organic linkers) of each MOF correspond to middle, and left and right pictures. Atom definition: blue - metal, red - oxygen, purple - nitrogen, grey - carbon, green - chlorine. Adapted image from Reference 12.

It is important to note that, depending on their connectivity, organic ligands can also be considered geometrical SBUs, since ligands themselves have complex structures with more than one node corresponding to a vertex of a net. In Figure 1.3 two examples of simple symmetric metal-containing SBUs joined by ditopic or tritopic ligands are showed. On the one hand, MOF-5 presents octahedrally shaped $Zn_4O(-CO_2)_6$ SBUs linked by ditopic 1,4- bdc ligands, forming a simple cubic net with six-coordinated (6-c) vertices that has the symbol **pcu**. On the other hand, in HKUST-1, the SBU is the paddlewheel $Cu_2(-CO_2)_4$ with four points of extension arranged at the vertices of a square. These SBUs are linked by tritopic 1,3,5-btc to a (3,4)-coordinated net with the RCSR symbol **tbo**.[14]

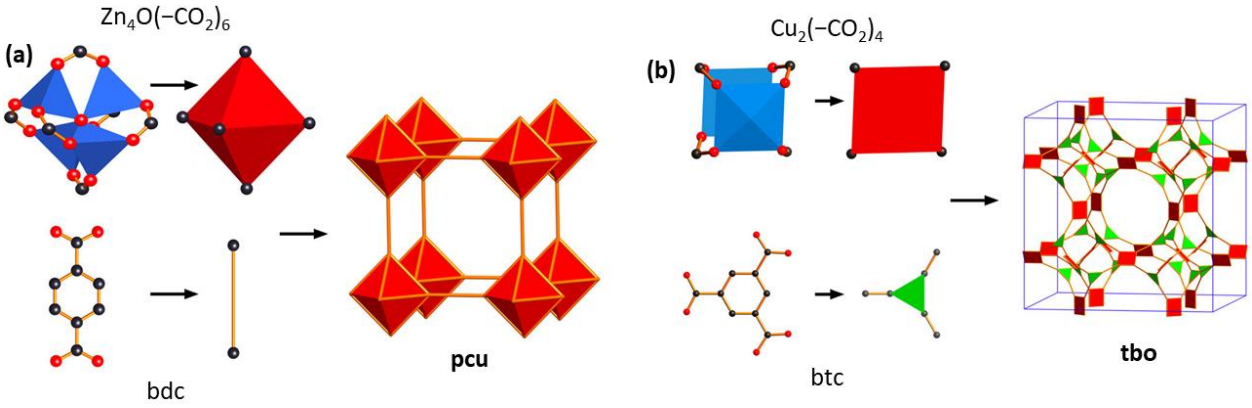

Figure 1.3. Two examples of the junction of metal-containing and ligand SBUs. **(a)** The components of MOF-5 showing the abstraction of the $Zn_4O(-CO_2)_6$ SBU as an octahedron, the ditopic 1,4-bdc linker as a rod, and their assembly into the **pcu** net. **(b)** The components of HKUST-1 showing the $Cu_2(-CO_2)_4$ paddlewheel abstracted as a square, the tritopic linker as a triangle, and their combination to form the **tbo** net. Adapted image from Reference 14a.

For MOFs with more complex ligands, their description as SBUs is an added difficulty; so, in general, only metals are described with these guidelines. Besides, it is important to highlight that the formation process of metal-SBUs during the MOF's synthesis makes them a key factor due to the following reasons: (1) its connecting points, along with the organic ligand, determine the framework topology; (2) in some cases, the cluster presents unsaturated sites than act as Lewis acids, improving certain properties of the material; and finally, (3) the stability of the MOF is determined by the bonding strength between the metal ion and the coordinative functional groups of organic ligands. For this latter, usually, bi- or multidentate ligands with carboxylate groups are used as organic ligands since they form chelates with the metal ions and lock them within the M-O-C cluster. Even so, nitrogen-containing ligands such as imidazoles are widely used for the synthesis of these materials.[15]

Porosity

The increasing interest in MOFs is partially given by their ultrahigh and chemically tailorable porosity since their high internal surface area is a desirable property in applications such as catalysis and storage.[16] Additionally, the extraordinary variety in terms of composition and crystalline structure allows these materials to display ultralow density and permanent porosity consisting of well-defined pores and channels which can be tuned according to the desired properties.[17]

With the discovery of MOF-5 with a Langmuir surface area of 2900 m^2/g,[18] the door was opened to studies on new MOFs for gas adsorption, establishing the relationship between structure, shape and size of the pore and the functionalization of the pore surface (internal surface) of the material.[19] Computational

studies indicate that the maximum value of the surface area achievable by a MOF is over 14600 m^2/g, although today the MOFs with the largest Brunauer–Emmett–Teller (BET) surfaces are NU-109 and NU-110, with 7010 and 7140 m^2/g, respectively.[20]

Based on the principles of isoreticular synthesis, organic ligands that differ in their length but are equivalent in the degree of connectivity can generate the same type of network without affecting the characteristics of the SBU; in other words, the geometrical characteristics of the structure are maintained, even if the topology changes.[11] IRMOF family is a known example: based on the structure of MOF-5 described above, several isostructural compounds of different topological characteristics were obtained using a series of ditopic carboxylate links.[21] In this way, functionalization and size of pore could be varied (for instance, IRMOF-74-XI has a pore aperture of 98 Å) without changing the original cubic topology.[11]

Interpenetration

As a general rule, increasing the linker length may bring a rise in the adsorption capacity since the generated pores would be bigger and, therefore, have a higher pore surface. However, this is not necessarily true because long organic linkers often lead to interpenetrating frameworks, in which two or more separate frameworks self-assemble within each other when the pore space of an individual net is sufficiently large to accommodate additional nets.[22] The increase in pore size results in an increase of the empty space, thus the structure can become unstable. Interpenetration could significantly enhance the stability of frameworks and prevent their collapse minimizing the empty space by the formation of repulsive forces through void filling.[23] Although this phenomenon has been considered as a drawback for a long time because of the associated decrease in the available void space, MOFs with interpenetrated structures have demonstrated great potential, since their pore apertures can be tuned to the size of the gas molecules and the number of adsorption sites and their selectivity towards the target molecules is increased.[24]

Flexibility

Structural flexibility is another factor that allows the variation of pore sizes and surface areas of a MOF, being these changes consequence of external stimuli (mechanical stress, temperature and interactions with light, or electrical and magnetic). Dynamic features of the framework structure of these materials, also called soft porous crystals (SPCs), suffers reversible structural crystal-to-crystal or crystal-to-amorphous (or less crystalline) transformations, which are essentially phase transitions that promote

a drastic change in the unit cell volume (pore volume) since these materials transform between open pore and closed pore (cp) or narrow pore (np) and large pore (lp) forms.[25] Structural flexibility can be presented in the next forms: (a) breathing mode, where the space group and unit cell volume change during the displacement of atoms of the framework; (b) swelling mode, in which the unit cell volume is changed but maintaining the unit cell shape and space group; (c) ligand rotation, in which the spatial alignment of a ligand is changed by turning around a rotational axis; and, (d) subnetwork displacement that can only happen with interconnected individual frameworks by weak forces (van der Waals interactions) like interpenetrated frameworks.[26]

Functionalization

In addition, the introduction of functional groups onto the surfaces and/or open metal sites can enhance adsorption capacity because they act as adsorption sites where interactions between the surface and the adsorbate species occur. It should be noted that these interactions can be specific, allowing selective separation during adsorption.[27]

Chirality

The versatility and robustness of the crystal structures of MOFs may be also nurtured with chiral motifs, which may provide MOFs with novel applications, which are not only limited to their metal-organic backbone but also their porous structure and large surface area which may be coupled to those of achiral materials.[28] Control of chirality is of vital importance because chirality is a property that controls both molecular structures and functions, meaning that the partial loss of chirality, even if it is derived from a non-racemic mixture, undermines the properties. A clear example is the case of thalidomide: in the 50s this drug was prescribed to alleviate the symptoms of pregnancy, until it was discovered that it was a racemic mixture of which the R-enantiomer had the desired sedative properties, while the S-enantiomer induced fetal malformations.[29]

Despite chirality can affect the properties of MOFs in a similar way to that just described, due to their modular nature, the preparation of pure chiral MOFs could be easy applying synthesis in which a chiral building block is available, although achiral reagents can also give materials with chiral structures.[30] As Figure 1.4 shows, there are several examples of chiral MOFs that are classified as follows:

- ***Chiral MOFs with chiral ligands***. These compounds are synthesized using enantiopure ligands, being Cu(GHG) MOF an example of a chiral MOF generated from the combination between the peptide glycyl-L-histidylglycine (ghg) and Cu(II) acetate.[31]

- ***Chiral MOFs with chiral and achiral ligands***. In this type of MOFs, the chiral ligand directs the reaction to a single enantiomer. This group includes the MOF [NaLn(L-tar)(bdc)(H_2O)$_2$] (Ln = Sm, Eu, Gd, Tb, Dy, Ho, Er, Yb, Y), where the L-tartrate is the element that induces the chirality of the structure.[32]

- ***Chiral MOFs with achiral ligands***. In this case, the chirality occurs spontaneously, especially in the presence of chelate ligands or adding resolution agents (reactants or pure chiral solvents that direct the chirality of the final product but are not part of the composition). Generally, the synthesized structures have helical motifs (which are another expression of chirality) that extend in one of the axes of the asymmetric unit.[30] An example of these helical chiral materials is the family of MOFs with the formula {[Ln(btc)(H_2O)]·x(solvent)}$_n$, where Ln = Nd, Eu, Tb and solvent = H_2O, DMF.[32]

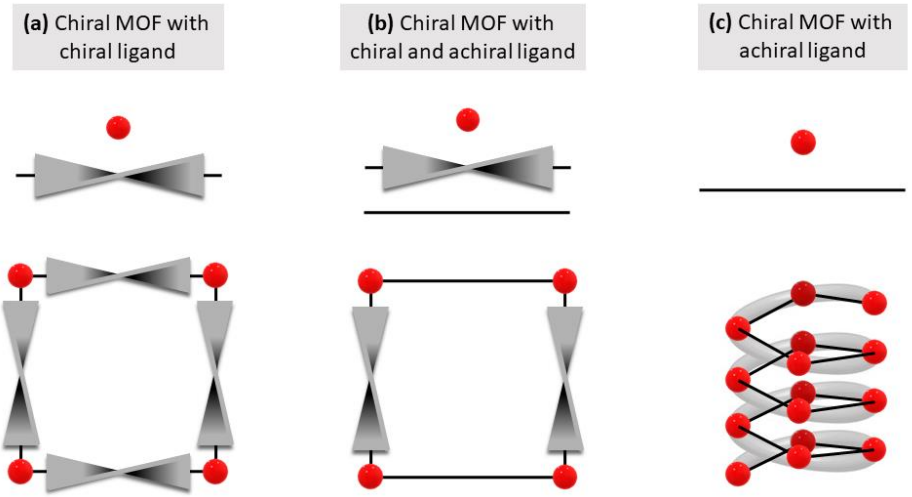

Figure 1.4. Schematic illustration of the three chiral MOFs types. Red dot: metal node; twisted bar: chiral ligand; straight line: achiral ligand.

This modular nature is the key to the application of MOFs: due to the great variety of existing ligands and metals, the number of possible combinations is infinite, making the chemical and structural richness of MOFs practically unique. In this way, by properly choosing between certain metals and ligands, MOFs with very specific properties can be designed and synthesized for a particular application; since, in general, the individual properties that the metals and the ligands can present are united when forming the MOF.[33] In

the following paragraphs, general physicochemical properties and applications of MOF´s will be introduced.

1.1.2. General physicochemical properties of MOFs

Due to the aforementioned structural and chemical versatility, CPs and MOFs display a wide variety of physicochemical properties that provide these materials with a large range of interesting applications (Figure 1.5).[34] In the biomedical field, MOFs are used as drug delivery systems (for antitumorals, nucleic acids, antivirals, antibacterial, biological gases, and cosmetics), as contrast agents with imaging properties, as molecular sensors (gases, ions, etc.) as non-enzymatic catalysts, and as biocatalyst, to cite some.[35] In the field of gas separation, MOFs can be used as molecular membranes to isolate pure or purer components from chemical mixtures, especially in gas separation processes where traditional technologies require high energy and economic intensity. The most important processes of this sector are hydrogen purification (H_2/N_2, H_2/CO, H_2/CO_2, H_2/hydrocarbons), air separation (N_2/O_2), natural gas sweetening (CO_2/CH_4), CO_2 capture (CO_2/air, CO_2/H_2), and hydrocarbon separation (olefins/paraffin, linear/branched isomers, etc.).[36] MOFs are also useful materials for purification and storage of valued products or toxic compounds. Among other applications, carbon dioxide capture is crucial to mitigate the greenhouse effect; hydrogen and methane storage is necessary to boost clean energy; and the separation and storage of toxic gases, such as carbon monoxide and ammonia, are important for pollution control and the synthesis of industrial chemicals.[37] Heterogeneous catalysis is a traditional application of MOFs since the porous and functionalized structures with their reusability, stability and easy separation become them in good candidates for a great number of catalytic reactions[38] including oxidation of alcohols or (cyclo)alkenes,[39] hydrogenation of unsaturated hydrocarbons,[40] photocatalytic CO_2 reduction and dye degradation,[41] and electrocatalytic hydrogen evolution,[42] to cite some. In the field of sensing, MOFs are divided into two classes: (a) insulating MOFs as optical sensors of small molecules, solvents and/or explosives, that undergo a colour or intensity change in the light emitted by the material; and, (b) conductive MOFs as electrochemical sensors, which emit electrical signals that facilitate the monitoring of catalytic reactions and adsorption processes, among other applications.[43] In the field of magnetism, ferromagnetic MOFs are emerging as promising and tuneable materials for data storage and processing. Currently, the materials par excellence in this application are inorganic semiconductors, as their electronic spin is easily modulated by the application of an electric or magnetic field but the use of hybrid materials such as MOFs allows the adjustment of electronic and magnetic properties for better performance.[44] In

this way, MOFs can be used as multifunctional materials for sensing, electronic applications, magnetic refrigeration, quantum computing or spintronics.[45]

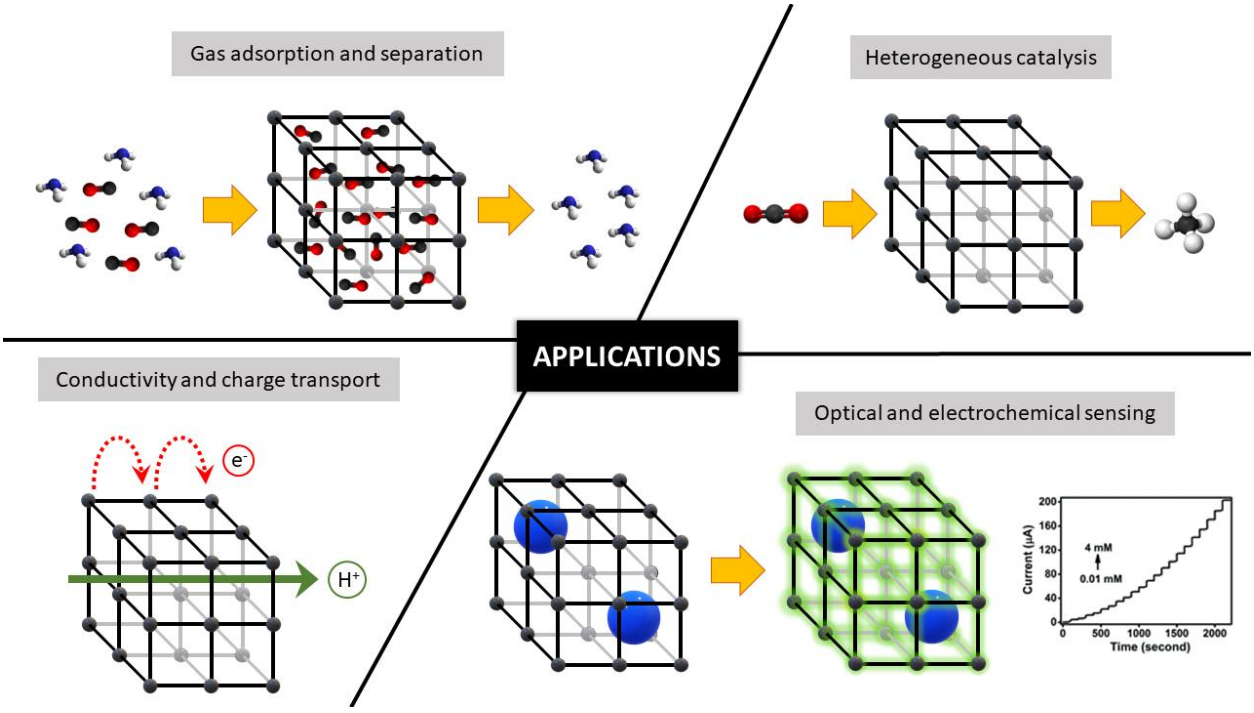

Figure 1.5. Some of the applications related to MOFs.

Thus, the application of each particular MOF is determined by its properties; therefore, in the following paragraphs, the properties of most interest for the development of the present thesis work will be detailed further.

Optical and electrochemical properties

Due to the sensing ability of MOFs is derived from their optical and/or electrochemical characteristics, the main physicochemical properties to be exploited in sensing MOFs are luminescence and/or conductivity.[46]

In the field of optical sensors, luminescent MOFs (LMOFs) with widely varied fluorometric sensing properties have been developed using the design principles of crystal engineering and structure-property correlations, resulting in a large and fast growth of literature related to this field. This has led to advancements in a number of crucial sensing domains, including biomolecules, environmental toxins, explosives, ionic species, and many others.[47]

The fact that both CPs and MOFs are designable and tuneable at the molecular level has caused them to become important materials in the field of photoluminescence (PL) based sensing since the combination of metal ions with organic ligands in crystalline structures enables a wide variety of excitation/emission scenarios that allow the characterization of the PL according to intrinsic factors (colour, intensity, lifetime) and also according to the response to external stimuli, such as temperature or pH changes, and presence of solvent molecules.[48] Luminescence of these materials arises from: (1) ligand-centered (LC) transitions; (2) metal-centered (MC) transitions; and, (3) charge transfer (CT) states, including ligand-to-ligand (LLCT), metal-to-ligand (MLCT), and ligand-to-metal (LMCT). LC and MC emissions are characterized for preserving to a large extent the luminescence of the free species, i.e. uncoordinated ligands and metal ions, respectively, whereas CT arises from interactions among ligands and ions, resulting in emissions highly dependent on a given CP. It should be noted that PL may also come from the interactions between a guest and the network. Through all these complex mechanisms and their combinations, CPs can present two types of PL emission processes: on the one hand is the fluorescence, which accounts for the direct re-emission of the absorbed light, involving a spin allowed transition with typical short lifetimes in the range of few nanoseconds centered at longer wavelength relative the absorption; and on the other hand is the phosphorescence, which is a spin-forbidden transition that has lifetimes of a timescale of seconds.[49] Currently, the material with the best luminescent properties described in the literature is the porous ZIF-8 of $\{[Zn_6(mim)_{12}]\cdot solvent\}_n$ formula with coronene molecules trapped in the pores, which presents an emission of a lifetime of ~22 s.[50]

In the field of electrochemical sensors and electronic devices, electrical conductivity and redox activity are the necessary properties to be exploited in MOFs. Typically, the insulating character of the ligands together with the minimal overlap between the π orbitals of these with the *d* orbitals of metals causes the poor electrical conductivity of CPs and MOFs.[51] Taking into account that electrochemical sensors are based on redox reactions of the analytes measured by electrical signals (current or electric potential), even though the potential use of MOFs because of their high surface area and pore volume, good absorbability, and high catalytic activity, their usual poor electrical conductivity makes difficult the application of MOFs in electrochemical systems.[52] That is why the study of different strategies to improve the conductivity of MOFs would enhance the development of new multifunctional conductive materials.[51] Until relatively recently, only one example of a MOF with electrical properties was known: the p-type $Cu[Ni(pdt)_2]$ (pdt = pyrazine-2,3-dithiolate) semiconductor with a conduction mechanism based on redox reactions.[53] At the present, the intrinsic conductivity of $[Fe(trz)_2]$ (trz = 1,2,3-triazolate) has also been demonstrated, although the conduction mechanism is still unknown.[54]

Magnetic properties

In the field of new generation electronic devices, magnetism and spin filtering ability are the physicochemical property of interest to be included in the MOFs. The simple preparation, versatility and control in the structural design of the CPs have made these materials also of great interest for the study of magnetism, especially in the field of Functional Molecular Magnetic Materials (FMMM)[55]. Research on these materials is focused on the search for single-molecule magnets (SMMs)[56] for their implementation in devices such as nanocoolers,[57] or in contrast agents for magnetic resonance imaging.[58] However, recently it has been shown that ions arranged in a metal-organic network are isolated due to the separation by the ligands, showing single-ion magnet (SIM) behaviour, which is very similar to that of SMMs.[59]

Both SIMs and SMMs are characterized by presenting a slow relaxation of magnetization, which is accompanied by a hysteresis below a blocking temperature (T_B) that indicates the presence of an energy barrier (U) for the change of magnetization's direction between ± M_S states.[60] The peculiarity of SIM/SMM-CPs is that each metal ion/cluster acts as an individual magnetic domain that responds to an external field because they are separated by ligands; so, the length of ligands has a direct influence over intramolecular interactions between magnetic domains located in the nodes, avoiding a negative effect in the magnetic properties of the material. Furthermore, given the hybrid and porous nature of these materials, they can present an association of various physical properties (magneto-optical, magnetic-porous), which would give rise to intelligent magnetic materials that respond to certain external stimuli.[61] In SIM-CPs metal clusters are based on paramagnetic transition metals (TM) and/or lanthanides (Ln) due to the (relative) large spin ground-state (S) and the anisotropic electron configurations, respectively.[62] Today, the best MOF with SIM behaviour is A 1D dysprosium chain constructed from a pyridine-N-oxide ligand with $\{[Dy(N'\text{-}(2\text{-hydroxybenzylidene})pyridine\text{-}N\text{-}oxide\text{-}carbohydrazide)(H_2O)_4]Cl_2{\cdot}2H_2O\}_n$ formula, which has an energy barrier of 227 K under zero *dc* field.[63]

Porosity

In the field of gas separation and/or gas storage, porosity is the main and necessary property to be exploited in MOFs. MOFs have large surface areas thanks to their porous structure, which is determined by the pore size and shape, and, as indicated below, these characteristics are important

because of their influence on gas diffusion and separation.[64] Regarding pore size, large pores permit an unrestricted gas diffusion that would not present differentiation between molecules according to size. But, as the pore size reduces, gas diffusion begins to be hindered by the confined space, and molecular diffusion will gradually evolve to surface diffusion. In this way, the diffusivity of each molecule becomes distinguishable because this characteristic is dependent on the kinetic diameter and molecular weight of each compound. Finally, when the pore size reaches a critical value, some molecules cannot cross the pore-structure because the high diffusion barriers, while the other components can be enriched in the internal cavities, giving molecular sieving separation.[65]

The shape of pores and channels also influences the adsorption processes depending on the shape and size of molecules. For example, bottleneck shaped channels will allow the diffusion of those compounds that can pass through the narrowest part of the channel. Likewise, channels with a zig-zag path have greater adsorption surfaces and larger distance to cross, improving interactions between molecules in diffusion and the surface. And finally, the shape of the pore-aperture can also influence both adsorption and selectivity; that is, even if the pore size is adequate, a bulky molecule will access a circular pore more easily than a triangular one.[66]

Selective adsorption can also occur owing to the affinity of specific compounds of the gas-mixture with the pore-surface. In this case, separation is based on the differences in physicochemical properties of mixture components such as the polarizability, the quadrupole moment or the acid-base behaviour, resulting in a higher enthalpy of adsorption of certain molecules over others. Hence, functionalization of pore surface is the most common strategy to achieve stronger binding interactions between adsorbates and the surface, improving the adsorption capacity of the CP/MOF.[67] Among the types of functionalization, open metal sites, also called coordinatively unsaturated sites (*cus*), are the most common in these materials and are considered key factors in many applications. This is because *cus* are considered the strongest binding sites for adsorption due to their Lewis acidity, which leads to higher adsorbent-MOF interactions compared to MOFs where the metal sites are fully occupied.[68]

Gas adsorption and purification have become important topics for the research related to energy storage and environmental remediation since these applications allow the use of H_2 and CH_4 as fuels and the CO_2 capture for greenhouse effect mitigation, among other things. As of today, MOFs have shown their usefulness for energy applications in the areas already mentioned. MOF-210 is the MOF with the highest capacity for H_2 storage while Al-soc-MOF-1 is a promising candidate for CH_4 storage,[69] and concerning CO_2 capture, the best results have been obtained with Mg-MOF-74 compound.[70]

Catalytic properties

Porosity is also a required property for MOF catalysts to improve interactions between adsorbed reactants and catalytic surfaces. To date, zeolites are the most used materials in catalytic applications due to their easy synthesis, variety in pore dimensions and their great thermal and hydrothermal stability, in addition to the great number of catalytically active sites of these inorganic structures. Considering that MOFs are analogous to zeolites, it can be thought that these coordination polymers can also be designed and prepared as catalysts to contain certain selective and active sites.[68]

In this field, photocatalytic MOFs are of particular interest for the present thesis work. Few years ago, MOF-5 was described as a hybrid material with semiconductor ZnO dots separated by bdc organic entities, being the first example of a MOF photocatalyst.[71] Since then, the development of MOFs as photocatalyst has become especially important since the possibility of organizing photoactive components in a functionalized structure makes them suitable materials to harvest solar energy.[72] Actually, NH_2-UiO-66 is one of the most studied MOFs regarding photocatalytic applications, which is based on a cubic structure built from hexameric Zr_6O_{32} units liked with ligands of 2-aminoterephthalate (ata).[73]

As will be discussed later, the present thesis work will partly focus on the development of MOFs with gas absorption properties and/or photocatalytic activity. In this sense, knowing the serious consequences of unlimited CO_2 emissions, there is no doubt about the urgency of taking action in the matter. Most of the research is focussed on the development of low- or zero-carbon alternatives, such as hydrogen gas, to minimize the use of fossil fuels.[74] But recently, carbon sequestering is getting attention for the possibility it provides for CO_2 recycling, opening a development opportunity to artificial photosynthesis as inexpensive, limitless and clean solar energy technology.[75]

Chirality

The aforementioned uses can be extended to chiral MOFs and, interestingly, in some cases, additional properties that arise from the unique interaction of chiral matter with electromagnetic waves and electronic currents can even be explored. The occurrence of a chiral crystal structure also opens the way to other less explored physical phenomena related to the intriguing interaction of these solids with the electromagnetic field, where left- and right-handed structures tend to manifest opposed effects,[76]

which are particularly useful and applied in non-linear optics and magnetic materials.[77] In particular, circularly polarized luminescence (CPL) has intriguing applications in spintronics,[78] quantum computation[79] and optical data storage.[80] Furthermore, it can be also used to induce exotic quantum phenomena such as the Floquet topological state,[81] as well as in other fields such as chirality sensing[82] and enhanced image contrast for advanced medical imaging technologies.[83] In all cases, the applicability of CPL demands a large value of the dissymmetry factor (g_{lum}), which is challenging since the mechanisms governing the chiroptical response are still somewhat obscure.[84] Despite the fact that most of studied materials so far are based on organic molecules, hybrid metal-organic materials can undoubtedly boost an enhanced performance by incorporating heavy atoms such as lanthanides(III).[85] As of today, the number of examples of chiral MOFs with chiroptical properties demonstrated by CPL is scarce. Among them are, on the one hand, the homochiral $\{[Zn_2(cam)_2(dap)]\}_n$ compound[86] and, on the other hand, the $[Tb_2(L/D\text{-}tar)_3(H_2O)_3]\cdot xH_2O\}_n$ compound which will be described in Chapter 4 of this thesis work.[87]

Although the applications of spin currents are important and very diverse (information storage devices, improvement of spin-dependent physicochemical processes), materials capable of acting as spin filters are limited in terms of variety and efficacy. These materials generate polarized currents of spins by scattering electrons with one of the spins and allowing the transfer of electrons with the "preferred" spin. Until 2012, the simplest method to achieve a current of this type was to pass an electronic current through a ferromagnetic material with a defined magnetization, which, due to the asymmetry in the density of states (DOS), filters one or another electronic spin. However, since the discovery in 2012 of the Chiral-Induced Spin Selectivity (CISS) effect, spintronics can be nourished by a new type of filters based on chiral and/or helical conductive materials, which are capable of coupling the electron's electronic spin with its linear momentum, favouring, likewise, the circulation of one of the spins and not that of the other.[88]

As of today, the scientific literature includes the next types of materials/molecules with different degrees of CISS effect: (1) there are those of a purely organic nature such as helicenes; (2) biomolecules such as proteins and peptides with a helical secondary structure, as well as chiral amino acids; [89] and, (3) a perovskite-type two-dimensional organic-inorganic hybrid system.[90] It is noteworthy that, to date, only a pair of enantiomeric chiral MOFs with CISS effect have been reported,[91] but their well-known versatility and ease of synthesis of this type of materials, as well as their solid nature, make them ideal materials for study as spin filters and potential implementation in solid devices with industrial applications.

1.2. Goals of the thesis

Based on the versatility of MOFs and the wide range of applications they offer, the present investigations were focused on the design, synthesis and structural characterization of novel (i) achiral and (ii) chiral multifunctional MOFs. The mentioned structural asymmetry/symmetry was a central property considered for the development of the new materials proposed in the present thesis project. In consequence, the goals of the thesis work, as well as the organization of the contents in the present document were also organized in the basis of the presence or absence of chirality in the synthesized MOFs, as summarized below:

GOAL 1. Design, synthesis, and structural and functional characterization of porous achiral MOFs.

The design, synthesis and characterization of achiral MOFs was performed with the goal of providing such materials with key properties including luminescence, gas absorption properties and/or photocatalytic properties. Thus, the work regarding porous MOFs has been organized as follows:

1.1) Design and synthesis of functionalized MOFs for gas adsorption and their subsequent full structural, thermal and chemical characterization.

1.2) Gas capture measurements (H_2, CO_2 and CH_4) and assessment of the selectivity.

1.3) Photocatalytic CO_2 reduction.

1.4) Analysis of additional properties (luminescence) that may involve new multifunctional applications.

GOAL 2. Design, synthesis, and structural and functional characterization of chiral/helicoidal MOFs.

The design, synthesis and characterization of chiral MOFs was performed with the goal of providing such materials with key properties including magnetism, CPL, conductivity and CISS effect. Based on these facts, the work related to chiral MOFs has been organized as follows:

2.1) Design and synthesis of enantiomerically pure pure pairs of chiral MOFs and their subsequent full structural, thermal and chemical characterization.

2.2) Analysis of purity and chiroptical properties, including UV-vis absorption spectroscopy, diffuse reflectande and circular dichroism (CD).

2.3) Analysis of additional properties as PL, CPL and magnetism that may involve new multifunctional applications.

2.4) Determination of the presence or absence of CISS effect in the synthesized MOFs, and their use in scenarios were the CISS effect is manifested, such as electronic spin filtering process. Measurement of electrical properties as bandgap, electron conductivity and spin filtering capability.

This dissertation therefore describes the design, synthesis and structural and functional characterization of new multifunctional MOFs:

Chapters 2 and 3 collect results in the field of new three-dimensional and porous heterometallic MOFs based on pyrimidine-4,6-dicarboxylic acid (H_2pmdc) and 5-cyanoisphthalic acid (H_2CNip) ligands are studied for gas adsorption and photocatalytic reduction of CO_2, while

Chapters 4 and 5 collect results related to three-dimensional enantiopure chiral MOFs mainly based on lanthanides (III) and 2,3-dihydroxybutanedioic acid (L/D-tartaric acid hereafter or L/D-H_2Tart), for the study of the CISS effect and their applications in spintronics, among others.

1.3. References

[1] Slater, A. G.; Cooper, A. I. "Porous materials. Function-led design of new porous materials", *Science* (2015), **348**, aaa8075.

[2] (a) Vermeiren, W.; Gilson, J. P. "Impact of zeolites on the petroleum and petrochemical industry", *Topics in Catalysis* (2009), **52**, 1131-1161. (b) Ribeiro, F. R. (**2012**). *Zeolites: science and technology*. Luxembourg, Springer Science & Business Media.

[3] Laxmi, S. K.; Sharmin, E.; Zafar, F.; Nishat, N. (2018). Coordination Polymers: A Brief Overview from Synthesis to Advanced Applications. In *Theoretical Models and Experimental Approaches in Physical Chemistry: Research Methodology and Practical Methods*. CRC Press.

[4] Yaghi, O. M.; Li, G.; Li, H. "Selective binding and removal of guests in a microporous metal-organic framework", *Nature* (1995), **378**, 703-706.

[5] Blay, V.; Bobadilla, L. F.; Cabrera-García, A. (2018). *Zeolites and Metal-Organic Frameworks: From lab to industry*. Amsterdam, Atlantis Press: Amsterdam University Press.

[6] Batten, S. R.; Champness, N. R.; Chen, X.; Garcia-Martinez, J.; Kitagawa, S.; Öhrström, L.; O'Keeffe, M., Paik Suh, M.; Reedijk, J. "Terminology of metal-organic frameworks and coordination polymers (IUPAC Recommendations 2013)", *Pure Appl. Chem.* (2013), **85**, 1715-1724.

[7] Rodrigues, M. O.; de Paula, M. V.; Wanderley, K. A.; Vasconcelos, I. B.; Alves Jr., S.; Soares, T. A. "Metal organic frameworks for drug delivery and environmental remediation: A molecular docking approach", *Int. J. Quantum Chem.* (2012), **112**, 3346-3355.

[8] Zhang, Z.; Zaworotko, M. J. "Template-directed synthesis of metal-organic materials", *Chem. Soc. Rev.* (2014), **43**, 5444-5455.

[9] Tan, Y. X.; Wang, F.; Zhang, J. "Design and synthesis of multifunctional metal-organic zeolites", *Chem. Soc. Rev.* (2018), **47**, 2130-2144.

[10] (a) Wang, B.; Xie, Y. B.; Yang, H.; Li, M.; Li, J. R. "A fluorescent 3-D metal-organic framework with unusual tetranuclear zinc secondary building units", *J. Coord. Chem.* (2014), **67**, 3484-3491. (b) Guillerm, V.; Kim, D.; Eubank, J. F.; Luebke, R.; Liu, X.; Adil, K.; Lah, M. S.; Eddaoudi, M. "A supermolecular building approach for the design and construction of metal-organic frameworks", *Chem. Soc. Rev.* (2014), **43**, 6141-6172.

[11] (a) Lu, W.; Wei, Z.; Gu, Z. Y.; Liu, T. F.; Park, J.; Park, J.; Tian, J.; Zhang, M.; Zhang, Q.; Gentle III, T. "Tuning the structure and function of metal-organic frameworks via linker design", *Chem. Soc. Rev.* (2014), **43**, 5561-5593. (b) Gándara, F. "Metal-organic frameworks: nuevos materiales con espacios llenos de posibilidades", *An. Quím.* (2012), **3**, 190-196.

[12] Deria, P.; Mondloch, J. E.; Karagiaridi, O.; Bury, W.; Hupp, J. T.; Farha, O. K. "Beyond post-synthesis modification: evolution of metal-organic frameworks via building block replacement", *Chem. Soc. Rev.* (2014), **43**, 5896-5912.

[13] Chui, S. S.; Lo, S. M.; Charmant, J. P.; Orpen, A. G.; Williams, I. D. "A chemically functionalizable nanoporous material $[Cu_3(TMA)_2(H_2O)_3]_n$", *Science* (1999), **283**, 1148-1150.

[14] (a) Li, M.; Li, D.; O'Keeffe, M.; Yaghi, O. M. "Yopological analysis of metal-organic frameworks with polytopic linkers and/or multiple building units and the minimal transitivity principle", *Chem. Rev.* (2014), **114**, 1343-1370. (b) O'Keeffe, M.; Eddaoudi, M.; Li, H.; Reineke, T.; Yaghi, O. M. "Frameworks for extended solids: geometrical design principles", *J. Solid State Chem.* (2000), **152**, 3-20.

[15] Bakuru, V. R.; DMello, M. E.; Kalidindi, S. B. "Metal-organic frameworks for hydrogen energy applications: advances and challenges", *ChemPhysChem* (2019), **20**, 1177-1215.

[16] Zhao, Dan; Timmons, Daren J; Yuan, Daqiang; Zhou, Hong-C. "Tuning the topology and functionality of metal-organic frameworks by ligand design", *Acc. Chem. Res.* (2011), **44**, 123-133.

[17] Furukawa, H.; Cordova, K. E.; O'Keeffe, M.; Yaghi, O. M. "The chemistry and applications of metal-organic frameworks", *Science* (2013), **341**, 1230444.

[18] Li, H.; Eddaoudi, M.; O'Keeffe, M.; Yaghi, O. M. "Design and synthesis of an exceptionally stable and highly porous metal-organic framework", *Nature* (1999), **402**, 276-279.

[19] Xu, T.; Jiang, Z.; He, M.; Gao, X.; He, Y. "Effect of arrangement of functional groups on stability and gas adsorption properties in two regioisomeric copper bent diisophthalate frameworks", *CrystEngComm* (2019), **21**, 4820-4827.

[20] Farha, O. K.; Eryazici, I.; Jeong, N. C.; Hauser, B. G.; Wilmer, C. E.; Sarjeant, A. A; Snurr, R. Q.; Nguyen, S. T.; Yazaydın, A. O.; Hupp, J. T. "Metal-organic framework materials with ultrahigh surface areas: is the sky the limit?", *J. Am. Chem. Soc.* (2012), **134**, 15016-15021.

[21] Eddaoudi, M.; Kim, J.; Rosi, N.; Vodak, D.; Wachter, J.; O'Keeffe, M.; Yaghi, O. M. "Systematic design of pore size and functionality in isoreticular MOFs and their application in methane storage", *Science* (2002), **295**, 469-472.

[22] Verma, G.; Butikofer, S.; Kumar, S.; Ma, S. (2020). Regulation of the degree of interpenetration in metal-organic frameworks. In *Metal-Organic Framework*. Springer, Cham.

[23] Jiang, H. L.; Makal, T. A.; Zhou, H. C. "Interpenetration control in metal–organic frameworks for functional applications", *Coord. Chem. Rev.* (2013), **257**, 2232-2249.

[24] Fernández, B.; Beobide, G.; Sánchez, I.; Carrasco-Marín, F.; Seco, J. M.; Calahorro, A. J.; Cepeda, J.; Rodríguez-Diéguez, A. "Controlling interpenetration for tuning porosity and luminescence properties of flexible MOFs based on biphenyl-4, 4'-dicarboxylic acid", *CrystEngComm* (2016), **18**, 1282-1294.

[25] Lee, J. H.; Jeoung, S.; Chung, Y. G.; Moon, H. R. "Elucidation of flexible metal-organic frameworks: Research progresses and recent developments", *Coord. Chem. Rev.* (2019), **389**, 161-188.

[26] Schneemann, A.; Bon, V.; Schwedler, I.; Senkovska, I.; Kaskel, S.; Fischer, R. A. "Flexible metal-organic frameworks", *Chem. Soc. Rev.* (2014), **43**, 6062-6096.

[27] D'Alessandro, D. M.; Smit, B.; Long, J. R. "Carbon dioxide capture: prospects for new materials", *Angew. Chem. Int. Ed.* (2010), **49**, 6058-6082.

[28] Gu, Z. G.; Zhan, C.; Zhang, J.; Bu, X. "Chiral chemistry of metal-camphorate frameworks", *Chem. Soc. Rev.* (2016), **45**, 3122-3144.

[29] Yoon, M.; Srirambalaji, R.; Kim, K. "Homochiral metal-organic frameworks for asymmetric heterogeneous catalysis", *Chem. Rev.* (2012), **112**, 1196-1231.

[30] Yan, Z. H.; Li, D.; Yin, X. B. "Review for chiral-at-metal complexes and metal-organic framework enantiomorphs", *Sci. Bull.* (2017), **62**, 1344-1354.

[31] Navarro-Sánchez, J.; Argente-García, A. I.; Moliner-Martínez, Y.; Roca-Sanjuán, D.; Antypov, D.; Campíns-Falcó, P.; Rosseinsky, M. J.; Martí-Gastaldo, C. "Peptide metal–organic frameworks for enantioselective separation of chiral drugs", *J. Am. Chem. Soc.* (2017), **139**, 4294-4297.

[32] Liu, W.; Tang, X. (2014). Chiral lanthanide metal-organic frameworks. In *Lanthanide Metal-Organic Frameworks* (29-74). Springer, Berlin, Heidelberg.

[33] (a) Zhu, Q. L.; Xu, Q. "Metal-organic framework composites", *Chem. Soc. Rev.* (2014), **43**, 5468-5512. (b) Kirchon, A.; Feng, L.; Drake, H. F.; Joseph, E. A.; Zhou, H. C. "From fundamentals to applications: a toolbox for robust and multifunctional MOF materials", *Chem. Soc. Rev.* (2018), **47**, 8611-8638.

[34] Gangu, K. K.; Maddila, S.; Mukkamala, S. B.; Jonnalagadda, S. B. "A review on contemporary metal-organic framework materials", *Inorg. Chim. Acta* (2016), **446**, 61-74.

[35] (a) Wheatley, P. S.; Butler, A. R.; Crane, M. S.; Fox, S.; Xiao, B.; Rossi, A. G.; Megson, I. L.; Morris, R. E. "NO-releasing zeolites and their antithrombotic properties", *J. Am. Chem. Soc.* (2006), **128**, 502-509. (b) Cai, H.; Huang, Y. L.; Li, D. "Biological metal-organic frameworks: Structures, host-guest chemistry and bio-applications", *Coord. Chem. Rev*. (2019), **378**, 207-221. (c) Giménez-Marqués, M; Hidalgo, T; Serre, C; Horcajada, P. "Nanostructured metal-organic frameworks and their bio-related applications", *Coord. Chem. Rev.* (2016), **307**, 342-360.

[36] (a) Lin, R. B.; Xiang, S.; Xing, H.; Zhou, W.; Chen, B. "Exploration of porous metal-organic frameworks for gas separation and purification", *Coord. Chem. Rev.* (2019), **378**, 87-103. (b) Kang, Z.; Fan, L.; Sun, D. "Recent advances and challenges of metal-organic framework membranes for gas separation", *J. Mater. Chem. A* (2017), **5**, 10073-10091. (c) Lin, J. Y. "Molecular sieves for gas separation", *Science* (2016), **353**, 121-122.

[37] (a) Li, H.; Wang, K.; Sun, Yu.; Lollar, C. T.; Li, J.; Zhou, H. C. "Recent advances in gas storage and separation using metal-organic frameworks", *Mater. Today* (2018), **21**, 108-121. (b) Li, B.; Wen, H. M.; Yu, Y.; Cui, Y.; Zhou, W.; Chen, B.; Qian, G. "Nanospace within metal-organic frameworks for gas storage and separation", *Mater. Today Nano* (2018), **2**, 21-49. (c) Ahmed, I.; Jhung, S. H. "Applications of metal-organic frameworks in adsorption/separation processes via hydrogen bonding interactions", *Chem. Eng. J.* (2017), **310**, 197-215.

[38] (a) Wen, Y.; Zhang, J.; Xu, Q.; Wu, X. T.; Zhu, Q. L. "Pore surface engineering of metal-organic frameworks for heterogeneous catalysis", *Coord. Chem. Rev.* (2018), **376**, 248-276. (b) Chughtai, A. H.; Ahmad, N.; Younus, H. A.; Laypkov, A.; Verpoort, F. "Metal-organic frameworks: versatile heterogeneous catalysts for efficient catalytic organic transformations*", Chem. Soc. Rev.* (2015), **44**, 6804-6849. (c) Liang, J.; Liang, Z.; Zou, R.; Zhao, Y. "Heterogeneous catalysis in zeolites, mesoporous silica, and metal-organic frameworks", *Adv. Mater.* (2017), **29**, 1701139.

[39] Dhakshinamoorthy, A.; Asiri, A. M.; Garcia, H. "Metal-organic frameworks as catalysts for oxidation reactions", *Chem. Eur. J.* (2016), **22**, 8012-8024.

[40] Wang, Q.; Astruc, D. "State of the art and prospects in metal-organic framework (MOF)-based and MOF-derived nanocatalysis", *Chem. Rev.* (2019), **120**, 1438-1511.

[41] Reddy, C. V.; Reddy, K. R.; Harish, V. V. N.; Shim, J.; Shankar, M. V.; Shetti, N. P.; Aminabhavi, T. M. "Metal-organic frameworks (MOFs)-based efficient heterogeneous photocatalysts: Synthesis, properties and its applications in photocatalytic hydrogen generation, CO_2 reduction and photodegradation of organic dyes", *Int. J. Hydrogen Energy* (2020), **45**, 7656-7679.

[42] Jin, S. "How to effectively utilize MOFs for electrocatalysis", *ACS Energy Lett.* (2019), **4**, 1443-1445.

[43] (a) Bhardwaj, S. K.; Bhardwaj, N.; Kaur, R.; Mehta, J.; Sharma, A. L.; Kim, K. H.; Deep, A. "An overview of different strategies to introduce conductivity in metal-organic frameworks and miscellaneous applications thereof", *J. Mater. Chem. A* (2018), **6**, 14992-15009. (b) Kumar, P.; Deep, A.; Kim, K. H. "Metal organic frameworks for sensing applications", *Trends Anal. Chem.* (2015), **73**, 39-53.

[44] Dong, R.; Zhang, Z.; Tranca, D. C.; Zhou, S.; Wang, M.; Adler, P.; Liao, Z.; Liu, F.; Sun, Y.; Shi, W. "A coronene-based semiconducting two-dimensional metal-organic framework with ferromagnetic behavior", *Nat. Commun* (2018), **9**, 1-9.

[45] Mínguez-Espallargas, G.; Coronado, E. "Magnetic functionalities in MOFs: from the framework to the pore", *Chem. Soc. Rev.* (2018), **47**, 533-557.

[46] Anik, Ü.; Timur, S.; Dursun, Z. "Metal-organic frameworks in electrochemical and optical sensing platforms: a review", *Microchim. Acta* (2019), **186**, 196.

[47] Lustig, W. P.; Mukherjee, S.; Rudd, N. D.; Desai, A. V.; Li, J.; Ghosh, Sujit K. "Metal-organic frameworks: functional luminescent and photonic materials for sensing applications", *Chem. Soc. Rev.* (2017), **46**, 3242-3285.

[48] San Sebastian, E.; Rodríguez-Diéguez, A.; Seco, J. M.; Cepeda, J. "Coordination polymers with intriguing photoluminescence behaviour: the promising avenue for greatest long-lasting phosphors", *Eur. J. Inorg. Chem.* (2018), 2155-2174.

[49] Heine, J.; Müller-Buschbaum, K. "Engineering metal-based luminescence in coordination polymers and metal-organic frameworks", *Chem. Soc. Rev.* (2013), **42**, 9232-9242.

[50] Mieno, H.; Kabe, R.; Notsuka, N.; Allendorf, M. D.; Adachi, C. "Long-lived room-temperature phosphorescence of coronene in zeolitic imidazolate framework ZIF-8", *Adv. Opt. Mater* (2016), **4**, 1015-1021.

[51] Talin, A. A.; Centrone, A.; Ford, A. C.; Foster, M. E.; Stavila, V.; Haney, P.; Kinney, R. A.; Szalai, V.; El Gabaly, F.; Yoon, H. P.; Leonard, F.; Allendorf, M. D. "Tunable electrical conductivity in metal-organic framework thin-film devices", *Science* (2014), **343**, 66-69.

[52] Fang, X.; Zong, B.; Mao, S. "Metal-organic framework-based sensors for environmental contaminant sensing", *Nano-Micro Lett.* (2018), **10**, 64.

[53] Kobayashi, Y.; Jacobs, B.; Allendorf, M. D.; Long, J. R. "Conductivity, doping, and redox chemistry of a microporous dithiolene-based metal-organic framework", *Chem. Mater.* (2010), **22**, 4120–4122.

[54] Gándara, F.; Uribe-Romo, F. J.; Britt, D. K.; Furukawa, H.; Lei, L.; Cheng, R.; Duan, X.; O'Keeffe, M.; Yaghi, O. M. "Porous conductive metal-triazolates and their structural elucidation by the charge-flipping method", *Chem. Eur. J.* (2012), **18**, 10595-10601.

[55] (a) Miller, J. S.; Drillon, M. (2001). *Magnetism: Molecules to materials IV*. John Wiley & Sons. (b) Gatteschi, D.; Bogani, L.; Cornia, A.; Mannini, M.; Sorace, L.; Sessoli, R. "Molecular magnetism, status and perspectives", *Solid State Sci.* (2008), **10**, 1701-1709.

[56] (a) Winpenny, R. (2012). *Molecular cluster magnets*. World Scientific Books, Singapore. (b) Brechin, E. K. "Introduction to the themed issue on molecular magnets", *Dalton Trans.* (2010), **39**, 4671-4671. (c) Feltham, H. L. C.; Brooker, S. "Review of purely 4*f* and mixed-metal n*d*-4*f* single-molecule magnets containing only one lanthanide ion", *Coord. Chem. Rev.* (2014), **276**, 1-33.

[57] Zheng, Y. Z.; Zhou, G. J.; Zheng, Z.; Winpenny, R. E. P. "Molecule-based magnetic coolers", *Chem. Soc. Rev.* (2014), **43**, 1462-1475.

[58] (a) Hingorani, D. V.; Bernstein, A. S.; Pagel, M. D. "A review of responsive MRI contrast agents: 2005-2014", *Contrast Media Mol. Imaging* (2015), **10**, 245-265. (b) Caravan, P.; Lauffer, R. B. (2005). Contrast agents: basic principles. In *Clinical Magnetic Resonance Imaging*. Saunders, Philadelphia, USA.

[59] (a) Ishikawa, N.; Sugita, M.; Ishikawa, T.; Koshihara, S. Y.; Kaizu, Y. "Lanthanide double-decker complexes functioning as magnets at the single-molecular level", *J. Am. Chem. Soc.* (2003), **125**, 8694-8695. (b) Jurca, T.; Farghal, A.; Lin, P. H.; Korobkov, I.; Murugesu, M.; Richeson, D. S. "Single-molecule magnet behavior with a single metal center enhanced through peripheral ligand modifications", *J. Am. Chem. Soc.* (2011), **133**, 15814-15817. (c) Baldoví, J. J.; Coronado, E.; Gaita-Ariño, A.; Gamer, C.; Giménez-Marqués, M.; Minguez Espallargas, G. "A SIM-MOF: three-dimensional organisation of single-ion magnets with anion-exchange capabilities", *Chem. Eur. J.* (2014), **20**, 10695-10702. (d) Zhu, Y. Y.; Zhang, Y. Q.; Yin, T. T.; Gao, C.; Wang, B. W.; Gao, S. "A family of $Co^{II}Co^{III}_3$ single-ion magnets with zero-field slow magnetic relaxation: fine tuning of energy barrier by remote substituent and counter cation", *Inorg. Chem.* (2015), **54**, 5475-5486.

[60] Frost, J. M.; Harriman, K. L. M.; Murugesu, M. "The rise of 3-*d* single-ion magnets in molecular magnetism: towards materials from molecules?", *Chem. Sci.* (2016), **7**, 2470-2491.

[61] Milios, C. J.; Winpenny, R. E. (2014). Cluster-based single-molecule magnets. In *Molecular Nanomagnets and Related Phenomena*. Springer, Berlin, Heidelberg.

[62] Katsenis, A. D.; Brechin, E. K.; Papaefstathiou, G. S. (2014). Metal-Organic Frameworks from Single-Molecule Magnets. In *Metal-Organic Framework Materials - Encyclopedia of Inorganic and Bioinorganic Chemistry*. John Wiley & Sons.

[63] Chen, Q.; Meng, Y. S.; Zhang, Y. Q.; Jiang, S. D.; Sun, H. L.; Gao, S. "A 1D dysprosium chain with slow magnetic relaxation constructed from a pyridine-N-oxide ligand", *Chem. Commun.* (2014), **50**, 10434-10437.

[64] Wang, Y.; Tan, C.; Sun, Z.; Xue, Z.; Zhu, Q.; Shen, C.; Wen, Y.; Hu, S.; Wang, Y.; Sheng, T.; Wu, X. "Effect of functionalized groups on gas-adsorption properties: syntheses of functionalized microporous metal-organic frameworks and their high gas-storage capacity", *Chem. Eur. J.* (2014), **20**, 1341-1348.

[65] Wang, Yuxiang; Zhao, D. "Beyond equilibrium: metal-organic frameworks for molecular sieving and kinetic gas separation", *Cryst. Growth Des.* (2017), **17**, 2291-2308.

[66] Ramsahye, N. A.; Trens, P.; Shepherd, C.; Gonzalez, P.; Trung, T. K.; Ragon, F.; Serre, C. "The effect of pore shape on hydrocarbon selectivity on UiO-66(Zr), HKUST-1 and MIL-125(Ti) metal organic frameworks: Insights from molecular simulations and chromatography", *Microporous Mesoporous Mater.* (2014), **189**, 222-231.

[67] Kazemi, Sima; Safarifard, V. "Carbon dioxide capture in MOFs: the effect of ligand functionalization", *Polyhedron* (2018), **154**, 236-251.

[68] (a) Kökçam-Demir, Ü.; Goldman, A.; Esrafili, L.; Gharib, M.; Morsali, A.; Weingart, O.; Janiak, C. "Coordinatively unsaturated metal sites (open metal sites) in metal-organic frameworks: design and applications", *Chem. Soc. Rev.* (2020), **49**, 2751-2798. (b) Liu, J.; Chen, Li.; Cui, H.; Zhang, J.; Zhang, L.; Su, C. Y. "Applications of metal-organic frameworks in heterogeneous supramolecular catalysis", *Chem. Soc. Rev.* (2014), 43, 6011-6061.

[69] Li, H.; Li, L.; Lin, R. B.; Zhou, W.; Zhang, Z.; Xiang, S.; Chen, B. "Porous metal-organic frameworks for gas storage and separation: Status and challenges", *EnergyChem* (2019), **1**, 100006.

[70] Yu, J.; Xie, L. H.; Li, J. R.; Ma, Y.; Seminario, J. M.; Balbuena, P. B. "CO_2 capture and separations using MOFs: computational and experimental studies", *Chem. Rev.* (2017), **117**, 9674-9754.

[71] Alvaro, M.; Carbonell, E.; Ferrer, B.; Llabrés i Xamena, F. X.; Garcia, H. "Semiconductor behaviour of a metal-organic framework (MOF)", *Chem. Eur. J.* (2007), **13**, 5106-5112.

[72] Xu, H. Q.; Hu, J.; Wang, D.; Li, Z.; Zhang, Q.; Luo, Y.; Yu, S. H.; Jiang, H. L. "Visible-light photoreduction of CO_2 in a metal-organic framework: boosting electron-hole separation via electron trap states", *J. Am. Chem. Soc.* (2015), **137**, 13440-13443.

[73] Sun, D.; Fu, Y.; Liu, W.; Ye, L.; Wang, D.; Yang, L.; Fu, X.; Li, Z. "Studies on photocatalytic CO_2 reduction over NH_2-UiO-66(Zr) and its derivatives: Towards a better understanding of photocatalysis on metal–-organic frameworks", *Chem. Eur. J.* (2013), **19**, 14279-14285.

[74] Llamas, B.; Navarrete, B.; Vega, F.; Rodriguez, E.; Mazadiego, L. F.; Cámara, Á.; Otero, P. (2016). Greenhouse Gas Emissions - Carbon Capture, Storage and Utilisation. In *Greenhouse Gases*. BoD-Books on Demand.

[75] (a) Das, S.; Daud, W. M. A. W. "A review on advances in photocatalysts towards CO_2 conversion", *RSC Adv.* (2014), **4**, 20856-20893. (b) Kondratenko, E. V.; Mul, G.; Baltrusaitis, J.; Larrazábal, G. O.; Pérez-Ramírez, J. "Status and perspectives of CO_2 conversion into fuels and chemicals by catalytic, photocatalytic and electrocatalytic processes", *Energy Environ. Sci.* (2013), **6**, 3112-3135.

[76] Liu, W.; Tang, X. (2014). Chiral lanthanide metal-organic frameworks. In *Lanthanide Metal-Organic Frameworks*. Springer, Berlin, Heidelberg.

[77] (a) Kesanli, B.; Lin, W. "Chiral porous coordination networks: rational design and applications in enantioselective processes", *Coord. Chem. Rev.* (2003), **246**, 305-326. (b) Férey, G. "Hybrid porous solids: past, present, future", *Coord. Chem. Rev.* (2008), **37**, 191-214. (c) Verbiest, T.; Van Elshocht, S.; Kauranen, M.; Hellemans, L.; Snauwaert, J.; Nuckolls, C.; Katz, T. J.; Persoons, A. "Strong enhancement of nonlinear optical properties through supramolecular chirality", *Science* (1998), **282**, 913-915.

[78] (a) Farshchi, R.; Ramsteiner, M.; Herfort, J.; Tahraoui, A.; Grahn, H. T. "Optical communication of spin information between light emitting diodes", *Appl. Phys. Lett.* (2011), **98**, 162508. (b) Žutić, I.; Fabian, J.; Sarma, S. D. "Spintronics: Fundamentals and applications", *Rev. Mod. Phys.* (2004), **76**, 323.

[79] (a) Wagenknecht, C.; Li, C. M.; Reingruber, A.; Bao, X. H.; Goebel, A.; Chen, Y. A.; Zhang, Q.; Chen, K.; Pan, J. W. "Experimental demonstration of a heralded entanglement source", *Nat. Photonics* (2010), **4**, 549-552. (b) Sherson, J. F.; Krauter, H.; Olsson, R. K.; Julsgaard, B.; Hammerer, K.; Cirac, I.; Polzik, E. S. "Quantum teleportation between light and matter", *Nature* (2006), **443**, 557-560.

[80] Wang, C.; Fei, H.; Qiu, Y.; Yang, Y.; Wei, Z.; Tian, Y.; Chen, Y.; Zhao, Y. "Photoinduced birefringence and reversible optical storage in liquid-crystalline azobenzene side-chain polymers", *Appl. Phys. Lett.* (1999), **74**, 19-21.

[81] (a) Oka, T.; Aoki, H. "Photovoltaic Hall effect in graphene", *Phys. Rev. B* (2009), **79**, 081406. (b) Wang, Y. H.; Steinberg, H.; Jarillo-Herrero, P.; Gedik, N. "Observation of Floquet-Bloch states on the surface of a topological insulator", *Science* (2013), **342**, 453-457.

[82] Yang, Y.; Da Costa, R. C.; Fuchter, M. J.; Campbell, A. J. "Circularly polarized light detection by a chiral organic semiconductor transistor", *Nat. Photonics* (2013), **7**, 634-638.

[83] Novikova, T.; Pierangelo, A.; De Martino, A.; Benali, A.; Validire, P. "Polarimetric imaging for cancer diagnosis and staging", *Opt. Photonics News* (2012), **23**, 26-33.

[84] (a) Wakabayashi, M.; Yokojima, S.; Fukaminato, T.; Shiino, K. I.; Irie, M.; Nakamura, S. "Anisotropic dissymmetry factor, g: Theoretical investigation on single molecule chiroptical spectroscopy", *J. Phys. Chem. A* (2014), **118**, 5046-

5057. (b) Abbate, S.; Lebon, F.; Longhi, G.; Passarello, M.; Liveri, V. T. "Triggering dissymmetry in achiral dye molecules by chiral solvents: Circular dichroism experiments and DFT calculations", *Chirality* (2011), **23**, 910-915. (c) Mori, T.; Grimme, S.; Inoue, Y. "A combined experimental and theoretical study on the conformation of multiarmed chiral aryl ethers", *J. Org. Chem.* (2007), **72**, 6998-7010.

[85] (a) Carr, R.; Evans, N. H.; Parker, D. "Lanthanide complexes as chiral probes exploiting circularly polarized luminescence", *Chem. Soc. Rev.* (2012), **41**, 7673-7686. (b) Bozoklu, G.; Gateau, C.; Imbert, D.; Pécaut, J.; Robeyns, K.; Filinchuk, Y.; Memon, F.; Muller, G.; Mazzanti, M. "Metal-controlled diastereoselective self-assembly and circularly polarized luminescence of a chiral heptanuclear europium wheel", *J. Am. Chem. Soc.* (2012), **134**, 8372-8375.

[86] Chen, S. M.; Chang, L. M.; Yang, X. K.; Luo, T.; Xu, H.; Gu, Z. G.; Zhang, J. "Liquid-phase epitaxial growth of azapyrene-based chiral metal-organic framework thin films for circularly polarized luminescence", *ACS Appl. Mater. Interfaces* (2019), **11**, 31421-31426.

[87] Huizi-Rayo, U.; Zabala-Lekuona, A.; Terenzi, A.; Cruz, C.M.; Cuerva, J. M.; Rodríguez-Diéguez, A.; García, J. A.; Seco, J. M.; San Sebastian, E.; Cepeda, J. "Influence of thermally-induced structural transformations over magnetic and luminiscence properties of tartrate-based chiral lanthanide organic-frameworks", *J. Mat. Chem. C* (2020), **8**, 8243-8256.

[88] (a) Binasch, G.; Grünberg, P.; Saurenbach, F; Zinn, W. "Enhanced magnetoresistance in layered magnetic structures with antiferromagnetic interlayer exchange", *Phys. Rev. B* (1989), **38**, 4828-4830. (b) Baibich, M. N.; Broto, J. M.; Fert, A.; Van Dau, F. N.; Petroff, F.; Etienne, P.; Creuzet, G.; Friederich, A.; Chazelas, J. "Giant magnetoresistance of (001) Fe/(001) Cr magnetic superlattices", *Phys. Rev. Lett.* (1988), **61**, 2472-2475.

[89] (a) Göhler, B.; Hamelbeck, V.; Markus, T. Z.; Kettner, M.; Hanne, G.F.; Vager, Z.; Naaman, R.; Zacharias, H. "Spin selectivity in electron transmission through self-assembled monolayers of double-stranded DNA", *Science* (2011), **331**, 894-897. (b) Carmeli, I.; Skakalova, V.; Naaman, R.; Vager, Z. "Magnetization of chiral monolayers of polypeptide: a possible source of magnetism in some biological membranes", *Angew. Chem. Int. Ed.* (2002), **41**, 761-764. (c) Xie, Z.; Markus, T. Z.; Cohen, S. R.; Vager, Z.; Gutierrez, R.; Naaman, R. "Spin specific electron conduction through DNA oligomers", *Nano Lett.* (2011), **11**, 4652-4655. (d) Kettner, M; Göhler, B; Zacharias, H; Mishra, D; Kiran, V; Naaman, R; Fontanesi, C.; Waldeck, D. H; Sęk, S.; Pawłowski, J. "Spin filtering in electron transport through chiral oligopeptides", *J. Phys. Chem. C* (2015), **119**, 14542-14547. (e) Aragonès, A. C.; Medina, E.; Ferrer-Huerta, M.; Gimeno, N.; Teixidó, M.; Palma, J. L.; Tao, N.; Ugalde, J. M.; Giralt, E.; Díez-Pérez, I. "Measuring the spin-polarization power of a single chiral molecule", *Small* (2017), **13**, 1602519. (f) Kettner, M.; Maslyuk, V. V.; Nürenberg, D.; Seibel, J.; Gutierrez, R.; Cuniberti, G.; Ernst, K.-H.; Zacharias, H. "Chirality-dependent electron spin filtering by molecular monolayers of helicenes", *J. Phys. Chem. Lett.* (2018), **9**, 2025-2030. (g) Torres-Cavanillas, R.; Escorcia-Ariza, G.; Brotons-Alcázar, I.; Sanchis-Gual, R.; Mondal, P. C.; Rosaleny, L. E.; Giménez-Santamarina, S.; Sessolo, M.; Galbiati, M.; Tatay, S. "Reinforced room-temperature spin filtering in chiral paramagnetic metallopeptides", *J. Am. Chem. Soc.* (2020), **142**, 17572-17580. (h) Wierzbinski, E.; Venkatramani, R.; Davis, K. L.; Bezer, S.; Kong, J.; Xing, Y.; Borguet, E.; Achim, C.; Beratan, D. N.; Waldeck, D. H. "The single-molecule conductance and electrochemical electron-transfer rate are related by a power law", *ACS Nano* (2013), **7**, 5391-5401. (i) Lu, H.; Wang, J.; Xiao, C.; Pan, X.; Chen, X.; Brunecky, R.; Berry, J. J.; Zhu, K.; Beard, M. C.; Vardeny, Z. V. "Spin-dependent charge transport through 2D chiral hybrid lead-iodide perovskites", *Sci. Adv. (*2019), **5**, eaay0571.

[90] Lu, H.; Wang, J.; Xiao, C.; Pan, X.; Chen, X.; Brunecky, R.; Berry, J. J.; Zhu, K.; Beard, M. C.; Vardeny, Z. V. "Spin-dependent charge transport through 2D chiral hybrid lead-iodide perovskites", *Sci. Adv.* (2019), **5**, eaay0571.

[91] San Sebastian, E.; Cepeda, J.; Huizi-Rayo, U.; Terenzi, A.; Santos, J.I.; Matxain, J.M.; Ugalde, J. M.; Mujica, V. "Enantiospecific response in cross-polarization solid-state nuclear-magnetic-resonance of optically active metal organic frameworks", *J. A.m. Chem. Soc.* (2020), **142**, 42, 17989-17996.

Chapter 2

Porous Metal-Organic Frameworks based on H_2pmdc Ligand for Gas Adsorption

2.1. Introduction

Porous crystalline materials have widespread uses in adsorption, catalysis, separation, purification, and energy storage and production. For years, the most attractive materials have been purely inorganic systems such as zeolites, due to their efficient manufacturing infrastructure and the inexpensive raw materials. Moreover, besides their applicability in adsorption and catalysis, porous materials have potential as electronic devices, in light-harvesting and energy transduction, as proton conductors, and in applications such as molecular sensing.[1] Still, zeolites lack several functionalities since their pore size, volume and specific surface area are limited and their surface chemistry is difficult to modulate by in situ or post-synthetic methods, hindering their application in other fields.[2]

Many of the current developments require new materials to be designed and built on demand, emphasizing the need for molecular-level control of the entire process, which is largely possible in the case of MOFs but not in zeolites due to their limited versatility.[3] Among porous materials, MOFs have greater potential in terms of diversity of applications, since their design based on the combination of inorganic polynuclear clusters (or SBUs) and organic linkers has enabled the creation of an enormous family of crystalline materials with infinite architectures, pore sizes and shapes. In addition, they generally possess thermal stability, ordered structure, ultra-low densities, large internal surface area, and simple synthesis. They have largely been studied now and have shown to be materials with broad-spectrum properties suited for plenty of physical and chemical applications.[4]

Porosity is the most characteristic property of MOFs, and its combination with other properties provided by building units, makes these materials largely multifunctional and applicable in various areas.[5] The peculiarity of porous adsorbents is that their surface can be subdivided into an external surface, which is defined as the interparticle surface outside the pores, and an internal surface, which is the surface of all pore walls. Although the pores can have a very varied morphology, since the combinations between the geometric shape and the pore structure (including the width and volume of the pores) can be diverse,[6] IUPAC recommends the following classification based on pore size: (a) macropores (diameter higher than 50 nm); (b) mesopores (diameter between 2 nm and 50 nm); and (c) micropores (diameter smaller than 2 nm). There is also the term nanopore, which covers the three previous categories but with an upper limit of ~100 nm.[7] Because construction units determine the structure of MOFs, these materials can have defined pores with diameters usually ranging in the micropore region, yet some mesoscopic MOFs are already known.[8]

It is worth mentioning the use of these porous materials in gas adsorption Design and tuneability of pore sizes, shapes and functionalities allows the use of MOFs in gas purification and/or storage, concretely in the storage of non-fossil fuels, such as H_2, or in the atmospheric CO_2 capture for greenhouse effect mitigation.[9] Porosity is also a very useful property for optical sensing. Porous MOFs perform as light-emitting sensors since their luminescent properties could be modified by the insertion of a guest molecule in the channel system and/or by the solvent exchange in the coordination sphere of the metal.[10] In the biomedical field, porous MOFs can also be used in drug delivery, since their drug loading ability, biodegradability, and adaptable functionality make them viable carriers for controllable drug release and to reduce side effects.[11] MOFs with permanent porosity are also useful in catalysis, since the tuneability of pore size and the pore surface functionalization to include dispersed active sites allows their application as heterogeneous catalysts to carry out selective reaction depending on the size of substrates and products, or on the affinity of the substrate with the pore surface.[12]

As stated in the General Introduction section of this thesis, one of the main general goals of this work was (GOAL 1) "The design, synthesis and structural and functional characterization of porous (achiral) MOFs, with the goal of providing such materials with key properties including luminescence, magnetism, gas absorption properties and/or photocatalytic properties". In particular, the present chapter collects the studies related to milestones 1.1, 1.2 and 1.4 (see page x of Chapter 1), *i.e.*: design and synthesis of functionalized MOFs for gas adsorption and their subsequent full structural, thermal and chemical characterization to carry out gas capture measurements (H_2, CO_2 and CH_4), assessment of the selectivity and to analyse additional properties such as luminescence that may involve new multifunctional applications.

Before jumping into the procedures and obtained results, the basics of adsorption phenomena are summarized below, which will aid in the interpretation and understanding of the results obtained and presented hereafter.

2.1.1 Porous materials and adsorption processes

Adsorption is a process of adhesion of a fluid (adsorbate) to a solid surface (adsorbent) with which it is in contact, giving a thin film of the adsorbate on the surface of the solid that leads to the enrichment of the fluid density at the interface.[13] There are two types of adsorption processes differentiated by the type of adsorbate-surface interaction. The processes originating from weak electric dipole interactions are included in the physical adsorption or physisorption, while the processes that generate changes in the

structure of bonding molecules are part of the chemical adsorption or chemisorption. So, being a surface-based physicochemical process consequent of surface energy, the surface concentration of the adsorbate molecules will be limited by surface morphology, porosity, pressures, and temperatures.[14] Although adsorption can occur on any type of surface, porosity improves this capacity since the surface exposed to the adsorbates is much larger. This is because, during the adsorption process, the species of the fluid phase flow into the porous solid adsorbent by diffusion to enter the inner surface of the adsorbent.[15]

Porous materials can be considered as a combination between a solid phase and different channels and cavities that pass through it,[16] and this type of material is characterized by having low density, large specific surface area and a range of novel properties in the physical, mechanical, thermal and electrical fields.[17] The characteristics and structure of this porosity will determine the potential uses of the solid since they have an important influence on the properties of the material.[16] As mentioned before, although porous materials can be designed to adsorb a plethora of substances, such as gas molecules or drugs,[18] the correct understanding of the internal structure is necessary to improve their properties and applications. This involves the characterization of basic parameters.[19]

Among the basic parameters that characterize porous materials, the most interesting are those defined below:[20]

- **Pore volume.** It is defined as the total empty volume generated by the cavities and channels of the porous material and is indicated in the units of cm^3/g.
- **Pore size.** This parameter is generally the distance between two opposite walls of the pore (diameter of cylindrical pores or width of slip-shaped pores), and it can determine the type of molecules that can access the internal structure according to their kinetic radius.
- **Specific surface area.** IUPAC defines it as the accessible area of solid surface per unit mass of a material. It should be noted that the value of the specific surface area depends on porosity, pore size distribution, shape, size, and roughness.[21]

Although all parameters are determinant in the adsorption process, the characterization of the specific surface area is the most important because it describes the available portion of the total surface area for adsorption. This characterization is usually done by physical adsorption of a gas (argon, krypton, or nitrogen) on the surface of the sample at cryogenic temperature.[22] Through this experiment, usually carried out with N_2 gas at 77 K, the adsorption isotherm is obtained, which indicates the amount of adsorbed molecules as a function of the partial pressure. Taking into account that the shape of such

isotherms holds a lot of information regarding the nature of the adsorption process, the IUPAC proposes the following classification of six types of adsorption isotherms (Figure 2.1):[7]

- **Type I.** This isotherm describes the adsorption of gas molecules on a microporous solid adsorbent (e. g. activated carbons, molecular sieve zeolites, COFs/MOFs, and certain porous oxides), which indicates that the surface is covered with a monolayer of adsorbed molecules.
- **Type II.** This is the usual shape for non-porous or macroporous adsorbents. It describes an unrestricted monolayer-multilayer adsorption since the curve does not display any saturation point, and the slope continues increasing because of the formation of the multilayer after the coverage of the surface with a monolayer.
- **Type III.** Non-porous or macroporous materials with very weak adsorbate-surface interactions usually display this type of isotherm. Despite this, interactions between adsorbate molecules are greater and at high pressures can give an unrestricted multilayer formation process.
- **Type IV.** This type of isotherms are found with mesoporous materials. The initial part of the curve is similar to Type II, indicating a monolayer-multilayer adsorption, followed by a hysteresis loop which is associated with capillary condensation taking place in mesopores.
- **Type V.** Mesoporous materials with weak adsorbate-surface interactions presents this type of isotherm, which also has a hysteresis because of the capillary condensation processes.
- **Type VI.** Non-porous materials with a homogeneous surface that undergo the stepwise formation of a multilayer present this type of staggered isotherms.

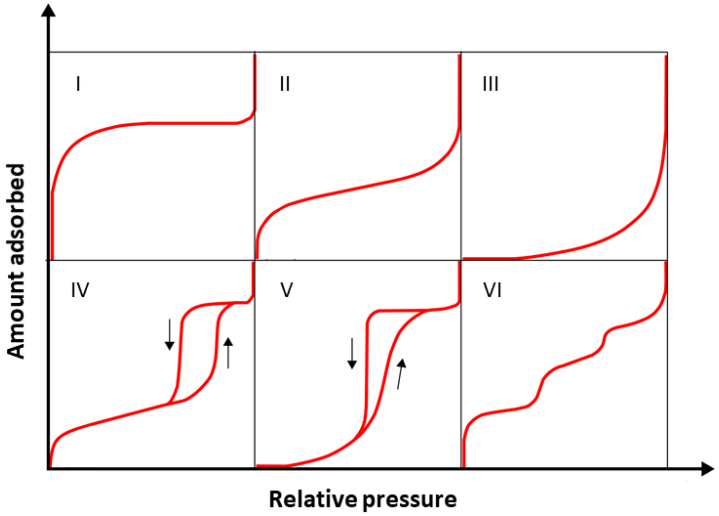

Figure 2.1. IUPAC classification of adsorption isotherms. Adapted image from Reference 7.

These isotherms are studied using different adsorption models that allow obtaining information such as the type of absorbate/surface interactions, the specific surface area, and the pore size and network (because the material can have different interconnected pore sizes), being the Langmuir and BET (Brunauer, Emmett and Teller) models the most extensively used.[23]

Langmuir isotherm model describes the adsorption process of a monolayer over a homogeneous surface, where interactions between adsorbates are considered negligible. This model is based on the relation of the adsorbed volume with the partial pressure of the adsorbate to calculate the fractional occupancy of the adsorption sites.[24] After the Langmuir model, other types of models have been developed, although the first to describe a multilayer adsorption was the BET model. This theory extends Langmuir's model of monolayer adsorption to multilayer adsorption, based on the fact that the adsorbed molecules can interact with adjacent molecules to form new layers. The BET model allows for the calculation of both total surface area (S_{total}) and the specific surface area (S_{BET}).[25]

These models demonstrate the importance of the characterization of porous materials, since the determination of parameters such as pore size and the specific surface area provide information on the potential of a material to be used in gas separation and adsorption. Nonetheless, it must be mentioned that MOFs materials, being characterized for possessing somewhat irregular pore surfaces, do not fit well to any of the common adsorption models, the reason why the information obtained by these fitting models must be only considered as approximations.[26] The most important applications of MOFs in the field of porous materials are discussed in the following section.

2.1.2. Gas separation and adsorption: applicability in H_2 and CH_4 storage, and CO_2 capture

In recent decades MOFs are gaining prominence since their high specific surface area and the large amount of space inside and outside the channels makes the adsorption capacity of MOFs far greater than other porous materials.[27] Among all the possible adsorption applications, the most studied is gas adsorption, since MOFs allow the storage of gaseous fuels and the separation and adsorption of toxic compounds.

2.1.2.1. H_2 storage

In the current situation where it is betting on alternative energy sources to fossil fuels, research of H_2 storage is of great importance. Hydrogen gas is a clean, highly abundant, and non-toxic renewable energy vector that releases only water vapor as a by-product because of its combustion process.[28] The

term "energy vector" means that the chemical energy released during the combustion of hydrogen is converted into electrical energy; that is, H_2 is not used directly as a fuel, but instead acts as a vector to obtain electrical energy.[29]

A competitive hydrogen fuel cell, which yields electrical energy through electrochemical reactions, should provide enough energy to cover a distance of 500 km for different means of transport, and for this, 6 kg of this gas would be sufficient since hydrogen has an optimum energy density in gravimetric terms (120 MJ/kg). At standard conditions, H_2 has a density of 0.089 g/L, so a spherical space of 5 m in diameter is required to store this amount of gas, making the implementation of these tanks unfeasible in any transport. Today's fuel cell vehicles rely on high-pressure tanks rated at 350 or 700 bar for on-board storage of gaseous hydrogen to minimize tank volume, requiring extra safety measures that make the fabrication process more expensive.[30]

The use of adsorbent materials is an attractive alternative that allows the H_2 storage without compression or liquefaction processes, in addition to the quick filling, use and reuse of the materials due to the fast kinetics of H_2 adsorption-desorption. Among porous materials, MOFs may be the most promising in H_2 adsorption, since their structural diversity and tuneability allow the improvement of adsorption and deliverable capacity through the design of pore size and volume, the inclusion of open metal sites, and other strategies.[31]

Although the optimal working conditions for hydrogen fuel cells is the storage of this gas at room temperature, under these conditions, MOFs and H_2 are limited to weak van der Waals interactions, which considerably decrease the adsorption capacity. Research has also shown that the gravimetric H_2 storage capacities at 77 K and high pressure are mostly proportional to the pore volumes and/or surface areas of MOFs, in such a way H_2 adsorption studies are mostly conducted under those conditions. The volumetric capacity of these materials must also be taken into account since absorbent MOFs have to be able to uptake large amounts of H_2 in a minimum volume. Table 2.1 shows some MOFs with optimal adsorption capacities in cryogenic conditions,[32] in addition to Ni_2(*m*-dobdc) (*m*-dobdc^{4-} = 4,6-dioxide-1,3-benzenedicarboxylate) MOF[33] that operates at room temperature thanks to its large number of *cus*.

Table 2.1. Selected examples of MOFs for H_2 storage.[32]

MOFs	S_{BET} (m^3/g)	Temperature (K)	Pressure (bar)	Total gravimetric capacity (wt %)	Total volumetric capacity (g/L)
MOF-5	3800	77	100	10	66
NOTT-112	3800	77	77	10	50.3
NU-111	5930	77	70	13.6	-
NU-100/PCN-610	6143	77	70	16.4	-
MOF-210	6240	77	80	17.6	44
IRMOF-20	4073	-	-	9.1[a]	51.0[a]
Ni_2(*m*-dobdc)	1321	298	-	-	11.0[b]
SNU-16	2590	77	70	10.0	
MOF-200	4530	77	80	16.3	36
MOF-205	4460	77	80	12.0	46
Mg-MOF-74	1510	77	100	4.9	49
PCN-46	2500	77	97	6.88	45.7
NOTT-115	3394	78	60	7.5	49.3
Mn-BTT	2100	77	90	6.9	60

2.1.2.2. CO_2 capture and sequestration

Carbon dioxide is also a gas closely related to the energy sector and the environment. The quest for new alternative energy sources mainly comes from the necessity to drop CO_2 emissions to the atmosphere during the combustion of fossil fuels, which is the main responsible for the greenhouse effect that is having large impact on global climate change. This has caused the need to develop, on the one hand, low-or zero-carbon alternatives to minimize the use of fossil fuels (a long-term strategy since existing systems are not prepared for this energy source), and on the other hand, carbon capture and storage (CCS) technologies which can separate and sequester CO_2 by certain devices.[34]

In the current environmental scenario, CCS provides the large-scale separation and long-term isolation of CO_2 emitted by sectors such as power generation and heavy chemical manufacturing. These technologies can be used as post-combustion, pre-combustion and oxyfuel combustion capture, even though the most studied and established strategy is the post-combustion. The post-combustion unit is placed next to power plants to CO_2 capture from previously purified flue gas. This previous step reduces the concentration of contaminants such as NO_x, SO_x, and particulate matters, and improves CO_2 capture[35] based on the chemical adsorption using different types of adsorbents, usually alkanolamine solutions. Still, the formation of C-N bonds between CO_2 and amine functionalities hinders the regeneration of the

adsorbent solution and increasing the costs.[36] Another problem is the low partial pressure of CO_2 since flue gas is at atmospheric pressure and its content in CO_2 is very low (13-15%). This decreases significantly the driving force for CO_2 separation and directly affects in its capture.[35]

To optimize the regeneration process of the adsorbents, materials with physical sorption properties such as activated carbon, zeolites, and porous polymers have been studied in CO_2 capture, paying special attention to MOFs. The wide variety of combinations between metal clusters and organic ligands allows to design and tune the physicochemical properties of MOFs by the predesign in synthesis and post-synthetic modifications. Therefore, high pore volumes and surface areas along with the tuneability of pore structures, surface functions, and other properties make MOFs promising candidates for CO_2 capture. Regarding CO_2 adsorption in MOFs, the material should work both at high and low pressures, since in the first case the material would serve to store CO_2 whereas it would be useful in the separation and sequestration of CO_2 in post-combustion flue gas (among other things) in the second case. Table 2.2 summarizes several MOFs studied in CO_2 adsorption.[37]

Table 2.2. Top 20 MOFs with high gravimetric CO_2 adsorption capacity at 298 K and 1 bar.[37]

MOF	Temp (K)	CO_2 uptake (mmol/g) / (mmol/cm³)			BET/Langmuir surface area (m²/g)	pore volume (cm³/g)	pore size (Å)
		1 bar	0.15 bar	0.1 bar			
Mg-MOF-74	298	8.6/7.7			1174/1733	0.648	10.2
	296	8.0/7.2	6.1/5.5	5.4/4.9	1495/1905		11
$Cu_3(btc)_2(H_2O)_{1.5}$ (hydrated 4 wt%)	298	8.4/–					
Co-MOF-74	298	7.5/–		2.8/–	957/1388	0.498	
MAF-X25ox	298	7.1/8.8	4.1/5.0		–/1286	0.46	
Ni-MOF-74	298	7.1/–		4.1/–	936/1356	0.495	
HP-e	298	7.0/–			1210/1270	0.45	9.1
MAF-X27ox	298	6.7/9.1	4.0/5.5		–/1167	0.41	
Mg_2(dobpdc)	298	6.4/–	4.9/–		3270/–	1.25	18.4
[Cu(Me-4py-trz-ia)]	298	6.1/–			1473/–	0.586	
Cu-TDPAT	298	5.9/4.6		1.4/1.1	1938/2608	0.93	
CPM-200-Fe/Mg	298	5.7/–			1459/2024	0.72	
CPM-33b	298	5.6/–			808/–	0.399	
$Cu_3(BTC)_2$(dry)	293	5.6/–			1400/–	0.57	
SIFSIX-2-Cu-i	298	5.4/6.7		1.7/2.1	735/821	0.26	5.15
MAF-X25	298	5.4/5.8			1566/–	0.56	
SIFSIX-1-Cu	298	5.3/–			1468/1651	0.56	8
CuTPBTM	298	5.3/–			3160/3570	1.268	
[Zn(btz)]	298	5.0/–			1151/1222	0.65	5.5
PEI-MIL-101-100	298	5.0/–	4.2/–		608.4/–	0.292	
dmen-Mg_2(dobpdc)	298	5.0/–	3.8/–		675/–		

2.1.2.3. CH_4 storage

The need for the development of low-carbon energy sources and substitution of fossil fuels has already mentioned above, even though this goal is set in the mid- to long-term because current energy systems are not ready for use with alternative energy forms. Still, the use of cleaner energy sources than fossil fuels during the transition is of great importance to mitigate CO_2 emissions to the atmosphere. In this regard, compounds with a high quantity of hydrogen atoms such as formic acid, methanol, and CH_4 are presented as potential fuels for the transition period, being CH_4 the most promising alternative.[38]

Methane has a higher hydrogen content than any other hydrocarbon fuel and a heat of combustion of ΔH^{298} = -890 kJ/mol, so CH_4 combustion produces high quantities of energy with relatively low CO_2 emissions. For this and its abundance and lower cost, natural gas, which consists mainly of CH_4, is a

potential substitute for diesel fuel.[39] However, its low energy density requires storage methods based on compression or liquefaction processes (Liquefied Natural Gas (LNG) or Compressed Natural Gas (CNG), among others). To promote the use of CH_4 as fuel, the development of new technologies with high volumetric energy density is necessary, betting on technologies based on adsorption processes due to its performance at low pressures and room temperature.[40]

Porous adsorbents such as zeolites and activated carbons have been studied to develop Adsorbed Natural Gas (ANG) technologies; but the relatively high packing densities, low micropore and hydrophilicity of zeolites, and the limited tuneable porosity of activated carbons, make MOFs the best option for CH_4 storage. Research has demonstrated the adequate CH_4 adsorption capacity of MOF because the interaction between the gas and the surface of MOFs is large enough. Thanks to the versatility and tuneability of MOFs, the porous structure can be modified and improved to obtain materials with adsorption capacities similar to the best activated carbons.[41] Some of the MOFs studied in this application field are listed in Table 2.3.[32]

Table 2.3. Selected examples of MOFs for CH_4 storage.[32]

MOFs	Framework density D_c (g/cm³)	BET surface area (m²/g)	Total uptake[a]		Working capacity[b]	
			(cm³/g)	(cm³/cm³)	(cm³/g)	(cm³/cm³)
HKUST-1	0.883	1850	302 (257)	267 (227)	215 (170)	190 (150)
UTSA-76	0.699	2820	363 (302)	257 (211)	282 (216)	197 (151)
Co(bdp)	-	2911	-	203 (161)	-	197 (155)[c]
Al-soc-MOF-1	0.34	5585	579 (362)	197 (123)	518 (306)	176 (104)
MOF-177	0.427	4500	475 (307)	203 (131)	426 (258)	182 (110)
UTSA-110	0.600	3241	402 (312)	241 (187)	317 (227)[c]	190 (136)[c]
NJU-Bai 43	0.639	3090	396 (315)	254 (202)	308 (228)	198 (146)
MOF-905	0.549	3490	377 (264)	207 (145)	331 (219)	182 (120)
MAF-38	0.761	2022	346 (297)	263 (226)	246 (197)	187 (150)
MFM-115a	0.611	3394	389 (204)	238 (186)	312 (226)	191 (138)
LIFM-82	0.922	1624	267 (214)	245 (196)	209 (156)	192 (143)
NU-125	0.589	3286	395 (315)	232 (182)	312 (226)	183 (133)
NU-111	0.409	4930	503 (337)	206 (138)	437 (271)	179 (111)

In short, MOFs are very useful materials in the field of gas adsorption, and their potential applicability depends on the structural design. The next section focuses on the design features of MOF both to improve adsorption capacities and the selective adsorption of the aforementioned gases (H_2, CO_2 and CH_4), since the functionalization of the MOF can change notably the physicochemical properties.

2.1.3. Design of MOFs for gas adsorption

Albeit porosity and surface area are leading factors determining the adsorption capacity of MOFs, attention must be paid also in those factors enhancing the interactions between adsorbate and pore surface of the MOF, which may be even selective for a particular molecule. This is because the adsorption mechanism depends on the characteristics of adsorbates and/or adsorbents (Figure 2.2), including their electrostatic interaction, acid-base interaction, H-bonding, π–π stacking/interaction, hydrophobic interactions, coordination, π-complexation and so on.[42]

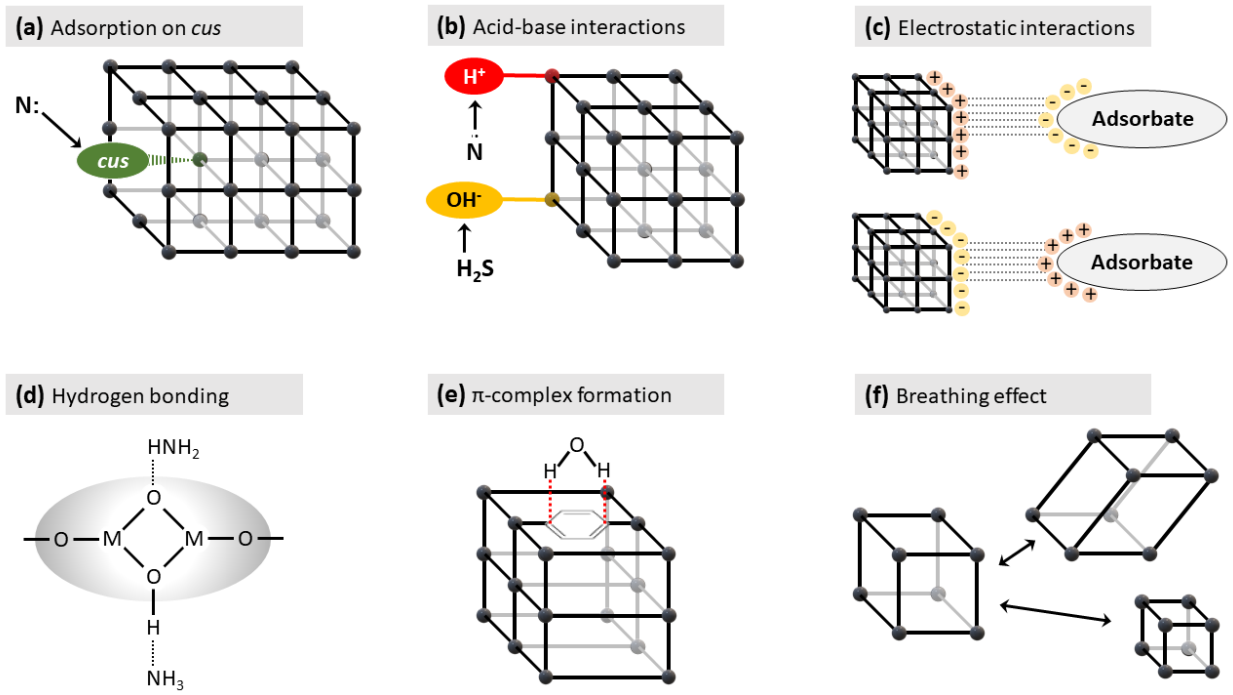

Figure 2.2. Some of the adsorbate-adsorbent interactions involved in the adsorption mechanisms in MOFs. Adapted image from Reference 43.

In this regard, most of the strategies for improving adsorption are based on the functionalization of MOFs, since these modifications alter the interaction/affinity between the guest and MOF framework. This functionalization can be carried out by two main approaches: using ligands with functional groups that can interact with adsorbate (either introduced during MOF synthesis or included by post-synthetic methods), and enabling of *cus* that provide open metal sites as adsorption points.[44] Both strategies are discussed in detail below.

2.1.3.1. Functionalized ligands

A common strategy to improve the adsorption properties of a MOF is the use of functionalized ligands. Although the introduction of functional groups on the pore surface can alter the MOF topology, in most cases it is possible to maintain the overall structure of the parent compound. The IRMOF family described in the General Introduction of this thesis (see page X of Chapter 1) is an example that several isostructural compounds of different pore sizes and functionalities can be obtained.[45]

Improving H_2 adsorption

As shown in Figure 2.3, although interactions with the metal cluster predominate in hydrogen adsorption, the weaker and dispersive interactions between H_2 molecules and the organic linkers can also influence the adsorption process. H_2 shows a moderate binding affinity towards aromatic rings, therefore MOFs with narrow pores (due to the size of H_2) and aromatic molecules oriented inside the pore can have a good adsorption capacity.[46] These aromatic rings can contain different multi-electron functional groups that enhance van der Walls interactions between the framework and H_2 molecules. Several computational studies focused on the influence of functional groups, such as −OH, $-NO_2$, $-CH_3$, −CN and −I,[47,48] conclude that the presence of any of the previous groups may also bring an increase in the adsorption capacity among which -CN functional group has shown the best results.[48]

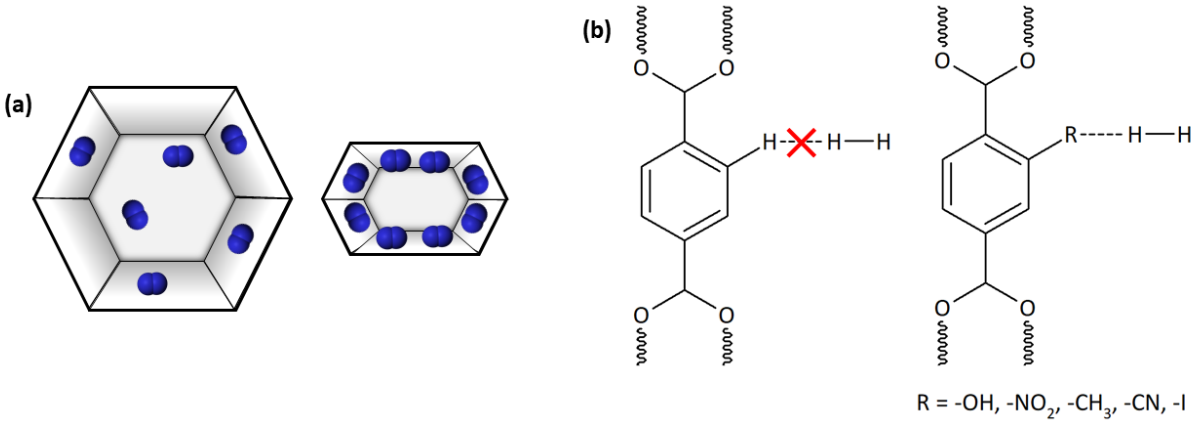

Figure 2.3. Principal strategies to improve H_2 adsorption: **(a)** Small pore sizes, and **(b)** Functionalized aromatic ligands.

Improving CO_2 adsorption

Some properties of CO_2 can provide interactions between the molecule and pore surface of the MOF, since CO_2 has quadrupolar moment, is polarisable, and presents Lewis acidity and basicity (Figure 2.4). In organic ligands with aromatic rings, π–quadrupole interactions occur placing a CO_2 molecule partially displace from the center of the ring to allow interactions between the oxygen and positively charged H atoms.[49] In addition to aromatic rings, basic functional groups such as azo-derivatives or amines are used to improve CO_2 adsorption through acid-base interactions.[50] CO_2 can also generate H-bonds with N-H functional groups, in addition to dipole-quadrupole interactions with C=O groups. Something similar happens with hydroxyl groups: oxygen atom serves as an electron-rich center and forms specific interactions with CO_2 due to its large quadrupole moment and high polarizability value. Finally, there is the pyridinic-N functional group that easily interacts with CO_2 due to the high Lewis basicity.[51]

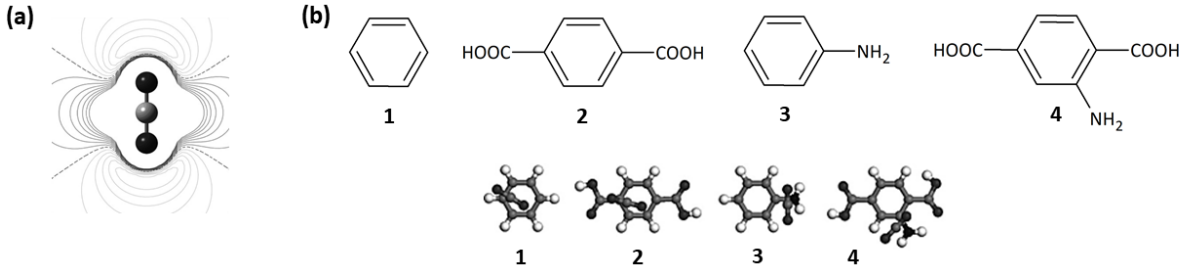

Figure 2.4. Description of the influence of the CO_2 quadrupolar moment over its adsorption. **(a)** Electrostatic potential map of the CO_2 molecule in the plane of the atoms. **(b)** Adsorption geometries of CO_2 in some organic compounds. Adapted image from Reference 49.

Improving CH_4 adsorption

CH_4 gas features weak binding affinity towards aromatic rings like H_2, so improving adsorbate/framework interactions demands the occurrence of polar groups into the organic ligand in order to enhance Coulombic interactions. N-rich aromatic ligands such as pyrazine, pyridine and thiophene[52] or the introduction of C≡C also enhances the adsorption capacity of MOF.[53] It should be noted that -NO_2 is the one that best interacts with CH_4 due to its electron withdrawing nature.[54] Figure 2.5 shows some examples of CH_4 and framework interactions.

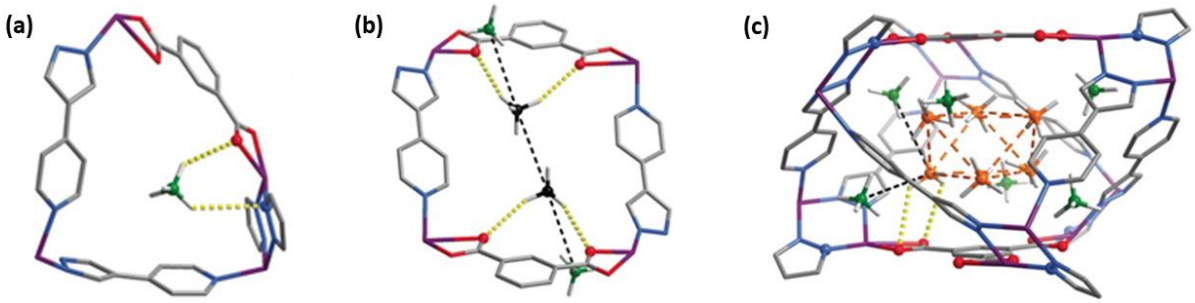

Figure 2.5. Adsorption sites of CH_4 in MAF-38 compound, where multiple host–guest contacts are indicated. Adapted image from Reference 55.

2.1.3.2. Coordinative unsaturated sites

Another way to improve gas adsorption is the presence of *cus* in pore surface. As-synthesized MOFs are prone to contain fully coordinated metal ions or clusters, that is, their coordination sphere is complete by the bonds formed with organic ligands and solvents. Provided that some of those bonds correspond to coordinated solvents, they can be removed during the activation of the material to make *cus* accessible, which act as Lewis acid sites on the surface that, as shown in Figure 2.6, specifically interact with gas molecules. *Cus* are usually the first loading sites since they may serve as charge-dense binding sites that interact strongly with gas molecules.[56] It must be noticed that this strategy is by far more challenging than ligand functionalization, since it requires an accurate design of not only initial components of the MOF but also the SBUs, at which coordination vacancies may occur. Besides, the introduction of *cus* can affect the robustness and stability of the MOF.[57]

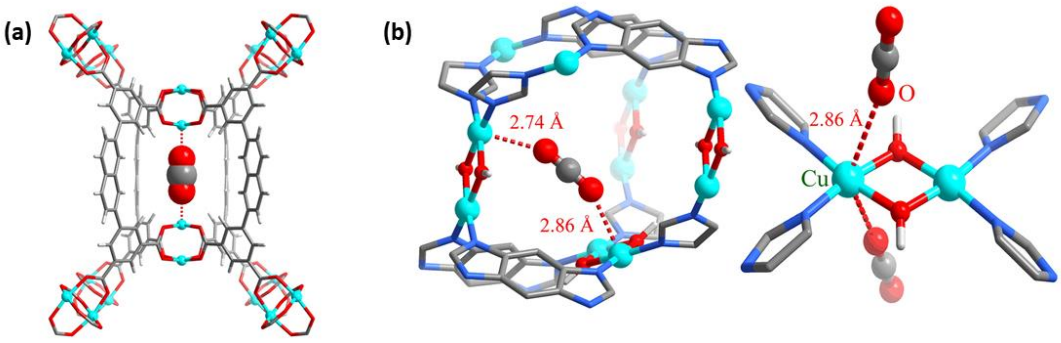

Figure 2.6. Examples of CO_2 adsorption in *cus* of **(a)** PCN-88 and **(b)** MAF-35.Adapted image from Reference 56.

Although these two strategies can be applied individually with the aim of improving the adsorption properties of a MOF, some types of organic ligands can provide these functional groups while also generating *cus* on metals due to their rigidity and structural geometry.

This is the case of the 4,6-pyrimidinedicarboxylate (pmdc) compound, which includes some of the above-mentioned features and is described in more detail in the following section.

2.1.4. pmdc ligand-based MOFs for gas adsorption

When the objective is the obtention of MOFs for their study in gas adsorption, it is very common to use rigid and directional heterofunctional organic ligands such as pmdc in its design (Figure 2.7), since they facilitate the synthesis guided by the five-membered chelating rings established with N-, O-heterocoordination to a metal ion. The advantage of this type of ligand lies on its capacity to further extend the coordination through the non-chelating carboxylate oxygen atoms, which can occupy few positions in the coordination sphere while they also impose large steric hindrance. Therefore, metal ions become saturated only if additional molecules are coordinated (hopefully solvent molecules) in such a way that secondary building blocks of the type MN_4O_2 and MN_4O_4 are rendered, which resemble the MN_4 tetrahedral building units (TBUs) that are so necessary for the construction of zeolite-like metal-organic frameworks (ZMOFs).[58]

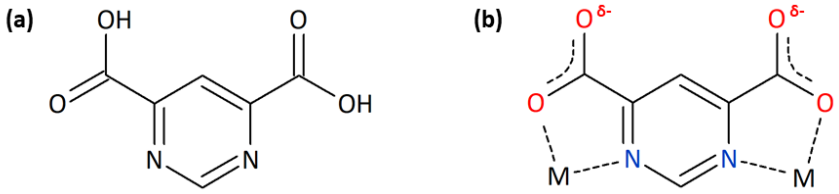

Figure 2.7. Different schemes of pmdc ligand. **(a)** 4,6-pyrimidinedicarboxylic acid (H_2pmdc) compound. **(b)** Scheme of pmdc forming five-membered chelating rings and the steric effect over non-chelating carboxylate oxygen atoms.

As shown in Figure 2.7, the chemical structure of pmdc is very suitable for the synthesis of MOFs with adsorption properties. This ligand contains an aromatic ring that can establish moderate/significant interactions with adsorbates. Besides, this ring contains pyrimidinic-N functional groups that can act as Lewis bases and generate new adsorption sites if exposed to the pore surface. As stated before, the two adjacent carboxylate groups can coordinate to a metal ion in a bidentate mode or through a carboxylate oxygen, leaving the other oxygen atoms as an electron-rich site that would improve interactions between the gas and the surface.

The first MOF showing permanent porosity reported with pmdc ligand was a sodalite-like In(III)-based material, in which indium metal ions present a fully saturated coordination sphere formed by four chelate rings with bis(bidentate) pmdc ligands. This microporous cationic MOF of formula

$[InNa_{0.36}K_{1.28}(pmdc)_2]_n^{0.64+}$ is counter-balanced by nitrate anions hosted in the pores, a fact that reduces the total pore-volume expected for the ideal sodalite-like framework.[59] Shortly after, an isostructural MOF to In(III)-pmdc was described based on Mn(II) ion, which obtained as crystalline powder which prevented its full structural X-ray characterization.[60] Despite its larger ionic radius, several tests were performed with Cd(II) based on the hypothesis that the latter metal ion would be able to support the eight-coordination geometry required by the structure, since it adopts analogous coordination environments to Mn(II). Fortunately, the Cd(II)-pmdc X-ray structure could be characterized, showing a 3D neutral MOF of $\{[Cd_2(\mu_4\text{-}pmdc)_2(H_2O)_2]\cdot 0.5DMF\cdot 4H_2O\}_n$ formula. It should be noted that, this MOF exhibited poor crystallinity which affected its porosity, so an exhaustive study to evaluate the influence of the synthetic method was accomplished, concluding that the solvent-free solid-state synthesis yields crystalline materials with an improved adsorptive capacity. It was also possible to partially replace Cd(II) with Mn(II) and Zn(II) in order to check the influence of the metal in the gas adsorption process.[61] Finally, another pair of heterometallic MOFs were obtained with Sc(III) ions, which combined with alkali metal M(I) (M = Li, Na), managed to replace Cd(II) by yielding a porous and neutral 3D structure. Although many synthetic methods were evaluated, these materials could only be grown as polycrystalline powders.[62]

MOFs based on pmdc ligand possess a porous three-dimensional structure that makes them good candidates for gas adsorption. Furthermore, the building units of these compounds grant certain structural properties that can significantly improve the adsorptive capacity of MOFs. On the one hand, the pmdc ligand itself, which is oriented towards the interior of the pore leaving accessible the adsorption points provided by the pyrimidine ring. On the other hand, is the fact that one of the metal coordination environments is accessible from the pore. This is because the planar geometry of the pmdc does not allow the metal coordination sphere to be saturated only with ligands, allowing the coordination of solvent molecules. Therefore, it is possible that, after a removal of solvent and subsequent activation, to transform these sites into *cus* that increase adsorbate/surface interactions during the adsorption process. In addition, thanks to previous studies, it has been shown that this structure can be formed by different metals, so this allows a study on the selectivity of adsorption due to the effect of *cus*.[61]

Due to the background of pdmc in terms of construction of 3D MOFs with gas adsorption capacity, this chapter aims to provide a further study on the adsorption properties of compounds $\{[ScM(\mu_4\text{-}pmdc)_2(H_2O)_2]\cdot solvent\}_n$ [where M(I) (M = Li, Na)]. The interest in the gas adsorption is derived from the presence of electropositive alkali metals, which increase the polar nature of these adsorption sites and may, hence, act as Lewis bases increasing electrostatic interactions with gases.[63] However, this kind of

metals detracts from the fact that their structure can undergo hydrolysis and collapse easily because of the high ionic character of M-O bond.[64] Therefore, it is necessary to use another metal that provides stability to the structure. Sc(III) is a good candidate since, in addition to being a transition metal that admits high coordination numbers, it affords a stable tripositive oxidation-state which balances the charges to generate a neutral structure, thus preventing the insertion of other ions into the pore system of the MOF.[65]

Different synthetic methods have been applied in order to obtain, on the one hand, single crystals that allow a complete structural characterization, and on the other, to see the influence that the synthesis has on the quality of the sample. As mentioned in previous reports, the synthetic methodology not only determines the compound to be crystallized, meaning that various compounds may be obtained under different synthetic conditions, but it also may lead to compounds with different morphology without affecting the structure and topology.[66] For instance, MOF-5 can be yielded as crystalline samples, showing specific surface areas between 3100 and 800 m^2/g depending on the synthesis.[67] Once the purity of the samples was verified, the thermal stability of these MOFs has been determined. To study both adsorption properties and applicability in the field of gas adsorption, porous materials must be pre-treated with an outgassing and activation process that requires vacuum conditions and temperatures above the boiling point of possible guests and coordinated solvent molecules to leave both pores and *cus* accessible; so, the structures must remain stable in this previous step to carry out the adsorption studies. Once the appropriate conditions for the outgassing and activation process have been determined, an adsorption study will be carried out using H_2, CO_2 and CH_4 gases. In this way, the adsorption capacity of the samples will be determined, and, at the same time, the effect of the metals present in the *cus* on the adsorption selectivity will be assessed.

2.2. Materials and methods

2.2.1. Compound synthesis

As aforementioned, although different synthetic methods could yield different compounds, in some cases the same MOF is obtained, even though some features as crystallinity or particle size could change. This dissertation describes MOFs based in pmdc ligand which were obtained with two different synthetic methods. Firstly, single crystals were synthesized applying the diffusion with interphase method. Low reaction yields and difficulties to separate single crystals from the reaction medium because of the

gelling of the solvents made necessary to synthesize the compounds through a simpler method, such as a solvent-free, obtaining the same MOFs as crystalline powder.[62] Table 2.4 lists the MOFs compounds herein reported, including the synthetic method used to obtain them.

Table 2.4. Synthesized and characterized compounds.[a,b]

Synthesis	Compound	Code
Diffusion with interphase	{[NaSc(μ-pmdc)$_2$(H_2O)$_2$]·2DMF}$_n$ Poly{[diaquabis(μ$_4$-pyrimidine-4,6-dicarboxylato-k^{2}N,O:k^{2}N',O':kO'':kO''')-scandium(III)sodium] bis(dimethylformamide)}	**NaSc (1)**
Solid-state (solvent-free)	{[NaSc(μ-pmdc)$_2$]}$_n$ Poly{[(μ$_4$-pyrimidine-4,6-dicarboxylato-k^{2}N,O:k^{2}N',O':kO'':kO''')-scandium(III)sodium]}	**NaSc_SF (2)**
	{[LiSc(μ-pmdc)$_2$(H_2O)$_2$]}$_n$ Poly{[(μ$_4$-pyrimidine-4,6-dicarboxylato-k^{2}N,O:k^{2}N',O':kO'':kO''')-scandium(III)lithium]}	**LiSc_SF (3)**

[a] pmdc = pyrimidine-4,6-dicarboxylato = $C_6H_2N_2O_4^{2-}$ [b] DMF = dimethylformamide = C_3H_7NO

Single crystals of NaSc (1). 5 mL of a solution of H_2O containing 0.1 mmol of $NaNO_3$ (0.0085 g) and 500 μL of $ScCl_3$ 0.2 M solution in HCl were poured into the bottom of a test tube (20 mL). Preparation of the $ScCl_3$ solution is detailed in Appendix I. 3 mL of a H_2O:DMF solution (1:1) were added dropwise to form the interphase. A third phase formed by 5 mL of a solution of DMF with two drops of MeOH containing H_2pmdc (0.0408 g, 0.2 mmol) was added dropwise, and finally, the test tube was sealed. Figure 2.8 represents the assembly where a test tube is inclined to slow down the diffusion of the phases. The slow diffusion of the solutions into the interphase yielded colourless cubic single crystals after one week, which were carefully removed from the test tube and washed with DMF and water. Unfortunately, difficulties to separate single crystals from the mother liquors because of the gelling of the reaction medium resulted in a low reaction yield.

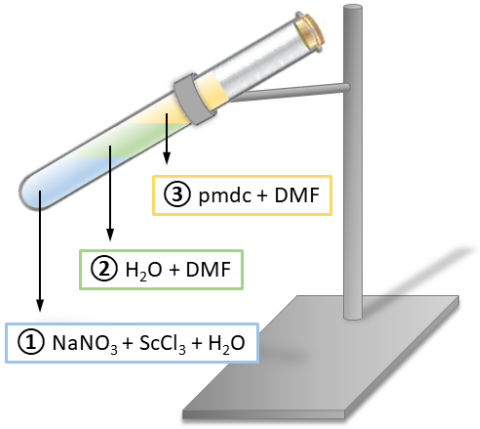

Figure 2.8. Assembly for the synthesis of NaSc (**1**) by diffusion method with interface in a test tube.

Powder of NaSc_SF (2). To synthesize this compound using solvent-free method,[62] 0.310 mmol of H_2pmdc (0.0633 g) was thoroughly grinded with 0.155 mmol of $NaNO_3$ (0.0132 g) by means of a mortar until a fine homogeneous powder was obtained. Then 0.075 mmol of Sc_2O_3 (0.0103 g) was grinded with the previous mixture, and the resulting powder was sealed into a long-stem glass beaker (1 cm × 10.8 cm, 1 mL capacity) and heated in an oven at 110 °C for 72 h, and slowly cooled down to room temperature (5 °C/h). The obtained product was washed with H_2O and MeOH.

Powder of LiSc_SF (3). The synthesis was equivalent to the synthesis of compound NaSc_SF (**2**), but 0.155 mmol of LiCl (0.0066 g) were used instead of $NaNO_3$.

2.2.2. Gas adsorption

The CH_4 (273 K), CO_2 (273 K) and H_2 (77 K) adsorption equilibrium isotherms were measured in a high-pressure volumetric adsorption system (up to 2800 KPa for CH_4 and CO_2 and 1500 KPa for H_2) built for this purpose. The equipment consists of a stainless-steel volumetric adsorption apparatus equipped with mass flow and backpressure controllers to set the desired gas pressure in the system. Two MKS Baratron absolute pressure transducers are used to accurately measure the pressure in the range of 0–1 bar and 1–32 bar. For each adsorption isotherm, approximately 0.2 g of the sample were degassed at 150 °C for at least 12 h down to a pressure of 10^{-5} mbar. Then the sample container was set to the adsorption temperature and increasing doses of the adsorptive gas were admitted. The Peng–Robinson equation applied to the adsorptive curves was used for the calculation of the adsorbed amount at each pressure, accounting for the non-ideality of the gases under the adsorption conditions. Isotherms are expressed as excess adsorbed amount as a function of the adsorptive pressure.

2.2.3. Luminescence

Fluorescence excitation and emission spectra were recorded on a Varian Cary-Eclipse Fluorescence Spectrofluorimeter (at room temperature RT) equipped with a xenon discharge lamp (peak power equivalent to 75 kW), Czerny–Turner monochromators, and an R-928 photomultiplier tube. For the fluorescence measurements, the photomultiplier detector voltage was fixed at 600 V while the excitation and emission slits were set at 5 and 2.5 nm. PL measurements at 50 K were done using a close cycle helium cryostat enclosed in an Edinburgh Instruments FLS920 spectrometer. For steady-state measurements in the UV-Vis range, an IK3552R-G HeCd continuous laser (325 nm) was used as excitation source, whereas a Müller-Elektronik-Optik SVX1450 Xe lamp was employed to collect the excitation spectra.

2.3. Results and discussion

2.3.1. Crystallographic analysis

Table 2.5 contains crystallographic data obtained for NaSc (**1**) compound at 100 K. Refinement conditions are detailed in Appendix I.

Table 2.5. Crystallographic data of NaSc (**1**).

Parameters	NaSc (1)
Empirical formula	$C_{18}H_{22}NaN_6O_{12}Sc$
M (g mol^{-1})	582.35
Cryst. System	Cubic
Space group	*Im-3m*
***a* (Å)**	18.9010(7)
***b* (Å)**	18.9010(7)
***c* (Å)**	18.9010(7)
V (Å^3)	6752.3(8)
Z	12

The electron density at the voids due to the presence of disordered solvent molecules was subtracted from the reflection data by the "squeeze" method as implemented in PLATON program. The count of electrons subtracted per void volume (of 1018 electrons in 2693 Å^3 for NaSc (**1**)), confirms that the compound contains two DMF molecules crystallized per formula unit. Additionally, the Na atoms showed a significantly high atomic displacement parameter along the O1w–Na–O2w vector, which was modeled

by disordering the atom into two positions. This disorder affects the coordination water molecules, being only possible to locate them for the Na site with the highest occupancy factor.

The following section provides more details on the structure of this MOF, which has been described using single-crystal X-ray diffraction (SCXRD) techniques.

2.3.2. Structural characterization of single crystals

Single-crystal X-ray diffraction

Crystallographic analysis of NaSc (**1**) reveals that this 3D and porous metal-organic framework is isostructural to the aforementioned family of porous compounds of indium-pmdc[59] and cadmium-pmdc.[61] Continuous Shape Measurements (CShMs) shows that these neutral structures present two different molecular building blocks (MBB) established by scandium (Sc^{3+}) and sodium (Na^{+}) ions coordinated to the pmdc ligands (see Appendix I). On the one hand, a tetrahedral building unit (TBU) is formed by the N_4O_4 donor set around the Sc1 atom, which has a triangular dodecahedron geometry (S_{DD} = 0.458) built up from the coordination of four chelating N/O moieties of pmdc (Figure 2.9a). On the other hand, alkali metal ions have a distorted octahedral geometry (S_{OC} = 0.366) formed by four nonchelating oxygen atoms of pmdc and two coordination water molecules (Figure 2.9b,

Table **2.6**), generating an arrangement that corresponds to a pseudo-square planar building unit (PSPBU). It is worth noticing that Na2 atom is severely disordered between two main dispositions along the O1w–Na2–O2w axis. Hence, in these MOFs the coordination mode exhibited by pmdc ligand is the μ_4-*$k^2N,O:k^2N',O':kO'':kO'''$* (Figure 2.10).

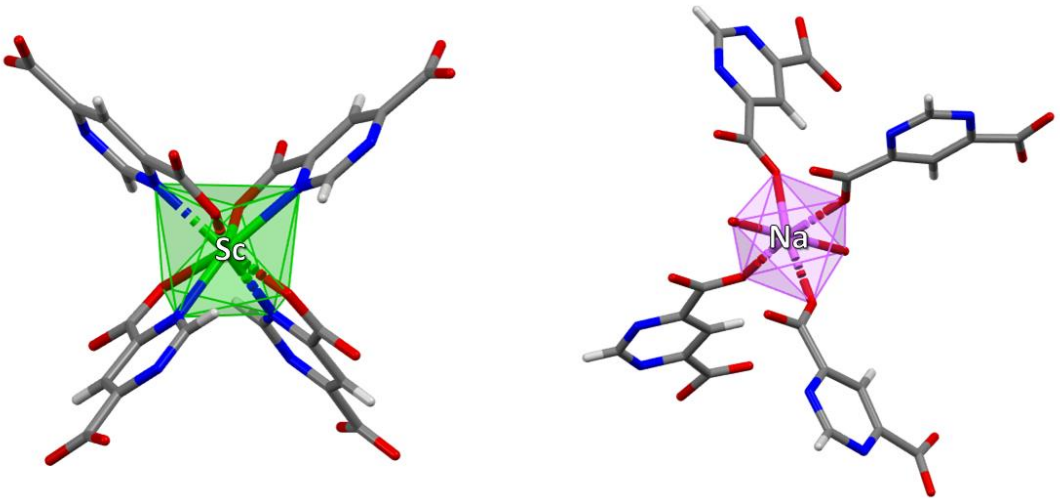

Figure 2.9. Building units of compound NaSc (**1**) with the atomic numbering scheme.

Table 2.6. Coordination bond lengths of NaSc (**1**) compound at 100 K.[a]

Bond	Length (Å)	Bond	Length (Å)
Sc1–N1 x 3	2.395(4)	**Na1–O2 x 2**	2.260(4)
Sc1–N1(i)	2.395(4)	**Na1–O2(ii)**	2.260(4)
Sc1–O1 x 3	2.165(3)	**Na1–O2(iii)**	2.260(4)
Sc1–O1(i)	2.165(3)	**Na1–O1w**	2.34(5)
		Na1–O2w	2.23(3)

[a] Symmetries: (i) x, -y, 1-z; (ii) z, y, 1-x; (iii) 1-x, y, z.

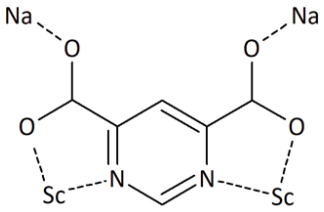

Figure 2.10. Coordination mode of the pmdc ligand.

As a result of such large connectivity afforded by the polytopic pmdc ligand, four TBU and two PSPBU are further linked one another into truncated octahedral β-cages, which may be considered as the secondary building unit (SBU) of the network. The connection of an octahedron with other four through TBU vertexes generates a **nbo** topological network (4-c) with the ($6^4.8^2$) point symbol,[68,69,70] which encloses big voids surrounded by β-cages (Figure 2.11).

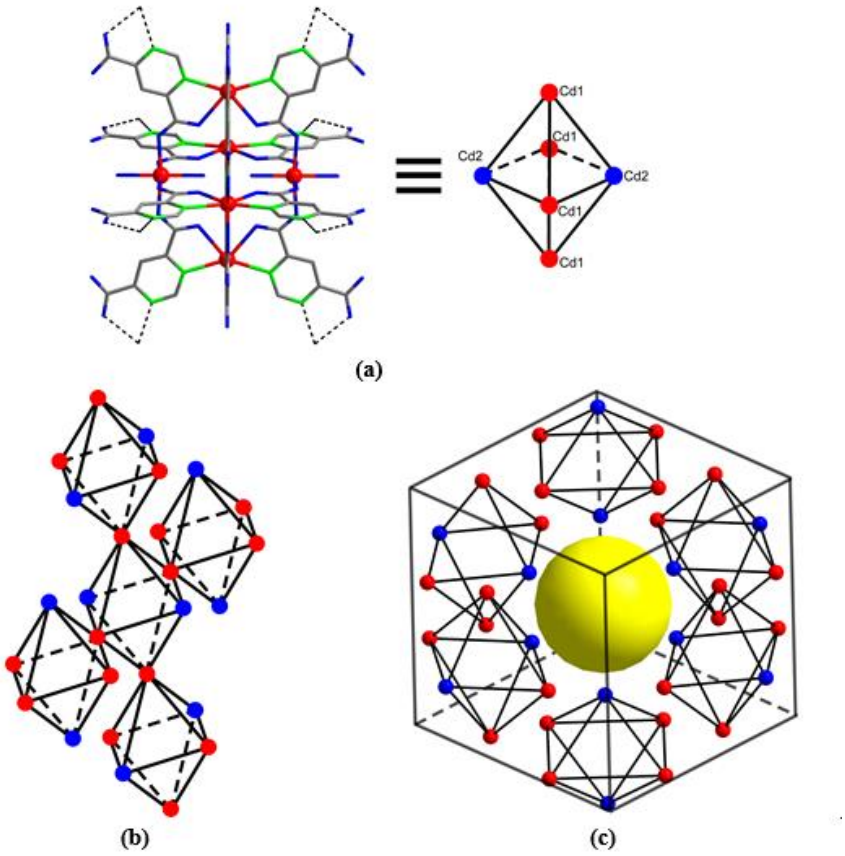

Figure 2.11. Topological network of NaSc (**1**). **(a)** Octahedral β-cage. **(b)** Interconnection between octahedra. **(c)** Schematic drawing of the biggest cavity within the structure.[62]

Cavities of NaSc (**1**) have been analyzed[71] by Monte Carlo procedure implemented in a code developed by Herdes and Sarkisov[72] in which a probe of incremental size explores the free volume. Before discussing the results obtained, it should be noted that in order to carry out these calculations, the hydrogens have had to be suppressed and the distance from the Na-Ow bond shortened to 2.1 Å; therefore, the values obtained will be slightly lower than those that will be specified below. As Figure 2.12a shows, this MOF presents two different scenarios depending on the presence of solvent molecules. Cavities of hydrated NaSc (**1**) with crystallization DMF molecules are interconnected by a 3D channel system that represents 38.1 % of the unit cell volume (Figure 2.12b). Its porous structure is a set of three main contributions: small cubic cavities of 2.72 Å inside β-cages with eight long "blades" of diameter of 6.03 Å, and isolated cages 2.72 Å. In the second scenario, where the anhydrous of NaSc (**1**) compound is obtained through the remove of solvent molecules, the pore sizes increase significantly giving β-cages with a diameter of 9.11 Å, cubes of 4.03 Å and bottleneck tunnels around 4.5 Å. In this way, and as can be seen in Figure 2.12c, the porosity of the anhydrous compound is enhanced to a 42.9 % of the unit cell volume. Considering

these results, gas molecules such as N_2, CO_2, and CO, which possess smaller kinetic radii (1.82, 1.65, and 1.85 Å, respectively) than the narrower regions of the framework, should be able to diffuse through the channel system. An interesting structural feature is that sodium atom occupying the PSPBU lies on the faces of the biggest cubic pore, so they could a priori behave as open-metal sites once the coordination water molecules are released (see Figure 2.11c).

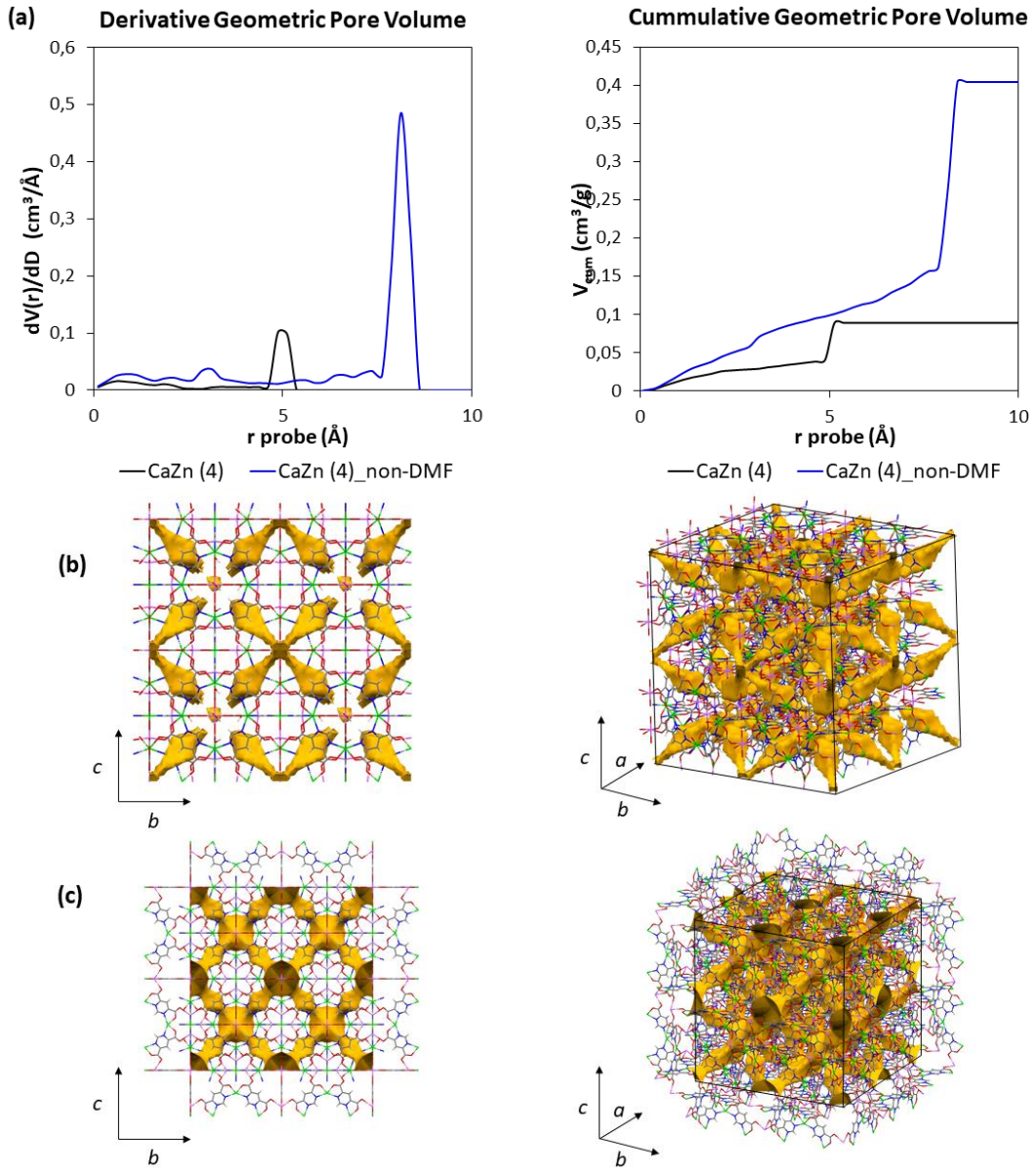

Figure 2.12. Description of porous structure of NaSc (**1**) and its anhydrous derivatives. **(a)** Exploration of free volume by Monte Carlo procedure; **(b)** Packing and potential accessible surface of NaSc (**1**) compound; **(c)** Packing and potential accessible surface of anhydrous NaSc (**1**) compound.

As aforementioned, sodium atom of the NaSc (**1**) crystal structure exhibits an octahedral coordination containing two coordinated water molecules. Their removal renders a *cus* that differs from the well-known open metal sites in the fact that the metal atom is sunk on the site being arranged below the pore surface, being somewhat hindered by the donor atoms in an attempt to maximize the coordination of the metal with carboxylate oxygen atoms. In fact, its disordered disposition with a minor occupancy placed so as to allow carboxylate moieties to establish chelating rings should be taken as an evidence. Therefore, this fragment may be considered as a pseudo-open-metal site (Figure 2.13).

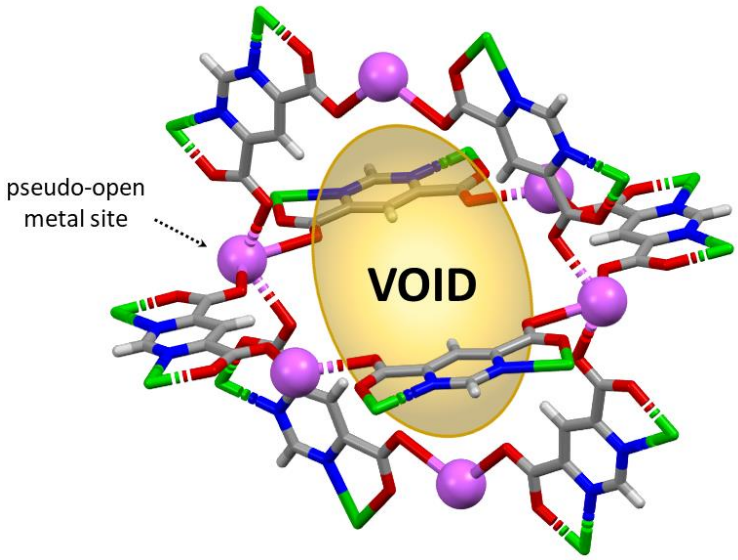

Figure 2.13. Blocked coordinatively unsaturated site (pink spheres) due to the hindering of the coordination environment around alkaline ion.

Even though MOFs synthesized by solvent free method have no accessibility to solvent molecules, these compounds may contain crystallization water molecules trapped into pores. There are two reasons for this: the hygroscopic nature of the reactive metallic salts may provide water molecules to the reaction, and pure pmdc ligand also contains crystallization waters. Given this fact, the pseudo-open metal site of the alkali metal may be accessible due to the lack of coordinatively water molecules.

Although the sample required a more complete characterization of their purity and stability through Powder X-Ray Diffraction (PXRD) and Thermogravimetric Analysis (TGA), the impossibility to obtain enough pure sample (as aforementioned, single crystals were mixed with a gelled phase) limited the complete study of NaSc (**1**). Thus, an alternative synthetic method such as solvent-free is necessary to improve and optimize both the synthesis of compounds and their characterization. It is important to confirm that MSc_SF (M = Na (**2**), Li (**3**)) compounds obtained in the solvent-free synthesis are isostructural

to NaSc (**1**) single crystals, so, purity and stability of solvent-free products will be studied by PXRD and TGA in the next section.

2.3.3. Structural characterization of crystalline powders

The fact of the difficult separation of single crystals from the gelled reaction media and the low yield of the reaction makes the solvent-free synthetic method a promising alternative owing to its simplicity and good performance. But it is important to verify that MSc_SF (M = Na (**2**), Li (**3**)) phases are isostructural to those described by single-crystal X-ray diffraction (SCXRD), since a different synthetic method can carry out a completely different structure and/or properties.

Powder X-Ray Diffraction

PXRD analysis of Figure 2.14 shows the good performance of the solvent-free synthetic method since, on the one hand, polycrystalline products are pure and highly crystalline, and on the other hand, obtained diffractograms reproduce well the theoretical diffractogram of single crystals. The good quality of obtained NaSc_SF (**2**) and LiSc_SF (**3**) can be attributed to the slow diffusion of the reactants within the melt formed by the hydrated nitrate/chloride salts given their hygroscopic nature. It should be noted that these solvent-free compounds are very crystalline despite not containing the original solvents (DMF molecules) crystallized in the pores, being this a good indicator of the stability of the structure and confirming a permanent porosity. It is worth noting that a decrease in cell parameters is appreciated in PXRD refinement data, showing a possible compression of the structure due to the different sizes of crystallization water molecules and DMF.

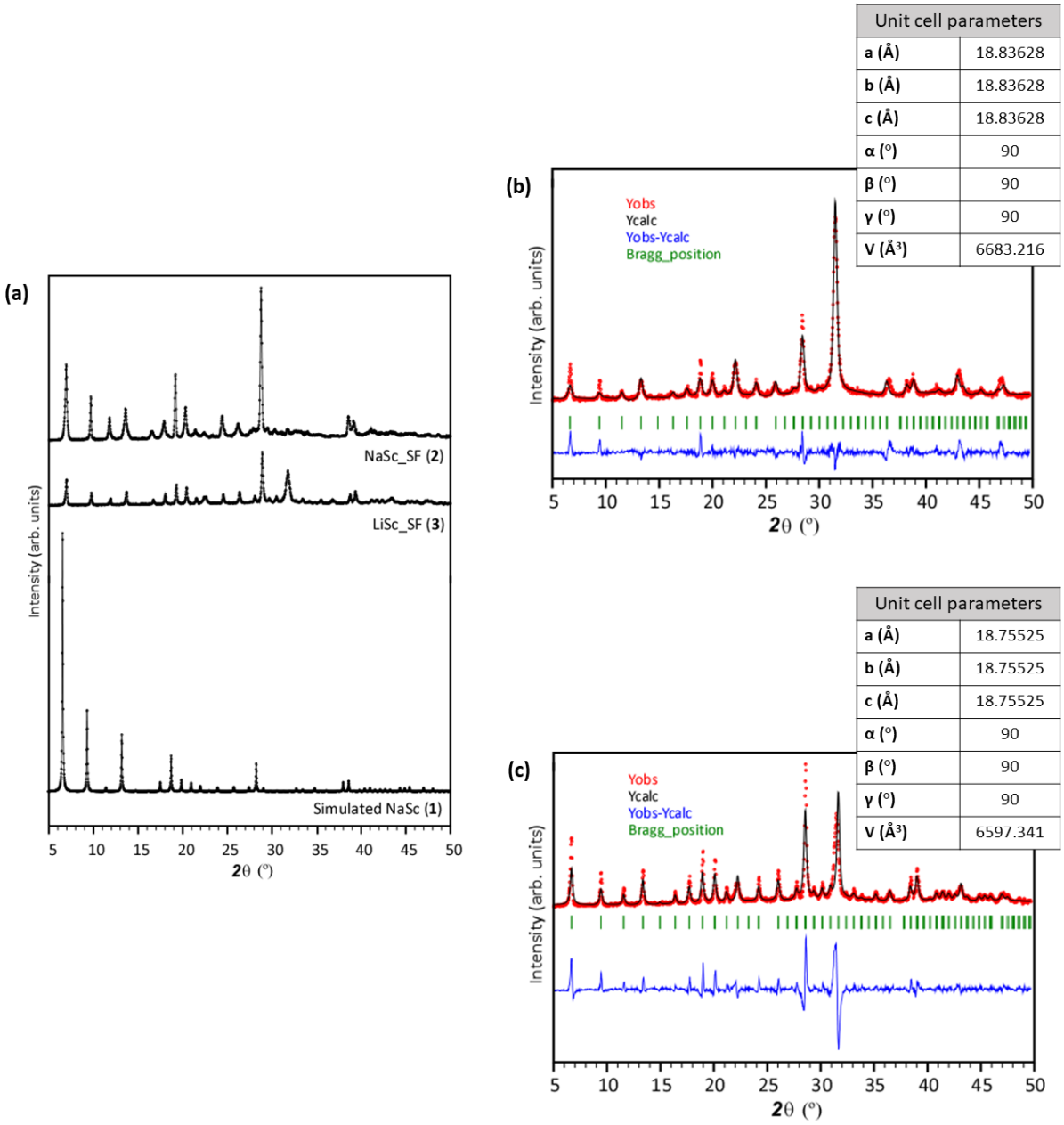

Figure 2.14. Powder X-ray diffraction analysis of compounds (**2**) and (**3**). **(a)** Experimental and simulated diffractograms of NaSc (**1**), NaSc_SF (**2**) and LiSc_SF (**3**). **(b)** Pattern-matching analysis of NaSc_SF (**2**) (Refinement parameters: R_F/R_B: 2.11/1.80; R_P/Chi^2: 15.5/2.37). **(c)** Pattern-matching analysis of LiSc_SF (**3**) (Refinement parameters: R_F/R_B: 3.45/4.06; R_P/Chi^2: 23.6/7.08)

The possible absence of coordinative water molecules makes of MSc_SF (M = Na (**2**), Li (**3**)) compounds promising candidates for gas adsorption since the *cus* would be accessible through moderate activation conditions. For this reason, the study of the stability of these MOFs is developed in the following section, which will allow establishing the activation conditions for gas adsorption.

Thermogravimetric analysis

As shown in Table 2.7 and Table 2.8, the elemental analysis and thermogravimetric data agree with the general $\{[MSc(\mu\text{-pmdc})_2]\cdot xH_2O\}_n$ formula for MSc_SF (M = Na (**2**), Li (**3**)).[62] In both cases, a single loss of mass occurs, so these compounds present crystallization waters in the pores, but there are no coordinated water molecules in alkali metals. This dehydration process occurs near 100 °C, giving rise to the anhydrous $\{[MSc(\mu\text{-pmdc})_2]\}_n$ framework. These frameworks are no longer stable after 310 °C and begin to decompose until the corresponding metal oxides are obtained as final products at ~550 °C.

Table 2.7. Elemental analysis and TG/DTA curves of NaSc_SF (**2**) compound.

NaSc_SF (2)
$\{[NaSc(pmdc)_2]\cdot 7H_2O]_n$ / $C_{12}H_{18}N_4NaO_{15}Sc$

Ti–Tf	ΣΔm(%)	$\Sigma\Delta m(\%)_{teor}$
20-120	24.23	23.96 ($-7H_2O$)
300–580	75.76	76.04 ($Sc_2O_3 + NaScO_2 + Na_2CO_3$)

Elemental analysis

Anal. Calc.: C, 23.11; H, 2.80; N, 8.98; Cd, 32.04%.
Found: C, 23.14; H, 2.65; N, 9.03; Cd, 32.02%.

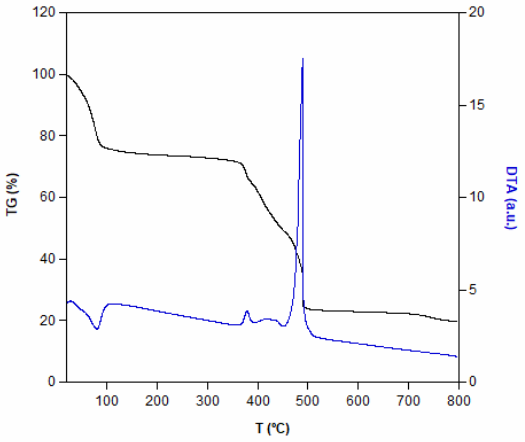

Table 2.8. Elemental analysis and TG/DTA curves of LiSc_SF (**3**) compound.

LiSc_SF (3)
$\{[LiSc(pmdc)_2]\cdot 6H_2O]_n$ / $C_{12}H_{16}LiN_4O_{14}Sc$

Ti–Tf	ΣΔm(%)	$\Sigma\Delta m(\%)_{teor}$
20–85	21.57	21.96 ($-6H_2O$)
350-520	78.43	78.04 ($Sc_2O_3 + LiScO_2 + Li_2CO_3$)

Elemental analysis

Anal. Calc.: C, 23.11; H, 2.80; N, 8.98; Cd, 32.04%.
Found: C, 23.14; H, 2.65; N, 9.03; Cd, 32.02%.

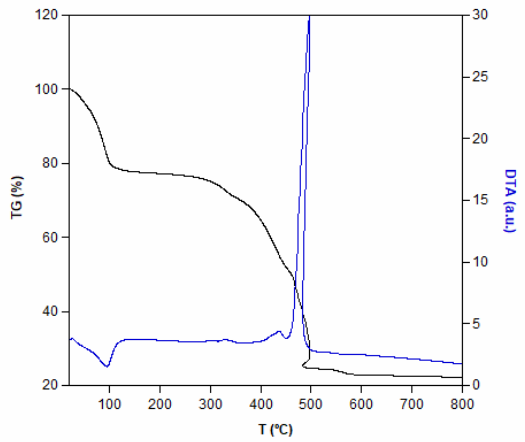

Considering that both solvent free compounds have a similar stability, the outgassing temperature is established at 150 °C in order to remove crystallization water molecules and leave the pores and *cus* accessible applying moderate activation conditions. So, in the next section we will discuss the gas adsorption results obtained for solvent-free compounds activated at 150 °C for 6 h under vacuum.

Porosity

Gas adsorption capacity of a MOF is closely related to the presence of a highly accessible network of channels; so, it is necessary to evaluate the porosity of the MOF by routine gas adsorption measurements. In the case of MSc_SF (**2**-**3**) compounds, permanent porosity was studied in a previous work[62] through N_2 adsorption isotherms at 77 K with an outgassing at 150 °C and vacuum, obtaining BET surface areas and unit cell volumes summarized in Table 2.9.

Table 2.9. Experimental and simulated accessible surface areas of MSc_SF (**2-3**) compounds.[62]

Compound	S_{BET}[a]	mol/unit cell[b]	V[c]
NaSc_SF (2)	848	43	6755
LiSc_SF (3)	762	39	6384

[a] BET specific surface area ($m^2\ g^{-1}$). [b] N_2 molecules adsorbed per unit cell. [c] Unit cell volume ($Å^3$).

Once the porosity of these MOFs is described, different gas adsorption measurements have been carried out, covering both low and high pressures. Concretely, adsorption of H_2, CO_2 and CH_4 has been studied since their smaller kinetic diameters (2.89, 3.30 and 3.80 Å, respectively) compared to pore-sizes of MSc_SF (**2**-**3**) compounds allow to access the 3D channel system of the MOFs.

2.3.4. Gas adsorption experiments

Knowing that these materials have adequate porosity and their potential applicability in gas adsorption, LiSc_SF (**3**) compound has been studied for H_2 and CH_4 storage and CO_2 capture.

As shown in Figure 2.15, LiSc_SF (**3**) presents type I adsorption isotherms for H_2 at 77 K and CO_2 and CH_4 at 273 K. It is worth mentioning that CO_2 isotherm does not show such a perfect plateau compared to previous isotherms. As the study of S_{BET} confirms the permanent microporosity of the structure and the presence of a saturation point is observed in the isotherm, the smaller rise of the CO_2 uptake at high

pressures may occur due to slower kinetics of the gas owing to the higher kinetics radious of this molecule. Thus, adsorption values at 15 bar will be compared as the highest uptake of each measure.

Type I adsorption is described with a Langmuir isotherm since adsorbed quantity increases with pressure (P) until it rearch a limit value. This is because the surface is coated with a monolayer formed through chemisorption processes involving strong chemical bonds between adsorbates and the surface. With H_2, the highest uptake occurs at low pressures (0-1 bar), reaching the saturation at 1.4 bar with an uptake of 8.13 mmol/g (1.64 wt %). Once the saturation point is reached, H_2 adsorption values stabilize around 10.12 mmol/g (2.04 wt %) even though the pressure continues to rise. CH_4 adsorption isotherm is similar to that shown for H_2, although CH_4 adsorption capacity lies below the H_2 values. In this case, saturation is also reached at values close to atmospheric pressure (1.3 bar) with a CH_4 uptake of 1.57 mmol/g (2.52 wt %), even though, once the system has stabilized, the amount of 3.56 mmol/g (5.71 wt %) is reached. Analyzing the CO_2 isotherm, it can be determined that the saturation occurs at 1.2 bar with an uptake of 4.03 mmol/g (17.72 wt %), although this value changes with the increasing pressure until it reaches the uptake of 5.79 mmol/g (25.47 wt %).

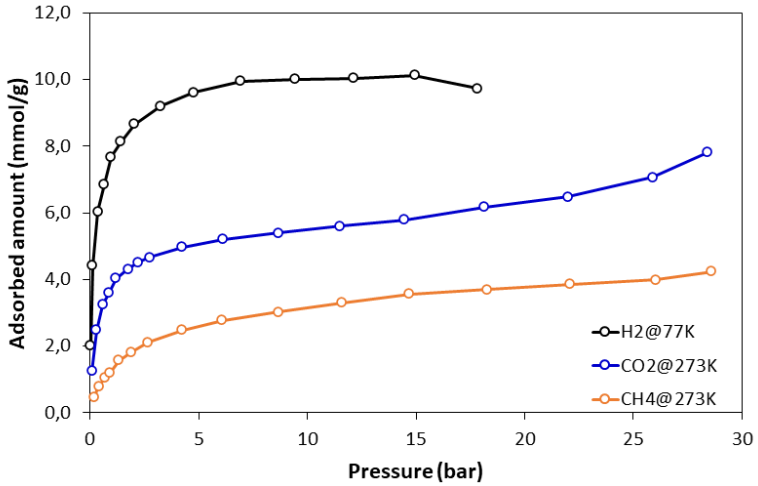

Figure 2.15. Adsorption isotherms of H_2 at 77 K and CO_2 and CH_4 at 273 K for LiSc_SF (**3**).

In addition to the shape of the curves, the step rises at low pressures in H_2 and CO_2 adsorptions are indicative of adsorbate/surface selectivity. Even so, CO_2 and CH_4 data will be compared since both experiments are conducted under the same conditions.

In the case of H_2, which was measured at 77 K, is a highly reactive gas that rapidly forms metal hydrides, a fact that corresponds to the fast increase of the curve at low pressures, indicating the intense interaction between adsorbates and *cus* of the pore surface. Adsorbate-ligand interactions may also occur, which

help in the adsorption process due to the van der Waals forces between the H_2 and the surface, allowing the formation of the monolayer (Figure 2.16).

Paying attention to CO_2 and CH_4 adsorption at low pressures (Figure 2.16), the fast rise of the CO_2 curve over the CH_4 indicates a high selectivity for carbon dioxide. The Lewis basicity nurtured in the free electron pairs located on the oxygen atoms of CO_2 allows to interact with open metal sites located on the alkali metals, since their Lewis acidity accepts CO_2 electrons, increasing interactions between CO_2 and *cus* and improving both adsorption and selectivity (Figure 2.17). Methane does not have a dipole/quadrupolar moment or free electron pairs, so, interactions with the *cus* are weaker. It should be noted that pmdc ligand also favours CO_2 adsorption, since pyrimidinic-N groups act as Lewis bases that interact with the carbon of CO_2, which has a Lewis acid behaviour. CH_4 also has binding affinity with the ligand, although these interactions are weaker compared to those with CO_2. All this makes that, at atmospheric pressure (1 bar), the compound LiSc_SF (**3**) adsorbs 3.60 mmol/g (15.85 wt %) of CO_2 and 1.20 mmol/g (1.93 wt %) of CH_4.

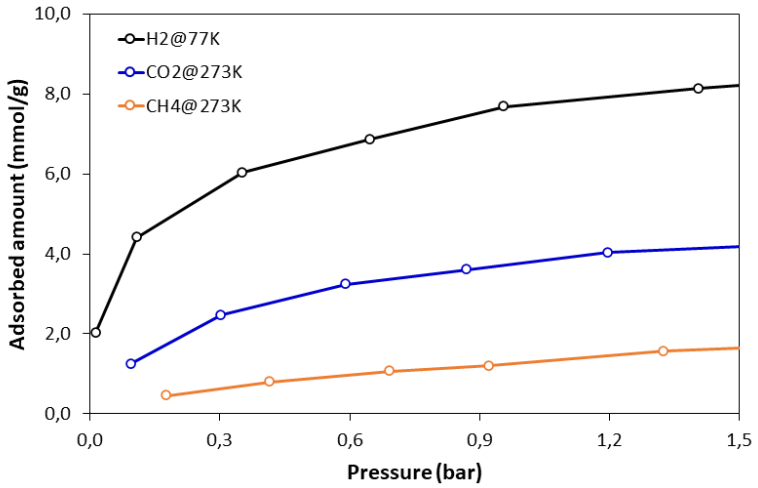

Figure 2.16. Low-pressure region (until 1.5 bar) of adsorption isotherms of LiSc_SF (**3**).

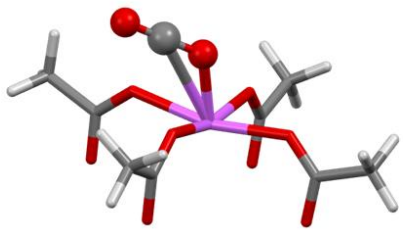

Figure 2.17. Adsorption model of a CO_2 molecule in a *cus* located over alkali metal.

As shown in Table 2.10, compared to other MOFs based on the pmdc ligand, LiSc_SF (**3**) has the highest CO_2 adsorption capacity due to the *cus* located in the pseudo-open alkali sites.

Table 2.10. Comparison of adsorption properties of pmdc-based MOFs.

MOF	H_2		CO_2		CH_4		Ref
	mmol/g	Wt%	mmol/g	Wt%	mmol/g	Wt%	
In-pmdc		0.9% 77K, 1 bar		-		-	59
Mn-pmdc			40 cm^3 g^{-1} 293K, 650 torr				60
Cd-pmdc			2.5 293K, 1bar				61
MnCd-pmdc			2.2 293K, 1bar				61
ZnCd-pmdc			1.9 293K, 1bar				61
LiSc_SF (3)	7.68	1.55	3.6	15.85	1.20	1.93	[a]

[a] Compounds described in this thesis work

2.3.5. Photoluminescence measurements

As indicated in Chapter 1 of the manuscript, a secondary goal of this work is the characterization of additional properties of the synthesized MOFs to evaluate their functionality in different application fields, and, in the case of MSc_SF (**2**-**3**) compounds, photoluminescence has been studied at different temperatures. It is important to point out that, given the composition and the structure of these MOFs, the absorption and emission of light is expected to be related to the pmdc ligand since the pyrimidinic ring and carboxylate groups could provide the necessary charge transfer. Besides, the closed-shell configuration of Sc^{3+} and M^{+} (M = Na and Li) could improve charge transfer and, consequently, enhance the photoluminescent emission.[73]

Photoluminescence measurements of NaSc_SF (**2**) have been carried out at room temperature and 13 K (λ_{em} = 405 nm) because, in the first experiment absorption bands were almost imperceptible (see Appendix I). Instead, in the low temperature excitation spectrum of Figure 2.18a two broad bands are observed at 300 and 340 nm. Based on this information, NaSc_SF (**2**) has been excited using an UV source (λ_{ex} = 325 nm) to obtain the emission spectrum of Figure 2.18b, in which only one intense band has been

observed at 420 nm. This indicates that the predominant process in light emission is fluorescence; that is, once NaSc_SF (**2**) is excited, the relaxation to the ground state occurs in a fast way.

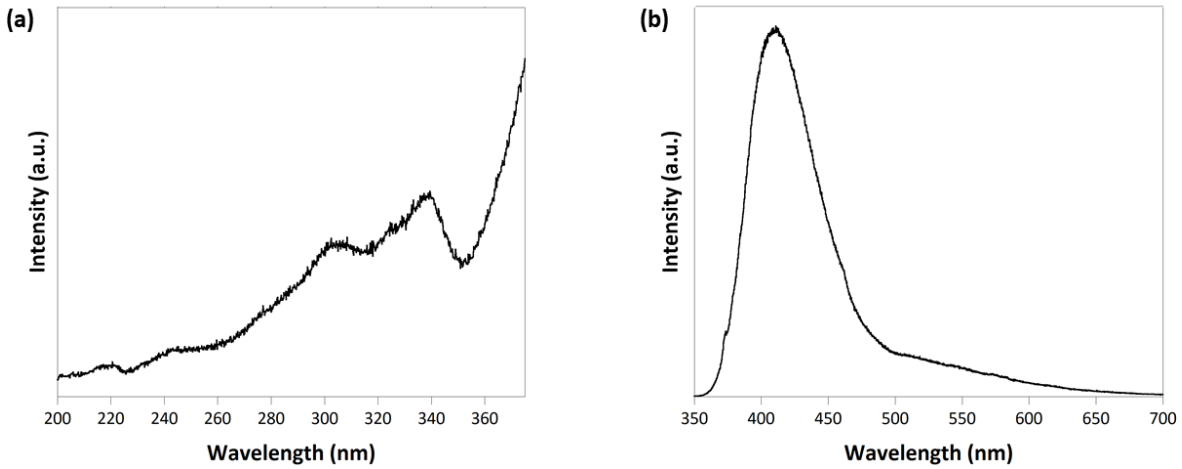

Figure 2.18. Photoluminescence measurements of NaSc_SF (**2**) at 13 K: **(a)** Excitation and **(b)** emission spectra.

2.4. References

[1] Slater, A. G.; Cooper, A. I. "Function-led design of new porous materials", *Science* (2015), **348**, aaa8075.

[2] Blay, V.; Bobadilla, L. F.; Cabrera García, A. (2018). *Zeolites and metal-organic frameworks*. Amsterdam University Press.

[3] Guillerm, V.; Kim, D.; Eubank, J. F.; Luebke, R.; Liu, X.; Adil, K.; Lah, M. S.; Eddaoudi, M. "A supermolecular building approach for the design and construction of metal-organic frameworks", *Chem. Soc. Rev.* (2014), **43**, 6141-6172.

[4] Kalmutzki, M. J.; Hanikel, N.; Yaghi, O. M. "Secondary building units as the turning point in the development of the reticular chemistry of MOFs", *Sci. Adv.* (2018), **4**, eaat9180.

[5] Lin, R. B.; Xiang, S.; Li, B.; Cui, Y.; Qian, G.; Zhou, W.; Chen, B. "Our journey of developing multifunctional metal-organic frameworks", *Coord. Chem. Rev.* (2019), **384**, 21-36.

[6] Thommes, M.; Kaneko, K.; Neimark, A. V.; Olivier, J. P.; Rodriguez-Reinoso, F.; Rouquerol, J.; Sing, K. S. W. "Physisorption of gases, with special reference to the evaluation of surface area and pore size distribution (IUPAC Technical Report)", *Pure Appl. Chem.* (2015), **87**, 1051-1069.

[7] Sing, K. S. W.; Everett, D. H.; Haul, R. A. W.; Moscou, L.; Pierotti, R. A. ; Rouquerol, J.; Siemieniewska, T. "IUPAC Recommendations 1984: reporting physisorption data for gas/solid systems with special reference to the determination of surface area and porosity", Pure Appl. Chem. (1985), 57, 603-619.

[8] (a) Chen, Y. Z.; Zhang, R.; Jiao, L.; Jiang, H. Long. "Metal-organic framework-derived porous materials for catalysis", *Coord. Chem. Rev.* (2018), **362**, 1-23. (b) Liu, D.; Zou, D.; Zhu, H.; Zhang, J. "Mesoporous metal-organic frameworks: synthetic strategies and emerging applications", *Small* (2018), **14**, 1801454.

[9] Hu, X. L.; Liu, F. H.; Wang, H. N.; Qin, C.; Sun, C. Y.; Su, Z. M.; Liu, F. C. "Controllable synthesis of isoreticular pillared-layer MOFs: gas adsorption, iodine sorption and sensing small molecules", *J. Mater. Chem. A* (2014), **2**, 14827-14834.

[10] Müller-Buschbaum, K.; Beuerle, F.; Feldmann, C. "MOF based luminescence tuning and chemical/physical sensing", *Microporous Mesoporous Mater.* (2015), **216**, 171-199.

[11] Wu, M. X.; Yang, Y. W. "Metal-organic framework (MOF)-based drug/cargo delivery and cancer therapy", *Adv. Mater.* (2017), **29**, 1606134.

[12] Wen, Y.; Zhang, J.; Xu, Q.; Wu, X. T.; Zhu, Q. L. "Pore surface engineering of metal-organic frameworks for heterogeneous catalysis", *Coord. Chem. Rev.* (2018), **376**, 248-276.

[13] Castaldo, R.; Ambrogi, V.; Gentile,G. (2019). Microporous Organic Polymer Nanocomposites for Adsorption Applications. In *Composite Nanoadsorbents*. Elsevier.

[14] Ma, Y. Z.; Sobernheim, D.; Garzon, J. R. (2016). Glossary for Unconventional Oil and Gas Resource Evaluation and Development. In *Unconventional Oil and Gas Resources Handbook*. Boston: Gulf Professional Publishing.

[15] Liu, L.; Luo,X. B.; Ding, L.; Luo, S. L. (2019). Application of Nanotechnology in the Removal of Heavy Metal From Water. In *Nanomaterials for the Removal of Pollutants and Resource Reutilization*. Elsevier

[16] Liu, P. S.; Chen, G. F. (2014). Characterization Methods: Basic Factors. In *Porous Materials*. Boston: Butterworth-Heinemann.

[17] Nishiyabu, K. (2012). Powder space holder metal injection molding (PSH-MIM) of micro-porous metals. In *Handbook of Metal Injection Molding*. Woodhead Publishing.

[18] Liu, P. S.; Chen, G. F. (2014). General Introduction to Porous Materials. In *Porous Materials*. Boston: Butterworth-Heinemann.

[19] Liu, P. S.; Chen, G. F. (2014). Characterization Methods: Physical Properties. In *Porous Materials*. Boston: Butterworth-Heinemann.

[20] IUPAC. (1997). Compendium of Chemical Terminology. In *The Gold Book*. Oxford: Blackwell Scientific Publications.

[21] Sahu, O.; Singh, N. (2019). Significance of bioadsorption process on textile industry wastewater. In *The Impact and Prospects of Green Chemistry for Textile Technology*. Woodhead Publishing.

[22] Amador, C.; Martin de Juan, L. (2016). Strategies for Structured Particulate Systems Design. In *Computer Aided Chemical Engineering. Tools For Chemical Product Design - From Consumer Products to Biomedicine*. Elsevier.

[23] Kecili, R.; Hussain, C. M. (2018). Mechanism of Adsorption on Nanomaterials. In *Nanomaterials in Chromatography*. Elsevier.

[24] Langmuir, I. "The adsorption of gases on plane surfaces of glass, mica and platinum", *J. Am. Chem. Soc.* (1918), **40**, 1361-1403.

[25] Brunauer, S.; Emmett, P. H.; Teller, E. "Adsorption of Gases in Multimolecular Layers", *J. Am. Chem. Soc.* (1938), **60**, 309-319

[26] Gómez-Gualdrón, D. A.; Moghadam, P. Z.; Hupp, J. T.; Farha, O. K.; Snurr, R. Q. "Application of consistency criteria to calculate BET areas of micro-and mesoporous metal-organic frameworks", *J. Am. Chem. Soc.* (2016), **138**, 215-224.

[27] Ma, Y.; Wang, Z.; Xu, X.; Wang, J. "Review on porous nanomaterials for adsorption and photocatalytic conversion of CO_2", *Chinese J. Catal.* (2017), **38**, 1956-1969.

[28] Niaz, S.; Manzoor, T.; Pandith, A. H. "Hydrogen storage: Materials, methods and perspectives", *Renew. Sustain. Energy Rev.* (2015), **50**, 457-469.

[29] Fonseca, J. D.; Camargo, M.; Commenge, J. M.; Falk, L.; Gil, I. D. "Trends in design of distributed energy systems using hydrogen as energy vector: A systematic literature review", *Int. J. Hydrog. Energy* (2019), **44**, 9486-9504.

[30] Ren, J.; Langmi, H. W.; North, B. C.; Mathe, M. "Review on processing of metal-organic framework (MOF) materials towards system integration for hydrogen storage", *Int. J. Energy Res.* (2015), **39**, 607-620.

[31] García-Holley, P.; Schweitzer, B.; Islamoglu, T.; Liu, Y.; Lin, L.; Rodriguez, S.; Weston, M. H.; Hupp, J. T.; Gomez-Gualdron, D. A.; Yildirim, T. "Benchmark study of hydrogen storage in metal-organic frameworks under temperature and pressure swing conditions", *ACS Energy Lett.* (2018), **3**, 748-754.

[32] Li, H.; Li, L.; Lin, R. B.; Zhou, W.; Zhang, Z.; Xiang, S.; Chen, B. "Porous metal-organic frameworks for gas storage and separation: Status and challenges", *Energy Chem.* (2019), **1**, 100006.

[33] Kapelewski, M. T.; Runčevski, T.; Tarver, J. D.; Jiang, H. Z. H.; Hurst, K. E.; Parilla, P. A.; Ayala, A.; Gennett, T.; FitzGerald, S. A.; Brown, C. M. "Record high hydrogen storage capacity in the metal–organic framework Ni_2(m-dobdc) at near-ambient temperatures", *Chem. Mater.* (2018), **30**, 8179-8189.

[34] Rackley, S. A. (2017) "Overview of carbon capture and storage". In *Carbon Capture and Storage*. Butterworth-Heinemann, Boston.

[35] Wang, Y.; Zhao, L.; Otto, A.; Robinius, M.; Stolten, D. "A review of post-combustion CO_2 capture technologies from coal-fired power plants", *Energy Procedia* (2017), **114**, 650-665.

[36] Theo, W. L.; Lim, J. S.; Hashim, H.; Mustaffa, A. A.; Ho, W. S. "Review of pre-combustion capture and ionic liquid in carbon capture and storage", *Appl. Energy* (2016), **183**, 1633-1663.

[37] Yu, J.; Xie, L. H.; Li, J. R.; Ma, Y.; Seminario, J. M.; Balbuena, P. B. "CO_2 capture and separations using MOFs: computational and experimental studies", *Chem. Rev.* (2017), **117**, 9674-9754.

[38] Liu, J.; Zou, R.; Zhao, Y. "Recent developments in porous materials for H_2 and CH_4 storage", *Tetrahedron Lett.* (2016), **57**, 4873-4881.

[39] Konstas, K.; Osl, T.; Yang, Y.; Batten, M.; Burke, N.; Hill, A. J.; Hill, M. R. "Methane storage in metal organic frameworks", *J. Mater. Chem.* (2012), **22**, 16698-16708.

[40] Koh, H. S.; Rana, M. K.; Wong-Foy, A. G.; Siegel, D. J. "Predicting methane storage in open-metal-site metal-organic frameworks", *J. Phys. Chem. C* (2015), **119**, 13451-13458.

[41] He, Y.; Zhou, W.; Qian, G.; Chen, B. "Methane storage in metal-organic frameworks", *Chem. Soc. Rev.* (2014), **43**, 5657-5678.

[42] Khan, N. A.; Jhung, S. H. "Adsorptive removal and separation of chemicals with metal-organic frameworks: Contribution of π-complexation", *J. Hazard. Mater.* (2017), **325**, 198-213.

[43] Khan, N. A.; Hasan, Z.; Jhung, S. H. "Adsorptive removal of hazardous materials using metal-organic frameworks (MOFs): a review", *J. Hazard. Mater.* (2013), **244**, 444-456.

[44] Xue, D. X.; Wang, Q.; Bai, J. "Amide-functionalized metal-organic frameworks: Syntheses, structures and improved gas storage and separation properties", *Coord. Chem. Rev.* (2019), **378**, 2-16.

[45] Eddaoudi, M.; Kim, J.; Rosi, N.; Vodak, D.; Wachter, J.; O'Keeffe, M.; Yaghi, O. M. "Systematic design of pore size and functionality in isoreticular MOFs and their application in methane storage", *Science* (2002), **295**, 469-472.

[46] Alkordi, M. H.; Belmabkhout, Y.; Cairns, A.; Eddaoudi, M. "Metal-organic frameworks for H_2 and CH_4 storage: insights on the pore geometry-sorption energetics relationship", *IUCrJ* (2017), **4**, 131-135.

[47] Xia, L.; Bo, Z.; Liu, Q.; Zhang, X.; Pei, Y. "Li-doped and functionalized metal-organic framework-519 for enhancing hydrogen storage: A computational study", *Comput. Mater. Sci.* (2019), **166**, 179-186

[48] Xia, L.; Liu, Q.; Wang, F.; Lu, J. "Improving the hydrogen storage properties of metal-organic framework by functionalization", *J. Mol. Model.* (2016), **22**, 254.

[49] Vitillo, J. G.; Savonnet, M.; Ricchiardi, G.; Bordiga, S. "Tailoring metal-organic frameworks for CO_2 capture: The amino effect", *Chem. Sus. Chem.* (2011), **4**, 1281-1290.

[50] López-Maya, E.; Montoro, C.; Colombo, V.; Barea, E.; Navarro, J. A. R. "Improved CO_2 capture from flue gas by basic sites, charge gradients, and missing linker defects on nickel face cubic centered MOFs", *Adv. Funct. Mater.* (2014), **24**, 6130-6135.

[51] Kazemi, S.; Safarifard, V. "Carbon dioxide capture in MOFs: the effect of ligand functionalization", *Polyhedron* (2018), **154**, 236-251.

[52] Lin, Y.; Kong, C.; Zhang, Q.; Chen, L. "Metal-organic frameworks for carbon dioxide capture and methane storage", *Adv. Energy Mater.* (2017), **7**, 1601296.

[53] He, Y.; Chen, F.; Li, B.; Qian, G.; Zhou, W.; Chen, B. "Porous metal-organic frameworks for fuel storage", *Coord. Chem. Rev.* (2018), **373**, 167-198.

[54] Rada, Z. H.; Abid, H. R.; Sun, H.; Shang, J.; Li, J.; He, Y.; Liu, S.; Wang, S. "Effects of $-NO_2$ and $-NH_2$ functional groups in mixed-linker Zr-based MOFs on gas adsorption of CO_2 and CH_4", *Pro. Nat. Sci-Mater.* (2018), **28**, 160-167.

[55] Lin, J. M.; He, C. T.; Liu, Y.; Liao, P. Q.; Zhou, D. D.; Zhang, J. P.; Chen, X. M. "A metal-organic framework with a pore size/shape suitable for strong binding and close packing of methane", *Angew. Chem.* (2016), **128**, 4752-4756.

[56] Zhang, W. X.; Liao, P. Q.; Lin, R. B.; Wei, Y. S.; Zeng, M. H.; Chen, X. M. "Metal cluster-based functional porous coordination polymers", *Coord. Chem. Rev.* (2015), **293**, 263-278.

[57] Uzun, A.; Keskin, S. "Site characteristics in metal organic frameworks for gas adsorption", *Prog. Surf. Sci.* (2014), **89**, 56-79.

[58] Eddaoudi, M.; Sava, D. F.; Eubank, J. F.; Adil, K.; Guillerm, V. "Zeolite-like metal-organic frameworks (ZMOFs): design, synthesis, and properties", *Chem. Soc. Rev.* (2015), **44**, 228-249.

[59] Sava, D. F.; Kravtsov, V. C.; Nouar, F.; Wojtas, L.; Eubank, J. F.; Eddaoudi, M. "Quest for zeolite-like metal-organic frameworks: on pyrimidinecarboxylate bis-chelating bridging ligands", *J. Am. Chem. Soc.* (2008), **130**, 3768-3770.

[60] Beobide, G.; Wang, W. G.; Castillo, O.; Luque, A.; Román, P.; Tagliabue, G.; Galli, S.; Navarro, J. A. R. "Manganese(II) pyrimidine-4, 6-dicarboxylates: synthetic, structural, magnetic, and adsorption insights", *Inorg. Chem.* (2008), **47**, 5267-5277.

[61] Cepeda, J.; Pérez-Yáñez, S.; Beobide, G.; Castillo, O.; Fischer, M.; Luque, A.; Wright, P. A. "Porous M^{II}/pyrimidine-4,6-dicarboxylato neutral frameworks: synthetic influence on the adsorption capacity and evaluation of CO_2-adsorbent interactions", *Chem. Eur. J.* (2014), **20**, 1554-1568.

[62] Cepeda, J.; Pérez-Yáñez, S.; Beobide, G.; Castillo, O.; Goikolea, E.; Aguesse, F.; Garrido, L.; Luque, A.; Wright, P. A. "Scandium/alkaline metal-organic frameworks: adsorptive properties and ionic conductivity", *Chem. Mater.* (2016), **28**, 2519-2528.

[63] Ma, X.; Li, L.; Chen, R.; Wang, C.; Zhou, K.; Li, H. "Doping of alkali metals in carbon frameworks for enhancing CO_2 capture: A theoretical study", *Fuel* (2019), **236**, 942-948.

[64] Tang, Y.; Kourtellaris, A.; Tasiopoulos, A. J.; Teat, S. J.; Dubbeldam, D.; Rothenberg, G.; Tanase, S. "Selective CO_2 adsorption in water-stable alkaline-earth based metal-organic frameworks", *Inorg. Chem. Front.* (2018), **5**, 541-549.

[65] Devic, T.; Serre, C. "High valence 3p and transition metal-based MOFs", *Chem. Soc. Rev.* (2014), **43**, 6097-6115.

[66] (a) Férey, G. "Hybrid porous solids: past, present, future", *Chem. Soc. Rev.* (2008), **37**, 191-214. (b) Stock, N.; Biswas, S.. "Synthesis of metal-organic frameworks (MOFs): routes to various MOF topologies, morphologies, and composites", *Chem. Rev.* (2012), **112**, 933-969. (c) Janiak, C.; Vieth, J. K. "MOFs, MILs and more: concepts, properties and applications for porous coordination networks (PCNs)", *New J. Chem.* (2010), **34**, 2366-2388.

[67] Tsao, C. S.; Yu, M. S.; Chung, T. Y.; Wu, H. C.; Wang, C. Y.; Chang, K. S.; Chen, H. L. "characterization of pore structure in metal-organic framework by small-angle X-ray scattering", *J. Am. Chem. Soc.* (2007), **129**, 15997-16004.

[68] TOPOS Main Page; http://www.topos.ssu.samara.ru (accessed Mar 2016).

[69] Blatov, V. A.; O'Keeffe, M.; Proserpio, D. M. "Vertex-, face-, point-, Schläfli-, and Delaney-symbols in nets, polyhedra and tilings: recommended terminology", *CrystEngComm* (2010), **12**, 44-48.

[70] Blatov, V. A.; Shevchenko, A. P.; Proserpio, D. M. "Applied Topological Analysis of Crystal Structures with the Program Package ToposPro", *Cryst. Growth Des.* (2014), **14**, 3576-3586.

[71] Spek, A. L. "PLATON, An Integrated Tool for the Analysis of the Results of a Single Crystal Structure Determination", *Acta Crystallogr. Sect. A* (1990), **46**, C34.

[72] Herdes, C.; Sarkisov, L. "Computer simulation of volatile organic compound adsorption in atomistic models of molecularly imprinted polymers", *Langmuir* (2009), **25**, 5352-5359.

[73] Pajuelo-Corral, O.; Rodríguez-Diéguez, A.; Beobide, G.; Pérez-Yáñez, S.; García, J. A.; San Sebastian, E.; Seco, J. M.; Cepeda, J. "Alkaline-earth and aminonicotinate based coordination polymers with combined fluorescence/long-lasting phosphorescence and metal ion sensing response", *J. Mater. Chem. C* (2019), **7**, 6997-7012.

Chapter 3

Porous Metal-Organic Frameworks based on H_2CNip Ligand for Photocatalytic CO_2 Reduction

3.1. Introduction

Since the term was coined by Yaghi et al. in the 90s,[1] hybrid and tuneable structures of MOFs have been of great interest because their diversity in porosity and crystallinity makes them suitable materials for bulk applications such as storage, catalysis and separation. In addition to these traditional applications related to porous materials, the structural flexibility, controllable synthesis and tuneable properties encourage the use of MOFs in chemical sensing, heterogeneous catalysis, solid-state material physics and biological applications.[2]

In recent years MOFs have gained attention in the field of sensing due to the self-assembly of light-harvesting components in the framework, in addition to the possibility to encapsulate or guest molecules into frameworks or dope them to tune the final optical properties.[3] For this reason, luminescent MOFs (LMOFs) are emerging as potential materials for sensing applications since the introduction of an analyte within the MOF (*i.e.* gases, solvents, explosives, and small molecules) can change its luminescent properties by (a) changes in the intermolecular distances between metal ions and ligands; (b) interaction of the analytes with the metal/metal cluster through chemical bonding; and, (c) interaction of the analyte with ligands through host-guest chemistry.[4]

Another application related to light absorption is the photocatalysis, which allows selective light-induced organic transformations. Semiconductors (SC) of wide bandgap such as TiO_2, ZnO and Nb_2O_5 are the most commonly used to photocatalyze organic reactions under ultraviolet-light (UV) irradiation. Still, the fact that UV-induced photocatalytic reactions lead to low selectivity because of the formation of radical intermediates, makes necessary the development of new photocatalysts which may perform organic transformations under visible light.[5] In this regard, MOFs are promising materials since, along with their large surface areas and permanent porosity, the tunability of their structures and properties allow the insertion of catalytically active metals and/or functionalized ligands in the framework. This makes possible the use of MOFs as heterogeneous photocatalysts in reactions such as water splitting, CO_2 reduction and degradation of organic molecules, among others.[6]

As mentioned in this thesis, the first main general goal was the design, synthesis and complete characterization of porous achiral MOFs in order to obtain multifunctional materials for the study of luminescent, magnetic, adsorption and photocatalytic properties. Based on this general goal, the present chapter focuses on studies related to milestones 1.1, 1.2, 1.3 and 1.4 (see page 38 of Chapter 1), which deal with the design and synthesis of multifunctional MOFs and their structural, thermal and chemical

characterization to carry out a study of the luminescent properties at different temperatures and the behaviour of MOFs as photocatalysts in the photocatalytic reduction of CO_2.

The following section describes the basic items about luminescence and photocatalysis, which are necessary to allow for a correct interpretation and understanding of the results obtained and exposed in this chapter.

3.1.1. Luminescence in MOFs

3.1.1.1. Understanding luminescence in MOFs

As aforementioned, optical sensing is one of the numerous fields of applications of porous MOFs, which may be related to luminescent properties in the MOF, arising from the basic building units of the hybrid structure and/or the encapsulation of (photoactive) guests into the framework.[7] Before delving into the fundamental mechanisms related to luminescence, it is important to note that, although a brief introduction to the different luminescent processes will be done, the most studied process in this thesis work will be photoluminescence due to the properties and characteristics of synthetized MOFs. So, as will be described below, photoluminescent MOFs are compounds that emit light through the conversion of the excitation energy of an absorbed photon into an emitted electromagnetic radiation of another photon.[8]

In comparison to other traditional luminescent sensors, such as inorganic copper- or cobalt-doped zinc sulfide (ZnS) materials,[9] LMOFs have unique properties. Due to their permanent porosity, these materials can trap analyte molecules in low concentrations and contribute to increased signal sensitivity. In addition, the structural diversity of LMOFs directly influences the adsorption process, since this response can be selective towards specific analytes by functionalizing certain areas of the porous surface or by adjusting the pore size and apertures. The relatively strong coordination bonds of LMOFs provide the necessary stability to fulfil the material´s function in the presence of different solvents or temperature changes;[10] still, at the same time, these coordination bonds are flexible enough to generate dynamic stimuli-responsive materials that may undergo variations in photoluminescent properties due to environmental factors such as the presence of ions, solvents and vapours, pH changes, adsorption of gases, etc.[11] It should be noted that the photoluminescent properties of MOFs are enhanced because the self-quenching between adjacent luminophores can be reduced by the controlled spatial distribution of the highly ordered metal ions and ligands in their crystalline frameworks.[12]

The mechanisms underneath the phenomenon of photoluminescence (PL) are shown in the Jablonski diagram depicted in Figure 3.1. This general scenario is common to all materials, regardless of their chemical nature. This means that the luminescent processes explained below, based on a simplified model of luminescent organic molecules, may be modified depending on the type of luminescent material to be studied. PL can be divided into the following two steps:

1. Excitation of electrons. The absorption of a photon with an energy $h\upsilon$ is necessary to begin the photoluminescence, since this process provides energy to electrons in the ground state and promote them to higher electronic states in a vibrational state (v_0, v_1, …, v_m). Assuming a singlet ground state (S_0), the transition would be spin allowed (multiplicity is preserved), moving from S_0 to an excited singlet state (S_1, S_2, …, S_n) in a fast-radiative process of the order of 10^{-15} s. These excited electrons lose energy in a non-radiative way by vibrational relaxation (VR), going to the lowest vibrational state of the excited electronic state ($v_m \rightarrow v_0$). It is important to emphasize that, according to the Kasha's rule, any type of emission can only occur from the lowest energy excited electronic state (either singlet or triplet); meaning that non-radiatively internal conversions (IC) between highest and lowest excited states ($S_n \rightarrow S_1$) also take place through the coupling of vibrational states of S_n and S_1. The lifetime of both processes is of the order of 10^{-12} s.[13]

2. Emission of photons. Depending on the mechanism responsible for the light emission processes, PL can be referred to as either fluorescence, phosphorescence or delayed luminescence, as set out below:

> ***Fluorescence.*** In this mechanism, part of the electrons returns to S_0 by a spin allowed relaxation ($S_1 \rightarrow S_0$) with a typical lifetime of 10^{-9}-10^{-7} s, in which a photon of $h\upsilon'$ is emitted. Due to the emission process from the lowest vibrational level of the first excited state and the occurrence of some non-radiative processes that cause luminescence quenching, the energy of the emitted photon is lower than the energy of the excitation photon ($h\upsilon > h\upsilon'$); so, fluorescent emission is centered at longer wavelength than the absorption.
>
> ***Phosphorescence.*** In this mechanism, the excitation, vibrational relaxation and internal conversion of the system occurs as explained before but, prior to photon emission from S_1, a excited triplet state T_n (T_1, T_2, …, T_n) is populated via the so-called intersystem crossing (ISC). It is a spin forbidden process, where the spin of states is flipped, which is also considered as a slow non-radiative transition with lifetimes of 10^{-8}-10^{-3} s, caused by an electron-phonon vibrational coupling. Finally, vibrational relaxation and internal conversion occurs in triplet sates, followed by

the emission of a photon of energy *hυ''* from T_1 to S_0. The latter spin forbidden photon emission, with lifetimes in the range of 10^{-4}-10^{-1} s, is what defines phosphorescence. As this is a spin forbidden radiative transition, the process is slowed down and the emission continues even if the excitation energy ceases.[14,15]

It is worth noting that the phosphorescence is less common than fluorescence because the population of T_1 by direct absorption from S_0 is quantum mechanically forbidden. The phosphorescence phenomenon can only occur with the vibrational coupling of S_1 and T_1 by ISC; hence, fluorescence and phosphorescence compete with each other since the time required for an ISC and the lifetime of S_1 are of the same magnitude. In general, phosphorescent materials exhibit large fluorescence too.[15]

Delayed luminescence. This phenomenon refers to a decay of luminescence much slower than expected from the type of states involved. Although it is not a very common process, it can occur by the following mechanisms:

- S_1 gets populated by a thermally activated reverse intersystem crossing (RISC) from T_1, giving a delayed fluorescence with equal lifetimes to the concomitant phosphorescence.
- An interaction between two molecules in T_1 states can produce a new molecule in S_1 state by RISC. This process is also known as a triplet-triplet annihilation and its lifetime is half the value of the concomitant phosphorescence.
- The delayed emission is produced by the recombination of radical ions with electrons or of radical ions of opposite charge.[16]

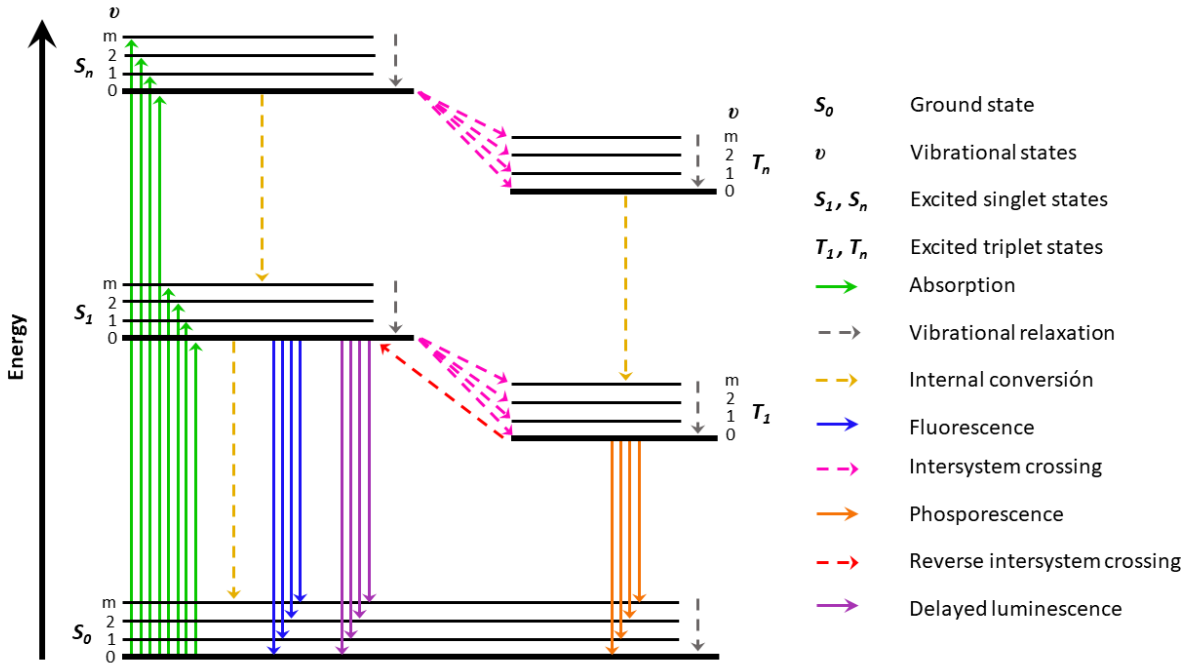

Figure 3.1. Illustration of the Jablonski diagram with processes involved in photoluminescence (fluorescence, phosphorescence, and delayed luminescence). Adapted image from Reference 13.

Although a material may have luminescent properties, its ability to act as light emitter may be limited by the performance of the charge transfer processes described above. Therefore, the light-emitting capacity is defined by the so-called quantum yield, which refers to the ratio between the emitted per photon absorbed and is determined by Equation *(3.1)* below.[17]

$$\Phi = \frac{photons\ emitted}{photons\ absorbed} \qquad (3.1)$$

In the particular case of LMOFs, and as a consequence of their hybrid nature, luminescent properties can stem from the organic ligand, the metal ion or cluster, or by the different charge transfers between multiple species. Figure 3.2 is a description of photoluminescence sources in LMOFs based on molecular complexes which is used to give a basic explanation of the observed luminescence, even though other effects such as host-guest interactions, or the formation of energy bands as a consequence of the solid-state character of LMOFs, are also present in the complex photoluminescent mechanism of these materials.[18]

Ligand-centered emission

When the emission is purely ligand-centered (LC), there is no energy transfer between coordinated ligands and metals or between ligands; so the luminescent properties of LMOFs are given directly by the luminophore ligand. In this regard, the framework acts as a support of single luminescence centers, and at the same time, decreases the entropy of the ligand, minimizing thermal/vibrational relaxation of the latter and, therefore, improving the quantum yield of the emission.[19] To obtain pure LC emission in MOFs, luminescent ligands are usually combined with closed-shell metal cations that do not disturb the process, being these metals alkaline and alkaline earth ions, closed-shell ions (usually Zn(II) and Cd(II)) transition metals cations with d^0 or d^{10} configurations, or 13-14 group metal cations such as In^{3+} or Sn^{4+}.[20]

Metal-centered emission

Metal-centered (MC) emission occurs between orbitals belonging to metal ions or clusters of the LMOF, which are usually formed by lanthanides or actinide cations, though there are also examples with transition and *p*-block metals, such as Ru, Rh, Ir, etc. typically found in complexes.

In the case of LMOFs with lanthanide and actinide metals (although there only few examples described for this second case), two types of transitions can occur depending on the type of orbitals that contribute to the luminescent process: (1) luminescence based on *f-f* transitions, which gives a very narrow emissions in the range of UV to near infrared (NIR) because the shielded nature of the f-electrons prevents the influence of the chemical environment of the lanthanide, and (2) luminescence based on *d-f* or *f-d* transitions, which is dependent of the coordination environment of the metal due to the participation of *d* states. The latter is quite unusual (it can be observed in Ce(II) and divalent lanthanide ions like Eu(II)) and it occurs when the energy of 5*d* states is significantly reduced by the chemical surrounding and the crystal field, resulting in broad absorption and emission bands, and strong brightness due to the parity allowed 5*d*-4*f*/4*f*-5*d* transitions.[18]

MC luminescence in transition and main group metals differs from the processes described for lanthanide and actinide metals, since *d-d* and *s-p* transitions often occur from ground state to anti-bonding excited state, respectively. In addition, the fact that these types of orbitals are not shielded makes the energy levels in these types of metals more sensitive to the environment; therefore, chemical or structural modifications significantly influence the luminescence of these metals due to possible changes in bond lengths, bond angles, covalence, and coordination number. This results in weak and broad emission bands,

only observable in rigid matrices at low temperatures. To this must be added the difficult identification of the nature of the transitions in transition or main group metal-based LMOFs because of the variety of possible processes occurring in the same compound; thus, the best compounds for pure MC luminescence are those containing s^2 ions such as lead(II) or bismuth(III).[21]

Charge transfer-based emission

Charge transfer (CT), such as ligand-to-metal (LMCT) and metal-to-ligand (MLCT), are allowed electronic transitions from a ligand-localized orbital to a metal-centered orbital or from a metal-centered orbital to a ligand localized orbital, respectively. These processes may compete with ligand-centered luminescence, resulting in both LMCT/MLCT and ligand-based emission bands.[22]

LMCT luminescence mainly occurs by the combination of easily oxidized ligands with easily reducible metals in high oxidation states, resulting in a charge transfer from an organic linker-localized orbital to a metal-centered orbital in a process which is dependent of the radius of the metal ion and the coordination geometry in the MOF. This is because both the ionic radius of the metal and the coordination environment influence the robustness of the ligand-metal coordination link and can favour the LMCT. In particular, metals with closed *d*-shells of d^0 and d^{10} configurations such as Zn(II) and Cd(II) are chosen for this type of charge transfer. MLCT luminescence is the opposite of LMCT: charge transfers occur from an easily oxidized metal-centered orbital, such as metals with d^6 or d^8 electron configurations, to reducible ligand-localized orbital. It should be noted that, in this type of process, the introduction of functional groups with electron withdrawing or donating effects can modulate the energy levels of the molecular orbitals and facilitate this type of transfer.[23]

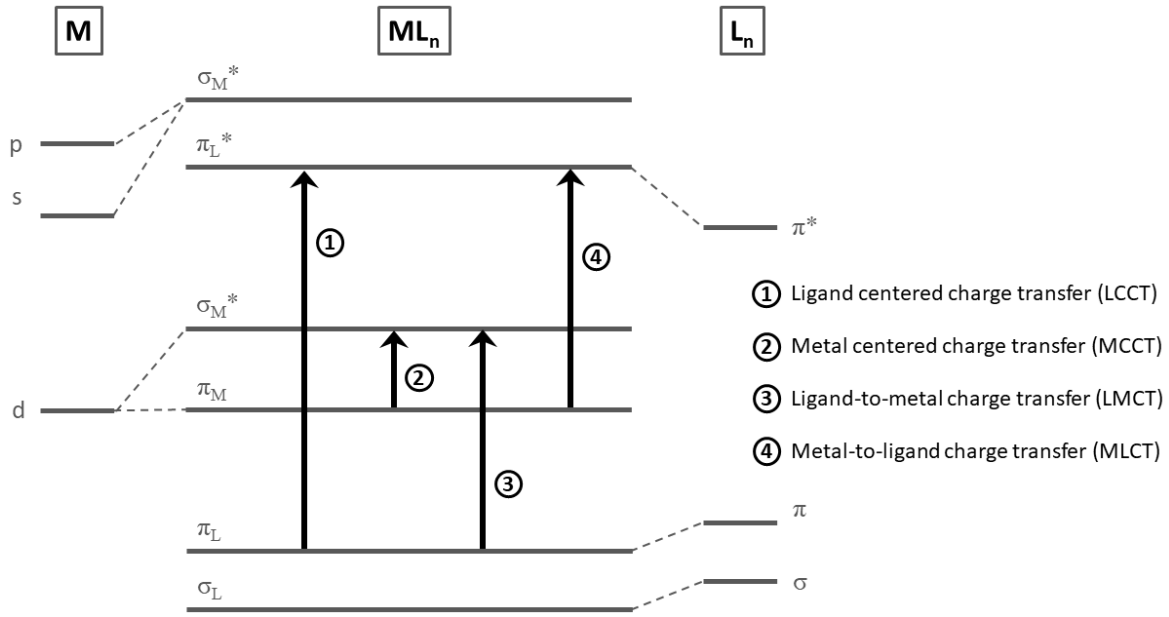

Figure 3.2. Molecular orbital scheme and possible excitations in transition metal complexes ML_n. Adapted image from Reference 18.

In addition to the already mentioned possible origins of the luminescent properties in MOFs, their porous nature allows the introduction of light emitter species through host-guest interactions. In this way, thanks to the encapsulation of guest chromophores by their adsorption over pore surfaces, some non-luminescent MOFs can present guest-centered emission.[24] Guests can be dyes, nanoparticles, quantum and/or carbon dots or chromophore molecules, which exhibit enhanced fluorescent properties because the MOF host provides stability to the species while preventing their aggregation.[25] It should be noted that, just as charge transfer that contribute to the luminescent properties of the MOF can occur between the building blocks, the guest species can also generate equivalent charge transfer to ligands and/or metals that form the MOF.[26]

Although the luminescent properties of LMOFs depend mainly on the building blocks and charge transfer through them, luminescence may be affected or modified by the factors described in the section below.

3.1.1.2. Factors influencing luminescence

The fact that MOFs are constituted by organic molecules and metal ions, while their porous structure favours the adsorption of different types of species, the luminescent properties can be influenced by the following factors.

Ligand scaffold

The use of organic molecules that contain chromophore groups as ligands is one of the simplest strategies to build up LMOFs since, in addition to providing the luminescent properties, the resulting ligand scaffold of the LMOFs structure enables the improvement and tuneability of the luminescence. This is because the rigidity of the crystalline structure reduces ligand's molecular vibrations, torsions, and rotations, preventing the non-radiative excitation decay, and also brings greater thermal stability to ligands.[27]

Ligand substituents

Some types of functional groups that contain O-H, N-H or C-H bonds may quench the luminescence since these bonds act as oscillators that cause the excitation energy decay by non-radiative vibration energy transfer processes.[28] Even so, electron-donor functional groups can benefit charge transfers and enhance the luminescence, particularly in the case of π-conjugated systems with organic functional groups with non-bonding electrons on heteroatoms.[29]

Metals

In some ligand-centered LMOFs, metals with closed-shell configuration such as Zn(II) and Cd(II) generate the heavy atom effect which enables intersystem crossings of electrons by spin-orbit coupling, favouring the population of triplet states where non-radiative deactivation is dominant.[30]

Antenna effect

The fact that *f-f* transitions of lanthanides are Laporte forbidden decreases the intensity of the emission, making of the so-called antenna effect a necessary partner in the luminescence of lanthanide ions. The mechanism of antenna sensitization involves the excitation of a ligand and the subsequent relaxation to the triplet state and transfer of energy to the lanthanide, although in some cases the energy transfer occurs directly from a singlet state. This mechanism circumvents the parity forbidden *f–f* transitions, resulting in much brighter emission, even if the emission depends on these transitions since f-state will be continuously populated.[31]

Guest molecules

The porous structure of LMOFs may host different types of molecules and/or species that allow various host-guest interactions via coordination-bond, hydrogen-bond, electrostatic force and van der Waals interaction, among others, to alter the environment of ligands and metals, causing a modification in luminescent properties of the LMOFs.[32] It should be noted that, in these types of interactions, electron-deficient guest molecules quench the luminescent emission of LMOFs, while electron-rich analytes have the opposite effect as the latter contribute to charge transfer.[33]

Excimer and exciplex formation

Excimer and exciplex are defined as short-lived species that can be generated in an excited state and are dissociated in the ground state. The difference between the two species consists in the fact that the excimer is generated from interactions between homonuclear diatomic complexes with identical ground state, while the interactions between an excited molecule of one type and a ground state molecule of a different type give rise to an exciplex. It should be noted that bonds formed by these physical phenomena are dependent on the lifetime of the excited states, and that their disassociation can occur through radiative or non-radiative relaxation processes.[34] In the case of MOFs, the formation of this type of species and the consequent luminescent emission can occur through two processes in which the arrangement and orientation of participating units inside the frameworks are determining factors:[35]

- Interactions between ligands, in which the orientation of the ligands is of great importance in order to form a complex in the excited state.
- Interactions between guest molecules and the framework.

Based on the above paragraphs, luminescence can be described as a process of charge transfers between different states of a compound. But those same charge transfers that occur between the ground state and the excitation state of a compound can give rise to properties other than luminescence, such as photocatalysis.

3.1.2. Similarities between luminescence and photocatalysis as processes based on charge transfer

Photoactive MOFs are very interesting and useful for luminescent applications, but their response to irradiation can be extended to other fields related to photoinduced energy/electron transfer processes, such as photocatalysis, which is also linked to the traditional functions of gas adsorption and separation of MOFs.[36]

These materials can integrate three common aspects between luminescence and photocatalysis, which constitute the mechanism of light-harvesting and energy transfer in MOFs: (1) absorption of photons; (2) generation of excited states; and, (3) charge transfer to excited states.[37] Even though historically MOFs have been described as SCs, theoretical studies suggest that there is no delocalization of the electronic states that would form valence and conduction bands because of the poor overlap between frontier orbitals. For this reason, a description based on localized molecular orbitals for the photocatalytic mechanism, which is also the base of the luminescence, is more suitable in MOFs.[38]

Taking into account the similarities between SCs and MOFs in luminescent and photocatalytic processes, Figure 3.3 has been depicted to make a comparison, on the one hand, between materials and, on the other hand, between both processes. The principal mechanisms in SCs and MOFs are identical with the main difference that molecular orbitals are involved in MOFs because of their self-assembled molecular behaviour, in contrast to delocalized states in SCs. Therefore, while photophysical and photochemical processes in MOFs are described from charge transfers between the highest occupied molecular orbital and lowest unoccupied molecular orbital (HOMO-LUMO), in SC materials these processes occur between the valence band (VB) and the conduction band (CB).[39]

As far as processes are concerned, the initial steps of both luminescence and photocatalysis are very similar, since the material is photoexcited by the absorption of a photon with an energy *hv*. It should be noted that this photoexcitation process is equivalent to the photoactivation of a photocatalyst.[40] As a consequence of this step, electrons are excited from the ground state or HOMO to an excited state or LUMO in MOFs, and from VB to CB in SCs, resulting in an excited electron in the LUMO/CB and a hole in the HOMO/VB.[41] As described in the previous section, in the case of luminescence, this excited electron returns to the ground estate by electron-hole recombination (Figure 3.3, upper section); but in the case of photocatalysis, both excited electrons and holes act as charge carriers that react with acceptor and donor species in other reduction and oxidation reactions, respectively (Figure 3.3, lower section).[40]

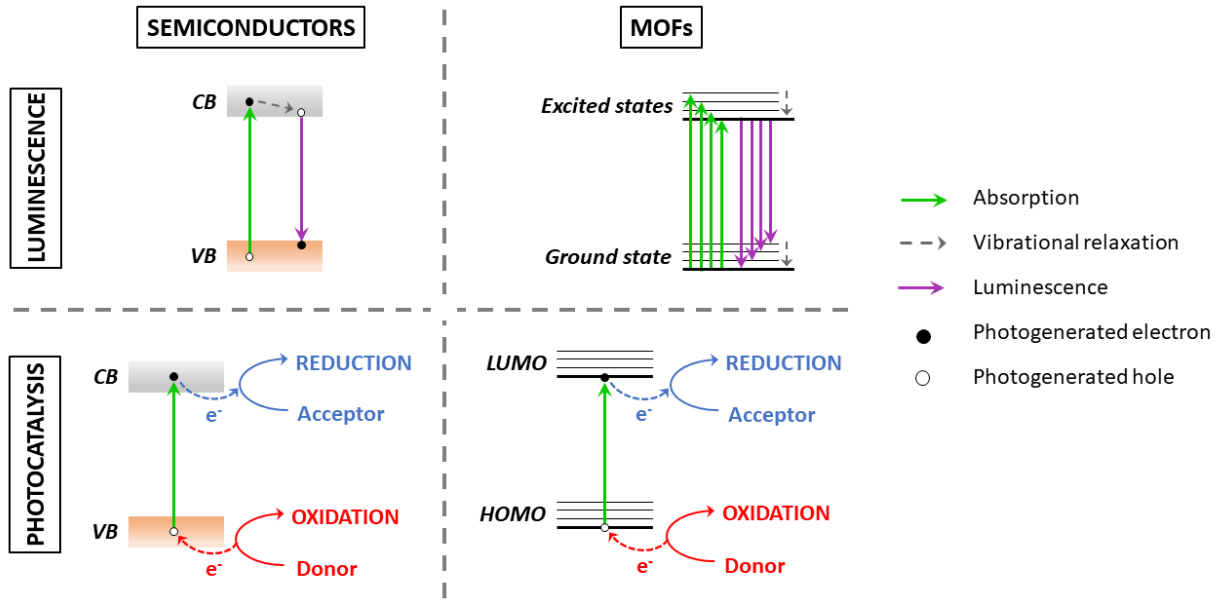

Figure 3.3. Comparison of luminescent and photocatalytic processes between SC and MOFs. Upper section: simplified luminescent mechanisms in a semiconductor with electronic bands (left) and a MOF with discrete energy levels (right). Lower section: simplified photocatalytic processes in semiconductors (left) and MOFs (right).

In the section below, emphasis will be placed on the basis of photocatalysis, paying special attention to the mechanisms related to MOFs that present this applicability, and the factors that influence the adsorption and reduction of CO_2.

3.1.3. Photocatalysis in MOFs

As mentioned in the Introduction of Chapter 2, currently, plenty of efforts are focussed on the development of low- or zero-carbon alternatives to fossil fuels, while carbon capture and storage/sequestration technologies (CCS) are being studied for CO_2 sequestration and reuse.[42] According to the International Energy Agency (IEA), in 2019 only 0.23 Gt of released CO_2 were reused of a total of 33.30 Gt (around 0.7 %);[43] therefore, the importance of developing CCS technologies lies in the possibility to store large quantities of CO_2 and reuse or recycling it, bringing the carbon cycle back into its natural balance.[44] Captured CO_2 can be reused directly, as is done with fire extinguishers, or transforming it into value-added products such as alcohols and hydrocarbons,[45] making use of different conversion processes (Figure 3.4). Unfortunately, for the reasons given below, in general, these materials are still costly and environmentally unsustainable:

- Requirement of high temperatures and electrical voltage to break down the CO_2 molecules. Its stability requires the application of substantial input of energy and very specific catalysts to get it chemically reduced.[46]
- Limitation of CO_2 sources. As stated in section "2.1.2 Gas separation and adsorption: applicability in H_2 storage and CO_2 capture" of Chapter 2, generally CO_2 capture takes place in post-combustion plants where the flue gas is composed of a mixture of CO_2, NO_x, SO_x, and particulate matters from which the CO_2 must be purified for subsequent reuse. This process has limitations due to the low partial pressure of CO_2 in the flue gas at atmospheric pressure and the low content of CO_2, hindering its separation and capture because of the decrease of driving forces.[47] In this point, CCS technologies are very important, but their development has high costs.[46]

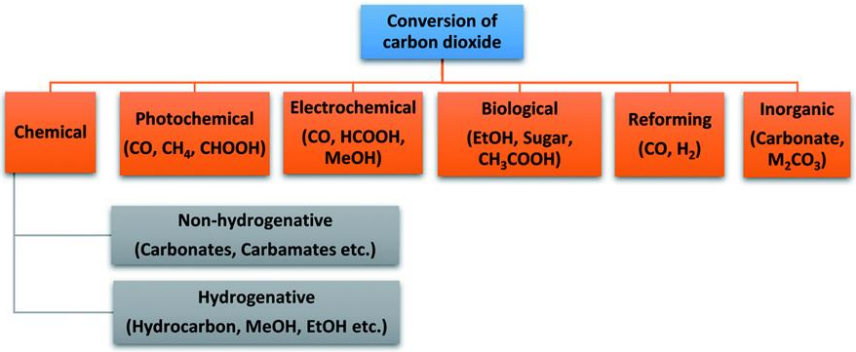

Figure 3.4. Well-known CO_2 transformation paths with potential products.[46]

From a sustainable viewpoint, renewable solar energy is the best alternative to satisfy global energy needs, opening a development opportunity to artificial photosynthesis as inexpensive, limitless and clean solar energy technology.[48] Photocatalysis is a type of heterogeneous catalysis which simulates the photosynthesis by the following five consecutive stages (Figure 3.5):

Stage 1: Transfer of reactants to the photocatalyst surface.

Stage 2: Adsorption of at least one of the reactants on the surface, producing an adsorbed surface.

Stage 3: Set of reactions in the adsorbed phase.

Stage 4: Desorption of products.

Stage 5: Removal of desorbed products from the interface region.

Mechanisms of both conventional heterogeneous catalysis and photocatalysis are similar except for the activation of the catalyst since, in the first one, it is related to thermal processes, whereas, in the second, the catalyst follows a photonic activation. This fact influences only the third stage of the whole catalytic

mechanism, which, as described below and showed in the zoom of Figure 3.5, can also be dissected in four additional and consecutive steps:[49]

Stage 3: Set of consecutive reactions in the adsorbed phase.

- **3.1.** Absorption of photons with suitable energy from a light source.
- **3.2.** Creation of electron-hole pairs (e^--h^+), also called charge carriers.
- **3.3.** Charge carriers' separation and transportation to the active site.
- **3.4.** Electron transfer based redox reactions between adsorbed reactants and charge carriers.

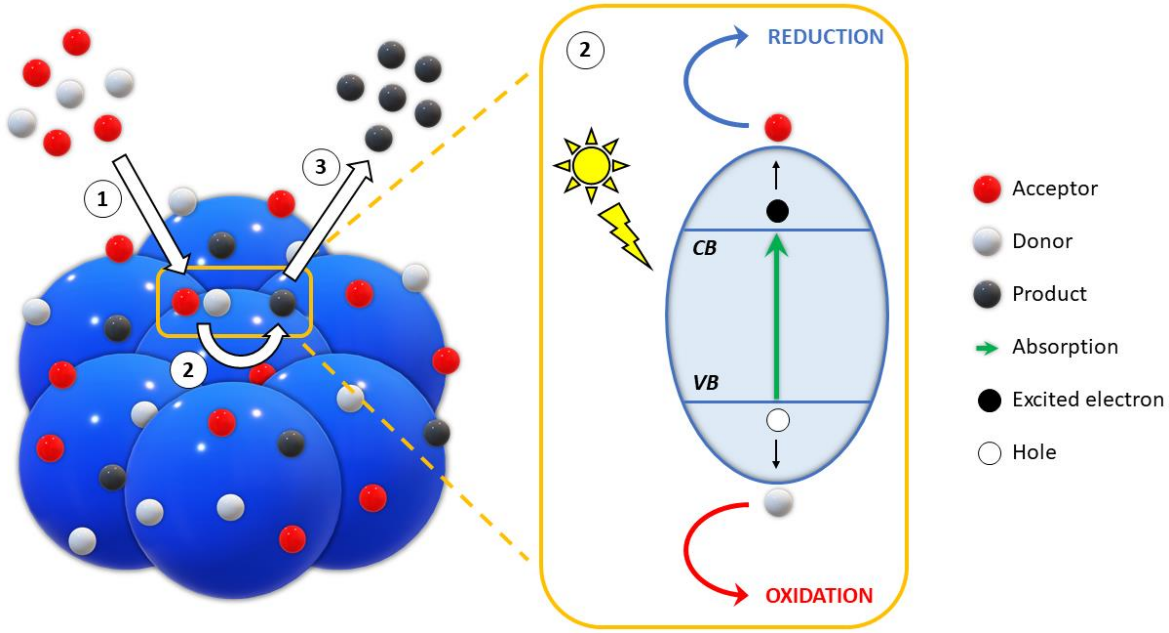

Figure 3.5. Schematic description of photocatalysis in a generic semiconductor material: (1) transfer and adsorption of the reactants on the surface; (2) set of photocatalytic reactions in the adsorbed phase; and (3) desorption and removal of formed products.

In this regard, materials such as inorganic and organic semiconductors, metal-incorporated zeolites, and metal complexes (to cite some) have been studied in photocatalytic applications, although they involve large cost derived from the expensive noble metals that form photocatalysts. The most promising materials are TiO_2-based photocatalysts since they are highly stable and have low cost, but these type of semiconductor materials present the following general problems: (1) they are active in the UV-region, which constitutes only the ~4% of solar energy, and (2) the weak CO_2 adsorption over the photocatalyst and the high C=O bond energy (750 kJ/mol) lead to low reduction efficiencies.[50]

Due to the cited drawbacks of traditional photocatalysts, MOFs appear as promising materials for photocatalytic applications because of their structural arrangement, which allows the incorporation of

photoactive and/or catalytic centers in a solid material, in addition to their tuneable functionalities that can provide specific and enhanced properties to the structure.[51] Before going into detail in the photocatalytic CO_2 reduction in MOFs, a description of the models used to describe the photo-induced mechanisms are explained.

3.1.3.1. Understanding photocatalysis in MOFs

The previous work carried out by Garcia's group demonstrated the semiconducting behaviour of MOF-5, which was described as semiconductor given the occurrence of ZnO quantum dots (QD) located in metal clusters and isolated by terephthalate ligands that act as photosensitizers of QD.[52] At present, in addition to being considered semiconducting materials, MOFs are classified as self-assembled molecular catalysts;[53] so as indicated in the previous section, their description can be approached by the following models.

(a) Molecule-based approach. This model follows the guidelines described in the luminescence mechanism in MOFs (Figure 3.6), since it considers that molecular orbitals of MOF are localized. This means that the photoactivation of the MOF occurs by the excitation of an electron from HOMO to LUMO orbitals and the nature of charge transfers will be defined by the ownership of the involved orbitals to the metal or the ligand.[54]

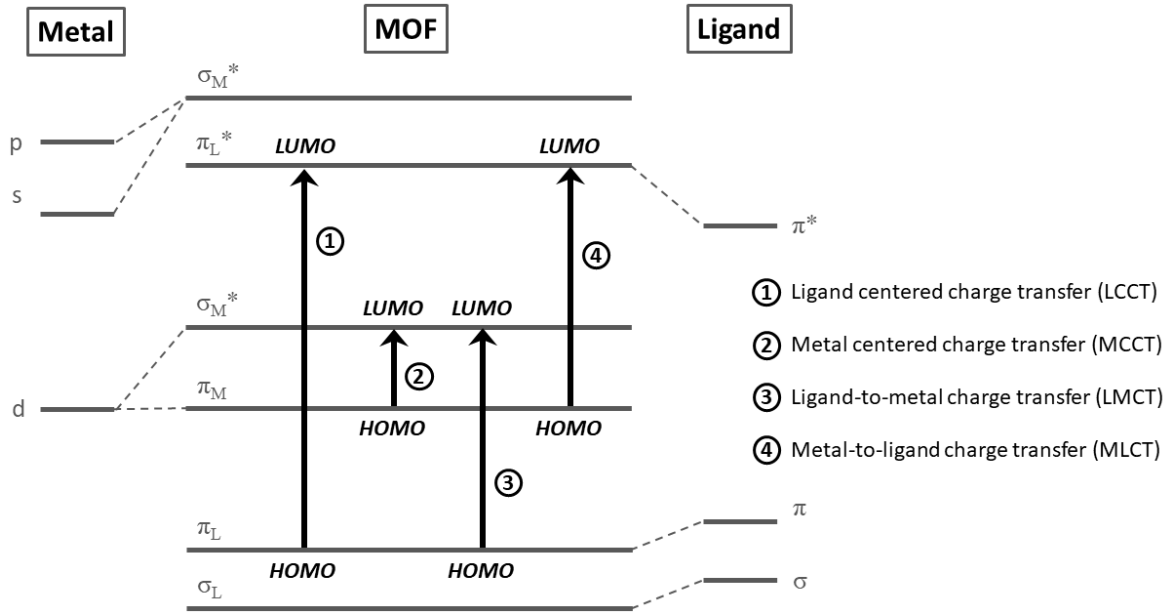

Figure 3.6. Molecular orbital scheme of a MOF and possible excitations between HOMO-LUMO. Adapted image from Reference 18.

(b) Solid-state band electronic structure. According to this model, the fact that MOFs consist of three-dimensional structures with periodically ordered and located metallic and organic elements causes the delocalization of molecular orbitals and energies due to the overlap that can occur between adjacent building blocks. So, as consequence of the combination of metal ions and organic ligands, delocalized electronic bands are formed in MOFs (Figure 3.7).[55]

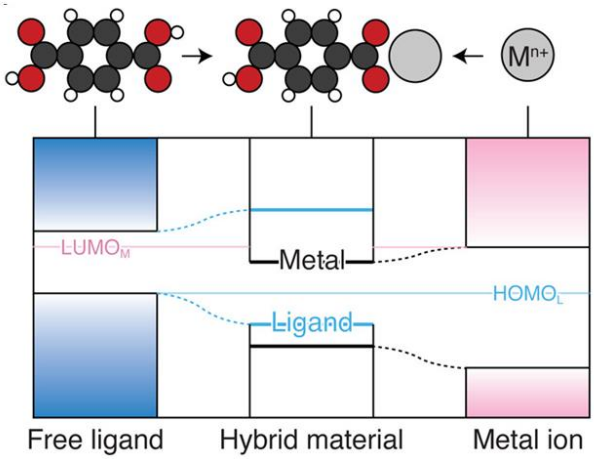

Figure 3.7. Orbital mixing in metal-organic frameworks, giving band edges aligned with metal/ligand energy levels.[55]

It should be noted that, although this document will work on the molecular orbital model, the reactions and mechanisms described below are equivalent to the model based on band structure. Based on the cited steps for the Stage 3 of a photocatalytic process, first, the MOF absorbs light irradiation with the energy *hu* equivalent to the HOMO-LUMO energy gap of the MOF to photoinduce the excitation of an electron from the HOMO to the LUMO and the photogeneration of holes on the HOMO orbital. This step of charge carriers generation and separation is classified according to the type of orbitals involved in the electron transfer, which can be described as charge transfers that occur in luminescence (LCCT, MCCT, LMCT, MLCT, …), although the most commonly used mechanism is ligand-to-metal charge transfer (LMCT).[53]

Regardless of the charge carriers generation and transfer mechanism, this process can be described by two different non-radiative pathways involving excited chemical groups, or donors (D), and ground-state chemical groups, also called acceptors (A).[56] Details of the scheme depicted in Figure 3.8 about Förster resonance energy transfer (FRET) and Dexter electron transfer (DET) are explained below:

(a) Förster resonance energy transfer. This mechanism is characterized by the nonradiative energy transfer through coulombic dipole-dipole coupling. In FRET, when D is excited (D*) and returns to its

fundamental state, a virtual photon is emitted. If an overlap of the emission spectrum of the D and absorption spectrum of the A occurs, the virtual photon is absorbed by A through a radiationless mechanism, also called resonance energy transfer. As a consequence, an electron of A is excited, leaving a positive hole in the ground state and generating the necessary charge carriers for the photocatalytic process.[57] Due to coulombic interactions, only spin allowed transfer can occur through FRET; that is, the multiplicity between the states of D and A remains the same. Equation *(3.2(3.2)* is the expression of FRET, which is independent from the distance between D and A, since the interaction radius is smaller than the virtual photon's wavelength (Figure 3.8).[56]

$$k_{FRET} = \frac{1}{\tau_D^0}\left(\frac{R_0}{r}\right)^6 \qquad (3.2)$$

τ^0_D = lifetime of the excited donor in the absence of transfer
R_0 = the critical quenching radius or Förster radius, i.e., the distance at which transfer and spontaneous decay of the excited donor are equally probable
r = distance between the donor and the acceptor

(b) Dexter electron transfer. Unlike in FRET, this mechanism induces an electron exchange between D and A by a non-radiative process when an overlap of emission spectra of D and absorption spectra of A, and also of the wavefunctions, occur. This means that, in addition to the overlap of electron-clouds, excited and ground states of both chemical groups should be close to make the electron exchange possible. For this reason, DET decays exponentially in function of the distance between D and A (Equation *(3.3)*), so it can only occur at short distances.[58] It should be noted that the absence of coulombic interactions allows energy transfer between spin forbidden states. In DET, an excited electron of D is transferred to an excited state of A in a non-radiative process, while another electron of the ground state of A is also transferred to the ground state of D, leaving an excited electron and a hole in A (Figure 3.8).[56]

$$k_{DET} \propto \frac{h}{2\pi} P^2 J e^{\frac{-2r}{L}} \qquad (3.3)$$

r = distance between the donor and the acceptor
L and P = constants not easily related to experimentally determinable quantities
J = spectral overlap integral

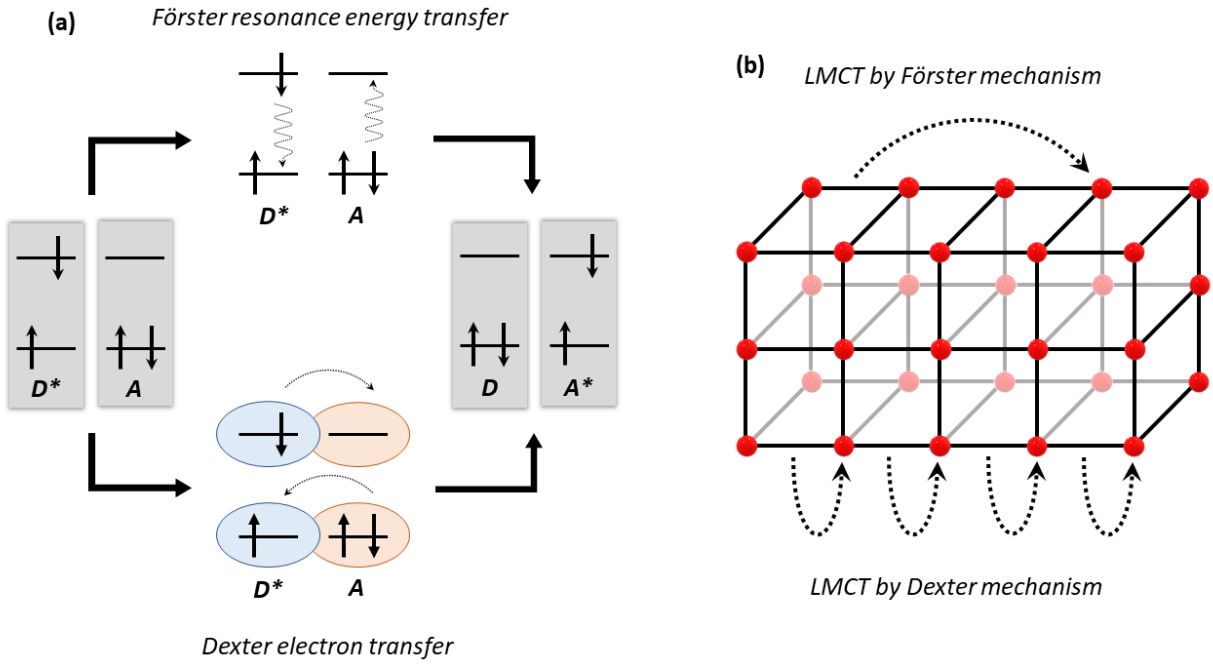

Figure 3.8. Charge carriers generation and transfer mechanisms: **(a)** Energy and charge transfer between D and A by Förster and Dexter mechanisms. **(b)** Schematic representation of LMCT in MOFs through Förster and Dexter mechanisms. Adapted image from Reference 56.

Once the e^--h^+ pairs have been photogenerated in the LUMO and HOMO orbitals, respectively, these charge carriers react with surface-adsorbed species by redox reactions: e^- reduce electron-acceptor molecules adsorbed on the surface (A_{ads}), while h^+ oxidize adsorbed donor molecules (D_{ads}). The redox reactions of Equations *((3.4) - (3.6))* explain the need for the photoactivation of the catalyst to start the photocatalytic reactions; for this reason, photons are considered reactants that are part of an "electromagnetic" fluid phase.[59]

$$hu + MOF \longrightarrow e^- + h^+ \qquad (3.4)$$

$$A_{ads} + e^- \longrightarrow A^-_{ads} \qquad (3.5)$$

$$D_{ads} + h^+ \longrightarrow D^+_{ads} \qquad (3.6)$$

According to the basic chemistry of reduction-oxidation processes, the reduction potential $E°$ is the limiting feature of redox reactions, since species with lower (more positive) $E°$ will be reduced (electron gain), whereas those with higher (more negative) $E°$ will be oxidized (electron loss). For this reason, in MOF photocatalysts, the level of the LUMO determines the reducing capability of photogenerated electrons just as HOMO dictates the oxidizing capability of the holes.[60] This makes essential the location of the LUMO above the reduction potential of the desired product of CO_2 reduction half-reaction,

generating an overpotential, while the HOMO must be located below the reduction potential of the oxidation half-reaction, achieving all reduction potentials of the CO_2 transformations fall within the energy gap of the MOF.[61] These requirements are illustrated in Figure 3.9, where *E*° of CO_2 reduction half-reactions and *E*° of water oxidation half-reaction are located into the HOMO-LUMO energy gap of the MOF.[60]

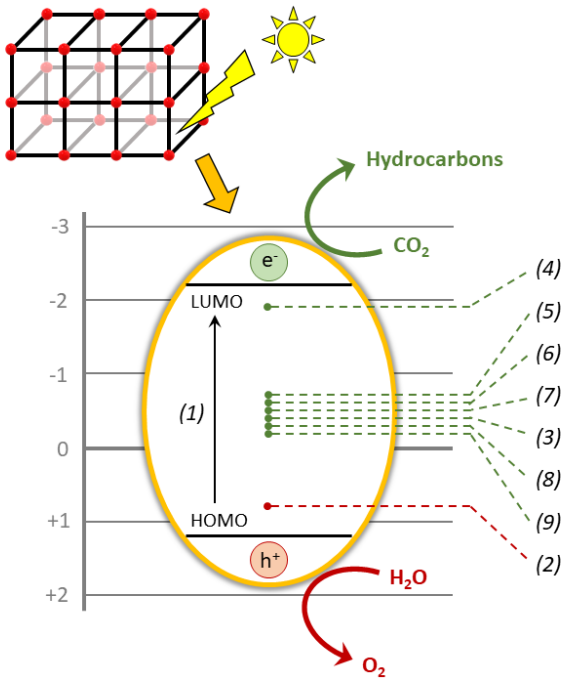

Photoactivation		
$MOF + h\nu \rightarrow e^- + h^+$		*(1)*
Photooxidation	**E° redox (V vs. NHE)**	
$H_2O + 2h^+ \rightarrow ½O_2 + 2H^+$	+0.81	*(2)*
Photoreduction	**E° redox (V vs. NHE)**	
$2H^+ + 2e^- \rightarrow H_2$	-0.42	*(3)*
$CO_2 + 2e^- \rightarrow CO_2^{\bullet -}$	-1.90	*(4)*
$CO_2 + 2H^+ + 2e^- \rightarrow HCOOH$	-0.61	*(5)*
$CO_2 + 2H^+ + 2e^- \rightarrow CO + H_2O$	-0.53	*(6)*
$CO_2 + 4H^+ + 4e^- \rightarrow HCHO + H_2O$	-0.48	*(7)*
$CO_2 + 6H_+ + 6e_- \rightarrow CH_3OH + H_2O$	-0.38	*(8)*
$CO_2 + 8H^+ + 8e^- \rightarrow CH_4 + 2H_2O$	-0.24	*(9)*

Figure 3.9. Photocatalytic CO_2 reduction in water with reduction potentials of half-reactions. The values are obtained using a normal hydrogen electrode as standard for zero potential.

Although the mechanism of the photocatalytic CO_2 reduction in MOFs is relatively simple, several factors significantly influence the photocatalytic process, directly affecting the selectivity and efficiency of the photocatalyst. Details are given below.

3.1.3.2. Factors influencing photocatalytic CO_2 reduction

Although it is a simple process that involves photo-induced redox reactions, the fact that the photocatalytic reduction of CO_2 occurs in several steps means that several factors can significantly influence the process.

Recombination of charge carriers

A proper separation of charge carriers is essential to ensure their migration to the photocatalyst´s surface and carry out the superficial redox reactions. But the recombination of e^--h^+ pairs described in Equation *(3.7*) and Figure 3.10 decreases significantly the proportion of charge carriers that reach the surface to less than 10 %,[62] causing the degradation of charge carriers into energy as heat or light emission.[63] Structural defects such as interstitial atoms, vacancies, and grain boundaries, provide recombination centers that induce the decay of photocatalytic activity, although the highly ordered and crystalline nature of MOFs eliminates a large part of these defects and, consequently, recombination is suppressed.[39]

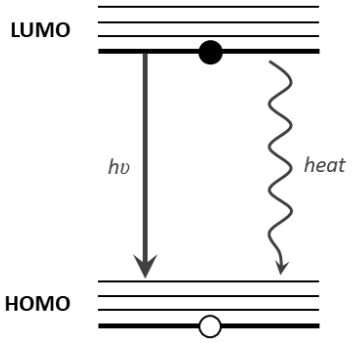

$$e^- + h^+ \longrightarrow N + E \qquad (3.7)$$

N: neutral center
E: energy (light $h\upsilon' \leq h\upsilon$ or heat)

Figure 3.10. Charge carrier recombination process.

Absorption of visible light for photocatalyst activation

To date, most of photocatalysts are photoactive under UV irradiation,[50] leading to low photoconversion yields and efficiency, because UV light constitutes less than 4 % of the solar spectrum.[64] Knowing that the solar spectrum consists mainly of visible and near-infrared light (45 % and 50 % approx., respectively), UV/vis/NIR active photocatalytic systems are more suitable in view of efficient solar-energy utilization.[65]

Adsorption and activation of CO_2

The lineal geometry and the strong C=O bonds give CO_2 great stability that makes this molecule inert, requiring large amounts of energy and appropriate catalysts to break the bonds and bend the structure.[46] According to research, CO_2 photoreduction occurs by single-electron transfer processes,

which involves the formation of $CO_2^{\bullet-}$ in the first step. This anion radical is the activated CO_2 molecule, and its formation is the limiting step of the CO_2 reduction process. This is because this intermediate has a very negative equilibrium potential (see reaction *(4)* of Figure 3.9) due to the reorganization of energies between the linear molecule of CO_2 and the bent radical anion; so, the activation step from CO_2 to $CO_2^{\bullet-}$ is thermodynamically disadvantaged. In addition to this, the electronic configuration of carbon and oxygen atoms in CO_2 due to the octet rule hinders the addition of an electron to activate the CO_2.[66]

In this regard, adsorption of CO_2 is a key step, since several studies indicate that this process generates a partially charged $CO_2^{\delta-}$ species due to atomic interactions with the surface, providing the transfer of one electron to CO_2 and forming the $CO_2^{\bullet-}$ anion radical. This may be possible because each oxygen has a lone pair of electrons, which can be donated to a Lewis acid center, while carbon can act as an electron acceptor to form carbonate-like species, leading to the bending of the CO_2 molecule due to adsorbate/surface interactions.[67] Figure 3.11 illustrates the possible adsorption modes for CO_2 on a metal oxide surface, four of which show a bent O–C–O bond angle: (a) adsorption may be linear through the O atom; (b) C atom may be adsorbed on the surface with exposed metal atoms to give C-linked species; (c) bidentate carbonate species are formed by the adsorption of CO_2 on the surface linked to metal and O atoms; (d) two O atoms of CO_2 bind with surface through two metals, while the C atom binds an O atom of the surface, forming a bridged carbonate geometry, and (e) two O atoms of CO_2 adsorb on the two metal atoms with the C atom of CO_2 upward. The break of the structural linearity decreases the LUMO level and generates a lower energy barrier to the reaction, enhancing charge transfers from the photocatalyst's surface to $CO_2^{\delta-}$.[68]

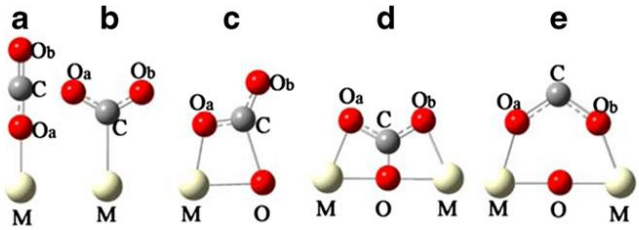

Figure 3.11. Possible structures of adsorbed $CO_2^{\delta-}$ on metal oxide surfaces.[68]

Even if all the above factors are important, for the photocatalytic CO_2 reduction, the adsorption of CO_2 on the photocatalyst surface is the most influencing factor that determines the efficiency of the photocatalytic cycle. Even though the photocatalyst can meet all the above requirements, CO_2 must be firstly adsorbed so as to be activated and its reduction be thermodynamically disabled; and secondly,

adsorption is necessary so that charge transfers between CO_2 and surface can occur and, therefore, the redox reactions for the transformation of CO_2 can take place.[69]

Competitive reaction of H_2 production

In the case of photocatalysis, the transformation of CO_2 is based on redox reactions photoinduced by a source of radiation, where the CO_2 is reduced to any of the products indicated in the reactions of Figure 3.9, while another electron-acceptor species is oxidizing. The most suitable molecule for this oxidation is water, since it is a source of e^- and H^+ that does not generate toxic or polluting products that influence the sustainability of the photocatalytic process. But this oxidation process, also known as water splitting, is also related to the production of H_2, since the H^+ are reduced by photogenerated e^- to give H_2.[70]

In the case of CO_2 reduction, in addition to the previously explained path involving the formation of the intermediate $CO_2^{\bullet -}$ via one-electron reduction reaction after its adsorption over photocatalyst's surface, there is another alternative path based on the proton-assisted multi-electron CO_2 reduction process that involve reactions with lower redox potentials. This process requires a number of proton and multi-electron transfer steps in order to carry out the carbon reduction, hydrogenation and C-coupling reactions; so, there are both kinetic and thermodynamic barriers that limit this process. Because the one-electron H^+ and the multi-electron CO_2 reductions use the photogenerated electrons and they have a similar reduction potential, both reactions compete with each other, although the H^+ reduction is more favoured by its simplicity.[71]

Due to the accessible high surface areas, tuneable pores, and versatile chemical functionalities, MOFs are emerging as promising materials for photocatalytic CO_2 reduction since they can be designed to absorb solar light, enhance the CO_2 adsorption by the introduction of functionalities such as *cus*, and to include accessible catalytically active sites because of the high porosity and surface areas.[72] The next section provides more detailed information on design strategies and the improvement of MOFs so that they can act as photocatalysts in CO_2 transformation processes.

3.1.3.3. Design of MOFs for photocatalytic CO_2 reduction

Photocatalytic activity of a MOF is linked to its structural properties, so the design of the material by the correct choice of metal clusters and ligands, and the insertion of a variety of functionalities is the

key for obtaining MOFs capable of performing the photocatalytic CO_2 reduction.[73] Several studies have shown that the features described below influence the efficiency of photocatalytic MOFs.

1. Absorption of sunlight. MOFs can be designed to absorb UV/vis irradiation by the correct choice of organic ligand and/or metal ions. In general, this characteristic is controlled by the organic ligand, which can contain aromatic molecules with electron-donating functional groups that enable the transfer and migration of electrons, providing a lower bandgap and broadening the absorption spectra to longer wavelengths.[74] A computational study performed over MIL-125 analogues revealed the influence of introducing a 10% of a functionalized bdc-R ligand (where R = $-NH_2$, $-OH$, $-CH_3$, $-Cl$) as linker in the energy gap of the system, finding that strong electron-donating substituents decrease considerably the optical gap of the MOF: from 3.57 eV in MIL-125 (unsubstituted) to 1.28 eV in MIL-125-$(NH_2)_2$.[75]

2. Improved charge transfer and separation. Even though the crystalline structure of MOFs avoids the formation of recombination sites, they present poor charge transport properties due to the low spatial overlap of orbitals between adjacent molecules. That is, the well separation of ligands in MOF hinders the electronic coupling and directly affects the charge transfer. π-conjugated building blocks are a good choice to enhance charge transfer properties, since the delocalization of charge carriers helps their transfer and separation.[76] One factor that influences the charge separation is the metal that forms the metal cluster, since it directly influences the energy gap of the photocatalyst; therefore, semiconductors such as transition metals with very negative reduction potential generate a greater energy gap by favouring the separation of the charge carriers.[77]

3. Adsorption of CO_2. In order to perform photocatalytic CO_2 reduction, the MOF must be able to selectively adsorb it. To this end, the structure can be functionalized by inserting *cus* and functional groups which improve interactions between CO_2 and the pore surface. As stated in Chapter 2, ligands based on aromatic rings functionalized with polar groups such as amino groups are the best option for CO_2 adsorption.[78]

4. Stability of the structure. A photocatalytic reaction involves the continuous application of a radiation source along with continuous exposure to moisture, which can cause degradation of the photocatalyst. Therefore, the structure of the MOF must be kept stable and robust for as long as possible, and this property can be improved by including hydrophobic functional groups in the MOFs.[77]

The study of structure and properties of MOFs, in addition to assisting in the design of on-demand materials for applications and fields of interest, provides valuable information on possible mechanisms of

material action. In the case of photocatalytic CO_2 reduction, such studies have been essential to understanding the photocatalytic cycle. Figure 3.12 is a representation of the general reaction mechanism based on LMCT processes in the well-known NH_2-UiO-66, one of the most studied MOFs in photocatalytic applications.[79] NH_2-UiO-66 is a MOF with cubic structure built up from hexameric Zr_6O_{32} units and 2-aminoterephthalate (ata) ligands, which was synthesized in the University of Oslo (Universitetet i Oslo = UiO).[80] According to the structure and composition of the MOF, this porous material has the necessary characteristics to photocatalyze the reduction of CO_2:

- As ata ligand is sensitive to UV/visible irradiation, photoexcitation will occur with sunlight.
- The aromatic ring of the ata can improve charge transfer processes.
- As the redox potential of Zr^{IV}/Zr^{III} is very negative, charge separation in excited states will be effective.
- The amino group of the ligand interacts with CO_2, improving its adsorption.[79]
- The big size of Zr^{IV} ions and its oxyphilic character allow metal clusters of coordination number 12, giving stability and robustness to the structure. Furthermore, the Zr_6 octahedra of the cluster is covered by μ_3-O eta μ_3-OH groups, providing hydrophobicity to the MOF and improving its stability.[81]

As the NH_2-UiO-66 compound meets the requirements for photocatalytic CO_2 reduction, several studies have been conducted that have proposed the following reaction mechanism:[79]

1. CO_2 is introduced into the pores by diffusion to be adsorbed on the internal surface of the MOF.
2. Photocatalyst is activated through light irradiation.
3. LMCT processes excite the $[Zr_6O_4(OH)_4(CO_2)_{12}]$ metal cluster, generating e^--h^+ charge carriers which reduce Zr^{IV} to Zr^{III}.
4. Zr^{III} is oxidized again to reduce the adsorbed CO_2. At the same time, triethanolamine (TEOA) is reduced, giving hydrogens that react with the CO_2 reduction product to yield formic acid, and acting as sacrificial agent which provides electrons to balance electron transfer processes.
5. Formic acid is released as a final product of the photoreduction.

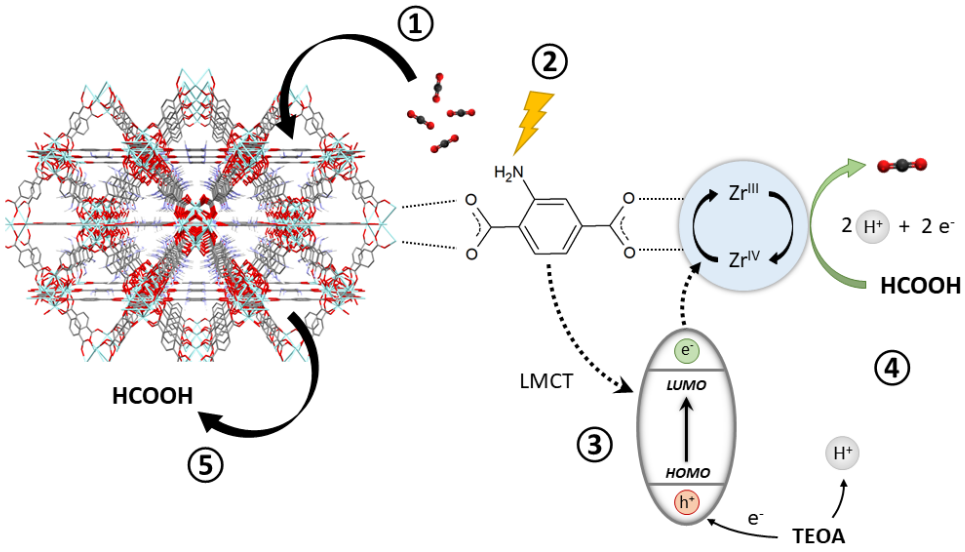

Figure 3.12. Proposed mechanism for photocatalytic CO_2 reduction over NH_2-Uio-66(Zr) under visible-light irradiation. Adapted image from Reference 79.

Based on the fact that both luminescent and photocatalytic properties are born from the change transfer ability of the MOF, the factors taken into account for the design of the MOF will affect both properties in a similar way. Therefore, in the following section, we will study the design of a new MOF based on the 5-cyanoisophthalate (CNip) ligand for its subsequent application in luminescence and photocatalytic CO_2 reduction.

3.1.4. CNip ligand-based MOFs for luminescence and photocatalysis

Being one of the objectives of this thesis work the synthesis and characterization of multifunctional MOFs with luminescent and photocatalytic applications, the design of the material must take into account that the same building blocks must provide the necessary qualities to the MOF so that they can contain both luminescent and selective photocatalytic properties. In this case, 5-cyanoisophthalic acid (H_2CNip) illustrated in Figure 3.13 was chosen as organic ligand given its rigidity based mainly on the aromatic carboxylate , which can provide enough robustness to build up stable porous structures. In addition, the wide variety of coordination modes of carboxylic groups with metal ions afford certain structural variability.[82] Even so, the bulkiness of –CN can also prevent the total substitution of the metallic coordination sphere by steric hindrance because of the limited distance between ligands in MOFs, allowing the coordination of solvents and generating possible *cus*.[83]

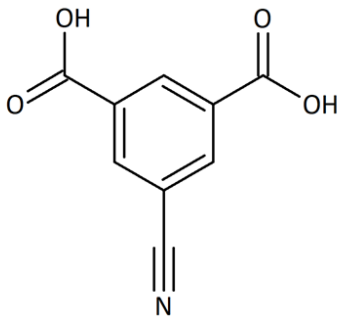

Figure 3.13. 5-cyanoisophthalic acid (H_2CNip) compound.

The chemical structure of this ligand presents some advantages that provide luminescent and photocatalytic properties. The simple π-conjugated system of this organic compound can benefit charge transfers because the coplanar geometry between the aromatic ring and the cyanide substituent enhances and stabilizes the delocalization of orbitals, decreasing the energy gap; and, besides, the triple bond of -CN blocks oscillations of the group and vibrational energy decay is avoided.[84] Functional groups composing this organic molecule permit different interactions with adsorbates, so it can be used to synthesize MOFs for applications in fields like sensing and/or photocatalytic CO_2 reduction. In the case of CO_2 adsorption, which is a crucial step for its photocatalytic reduction, CNip can establish π-quadrupole interactions with CO_2 through both the aromatic ring and the -CN triple bond.[78b] In the case the cyanide group is not coordinated to a metallic center, the N atom can act as a Lewis base and polarizes the CO_2 molecule to generate dipole-quadrupole interactions. The two carboxylate groups can also contribute to CO_2 adsorption since, if the metal coordination occurs by a unique carboxylate oxygen atom, the uncoordinated oxygen could act as an electron-rich site forming specific interaction with the gas of interest.[78d]

Among all MOFs described in the bibliography based on CNip ligand, none of them shows the cyanide group acting as a coordinating group. The first reported compound was a heterometallic porous MOF based on Fe(III) and Co(III), which has $[Co_2Fe_4(CNip)_5(\mu_3\text{-oxo})_2(\mu_2\text{-acetate-O,O'})_2(H_2O)_6]_n$ formula. This MOF was very similar to MIL-59, except for the fact that it contains a 5-connected cluster instead of a 6-connected, in which one CNip ligand is replaced by one acetic acid molecule.[83] Afterwards, a Dy(III)-MOF of formula $\{[Dy_2(CNip)_3(DMF)_4]\cdot DMF\}_n$ was obtained, in which the two crystallographically independent Dy(III) bridged by one CNip with bis-bridging intranuclear coordination mode and two other CNip with bridging-chelating internuclear mode build a porous 3D structure with solvent-occupied big channels along the *c* axis.[85] Shortly after, six new CNip based MOF families were characterized, which show magnetic, adsorption and luminescent properties. Among the compounds obtained, there are two

bidimensional MOFs of Cu(II) and Co(II) metals, although the connectivity in each case presented wide disparities. The Cu-based MOF, with $[Cu_3(\mu_3\text{-CNip})_2(\mu\text{-}H_2O)_2(\mu_3\text{-}OH)_2]_n$ formula, consist of 2D sheets formed by the coordination of three Cu atoms to CNip ligands in tris-bridging intradinuclear coordination mode, a bridging water molecule, and a μ_3-hydroxide anion. In the case of the other bidimensional $\{[Co_3(\mu_4\text{-CNip})_3(DMF)_4]\cdot\sim 2DMF\}_n$ compound, centrosymmetric trinuclear entities were connected through four-connected CNip linkers. It should be noted that the coordination of DMF molecules to external Co atoms prevented the polymerization of the structure, avoiding the formation of a three-dimensional structure. As mentioned above, 3D structures based on transition metals and lanthanides were also obtained: on the one hand, the $[Cd(\mu_4\text{-CNip})(DMF)]_n$ compound consists of the junction of rodlike chains generated by the coordination of a Cd atom with a tetradentate CNip ligand, building up a compact structure without solvent-accessible voids. On the other hand, the MOF of $\{[Zn_{32}(\mu_4\text{-CNip})_{12}(\mu\text{-CNip})_{12}(\mu_4\text{-O})_8(H_2O)_{24}]\cdot\sim 12DMF\}_n$ formula presents a structure formed from the union of open discrete cubic-shaped metal-organic cages through hydrogen-bonding interactions. Unfortunately, these cages, which contained eight Zn_4O clusters linked by twelve CNip, have no connectivity between them, so despite the large free volume (37.5 % per unit cell) enclosed in the structure, it is not stable enough as to exhibit permanent porosity. Regarding the lanthanide-based MOFs, the isostructural $\{[Ln_2(\mu_4\text{-CNip})(\mu_3\text{-CNip})_2(DMF)_4]\cdot\sim DMF\cdot H_2O\}_n$ (Ln = Dy, Tb, and Er) family, consists of two equivalent Ln atoms bridged by four CNip ligands coordinated in bis-bridging and bridging-chelating modes. In this way, the pore system of the 3D structure accounts for 13.3 % of the unit cell volume. Finally, structure described for the Ln-CNip MOFs, which has the formula $\{[Gd_6(\mu_3\text{-CNip})_6(\mu_4\text{-CNip})_2(\mu\text{-formate})_2(H_2O)\ (DMF)_{10}]\cdot\sim 3DMF\cdot 3H_2O\}_n$ and consists in a 3D network with intercrossed channels along *a* and *b* axes that account for the 29.3 % of the unit cell.[86]

Due to the wide variety of possible coordination modes described above (Figure 3.14), its charge transfer related properties, and the possibility to generate *cus* given the steric hindrance of -CN group, this chapter aims to increase knowledge about CNip-based MOF and their multifunctionality, especially in the fields of luminescence and photocatalysis. For the synthesis of these MOFs, a heterometallic alkaline earth-transition metal, such as calcium and zinc, may afford the desired properties material. As indicated in Chapter 2, electropositive metals such as alkaline and alkaline earth groups act as adsorption sites due to their polar nature, *i.e.* they exert electrostatic interactions with gases due to their Lewis basicity.[87] Even so, metals such as calcium can generate unstable structures that are easily hydrolysed due to the ionic character of the M-O bond; therefore, it is important to complement this metal with another that provides stability to the structure, such as transition metals.[88] Zinc is a highly plastic metal that accepts different

coordination environments as well as generating bonds strong enough to maintain robust structures.[30,86] Furthermore, being a metal with a d^{10} closed-shell configuration, it could favour the triplet states' population and generate a long-lived charge separations, enhancing both luminescent and photocatalytic properties.[30]

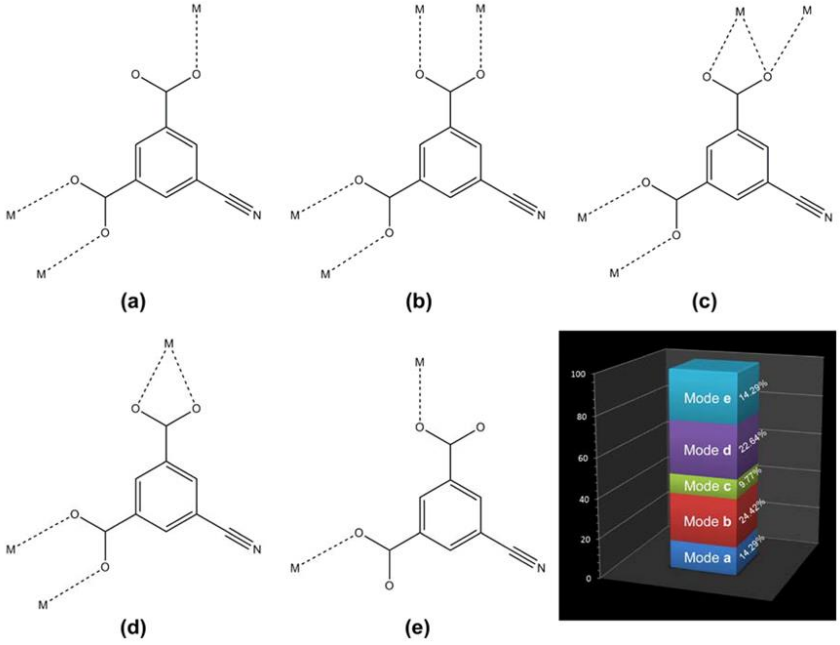

Figure 3.14. Possible coordination modes of the CNip ligand. **(a)** μ_3-CNip-κO:κO′:κO″, **(b)** μ_4-CNip-κO:κO′:κO″:κO‴, **(c)** μ_4-CNip-κ^2O,O′:κO′:κO″:κO‴, **(d)** μ_3-CNip-κ^2O,O′:κO″:κO‴, **(e)** μ-CNip-κO:κO″. Bar chart indicates the percentage of hits showing the coordination mode for 5-cyanoisophthalate ligand.[86]

Single crystals of a new 3D and porous MOF have been synthesized and fully characterized in order to obtain a complete knowledge of both the structure and the physicochemical properties. Along with this, several experiments have been carried out to activate the material, in order to assess the accessibility of the *cus* and its implication in CO_2 adsorption. These measures will provide the CO_2 adsorption capacity of the MOF and could also help clarify the role of the *cus* in this process, as the adsorption of CO_2 onto the metal cluster is essential for the photocatalytic process. Aware of the possible difficulties that could be generated during the activation of a MOF with coordinated DMF, a solvent exchange was used to obtain a new stable material which was characterized to assess the chemical stability of the initial MOF structure. This is because, although the anhydrous structure of a MOF may be stable, changes in the chemical composition (such as the use of another solvent) can significantly affect the properties of the material.[89] Once thoroughly studied, the applicability of the MOF will be tested, on the one hand, by carrying out the

photocatalytic reduction of CO_2 under UV light, and on the other hand, by performing solid-state photoluminescence experiments. The latter, in addition to revealing the phosphorescent behaviour of the materials at low temperatures, have provided information on the most likely mechanisms in which charge transfers can occur in the process of photocatalytic CO_2 reduction.

3.2. Materials and methods

3.2.1. Compound synthesis

Table 3.1 summarizes the three MOFs to be studied in this chapter.

Table 3.1. Synthesized compounds.[a,b,c]

Synthesis	Compound	Code
Solvent evaporation	$\{[CaZn(\mu_4\text{-}CNip)_2(DMF)_2]\cdot 2H_2O\}_n$ Poly[bis(mu4-5-cyanoisophthalate-kO:kO':kO'':kO''') bis(dimethylformamide)calcium(II)zinc(II)]dihydrate	**CaZn (4)**
Solvent exchange	$\{[CaZn(CNip)_2(MeOH)_2]\cdot ½DMF\}_n$ Poly{[bis(mu4-5-cyanoisophthalate- kO:kO':kO'':kO''')bis(methanol)calcium(II)zinc(II)] }	**CaZn_MeOH (5)**
	$\{[CaZn(CNip)_2(H_2O)_2]\cdot ½DMF\cdot 6H_2O\}_n$ Poly{[bis(mu4-5-cyanoisophthalate- kO:kO':kO'':kO''')diaquacalcium(II)zinc(II)]hexahydrated}	**CaZn_H_2O (6)**

[a] CNip = 5-cyanoisophthalate = $C_9H_3NO_4^{2-}$ [b] DMF = dimethylformamide = C_3H_7NO [c] MeOH = methanol = CH_4O

Crystalline CaZn (4). 2 mL of a solution of DMF containing 0.1 mmol of $Ca(NO_3)_2\cdot 4H_2O$ (0.0236 g) and 0.1 mmol of $Zn(NO_3)_2\cdot 6H_2O$ (0.0298 g) were mixed with another DMF solution (2mL) containing H_2CNip (0.2 mmol, 0.0382 g) in a vial. Solvent of the sonicated mixture was slowly evaporated at ~50°C in the partially sealed vial. After one week, yellowish crystals were grown, collected and washed with DMF for analysis as a crystalline powder. X-ray quality single crystals were obtained from the filtered solution after three months.

Crystalline CaZn_MeOH (5). 320 mg of crystalline CaZn (**4**) were stirred in 6 mL of MeOH for 24 h to obtain a lighter yellowish crystalline powder.

Crystalline CaZn_H_2O (6). 100 mg of crystalline CaZn (**4**) were sonicated in 2 mL of H_2O for 5 minutes to yield a white solid.

3.2.2. Gas adsorption

Dinitrogen (77 K) and carbon dioxide (273 and 298 K) physisorption data were recorded with a Quantachrome Autosorb-iQ MP. Prior to measurements all samples were thoroughly washed with ethanol (EtOH) and methanol (MeOH) to remove the remaining reagents from the pore, and thereafter, outgassed under vacuum at 140 °C for 6 hours. The specific surface area was calculated from the adsorption branch in the relative pressure interval using the Brunauer−Emmett−Teller (BET) method[90] and the consistency criteria proposed by Walton and Snurr that is commonly applied for MOFs,[91] while the micropore volume was estimated by fitting the measured N2 isotherms with the t-plot method.[92]

3.2.3. Adsorption mechanism

FTIR spectra were recorded on a Nicolet 6700 spectrometer (ThermoScientific, USA) with an ATR accessory and a DTGS detector, accumulating 32 scans with a resolution of 4 cm^{-1}. Spectra were collected at room temperature, under vacuum, at different temperatures (RT to 260 °C), and under gas atmospheres (H_2 and CO_2).

3.2.4. CO_2 Photoreduction

CO_2 photoreduction experiments were conducted in continuous flow mode in a gas-phase stainless steel photoreactor, with an effective volume of 190 mL and provided with a borosilicate window for irradiation. The powdered catalysts (0.1 g) were deposited on glass microfibre filters from aqueous suspensions. Pure carbon dioxide (99.9999%, Praxair) and water (Milli-Q) were fed into the reaction system with a CO_2:H_2O molar ratio of 7.25 by means of a Controlled Evaporator Mixer (CEM). The reaction conditions were set at 2 bar and 50°C. Irradiation was provided by four UV fluorescent lamps of 6 W each (λ_{max}=365 nm). In-line analyses of the reactor outlet gas were performed every 22 min using a Bruker 450-GC gas chromatograph equipped with three columns (BR-Q Plot, BR-Molsieve 5A and CP-Sil 5B), three detectors (2 FID and 1 TCD) and a methanizer. The reactor was firstly purged with Ar (100 mL/min) for 1 h in order to remove any residual compounds weakly adsorbed on the surface of the catalyst. Then, the reactor was fed in the dark with a CO_2 and H_2O mixture for 1 h to establish an adsorption-desorption balance at the reaction temperature. Prior to illumination, the reactor was pressurized and kept at the reaction flow rate for another 1 h. Cumulative productions were calculated by numerical integration of the formation rate versus time data obtained from in-line analyses.[93]

3.2.5. Luminescence

Fluorescence excitation and emission spectra were recorded on a Varian Cary-Eclipse Fluorescence Spectrofluorimeter (at RT) equipped with a xenon discharge lamp (peak power equivalent to 75 kW), Czerny–Turner monochromators, and an R-928 photomultiplier tube. For the fluorescence measurements, the photomultiplier detector voltage was fixed at 600 V while the excitation and emission slits were set at 5 and 2.5 nm. PL measurements at 50 K were done using a close cycle helium cryostat enclosed in an Edinburgh Instruments FLS920 spectrometer. For steady-state measurements in the UV-Vis range, an IK3552R-G HeCd continuous laser (325 nm) was used as excitation source, whereas a Müller-Elektronik-Optik SVX1450 Xe lamp was employed to collect the excitation spectra.

3.3. Results and discussion

This section is divided into two parts, the first of which presents the study and characterization of the new CaZn (**4**) MOF, whereas the second one discusses the chemical stability of the starting compound and the characterization of the derivatives obtained by solvent exchange method.

3.3.1. Crystallographic analysis of CaZn (4)

Table 3.2 collects a summary of the crystallographic data of CaZn (**4**) compound at 100 K. For further information about the refinement conditions employed for the structural resolution, see Appendix II.

Table 3.2. Crystallographic data of CaZn (**4**).

Parameters	CaZn (4)
Empirical formula	$C_{24}H_{24}CaN_4O_{12}Zn$
M (g mol^{-1})	665.94
Cryst. System	Trigonal
Space group	*R*-3*c*
a (Å)	28.2278(6)
b (Å)	28.2278(6)
c (Å)	19.4937(12)
α (°)	90
β (°)	90
γ (°)	120
V (Å^3)	13451.8(10)

Z	18

One of the two crystallization water molecules could be refined despite showing ADPs since they are disordered in the voids. Accordingly, the "squeeze" method implemented in PLATON program was used to subtract from the electron density corresponding to the second disordered solvent molecule present at the voids. The analysis of the electron density subtracted per void volume (of 231 electrons in 1932 $Å^3$) confirms that CaZn (**4**) contains another crystallization water molecule. The coordination DMF molecule was also found to be disordered in two equivalent dispositions, each of which was refined with 50 % of occupation. This fact precluded the refinement of hydrogen atoms belonging to the latter molecule.

3.3.2. Structural characterization of CaZn (4)

Single-crystal X-ray diffraction

Data obtained by SCXRD analysis shows that the new crystal structure of CaZn (**4**) consists of a three-dimensional neutral MOF. This porous structure is built up by the junction of zinc (Zn^{2+}) and calcium (Ca^{2+}) ions (Figure 3.15,

Table **3.3**) through CNip ligands, which act as connectors. The asymmetric unit contains half a calcium and zinc ions (because they lie on twofold axes), a CNip ligand, a coordination DMF molecule and two crystallographically independent lattice water molecules. Zn1 atom possesses a tetrahedral geometry (S_{Td} = 1.723), which is generated by the coordination of four non-chelating oxygen atoms of four symmetry-related CNip linkers, generating an O_4 donor set. Instead, Ca2 atom presents an octahedral geometry built up by four non-chelating oxygen atoms of CNip and two DMF molecules (S_{Oc} = 1.672), despite of which it may be also considered as a distorted TBU given the relative tetrahedral disposition of the carboxylate oxygen atoms and the fact that DMF act as terminal ligands (affording no further connectivity to the framework). In this sense, CShMs performed upon the CaO_4 node (considering only carboxylate oxygen atoms), corroborate its large distortion with regard to a tetrahedron (S_{Td} = 10.058) suggesting that it would be better referred to as a pseudo-TBU (PTBU).

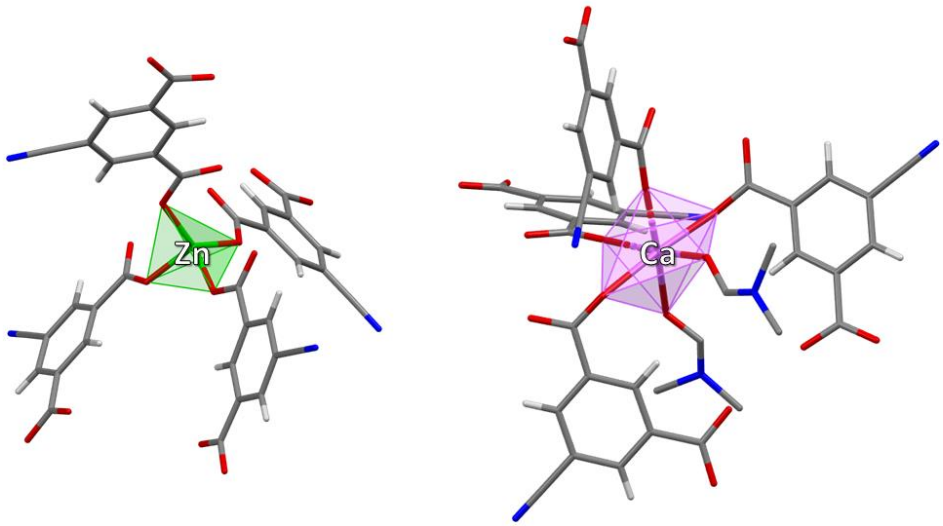

Figure 3.15. Building units of CaZn (**4**) compound with the atomic numbering scheme.

Table 3.3. Coordination bond lengths (Å) of CaZn (**4**) compound.[a] Note that only one of the disordered O_{DMF} atoms has been considered for clarity.

Bond	Length (Å)	Bond	Length (Å)
Zn1–O2	1.947(3)	**Ca2–O4(iv)**	2.230(3)
Zn1–O2(i)	1.947(3)	**Ca2–O4(iii)**	2.230(3)
Zn1–O3(ii)	1.990(3)	**Ca2–O1(v)**	2.323(3)
Zn1–O3(iii)	1.990(3)	**Ca2– O1**	2.323(3)
		Ca2– O_{DMF}(v)	2.358(6)
		Ca2– O_{DMF}	2.358(6)

[a] Symmetries: (i) y+2/3, x-2/3, -z+5/6; (ii) x+1/3, x-y-1/3, z+1/6; (iii) x-y+1/3, x-1/3, -z+2/3.; (iv) -y+2/3, -x+1/3, z-1/6; (v) x-y, -y, -z+1/2.

On its part, CNip ligand joins Ca(II)- and Zn(II)-based building units one another by means of the μ_4-k*O*:k*O'*:k*O''*:k*O'''* coordination mode (Figure 3.16), in such a way that each ligand links to four units (two TBU and two PTBU) and hence, it may be considered as four-connected linker. As a result of the junction among the two nodes through the aforementioned carboxylate-based connections, the network can be described as a **ptr** topological network with the ($4^3 \cdot 6^2 \cdot 8$) point symbol. A further inspection of the structural aspects of the framework reveals that the junction of Zn1 and Ca2 nodes gives rise to dimeric entities with $[CaZn(CNip)_2(DMF)_2]$ formula, in which Ca···Zn distance is around 6.28 Å. As shown in Figure 3.17a, the ligands generate planes that are almost parallel to each other, while the DMFs are directed outside these planes to give weak interactions with aromatic rings. Each dimer is connected to four other entities setting in 4.28 Å the distance of the double carboxylate mediated bridged Ca···Zn (Figure 3.17b

and c). Finally, the structure contains π-π interactions among the aromatic rings (see Figure 3.17d), which is consistent with the arrangement already described for the ligands (see Table 3.4 for more detail).

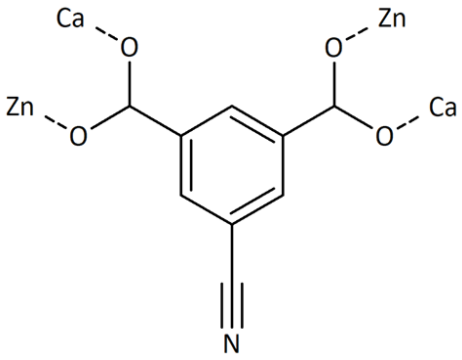

Figure 3.16. Coordination mode of the CNip ligand.

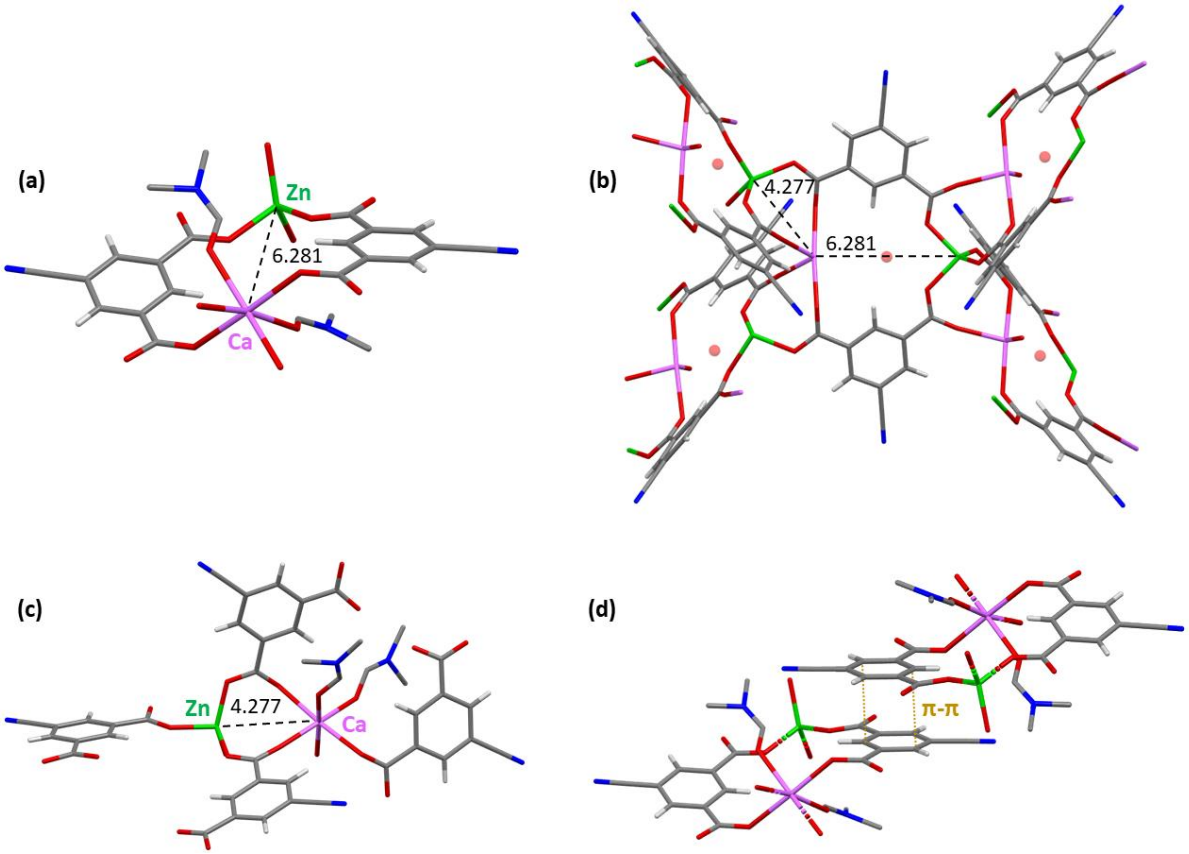

Figure 3.17. Structural details of CaZn (**4**): (a) dimeric entities of [CaZn(CNip)2(DMF)2]; (b) connection between five dimeric entities, where centroid of each entity is indicated by a red dot (DMF molecules have been deleted for better appreciation); (c) double carboxylate mediated bridged Zn···Ca; and, (d) π-π interactions of aromatic rings in parallel planes.

Table 3.4. Structural parameters (Å, °) of π–π interactions of compound (**4**).[a]

Ring...Ring[b]	α	DC	β	DZ	Dist.
1A–1A(i)	39.85	4.2438	37.7	4.1945	3.39–5.11
1A–1A(v)	77.46	5.0257	44.6	3.5765	3.39–5.11

[a] Symmetry: (i) -1/2+x, 3/2-y, 7/4-z. α: dihedral angle between mean planes of the rings (°), DC: distance between ring centroids (Å), β: angle between DC vector and normal to plane(I) (°), DZ: perpendicular distance of the centroids of ring(I) on plane of ring(II) (Å), Dist.: shorter distances between non-hydrogen atoms of rings (I) and (II). [b] Rings: **1A**: C1, C2, C3, C4, C5, C6.

The porous structure of CaZn (**4**) has also been studied[94] using a Monte Carlo procedure implemented in a code developed by Herdes and Sarkisov[95] in which a probe of incremental size explores the free volume. These calculations (Figure 3.18a) show that this MOF can present two possible situations with quite different scenarios. In the first case (Figure 3.18b), the removal of the two lattice water molecules, one of which establishes hydrogen bonds with carboxylate oxygen atoms and the other could not be found, generates cavities connected by small cylindric channels with diameters in the range of 3.1 and 5.1 Å located along the *c* axis, which accounts for 12.6 % of the unit cell volume and a specific surface area of 126.6 m^2/g. As shown in Figure 3.18c, the removal of coordination DMF molecules significantly change the characteristics of the pores, since, in addition to the bottleneck shaped regional of 4.9 Å of diameter, both specific surface area (805.0 m^2/g) and porosity (43.5 %) increase considerably. The latter is because DMF molecules are exposed to voids and their removal generates more accessible pores. So, in addition to the fact that the pore size of both compounds would allow the diffusion of N_2, CO_2, and CO because of their smaller kinetic radii, it is worth noting that the release of coordination DMF molecules of Ca2 atoms could lead to open metal sites, providing both adsorption and catalytically active sites since, as Figure 3.18d shows, Zn atoms are also exposed to voids.

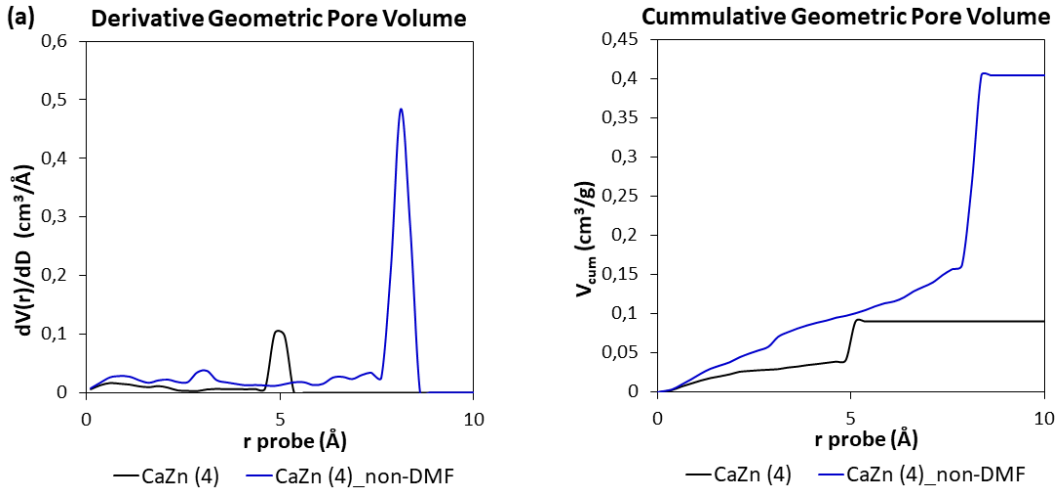

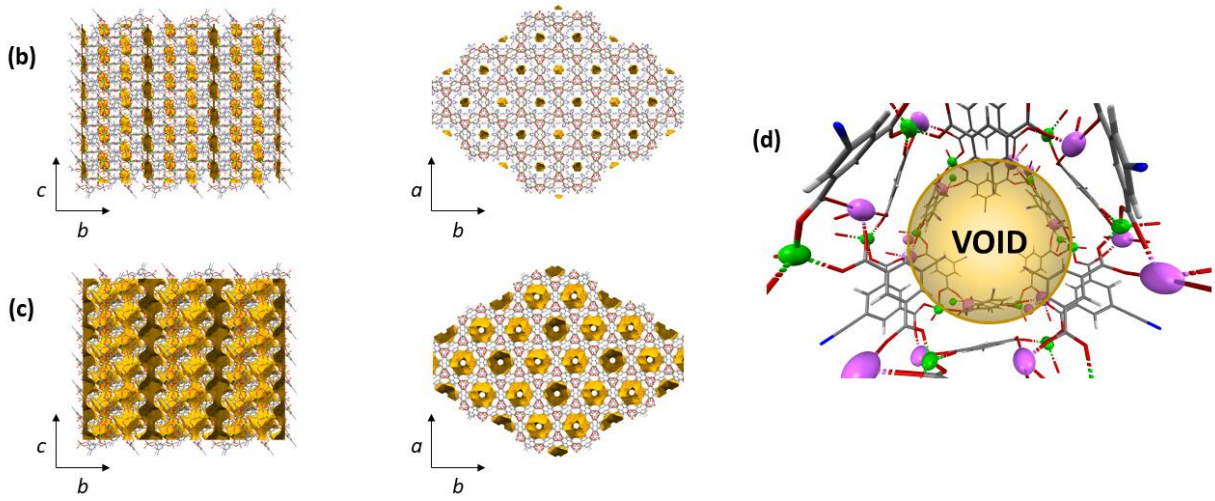

Figure 3.18. Description of porous structure of CaZn (**4**): **(a)** Exploration of free volume by Monte Carlo procedure; **(b)** Packing and potential accessible surface of CaZn (**4**) compound; **(c)** Packing and potential accessible surface of CaZn (**4**) compound without coordinated solvents; and, **(d)** Coordinatively unsaturated site in Ca atoms (pink dots) and Zn atoms (green dots) exposed to voids.

Once the structure of CaZn (**4**) has been described, homogeneity and the reproducibility of the synthesis has been studied by powder X-ray diffraction analysis (PXRD). Therefore, the next section shows the obtained information about the purity and crystallinity of the compound.

Powder X-Ray Diffraction

The PXRD data shown in Figure 3.19 confirms the purity and crystallinity of CaZn (**4**) compound, proving the good performance of the synthetic method due to the proper correspondence between the experimental and the theoretical diffractograms. Given that the experimental diffractogram was acquired at room conditions, this fact demonstrates its good stability. Refinement data summarized in Figure 3.19 indicate an elongation of the *c* parameter, which may be related to differences in temperature of single-crystal and powder diffraction measurements, since the low temperature at which crystallographic data is obtained could cause a slight contraction of the single-crystal structure.

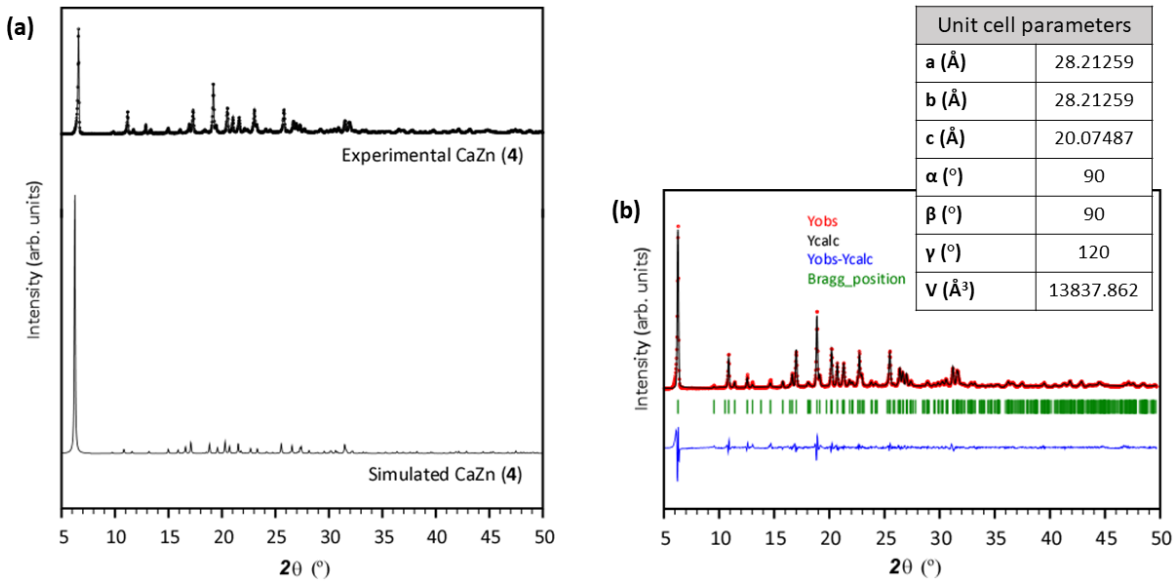

Figure 3.19. Powder X-ray diffraction analysis of compound (**4**). **(a)** Experimental and simulated diffractograms of CaZn (**4**). **(b)** Pattern-matching analysis of CaZn (**4**) (Refinement parameters: R_F/R_B: 3.54/1.83; R_P/Chi^2: 10.9/4.53).

Although compound CaZn (**4**) presents good stability at room temperature, the thermal stability needs to be first studied to check that crystal structure does not collapse during the activation before conducting gas adsorption and photocatalysis experiments. Thus, thermogravimetric analysis (TGA) of CaZn (**4**) has been carried out to study the thermal stability of the compound.

Thermogravimetric analysis

According to the TGA results (Table 3.5), CaZn (**4**) compound presents a relatively high thermal stability and potential capacity to behave as a permanent porous material. CaZn (**4**) collected in bulk differs slightly from that obtained in the crystallographic analysis. As described above, the crystal structure of the MOF possesses two crystallization water molecules inside the pores which are not completely distinguished in the TGA probably because of their spontaneous release from the void system of the MOF during its exposure to air, which is likely to happen in porous compounds due to the friction generated in the grinding of the sample. Even so, a small loss of 1.5 % can be seen at a temperature-range of 30-80 °C, which may be related to the release of water molecules. So, the general formula of the powdered sample of CaZn (**4**) is defined as $\{[CaZn(\mu_4\text{-}CNip)_2(DMF)_2]\cdot 2H_2O\}_n$. Coordination DMF molecules begin to release at around 140 °C, being a process that lasts up to 280 °C. From this point up to 420 °C, a large plateau

confirms the great stability of the anhydrous $\{[CaZn(\mu_4\text{-}CNip)_2]\}_n$ compound, which is decomposed above 430 °C to give CaO and ZnO as final products at 660 °C.

Table 3.5. Elemental analysis and TG/DTA curves of compound CaZn (**4**).

CaZn (4)

$\{[CaZn(CNip)_2(DMF)_2]\cdot xH_2O\}_n$ / $C_{24}H_{24}N_4CaO_{12}Zn$

T_i–T_f	$\Sigma\Delta m(\%)$	$\Sigma\Delta m(\%)_{teor}$
30-105	1.5	1.4 (– 0.5 H_2O)
140-280	24.1	22.9 (– 2 DMF)
420-660	73.5	75.7 (CaO + ZnO)

Elemental analysis

$\{[CaZn(CNip)_2(DMF)_2]\cdot 2H_2O\}_n$ / $C_{24}H_{24}N_4CaO_{12}Zn$

Calc.: C, 43.28; H, 3.64; N, 8.42; O, 28.83; Ca, 6.01; Zn, 9.82 %.
Found: C, 43.89; H, 3.15; N, 8.96 %.

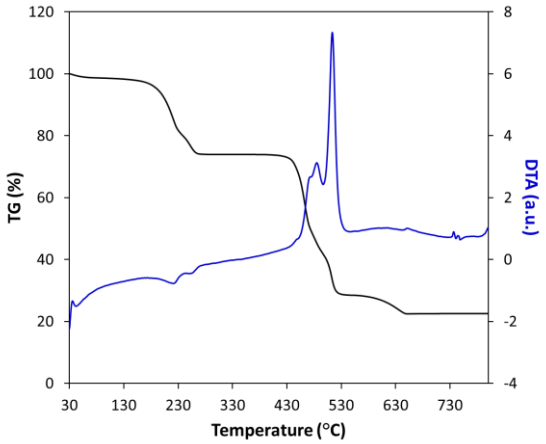

Despite the high stability of the MOF, outgassing and activation processes on CaZn (**4**) require the use of high temperatures even under vacuum to ensure the complete removal of solvents. This may lead to possible structural or phase changes that may influence the adsorption capacity of the material. Therefore, the results obtained from the study of the thermal evolution of CaZn (**4**) by thermodiffraction (TDX) measurements are especially relevant to approach the optimal outgassing conditions.

Thermal evolution of CaZn (4)

Before starting the TDX analysis, the stability of the sample under air and vacuum has been confirmed by PXRD at 30 °C, since the vacuum could cause a phase change. Figure 3.20a shows that both diffractograms measured under air and vacuum are identical. Given these results, the TDX measurements have been carried out under vacuum conditions in a temperature range of 30-550 °C and a heating rate of 5 °C/min. As can be seen in Figure 3.20b, there is a phase change at 140 °C related to the loss of DMF identified in the TGA (see Table 3.5), which remains stable up to ca. 470 °C where it completely decomposes to give the CaO and ZnO metal oxides.

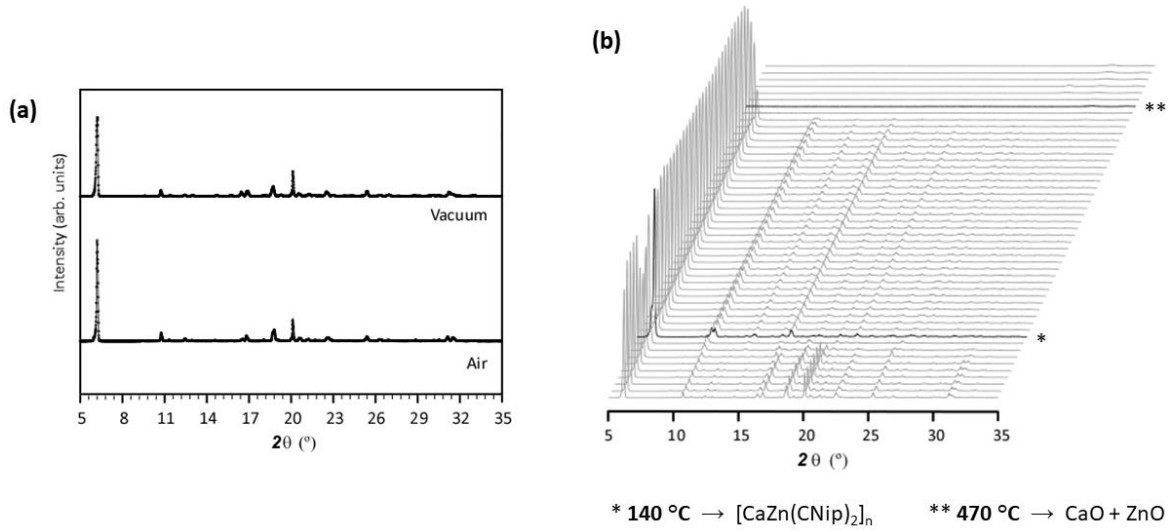

Figure 3.20. Thermal evolution of CaZn (**4**). **(a)** Diffractograms of CaZn (**4**) at 30 °C under air and vacuum. **(b)** Analysis of the thermal behavior of compound CaZn (**4**). Note: diffractograms shown in black correspond to temperatures at which phase transition takes place.

As mentioned above, a phase change occurs at 140 °C which could be related to DMF release; therefore, it is important to check that the structure remains stable and does not undergo major changes that would affect both the porous structure and the properties of the MOF. Small differences observed in diffractograms of Figure 3.21a indicate some change in the structure of CaZn (**4**) as a consequence of the increase of the temperature. According to the pattern-matching analysis (Figure 3.21b), the increase in temperature has generated a notable contraction of the unit cell, which may indicate that the MOF is in a closed-pore arrangement due to the release of the coordination DMF molecules directed into the pores.

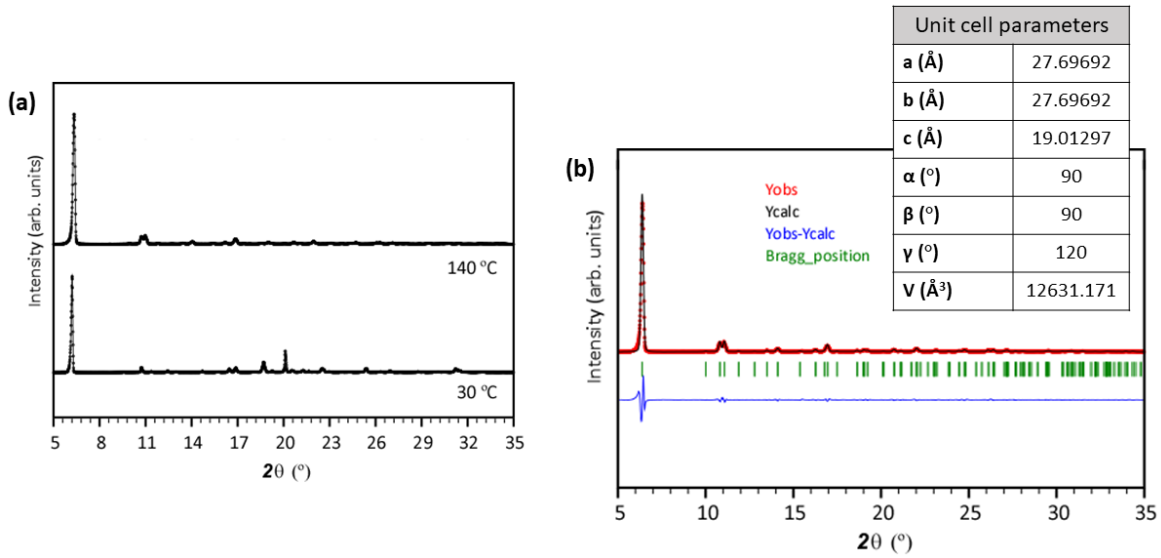

Figure 3.21. Phase identification at 140 °C by PXRD. **(a)** Diffractograms of CaZn (**4**) at 30 °C and 140 °C under vacuum. **(b)** Pattern-matching analysis of CaZn (**4**) at 140 °C under vacuum (Refinement parameters: R_F/R_B: 1.98 /0.696; R_P/Chi^2: 17.0 /1.46).

In order to confirm that this phase change is related to DMF loss, a study on the desorption of coordination solvents by Fourier-transform infrared (FTIR) spectroscopy has been carried out and is described below.

Desorption of coordination DMF molecules

To confirm the optimal conditions for the complete removal of coordination DMF molecules, FTIR spectrometry coupled to the thermal treatment has been carried out to study the DMF desorption mechanism in CaZn (**4**), in order to obtain information about the accessibility of the metal cluster once the activation takes place. The desorption has been conducted under a low vacuum (800 mbar) and heating the sample from room temperature (RT) up to 260 °C.

According to the spectra of Figure 3.22, CaZn (**4**) does not undergo significant changes until it reaches 240 °C. At this temperature, the characteristic band of C=O bond of the DMF situated at 1650 cm^{-1} disappears,[96] which is accompanied by widening of the bands, confirming the release of coordinated DMF molecules.

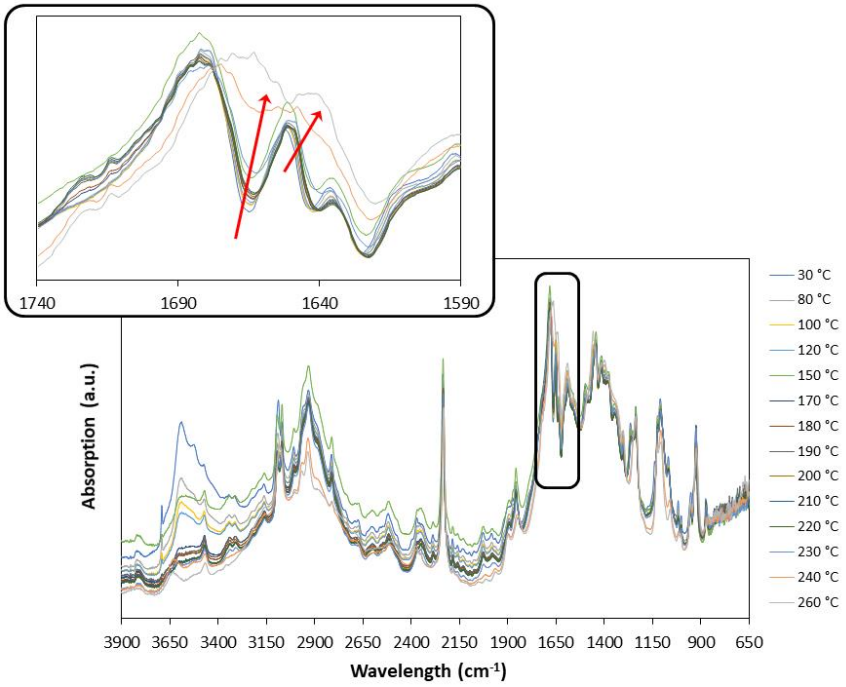

Figure 3.22. FTIR spectra of the evolution of CaZn (**4**) with temperature (from RT to 260 °C).

Once the coordinated DMF molecules have been eliminated, it is important to know whether the cus are involved in the CO_2 adsorption process, so the FTIR study is repeated in the presence of CO_2 with a previously activated sample.

Adsorption mechanism of CO_2

For the study of the CO_2 adsorption mechanism, CaZn (**4**) sample has been previously activated according to the next two steps: (1) overnight heating in an oven at 150 °C, and (2) heating at 190 °C for 4 hours and applying an Ar flow.

FTIR spectra (Figure 3.23a) are recorded at RT with a CO_2 flow of 10 cc/min (1% CO_2/Ar). During the experiment two significant changes in the spectra are experienced: on the one hand, two new bands appear at 1400 and 1420 cm^{-1}; and on the other hand, there is a shift in the band initially peaking at 955 to 965 cm^{-1}. These bands are related to monodentate carbonate species adsorbed on the surface; that is, CO_2 interacts with oxygen atoms of the metal cluster by linking the C atom of CO_2 with an oxygen atom on the surface.[97] These types of species have six IR-active bending and stretching modes (Figure 3.23b): ν_1, asymmetric bending $\delta(O_sCO)$; ν_2, symmetric bending $\delta(OCO)$; ν_3, out of plane deformation π; ν_4, symmetric stretch $\nu(C–O_s) + \nu(C–O)$; ν_5, symmetric stretch $\nu(C–O) + \nu(C–O_s)$; and ν_6, asymmetric stretch

v(C–O), where O_s denotes the surface oxygen. In the case of activated CaZn (**4**) only frequencies corresponding to v_4 and v_5 vibration modes have been detected due to the low CO_2 exposure.[98] According to vibrational modes, the band shift at 965 cm^{-1} is a consequence of the symmetric stretch *v*(C–O_s) + *v*(C–O), whereas bands at 1400 and 1420 cm^{-1} correspond to the symmetric stretch v(C–O) + v(C–O_s). It should be noted that the band around 1300 cm^{-1} is also slightly displaced as the experiment progresses owing to the increase of monodentate carbonate species which can aggregate into pairs and linear chains.[97]

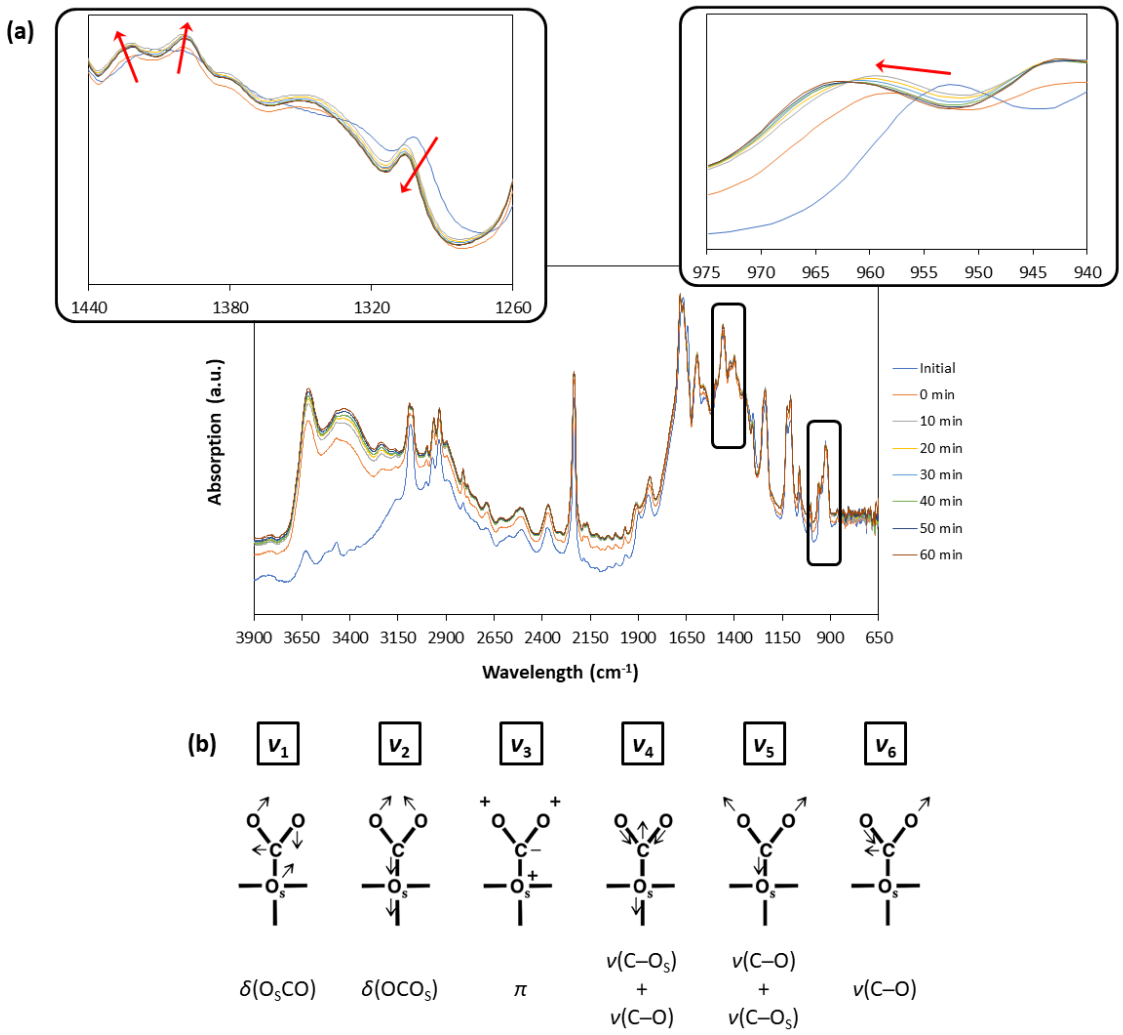

Figure 3.23. FTIR spectra of the CO2 adsorption over CaZn (**4**). **(a)** Evolution of activated CaZn (**4**) under CO_2 flow for 1 h. **(b)** Vibrational and bending modes in monodentate carbonate. O_s denotes the surface oxygen of the carbonate. Adapted image from Reference 98.

These measurements show that the elimination of DMF to generate *cus* improves the accessibility to the metal cluster, allowing the adsorption of CO_2 on it. Besides, the formation of a monodentate carbonate would provide the photocatalytic CO_2 reduction, since the bending of the molecule decreases the energy

barrier of the reaction. This compound presents potentiality in CO_2 capture, which is necessary to carry out the photocatalytic reduction of CO_2; so, to check the adsorption capacity, the following gas adsorption measurements have been conducted with CaZn (**4**) compound.

3.3.3. Gas adsorption experiments of CaZn (4)

Before starting with the CO_2 adsorption study, it should be noted that, due to the low pore size of this compound, the study of porosity by means of N_2 adsorption at 77 K revealed CaZn (**4**) no adsorption capacity. Even so, CO_2 molecules could diffuse through the pores of this MOF because they have a smaller kinetic radius than N_2 molecules; therefore, CO_2 adsorption at 273 K and 298 K has been studied with an activated sample at 140 °C and vacuum for 6 h. These outgassing and activation conditions have been chosen to obtain the data corresponding to the phase described above which is related to the loss of the coordinated DMF molecules.

As can be seen in Figure 3.24, the highest CO_2 adsorption capacity is reached at 1 atm in both experiments, obtaining adsorbed amounts of 1.81 mmol/g (7.97 wt%) at 273 K, and 1.11 mmol/g (4.89 wt%) at 298 K. Regarding the adsorption capacity of CaZn (**4**) at 298 K, it is noteworthy that the obtained value is closed to those reported for ZIF-8 (1.0 mmol/g)[99] and IRMOF-3 (1.2 mmol/g),[100] although it is still below the top value of 8.6 mmol/g reported for Mg-MOF-74.[101]

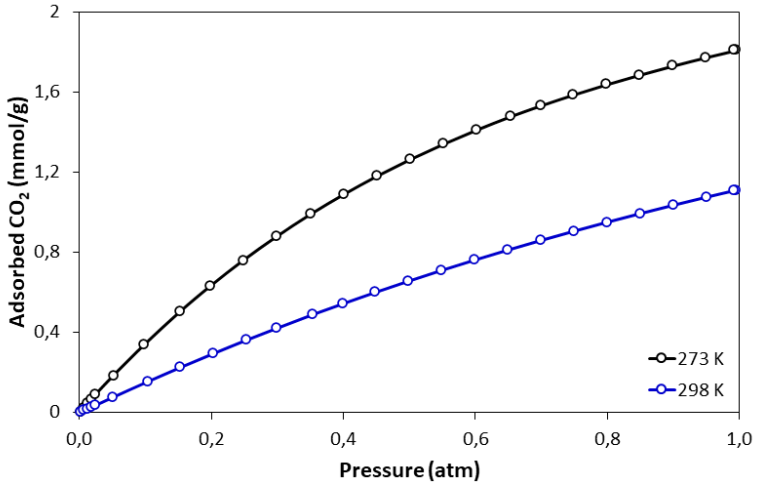

Figure 3.24. Adsorption isotherms of CO_2 at 273 K and 298 K for activated CaZn (**4**).

The isosteric heat of CO_2 adsorption has been calculated by the Clausius-Clapeyron equation[102] in order to elucidate the type of adsorbent-adsorbate interactions in CaZn (**4**), and obtained Q_{st} values at lowest CO_2 loadings indicate that the involvement of *cus* in CO_2 adsorption may be minimal (Figure 3.25). In

comparison to other MOFs containing open-metal sites,[103] CaZn (**4**) exhibits a lower isosteric heat (25.0 kJ/mol) since carboxylate oxygen atoms around the metal exert a steric hindrance that prevents a direct interaction between CO_2 and *cus*.

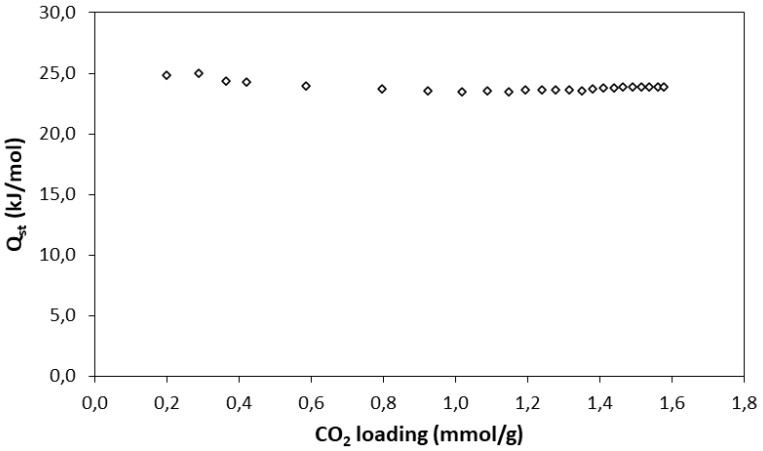

Figure 3.25. Isosteric heats of CO_2 adsorption for compound CaZn (**4**).

As confirmed by the different experiments, despite the fact that CaZn (**4**) compound is highly stable and has low CO_2 adsorption capacity, the high temperatures required for the desorption of coordinated solvent and subsequent structure activation are not suitable for the photocatalytic process. This difficulty can be avoided by a solvent exchange process by which the coordination DMF molecules are replaced by other volatile solvents. In addition, studying the stability in water of this MOF is also an important concern, since the sample for photocatalytic reduction of CO_2 will undoubtedly involve water (both from moisture and powder deposition on the reactor), making the behaviour of CaZn (**4**) in water an important task to be studied. The following section is an account of the studies carried out over CaZn_MeOH (**5**) and CaZn_H_2O (**6**), which are the products resulting from solvent exchange processes.

3.3.4. Chemical stability of CaZn (4)

Although CaZn (**4**) MOF has a thermal stable structure with permanent porosity once the product is activated, its applicability is somewhat hindered by the fact that the activation process requires extreme conditions. To overcome that limitation, we have employed solvent-exchange strategy, using a volatile solvent such as MeOH to replace DMF molecules coordinated in the pristine MOF, in such a way that molecules that those exchanged molecules would require low temperatures for their release.[104] Moreover, this experiment also gave the opportunity of checking the chemical stability of the MOF in dispersion media.

To take advantage of this strategy and study the chemical stability of the parent material, CaZn (**4**) compound was suspended in MeOH for 24 hours, or sonicated in water for 5minutes, in order to explore and characterize the products resulting from the solvent exchange hereafter CaZn_MeOH (**5**) and CaZn_H_2O (**6**) products, respectively, which are characterized below.

3.3.4.1. Structural characterization of CaZn_MeOH (5)

Before delving into a detailed characterization of CaZn_MeOH (**5**), it should be pointed that although single-crystals of the MOF have been obtained, they could not be measured by SCXRD technique because of their large number of defects and low stability. Even so, the techniques used that are described below have provided the necessary information to know both the structure and its properties.

Powder X-Ray Diffraction analysis

Through the suspension of CaZn (**4**) in MeOH, crystalline CaZn_MeOH (**5**) is achieved (Figure 3.26), being this a first demonstration of the chemical versatility of the starting MOF. According to the PXRD refinement, the observed decrease in cell parameters may be related to the dynamics experimented by the structure during the solvent-exchange. In particular, crystallographic *a* and *b* axes are slightly shrunk while *c* axis is lengthened, which suggests that the pores of the framework have undergone some contraction such that CaZn_MeOH (**5**) is rendered in a closed-pore arrangement, preventing the introduction of solvent molecules is the porous system. This fact demonstrates the flexibility of this MOF, which can adapt its structure to coordination solvents and/or guest molecules in voids.

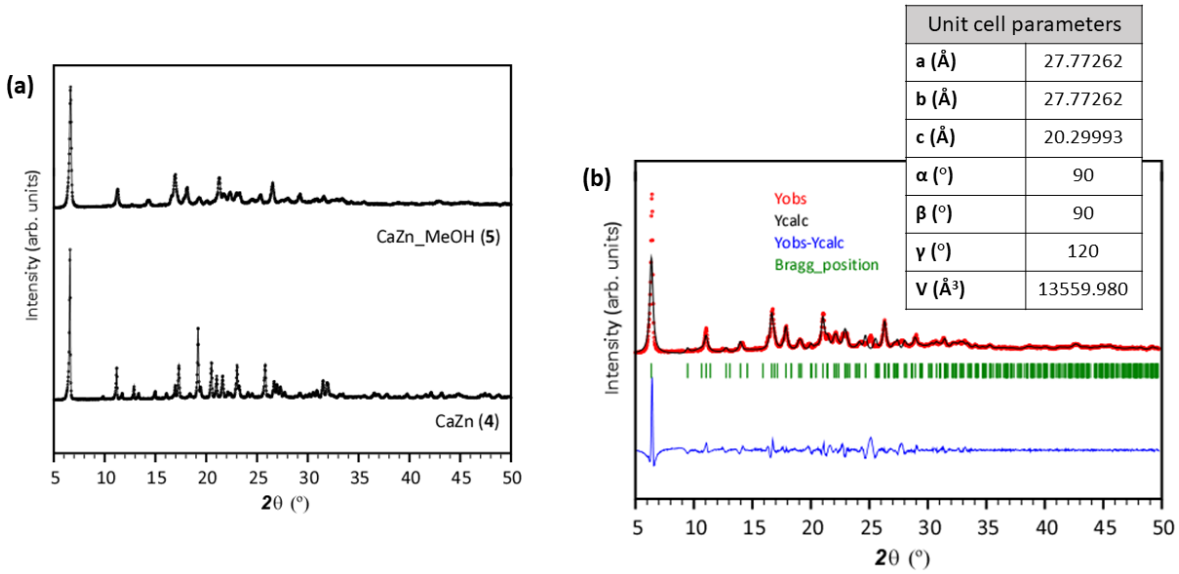

Unit cell parameters	
a (Å)	27.77262
b (Å)	27.77262
c (Å)	20.29993
α (°)	90
β (°)	90
γ (°)	120
V (Å³)	13559.980

Figure 3.26. Powder X-ray diffraction analysis of compound (**5**) **(a)** Diffractograms of CaZn (**4**) and CaZn_MeOH (**5**). **(b)** Pattern-matching analysis of CaZn_MeOH (**5**) (Refinement parameters: R_F/R_B: 1.10 /0.889; R_P/Chi^2: 16.3/12.3).

In spite of the high crystallinity and the similarity of the MOF, the fact of having exchanged DMF by MeOH could affect the properties of CaZn_MeOH (**5**), including its thermal stability. Therefore, a TGA has been carried out to study the robustness of the novel compound.

Thermogravimetric analysis

Table 3.6 summarizes the elemental analysis and thermogravimetric data, which are in agreement with the general $\{[CaZn(\mu_4\text{-}CNip)_2(MeOH)_2]\}_n$ formula. According to the TGA, the two coordination MeOH molecules are lost at 100 °C to give the anhydrous $[CaZn(\mu_4\text{-}CNip)_2]_n$ compound. The framework remains stable up to 370 °C, temperature at which it starts to decompose yielding the corresponding metal oxides at 660 °C. It should be noted that between 100 and 370 °C there is a slow mass loss of 7.5 %, which may be related to an incomplete exchange meaning that a small portion of DMF could still be present in the sample.

Table 3.6. Elemental analysis and TG/DTA curves of CaZn_MeOH (**5**) compound.

CaZn_MeOH (5)

$\{[CaZn(CNip)_2(MeOH)_2]\cdot ½DMF\}_n$ / $C_{21.5}H_{17.5}N_{2.5}CaO_{10.5}Zn$

T_i–T_f	ΣΔm(%)	$ΣΔm(\%)_{teor}$
30-100	10.8	11.0 (– 2 MeOH)
100-370	7.5	6.3 (– 0.5 DMF)
370-660	81.7	82.7 (CaO + ZnO)

Elemental analysis

$\{[CaZn(CNip)_2(MeOH)_2]\cdot ½DMF\}_n$ / $C_{21.5}H_{17.5}N_{2.5}CaO_{10.5}Zn$

Calc.: C, 44.19; H, 3.02; N, 5.99; O, 28.75; Ca, 6.85; Zn, 11.19 %.
Found: C, 41.17; H, 2.48; N, 7.024 %.

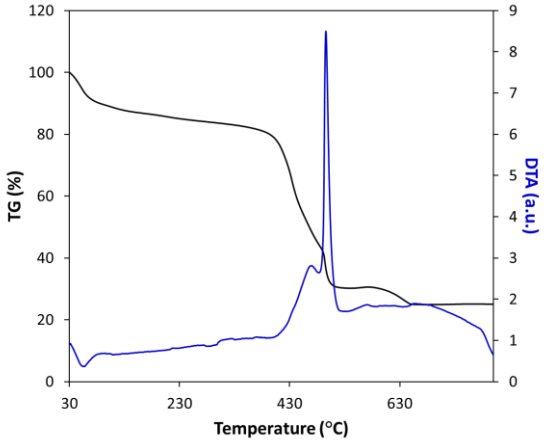

With the above-mentioned information, it can be concluded that the robustness of both CaZn (**4**) and CaZn_MeOH (**5**) is suitable for their application in gas adsorption and photocatalytic reactions, since they can withstand the high temperatures of the outgassing and activation processes, and they could also remain stable during different catalytic cycles. As one of the goals of Chapter 3 is the study of the photocatalytic reduction of CO_2, the MOF needs to be able to adsorb CO_2 to carry out the catalysis. To check the adsorption capacity, the following gas adsorption measurements have been conducted with CaZn (**4**) compound.

3.3.4.2. Gas adsorption experiments of CaZn_MeOH (5)

CO_2 adsorption experiments have been performed with activated CaZn_MeOH (**5**) (140 °C for 6 h under vacuum), obtaining results summarized in Figure 3.27. In comparison to the pristine MOF, CO_2 adsorption capacity of CaZn_MeOH (**5**) decreases considerably probably due to the narrowing of pores as a consequence of the solvent-exchange between MeOH and DMF. Therefore, the maximum adsorbed amounts for CaZn_MeOH (**5**) are obtained at 1 atm with uptakes of 0.85 mmol/g (3.72 wt%) at 273 K, and 0.52 mmol/g (2.27 wt%) at 298 K.

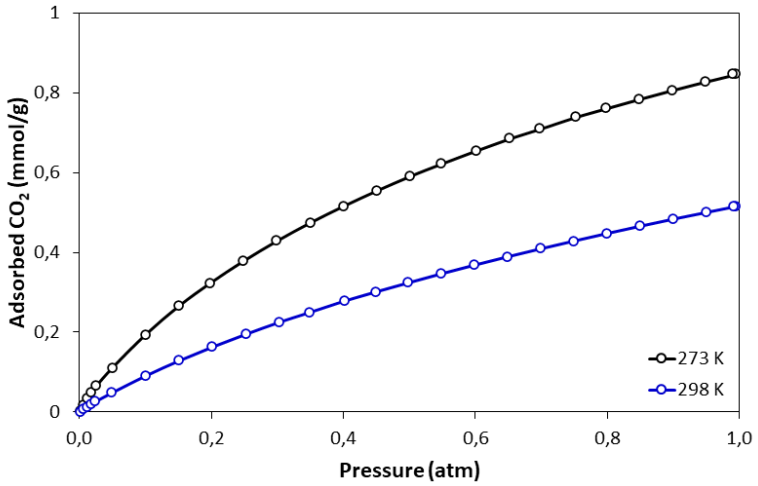

Figure 3.27. Adsorption isotherms of CO_2 at 273 K and 298 K for activated CaZn_MeOH (**5**).

As CaZn_MeOH (**5**) has also *cus* that can encourage CO_2 adsorption, isosteric heat has been calculated (Figure 3.28). Although the values are similar to those of CaZn (**4**), the fact that at the lowest CO_2 loading the Q_{st} value reaches 27.20 kJ/mol indicates that there is greater involvement of the *cus* in the adsorption process. this may be because the narrowing of the pore size has decreased the steric hindrance generated by the carboxylate oxygen atoms of the metal's surroundings.

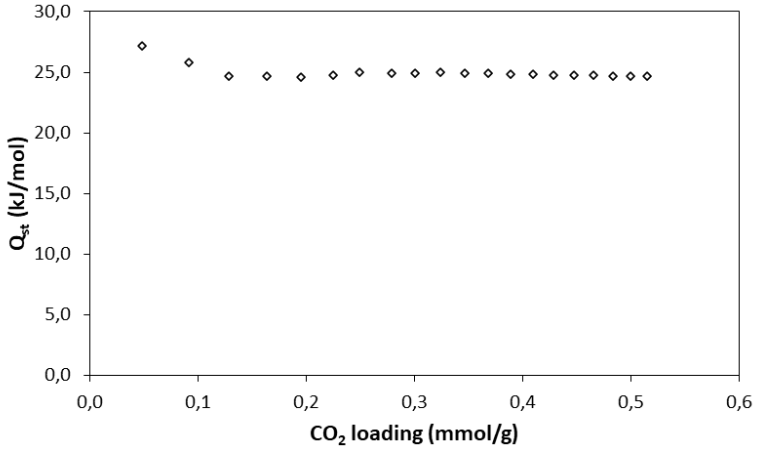

Figure 3.28. Isosteric heats of CO_2 adsorption for compound CaZn_MeOH (**5**).

Solvent-exchange method has been useful to obtain the CaZn_MeOH (**5**) compound, which presents better outgassing and activation conditions for gas adsorption and photocatalytic applications due to the exchange of coordinated DMF molecules with MeOH. The study described above is a good indication of the chemical stability of this MOF, although it is also important to check it in an aqueous medium, since, in addition to the water molecules that the material can adsorb from the ambient humidity, the

photocatalytic reactions to be studied are performed in the presence of water. The following section presents the information obtained during the characterization of the compound CaZn_H_2O (**6**), which contains water molecules instead of DMF.

3.3.4.3. Structural characterization of CaZn_H_2O (6)

As in the previous compound, CaZn (**4**) has been sonicated in water to obtain a whitish solid corresponding to CaZn_H_2O (**6**). In this case, the starting product is dissolved and then precipitated as a crystalline powder, so a crystallographic analysis of single crystals could not be performed.

Powder X-Ray Diffraction analysis

Unlike compound CaZn_MeOH (**5**), in this process, a different phase from the starting MOF has been obtained in CaZn_H_2O (**6**), as confirmed by the diffractogram of Figure 3.29a. In order to identify a possible space group with an approximate unit cell, an indexation has been made based on the cell volume of the starting MOF. Through this study, it has been possible to establish that the initial trigonal structure has been transformed into a monoclinic cell with $P2_1/c$ space group (Figure 3.29b), and, as shown in Figure 3.29c, this transformation, assuming the lower size of water compared to DMF, could have caused the opening of the pores that would help the adsorption of solvents and gases.

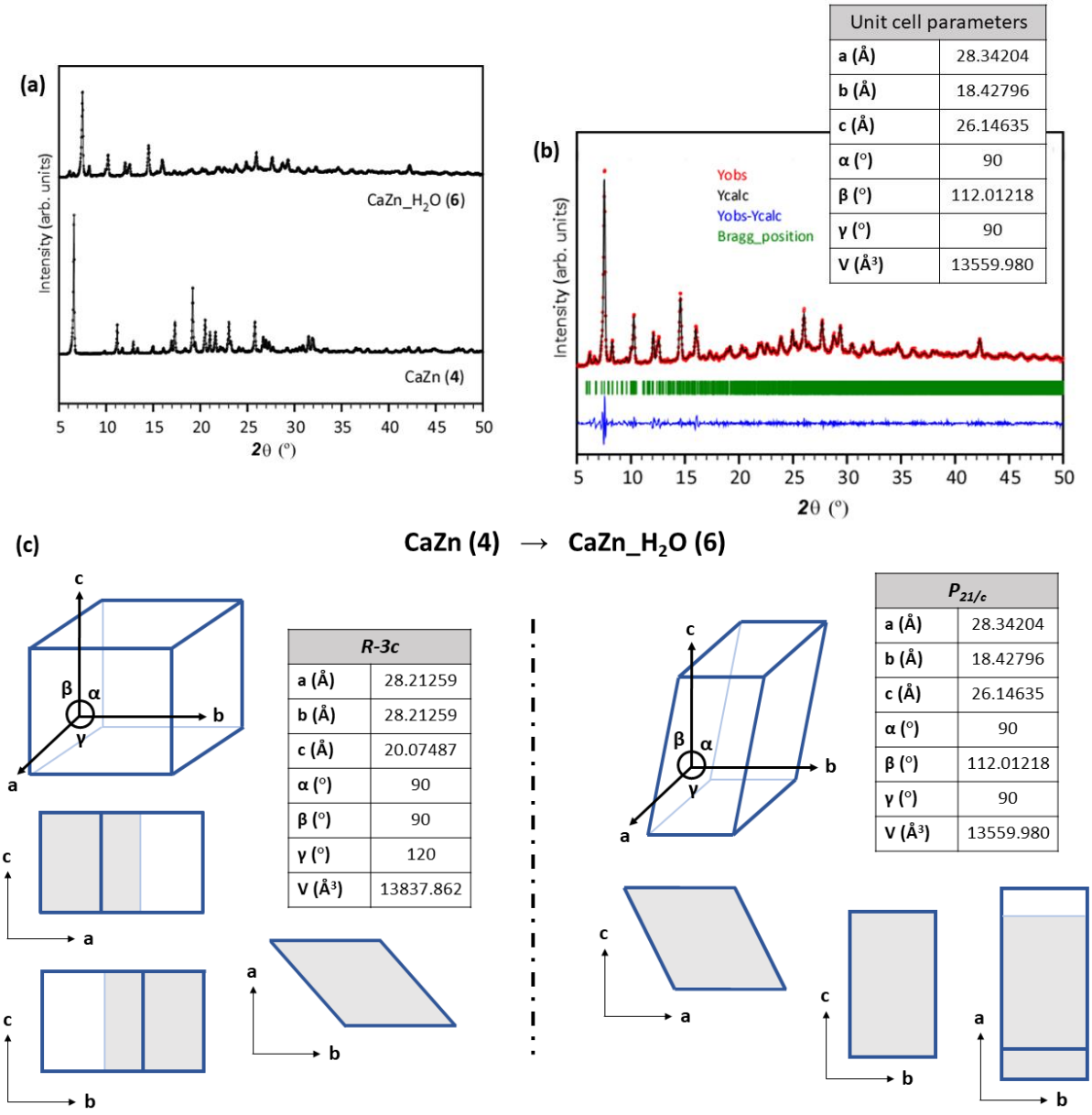

Figure 3.29. Powder X-ray diffraction analysis of compound (**6**). **(a)** Diffractograms of CaZn (**4**) and CaZn_H_2O (**6**). **(b)** Indexation and adjustment of CaZn_H_2O (**6**) compound to *$P2_1/c$* space group (Refinement parameters: R_F/R_B: 13.8/6.23; R_P/Chi^2: 5.72/1.40). **(c)** Illustration of cell transformation from CaZn (**4**) to CaZn_H_2O (**6**) (the shaded shapes belong to the backside of each view).

CaZn_H_2O (**6**) compound obtained by the solvent exchange method has interesting structural properties even though no information on the structure of the material has been provided. In order to clarify a possible molecular formula and to study its thermal behaviour, the following TGA has been carried out.

Thermogravimetric analysis

Attending to the TG of Table 3.7, the shape of the curves and mass-loss ranges obtained for CaZn_H_2O (**6**) are very similar to the pristine MOF studied in this Chapter. This may be an indicator of the chemical stability of the CaZn (**4**) structure, as water molecules would have replaced the coordinated DMFs to give a related compound CaZn_H_2O (**6**) with coordinated waters. These data would correspond to $\{[CaZn(\mu_4\text{-}CNip)_2(H_2O)_2]\cdot 6H_2O\}_n$ formula which is deducted by two mass losses between 30-120 °C and 375-680 °C. In the first range, eight water molecules are lost, concretely, two coordination and six crystallization water molecules. The explanation for the high content of water in this material may lie in the monoclinic cell, which may possess an open porous system that allows the easy adsorption of solvent molecules. Anhydrous $\{[CaZn(\mu_4\text{-}CNip)_2]\}_n$ compound remains stable up to 375 °C, to then start the decomposition process which ends at 680 °C, giving CaO and ZnO as residual products. Like the previous compound, CaZn_H_2O (**6**) also has a slow and continuous mass loss of 6.4 % between 120 and 375 °C, which can be justified by the presence of small amounts of DMF as impurities.

Table 3.7. Elemental analysis and TG/DTA curves of CaZn_H_2O (**6**) compound.

CaZn_H₂O (6)

$\{[CaZn(CNip)_2(H_2O)_2]\cdot ½DMF\cdot 6H_2O\}_n$ / $C_{19.5}H_{27.5}N_{2.5}CaO_{16.5}Zn$

Ti–Tf	ΣΔm(%)	$\Sigma\Delta m(\%)_{teor}$
30-120	23.5	21.7 (– 8 H_2O)
120-375	6.4	5.5 (– 0.5 DMF)
375-680	70.1	72.8 (CaO + ZnO)

Elemental analysis

$\{[CaZn(CNip)_2(H_2O)_2]\cdot ½DMF\cdot 6H_2O\}_n$ / $C_{19.5}H_{27.5}N_{2.5}CaO_{16.5}Zn$

Calc.: C, 35.28; H, 4.18; N, 5.27; O, 39.73; Ca, 6.02; Zn, 9.84 %.
Found: C, 30.43; H, 1.46; N, 4.24 %.

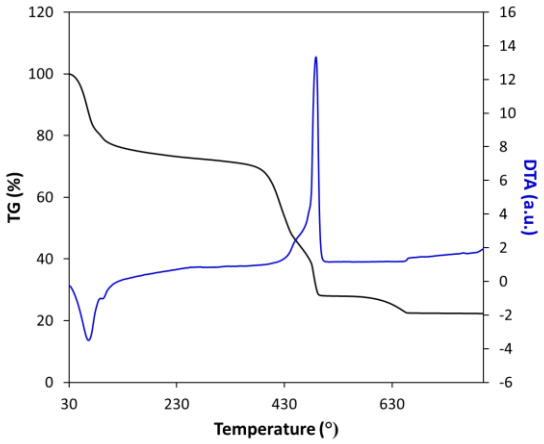

In addition to demonstrating the robustness of the starting MOF and its derivatives, these analyses have shown the modulating capacity of the porous structure of CaZn (**4**), which can adapt to the presence of different solvents or the humidity of the environment.

3.3.5. Photocatalytic CO_2 reduction

These measurements with CaZn (**4**) sample (see Appendix II for further information about the sample preparation) have been made under visible light and a continuous flow of CO_2 and water vapour for 24 h, obtaining the results compiled in Figure 3.30. From the blue and black dots in the graph, it can be seen that in the first catalytic cycle CO_2 is reduced to CO (21.8 µmol/g) and H_2 is also formed (11.1 µmol/g) after 17 h under visible irradiation. In view of these results, it seems that the photocatalytic reduction of CO_2 is accompanied by the decomposition of the DMF traces that can still be adsorbed in the MOF.

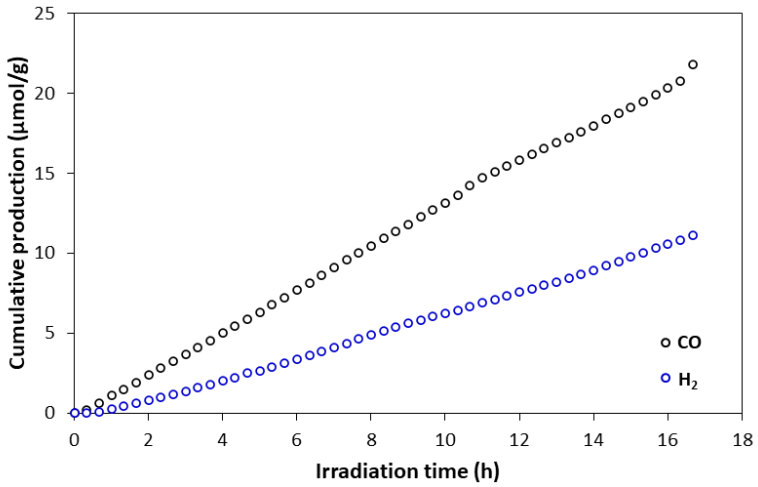

Figure 3.30. Evolution of the photocatalytic CO_2 reduction under CO_2 and H_2O flow at variable times of visible light irradiation.

In order to check the source of the CO formed, the experiment has been repeated but using an Ar and H_2O flow without CO_2. These results show the presence of CO, concretely 15.5 µmol/g after 17 h, indicating that CaZn (**4**) is degraded under visible light; but H_2 or other products have not been detected (see Figure 3.31 and Appendix II). Given this scenario, it can be said that CaZn (**4**) a single-use MOF photocatalyst due to its easy degradation.

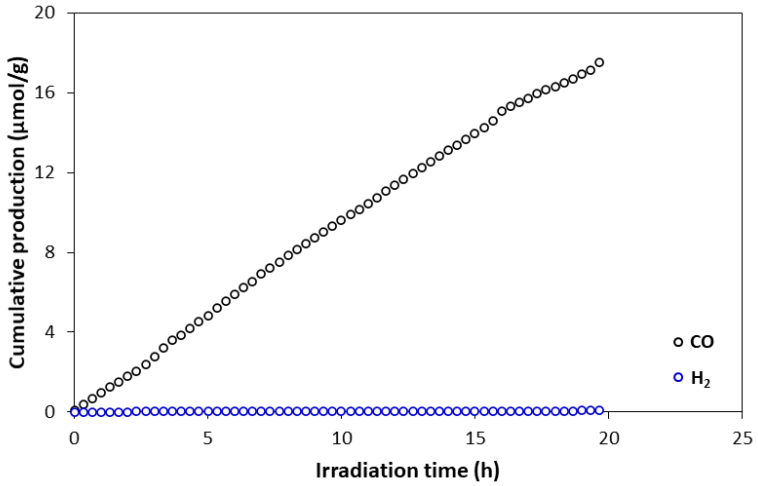

Figure 3.31. Evolution of the photocatalytic CO_2 reduction under Ar and H_2O flow at variable times of visible light irradiation.

It is known that the degradation of catalysts affects their effectiveness during a reaction, so a second cycle of the CO_2 photoreduction has been carried out under CO_2 and H_2O flow to assess the influence of the degradation on the production of CO and H_2. Plots of Figure 3.32 demonstrate a considerable decrease in the effectiveness of CaZn (**4**) (6.8 µmol CO/g and 4.1 µmol H_2/g after 17 h under visible irradiation), confirming that the degradation of the MOF has a negative effect over the photocatalytic process.

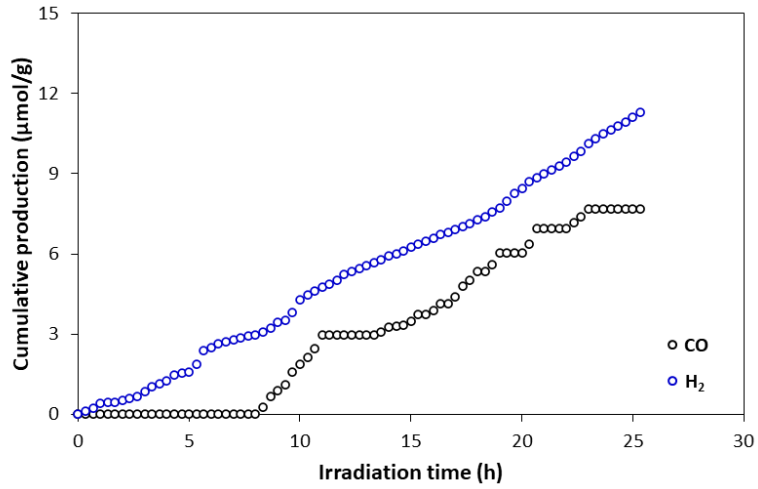

Figure 3.32. Evolution of the second photocatalytic CO_2 reduction cycle under CO_2 and H_2O flow at variable times of visible light irradiation.

Although the material loses effectiveness with its use making the CaZn (**4**) a single-use photocatalyst, large quantities of products may be generated in long catalytic cycles. To check this possibility, the photocatalytic CO_2 reduction has been performed again for 48 hours under visible radiation with a new

CaZn (**4**) sample. The obtained results, which are shown in Figure 3.33, demonstrate the reproducibility of the reaction since the accumulated production of CO at 17 h (25.5 µmol/g) is very similar to that obtained in the short experiment, even there is a decrease in the production of H_2 to 7.9 µmol/g. As can be seen in the plot, both products show an increasing trend in their production, reaching the maximum at 48 h of reaction with values of 55.6 µmol CO/g and 21.1 µmol H_2/g.

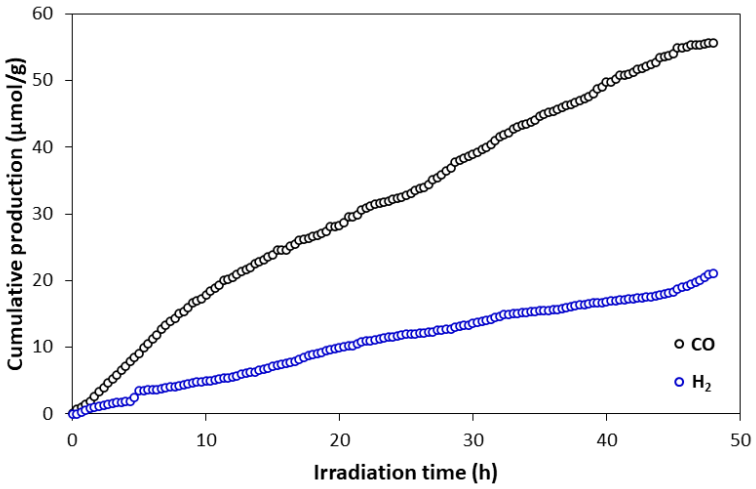

Figure 3.33. Long photocatalytic CO_2 reduction cycle under CO_2 and H_2O flow at variable times of visible light irradiation.

This study demonstrates that CaZn (**4**) is capable of photoreducing CO_2 to CO. However, this MOF can only photocatalyze one reaction cycle as a result of its photodegradation. As has been pointed out in Chapter 3, photocatalytic processes depend on the charge transfer that can occur in the material; so, the understanding of those transfers could be crucial to explain the photocatalytic behaviour of CaZn (**4**). The following are the results obtained in the study on charge transfer in this MOF, carried out by means of photoluminescence experiments.

3.3.6. Photoluminescence measurements

MOFs built up from closed-shell metal ions such as alkaline-earth and group 12 metal ions, calcium and zinc in the present case, and carboxylate ligands with aromatic rings, such as CNip, are promising candidates for showing solid-state photoluminescence since they allow for efficient charge transfer processes to take place, leading to both strong fluorescence and phosphorescence emissions.[105]

3.3.6.1. Luminescent properties of CaZn (4)

Two excitation spectra have been measured at λ_{em} = 445 nm and λ_{em} = 550 nm, in which, as Figure 3.34a shows, an occurrence of a main band or a shoulder before the Compton border is observed. This means that both emission processes come from the same excitation pathway. Comparing the spectrum obtained at λ_{em} = 445 nm with the calculated, the best adjustment is obtained at the wavelength of 338 nm, which is related to a singlet HOMO-1 → LUMO+7, HOMO → LUMO+6 transition (Figure 3.34b). Time-dependent density-functional theory (TD-DFT) calculations of Figure 3.34c shows the molecular orbitals involved in the transition, and the location of HOMO orbitals on carboxylate groups and LUMO orbitals on aromatic rings indicates that the excitation process is based on π → π* transitions.

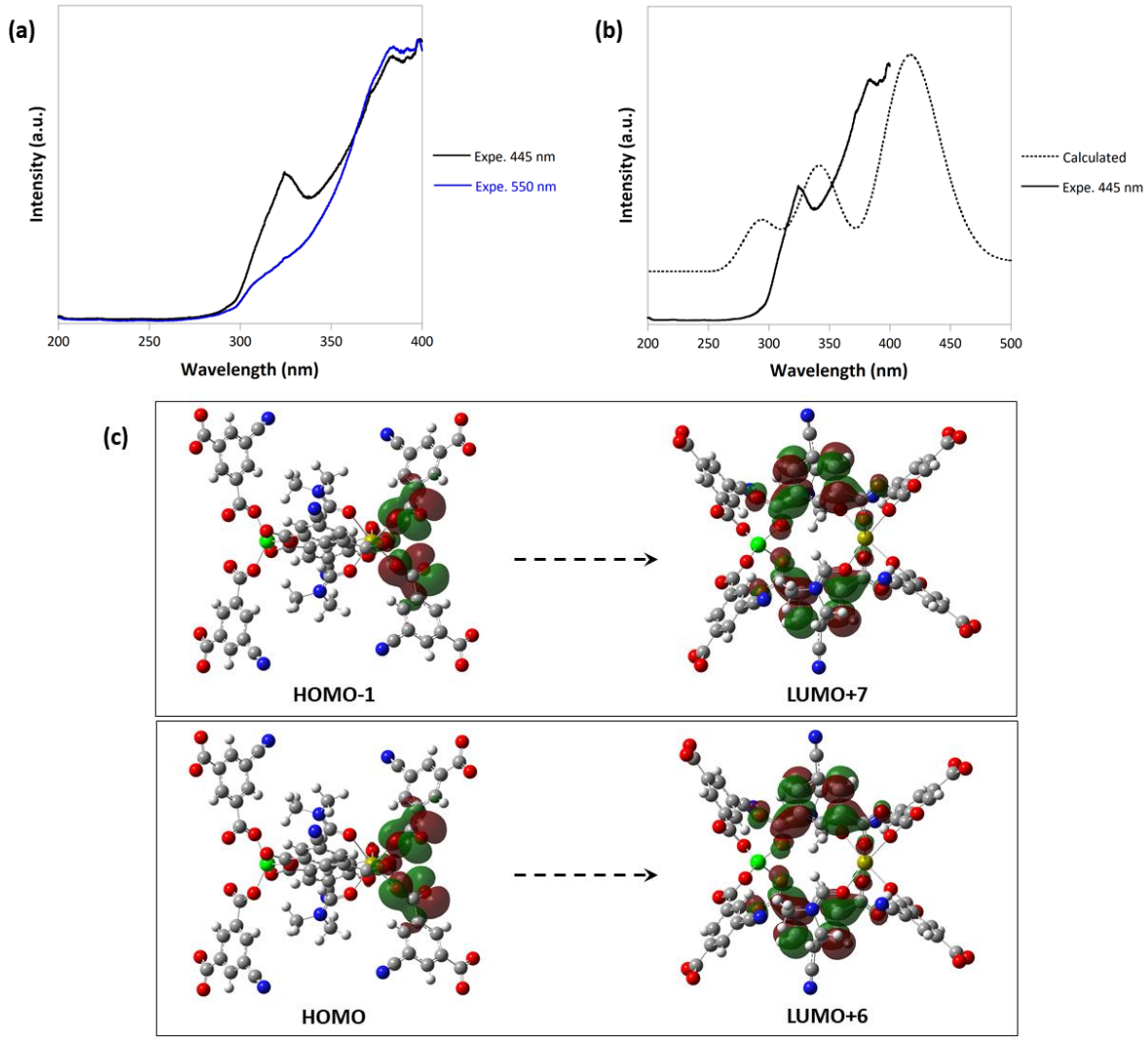

Figure 3.34. Absorption and excitation measurements of CaZn (**4**). **(a)** Excitation spectra obtained at RT using λ_{em} = 445 nm and λ_{em} = 550 nm. **(b)** Calculated and experimental excitation spectra of CaZn (**4**) compound under emission of 445 nm. **(c)** Molecular orbitals involved in the excitation transitions.

Once the system is excited, a non-radiative vibrational relaxation occurs to the lowest energy excited state S_1, where a photon of energy *hv'* is emitted. To collect emission spectra with such information, solid-state photoluminescence has been performed at RT and applying an excitation UV source (λ_{ex} = 325 nm). As can be seen in Figure 3.35a, where, in addition to a shoulder peaking at 500 nm, a broad and intense band is observed at 450 nm. The theoretical spectrum reproduces adequately the maximum at 450 nm, which is related to short lifetimes of fluorescence, while the band at 500 nm is of very low intensity. Taking into account that these spectra allow the calculation of the singlet-singlet transitions, it can be concluded that the second band corresponds to a phosphorescent triplet-singlet transition. The intense emission band at 450 nm corresponds to HOMO-11 → LUMO+5, HOMO-10 → LUMO+4 and HOMO-10 → LUMO+5 singlet transitions (Figure 3.35b).

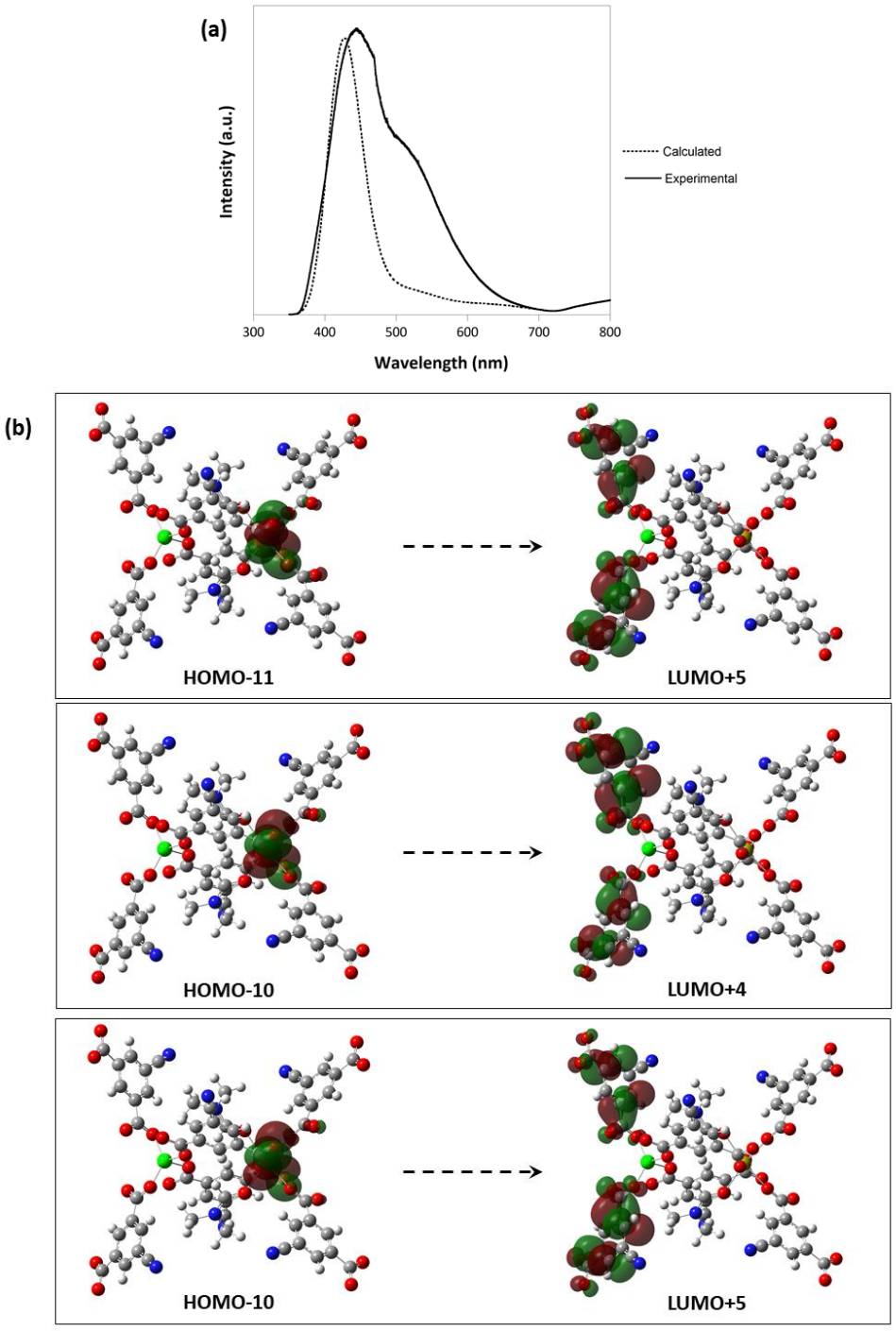

Figure 3.35. Emission measurements of CaZn (**4**). **(a)** Calculated and experimental emission spectra of CaZn (**4**) compound under excitation of 325 nm**. (b)** Molecular orbitals involved in the emission transitions.

The representation of the molecular orbitals involved in the emission process shows that HOMO levels mainly grow from the π orbitals of the carboxylate groups, while LUMO levels are centered over the π* orbitals of aromatic rings; so, CaZn (**4**) presents a LCCT photoluminescence. However, if attention is paid

to the enlarged Figure 3.36, it can be seen that at the HOMO-10 level there is a small contribution from the Ca atom orbitals, so there is also participation of LMCT in the luminescence.

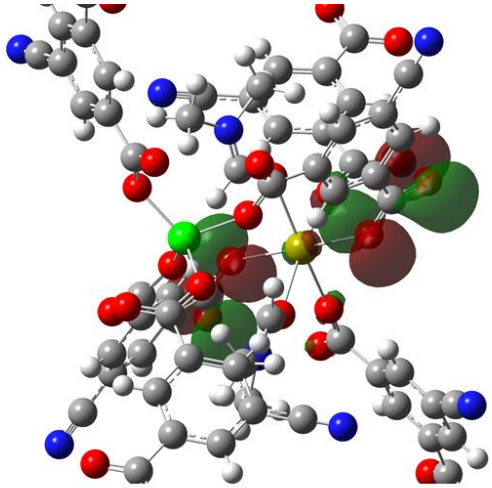

Figure 3.36. Contribution of Ca atoms to HOMO-10 level in the HOMO-10 ⟶ LUMO+4 and HOMO-10 ⟶ LUMO+5 emission transitions.

Low-temperature luminescence has also been measured in order to avoid the usual quenching derived from non-radiative vibrational processes occurring at RT, in such a way that PL emission is enhanced and bringing stronger phosphorescence signal.[15] The emission spectrum obtained at 50 K (λ_{ex} = 325 nm) of Figure 3.37a reveals a significant enhancement of the emitted light, which allowed distinguishing three bands of similar intensity at 410, 490 and 530 nm. Therefore, it may be concluded that the phosphorescent emission has gained importance given that the second and third bands (related to the longest-live emissions at RT) are almost of the same intensity of the first fluorescent band. These emission processes are related to LCCT, which are in good agreement with the bright blue emission and afterglow observed in the sample (Figure 3.37b).

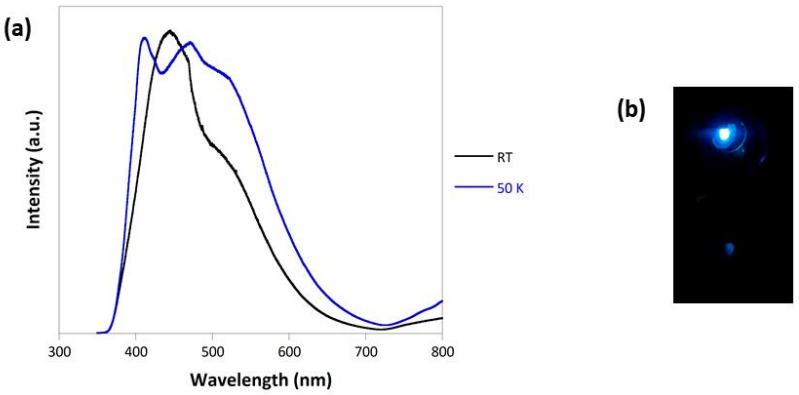

Figure 3.37. Photoluminescence measurements of CaZn (**4**) at low temperature. **(a)** Emission spectrum of CaZn (**4**) compound at 50 K and under excitation at 325 nm. **(b)** Blue emission and afterglow of CaZn (**4**) compound at 50 K and under excitation at 325 nm.

Measuring the low-temperature emission decay of CaZn (**4**) at the most intense emission band, a fluorescence of short lifetime ($5.5x10^4$ µs) and phosphorescence of $1.4x10^5$ µs are confirmed (Figure 3.38).

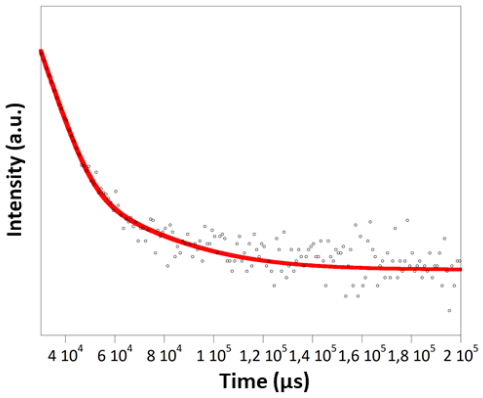

Figure 3.38. Emission decay curve showing the best fitting (Dots: decay, Red line: fitting).

As this MOF has luminescent properties resulting from LCCT, the chemical changes generated in CaZn (**4**) by the solvent exchange method can affect the excitation and emission processes of the material depending on the nature of the molecule introduced. So, the influence of MeOH and H_2O on this MOF is studied below.

3.3.6.2. Luminescent properties of CaZn_H_2O (6)

CaZn_H_2O (**6**) contains a significant amount of water molecules that, as discussed below, will decrease both absorption and emission of light; this is due to the fact that the oscillations of this molecule quench the luminescent signals. An example of this is the excitation spectrum (λ_{em} = 450 nm) of Figure

3.39, which was measured at 15 K because no signal was seen at RT. By decreasing the temperature, the oscillations of the guest molecules (in this case water) are avoided, and some bands of very low intensity can be appreciated.

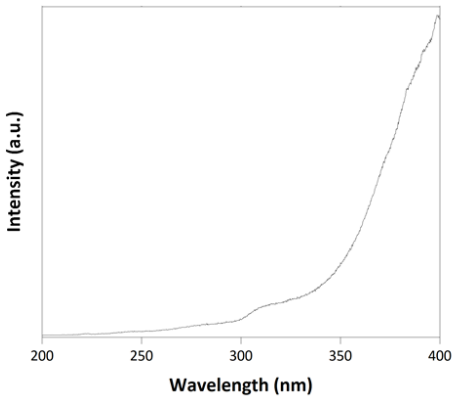

Figure 3.39. Excitation spectra obtained at 15 K using λ_{em} = 450 nm.

The emission spectrum of Figure 3.40a has been obtained at 30 K using an excitation source at 325 nm, in which two bands at 450 and 500 nm are observed. It should be noted that both signals are very similar to those described in CaZn (**4**). The main difference between compounds (**4**) and (**6**) is the quenching of the photoluminescence in the latter since the vibrations and oscillations of water molecules provokes a non-radiative vibration energy transfer that involves an emission decay.[28] This fact is confirmed by Figure 3.40a, in which short emission lifetimes of 2.5x10^5 µs can be seen.

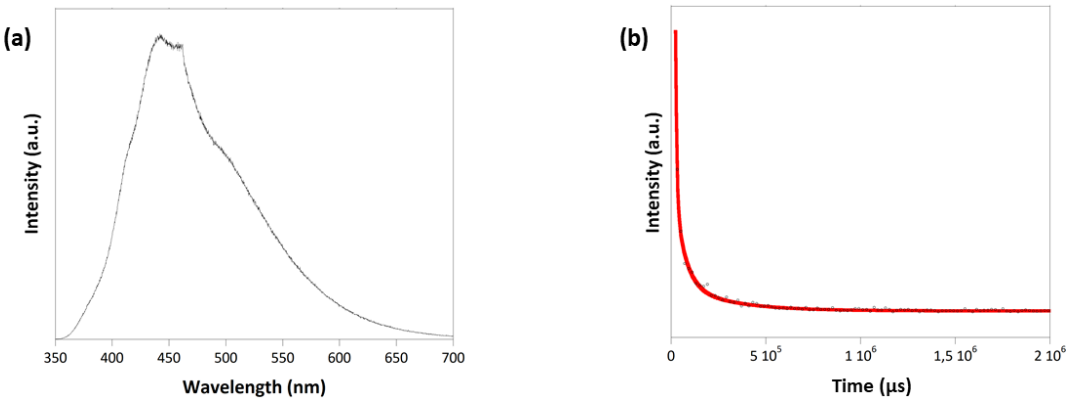

Figure 3.40. Photoluminescence measurements of CaZn_H_2O (**6**) compound. **(a)** Emission spectrum of CaZn_H_2O (**6**) compound at 30 K and under excitation at 325 nm. **(b)** Emission decay curve showing the best fitting (Dots: decay, Red line: fitting).

3.4. References

[1] Yaghi, O. M.; Li, G.; Li, H. "Selective binding and removal of guests in a microporous metal-organic framework", *Nature* (1995), **378**, 703-706.

[2] Anik, Ü.; Timur, S.; Dursun, Z. "Metal organic frameworks in electrochemical and optical sensing platforms: a review", *Microchim. Acta* (2019), **186**, 196.

[3] Li, Y.; Xiao, A. S.; Zou, B.; Zhang, H. X.; Yan, K. L.; Lin, Y. "Advances of metal-organic frameworks for gas sensing", *Polyhedron* (2018), **154**, 83-97.

[4] Kumar, P.; Deep, A.; Kim, K. H. "Metal organic frameworks for sensing applications", *Trends Analyt Chem.* (2015), **73**, 39-53.

[5] Deng, X.; Li, Z.; García, H. "Visible light induced organic transformations using metal-organic-frameworks (MOFs)", *Chem. Eur. J.* (2017), **23**, 11189-11209.

[6] Wang, S.; Wang, X. "Multifunctional metal-organic frameworks for photocatalysis", *Small* (2015), **11**, 3097-3112.

[7] Müller-Buschbaum, K.; Beuerle, F.; Feldmann, C. "MOF based luminescence tuning and chemical/physical sensing", *Microporous Mesoporous Mater.* (2015), **216**, 171-199.

[8] Dong, J.; Zhao, D.; Lu, Y.; Sun, W. Y. "Photoluminescent metal-organic frameworks and their application for sensing biomolecules", *J. Mater. Chem. A* (2019), **7**, 22744-22767.

[9] Song, X. Z.; Song, S. Y.; Zhang, H. J. (2014). Luminescent Lanthanide Metal–Organic Frameworks. In *Lanthanide metal-organic frameworks*. Springer, Berlin, Heidelberg.

[10] Zhang, Y.; Yuan, S.; Day, G.; Wang, X.; Yang, X.; Zhou, H. C. "Luminescent sensors based on metal-organic frameworks", *Coord. Chem. Rev.* (2018), **354**, 28-45.

[11] Wen, T.; Zhou, X. P.; Zhang, D. X.; Li, D. "Luminescent mechanochromic porous coordination polymers", *Chem. Eur. J.* (2014), **20**, 644-648.

[12] Lin, R. . Liu, S. Y.; Ye, J. W.; Li, X. Y.; Zhang, J. P. "Photoluminescent metal-organic frameworks for gas sensing", *Adv. Sci.* (2016), **3**, 1500434.

[13] Dramićanin, M. (2018). Luminescence: The Basics, Methods, and Instrumentation. In *Luminescence Thermometry*. Woodhead Publishing.

[14] Nguyen, T. N.; Ebrahim, F. M.; Stylianou, K. C. "Photoluminescent, upconversion luminescent and nonlinear optical metal-organic frameworks: From fundamental photophysics to potential applications", *Coord. Chem. Rev.* (2018), **377**, 259-306.

[15] San Sebastian, E.; Rodríguez-Diéguez, A.; Seco, J. M.; Cepeda, J. "Coordination polymers with intriguing photoluminescence behaviour: the promising avenue for greatest long-lasting phosphors", *Eur. J. Inorg. Chem.* (2018), 2155-2174.

[16] IUPAC. (1997). Compendium of Chemical Terminology. In *The Gold Book*. Blackwell Scientific Publications, Oxford. https://doi.org/10.1351/goldbook.D01579

[17] Lakowicz, J.R. (2013). Introduction to Fluorescence. In *Principles of Fluorescence Spectroscopy*. Springer science & business media.

[18] Heine, J.; Müller-Buschbaum, K. "Engineering metal-based luminescence in coordination polymers and metal-organic frameworks", *Chem. Soc. Rev.* (2013), **42**, 9232-9242.

[19] Lustig, W. P.; Li, J. "Luminescent metal-organic frameworks and coordination polymers as alternative phosphors for energy efficient lighting devices", *Coord. Chem. Rev.* (2018), **373**, 116-147.

[20] Briones, D.; Leo, P.; Cepeda, J.; Orcajo, G.; Calleja, G.; Sanz, R.; Rodríguez-Diéguez, A.; Martínez, F. "Alkaline-earth metal based MOFs with second scale long-lasting phosphor behavior", *Cryst. Eng. Comm.* (2018), **20**, 4793-4803.

[21] Bai, G.; Tsang, M. K.; Hao, J. "Luminescent ions in advanced composite materials for multifunctional applications", *Adv. Funct. Mater.* (2016), **26**, 6330-6350.

[22] Cui, Y.; Yue, Y.; Qian, G.; Chen, B. "Luminescent functional metal-organic frameworks", *Chem. Rev.* (2012), **112**, 1126-1162.

[23] Pamei, M.; Puzari, A. "Luminescent transition metal-organic frameworks: An emerging sensor for detecting biologically essential metal ions", *Nano-Struct. Nano-Objects* (2019), **19**, 100364.

[24] Yan, D.; Tang, Y.; Lin, H.; Wang, D. "Tunable two-color luminescence and host-guest energy transfer of fluorescent chromophores encapsulated in metal-organic frameworks", *Sci. Rep.* (2014), **4**, 1-7.

[25] Chen, L.; Liu, D.; Peng, J.; Du, Q.; He, H. "Ratiometric fluorescence sensing of metal-organic frameworks: Tactics and perspectives", *Coord. Chem. Rev.* (2020), **404**, 213113.

[26] Williams, D. E.; Shustova, N. B. "Metal-organic frameworks as a versatile tool to study and model energy transfer processes", *Chem. Eur. J.* (2015), **21**, 15474-15479.

[27] Lustig, W. P.; Wang, F.; Teat, S. J.; Hu, Z.; Gong, Q.; Li, J. "Chromophore-based luminescent metal-organic frameworks as lighting phosphors", *Inorg. Chem.* (2016), **55**, 7250-7256.

[28] Yi, P.; Huang, H.; Peng, Y.; Liu, D.; Zhong, C. "A series of europium-based metal organic frameworks with tuned intrinsic luminescence properties and detection capacities", *RSC Adv.* (2016), **6**, 111934-111941.

[29] Razavi, S. A. A.; Morsali, A. "Metal ion detection using luminescent-MOFs: Principles, strategies and roadmap", *Coord. Chem. Rev.* (2020), **415**, 213299.

[30] Seco, J. M.; Pérez-Yáñez, S.; Briones, D.; García, J. A.; Cepeda, J.; Rodríguez-Diéguez, A. "Combining polycarboxylate and bipyridyl-like ligands in the design of luminescent zinc and cadmium based metal-organic frameworks", *Cryst. Growth Des.* (2017), **17**, 3893-3906.

[31] Cui, Y.; Chen, B.; Qian, G. "Lanthanide metal-organic frameworks for luminescent sensing and light-emitting applications", *Coord. Chem. Rev.* (2014), **273-274**, 76-86.

[32] Wang, M.; Huang, R. Y.; Wang, Z. Q.; Wu, G. H. "Solvent-dependent luminescence behaviour of a new charge-transfer Cu(I)-MOF: An experimental and theoretical investigation", *Inorg. Chem. Commun.* (2015), **56**, 41-44.

[33] Banerjee, D.; Hu, Z.; Li, J. "Luminescent metal-organic frameworks as explosive sensors", *Dalton Trans.* (2014), **43**, 10668-10685.

[34] Omary, M. A.; Patterson, H. H. (2017). Luminescence, Theory. In *Encyclopedia of Spectroscopy and Spectrometry (Third Edition)*. Academic Press, Oxford.

[35] Samanta, P.; Dutta, S.; Ghosh, S. K. (2019). Metal-organic frameworks for detection and desensitization of environmentally hazardous nitro-explosives and related high energy materials. In *Metal-Organic Frameworks (MOFs) for Environmental Applications*. Elsevier.

[36] Jones, C. L.; Tansell, A. J.; Easun, T. L. "The lighter side of MOFs: structurally photoresponsive metal-organic frameworks", *J. Mater. Chem. A* (2016), **4**, 6714-6723.

[37] Dolgopolova, E. A.; Rice, A. M.; Martin, C. R.; Shustova, N. B. "Photochemistry and photophysics of MOFs: steps towards MOF-based sensing enhancements", *Chem. Soc. Rev.* (2018), **47**, 4710-4728.

[38] Zhang, T.; Lin, W. "Metal-organic frameworks for artificial photosynthesis and photocatalysis", *Chem. Soc. Rev.* (2014), **43**, 5982-5993.

[39] Xiao, J. D.; Jiang, H. L. "Metal-organic frameworks for photocatalysis and photothermal catalysis", *Acc. Chem. Res.* (2018), **52**, 356-366.

[40] Nasalevich, M. A. (2016). *Metal-Organic Frameworks for solar energy utilization*. Doctoral thesis. https://doi.org/10.4233/uuid:14f1f322-7013-46d5-b6a1-c5a02fa01a8c

[41] Zhang, T.; Jin, Y.; Shi, Y.; Li, M.; Li, J.; Duan, C. "Modulating photoelectronic performance of metal-organic frameworks for premium photocatalysis", *Coord. Chem. Rev.* (2019), **380**, 201-229.

[42] Llamas, B.; Navarrete, B.; Vega, F.; Rodriguez, E.; Mazadiego, L. F.; Cámara, Á.; Otero, P. (2016). Greenhouse Gas Emissions – Carbon Capture, Storage and Utilisation. In *Greenhouse Gases*. BoD-Books on Demand.

[43] IEA (2019), "Putting CO_2 to Use", IEA, Paris. https://www.iea.org/reports/putting-co2-to-use

[44] Mohammad, M.; Isaifan, R. J.; Weldu, Y. W.; Rahman, M. A.; Al-Ghamdi, S. G. "Progress on carbon dioxide capture, storage and utilization", *Int. J. Glob. Warm.* (2020), **20**, 124-144.

[45] Huang, C. H.; Tan, C. S. "A review: CO_2 utilization", *Aerosol Air Qual. Res.* (2013), **14**, 480-499.

[46] Das, S.; Daud, W. M. A. W. "A review on advances in photocatalysts towards CO_2 conversion", *RSC Adv.* (2014), **4**, 20856-20893.

[47] Wang, Y.; Zhao, L.; Otto, A.; Robinius, M.; Stolten, D. "A review of post-combustion CO_2 capture technologies from coal-fired power plants", *Energy Procedia* (2017), **114**, 650-665.

[48] Ma, Y.; Wang, Z.; Xu, X.; Wang, J. "Review on porous nanomaterials for adsorption and photocatalytic conversion of CO_2", *Chinese J. Catal.* (2017), **38**, 1956-1969.

[49] Herrmann, J. M. "Heterogeneous photocatalysis: state of the art and present applications", *Top. Catal.* (2005), **34**, 1-4.

[50] Wang, C. C.; Zhang, Y. Q.; Li, J.; Wang, P. "Photocatalytic CO_2 reduction in metal–organic frameworks: A mini review", *J. Mol. Struct.* (2015), **1083**, 127-136.

[51] Xu, H. Q.; Hu, J.; Wang, D.; Li, Z.; Zhang, Q.; Luo, Y.; Yu, S. H.; Jiang, H. L. "Visible-light photoreduction of CO_2 in a metal-organic framework: boosting electron-hole separation via electron trap states", *J. Am. Chem. Soc.* (2015), **137**, 13440-13443.

[52] Alvaro, M.; Carbonell, E.; Ferrer, B.; Llabrés i Xamena, F. X.; Garcia, H. "Semiconductor behaviour of a metal-organic framework (MOF)", *Chem. Eur. J.* (2007), **13**, 5106-5112.

[53] Zhang, X.; Wang, J.; Dong, X. X.; Lv, Y. K. "Functionalized metal-organic frameworks for photocatalytic degradation of organic pollutants in environment", *Chemosphere* (2020), **242**, 125144.

[54] Fang, Y.; Ma, Y.; Zheng, M.; Yang, P.; Asiri, A. M.; Wang, X. "Metal-organic frameworks for solar energy conversion by photoredox catalysis", *Coord. Chem. Rev.* (2018), **373**, 83-115.

[55] Hendon, C. H.; Rieth, A. J.; Korzyński, M. D.; Dincă, M. "Grand challenges and future opportunities for metal-organic frameworks", *ACS Cent. Sci.* (2017), **3**, 554-563.

[56] Subudhi, S.; Rath, D.; Parida, K. M. "A mechanistic approach towards the photocatalytic organic transformations over functionalised metal organic frameworks: a review", *Catal. Sci. Technol.* (2018), **8**, 679-696.

[57] IUPAC. (1997). Compendium of Chemical Terminology. In *The Gold Book*. Blackwell Scientific Publications, Oxford. https://doi.org/10.1351/goldbook.FT07381

[58] IUPAC. (1997). Compendium of Chemical Terminology. In *The Gold Book*. Blackwell Scientific Publications, Oxford. https://doi.org/10.1351/goldbook.D01654 and https://doi.org/10.1351/goldbook.R05063

[59] Saravanan, R.; Gracia, F.; Stephen, A. (2017). Basic principles, mechanism, and challenges of photocatalysis. In *Nanocomposites for visible light-induced photocatalysis*. Springer.

[60] Li, K.; An, X.; Park, K. H.; Khraisheh, M.; Tang, J. "A critical review of CO_2 photoconversion: catalysts and reactors", *Catal. Today* (2014), **224**, 3-12.

[61] Li, D.; Kassymova, M.; Cai, X.; Zang, S. Q.; Jiang, H. L. "Photocatalytic CO_2 reduction over metal-organic framework-based materials", *Coord. Chem. Rev.* (2020), **412**, 213262.

[62] Qian, R.; Zong, H.; Schneider, J.; Zhou, G.; Zhao, T.; Li, Y.; Yang, J.; Bahnemann, D. W.; Pan, J. H. "Charge carrier trapping, recombination and transfer during TiO_2 photocatalysis: An overview", *Catal. Today* (2019), **335**, 78-90.

[63] Syzgantseva, M. A.; Stepanov, N. F.; Syzgantseva, O. A. "Carrier Lifetimes and Recombination Pathways in Metal-Organic Frameworks", *J. Phys. Chem. Lett.* (2019), **10**, 5041-5046.

[64] Yuan, L.; Xu, Y. J. "Photocatalytic conversion of CO_2 into value-added and renewable fuels", *Appl. Surf. Sci.* (2015), **342**, 154-167.

[65] Sang, Y.; Liu, H.; Umar, A. "Photocatalysis from UV/vis to near-infrared light: towards full solar-light spectrum activity", *Chem. Cat. Chem.* (2015), **7**, 559-573.

[66] Vu, N. N.; Kaliaguine, S.; Do, T. O. "Critical aspects and recent advances in structural engineering of photocatalysts for sunlight-driven photocatalytic reduction of co_2 into fuels", *Adv. Funct. Mater.* (2019), **29**, 1901825.

[67] Chang, X.; Wang, T.; Gong, J. "CO_2 photo-reduction: insights into CO_2 activation and reaction on surfaces of photocatalysts", *Energy Environ. Sci.* (2016), **9**, 2177-2196.

[68] Xiang, X., Pan, F. & Li, Y. "A review on adsorption-enhanced photoreduction of carbon dioxide by nanocomposite materials", *Adv. Compos. Hybrid. Mater.* (2018), **1**, 6–31.

[69] Tu, W.; Zhou, Y.; Zou, Z. "Photocatalytic conversion of CO_2 into renewable hydrocarbon fuels: state-of-the-art accomplishment, challenges, and prospects", *Adv. Mater.* (2014), **26**, 4607-4626.

[70] Alkhatib, I. I.; Garlisi, C.; Pagliaro, M.; Al-Ali, K.; Palmisano, G. "Metal-organic frameworks for photocatalytic CO_2 reduction under visible radiation: A review of strategies and applications", *Catal. Today* (2020), **340**, 209-224.

[71] Christoforidis, K. C.; Fornasiero, P. "Photocatalysis for hydrogen production and CO_2 reduction: the case of copper-catalysts", *Chem. Cat. Chem.* (2019), **11**, 368-382.

[72] He, H.; Perman, J. A.; Zhu, G.; Ma, S. "Metal-organic frameworks for CO_2 chemical transformations", *Small* (2016), **12**, 6309-6324.

[73] Dhakshinamoorthy, A.; Li, Z.; Garcia, H. "Catalysis and photocatalysis by metal organic frameworks", *Chem. Soc. Rev.* (2018), **47**, 8134-8172.

[74] Dhakshinamoorthy, A.; Asiri, A. M.; García, H. "Metal-organic framework (MOF) compounds: photocatalysts for redox reactions and solar fuel production", *Angew. Chem. Int. Ed.* (2016), **55**, 5414-5445.

[75] Hendon, C. H.; Tiana, D.; Fontecave, M.; Sanchez, C.; D'arras, L.; Sassoye, C.; Rozes, L.; Mellot-Draznieks, C.; Walsh, A. "Engineering the optical response of the titanium-MIL-125 metal-organic framework through ligand functionalization", *J. Am. Chem. Soc.* (2013), **135**, 10942-10945.

[76] Patwardhan, S.; Schatz, G. C. "Theoretical investigation of charge transfer in metal organic frameworks for electrochemical device applications", *J. Phys. Chem. C* (2015), **119**, 24238-24247.

[77] Logan, M. (2018). Design, synthesis, stability, and photocatalytic studies of sustainable metal-organic frameworks. *Electronic Theses and Dissertations.* 5952.

[78] (a) Vitillo, J. G.; Savonnet, M.; Ricchiardi, G.; Bordiga, S. "Tailoring metal-organic frameworks for CO_2 capture: The amino effect", *Chem. Sus. Chem.* (2011), **4**, 1281-1290. (b) López-Maya, E.; Montoro, C.; Colombo, V.; Barea, E.; Navarro, J. A. R. "Improved CO_2 capture from flue gas by basic sites, charge gradients, and missing linker defects on nickel face cubic centered MOFs", *Adv. Funct. Mater.* (2014), **24**, 6130-6135. (c) Kazemi, S.; Safarifard, V. "Carbon dioxide capture in MOFs: the effect of ligand functionalization", *Polyhedron* (2018), **154**, 236-251. (d) Zhang, W. X.; Liao, P. Q.; Lin, R. B.; Wei, Y. S.; Zeng, M. H.; Chen, X. M. "Metal cluster-based functional porous coordination polymers", *Coord. Chem. Rev.* (2015), **293**, 263-278.

[79] Sun, D.; Fu, Y.; Liu, W.; Ye, L.; Wang, D.; Yang, L.; Fu, X.; Li, Z. "Studies on photocatalytic CO_2 reduction over NH_2-Uio-66(Zr) and its derivatives: towards a better understanding of photocatalysis on metal-organic frameworks", *Chem. Eur. J.* (2013), **19(42)**, 14279-14285.

[80] Garibay, S. J.; Cohen, S. M. "Isoreticular synthesis and modification of frameworks with the UiO-66 topology", *Chem. Commun.* (2010), **46**, 7700-7702.

[81] Cavka, J. H.; Jakobsen, S.; Olsbye, U.; Guillou, N.; Lamberti, C.; Bordiga, S.; Lillerud, K. P. "A new zirconium inorganic building brick forming metal organic frameworks with exceptional stability", *J. Am. Chem. Soc.* (2008), **130**, 13850-13851.

[82] Gangu, K. K.; Maddila, S.; Jonnalagadda, S. B. "A review on synthesis, crystal structure and functionality of naphthalenedicarboxylate ligated metal-organic frameworks", *Inorg. Chim. Acta* (2017), **466**, 308-323.

[83] Feng, D.; Wang, K.; Wei, Z.; Chen, Y. P.; Simon, C. M.; Arvapally, R. K.; Martin, R. L.; Bosch, M.; Liu, T. F.; Fordham, S. "Kinetically tuned dimensional augmentation as a versatile synthetic route towards robust metal-organic frameworks", *Nat. Commun.* (2014), **5**, 5723.

[84] Ye, R. P.; Zhang, X.; Zhai, J. Q.; Qin, Y. Y.; Zhang, L.; Yao, Y. G.; Zhang, J. "N-donor ligands enhancing luminescence properties of seven Zn/Cd (II) MOFs based on a large rigid π-conjugated carboxylate ligand", *CrystEngComm* (2015), **17**, 9155-9166.

[85] Oyarzabal, I.; Fernández, B.; Cepeda, J.; Gómez-Ruiz, S.; Calahorro, A. J.; Seco, J. M.; Rodríguez-Diéguez, A. "Slow relaxation of magnetization in 3D-MOFs based on dysprosium dinuclear entities bridged by dicarboxylic linkers", *CrystEngComm* (2016), **18**, 3055-3063.

[86] Seco, J. M.; Oyarzabal, I.; Pérez-Yáñez, S.; Cepeda, J.; Rodriguez-Dieguez, A. "Designing multifunctional 5-cyanoisophthalate-based coordination polymers as single-molecule magnets, adsorbents, and luminescent materials", *Inorg. Chem.* (2016), **55**, 11230-11248.

[87] Ma, X.; Li, L.; Chen, R.; Wang, C.; Zhou, K.; Li, H. "Doping of alkali metals in carbon frameworks for enhancing CO_2 capture: A theoretical study", *Fuel* (2019), **236**, 942-948.

[88] Devic, T.; Serre, C. "High valence 3*p* and transition metal-based MOFs", *Chem. Soc. Rev.* (2014), **43**, 6097-6115.

[89] Mouchaham, G.; Wang, S.; Serre, C. (2018). The Stability of Metal-Organic Frameworks. In *Metal-Organic Frameworks: Applications in Separations and Catalysis*. Wiley-VCH Verlag GmbH & Co. KGaA.

[90] Brunauer, S.; Emmett, P. H.; Teller, E. "Adsorption of Gases in Multimolecular Layers." *J. Am. Chem. Soc.* (1938), **60**, 309−319.

[91] Walton, K. S.; Snurr, R. Q. "Applicability of the BET Method for Determining Surface Areas of Microporous Metal−Organic Frameworks." *J. Am. Chem. Soc.* (2007), **129**, 8552−8556.

[92] de Boer, J. H.; Lippens, B. C.; Linsen, B. G.; Broekhoff, J. C. P.; van den Heuvel, A.; Osinga, T. V. "The t-curve of multimolecular N2-adsorption." *J. Colloid Interface Sci.* (1966), **21**, 405−414.

[93] Reñones, P.; Fresno, F.; Fierro, J. L. G.; de la Peña O'Shea, V. A. "Effect of La as Promoter in the Photoreduction of CO_2 Over TiO_2 Catalysts", *Top. Catal.* (2017), **60**, 1119-1128.

[94] Spek, A. L. "PLATON, an integrated tool for the analysis of the results of a single crystal structure determination", *Acta Crystallogr. Sect. A* (1990), **46**, C34.

[95] Herdes, C.; Sarkisov, L. "Computer simulation of volatile organic compound adsorption in atomistic models of molecularly imprinted polymers", *Langmuir* (2009), **25**, 5352-5359.

[96] Durgaprasad, G.; Sathyanarayana, D. N.; Patel, C. C. "Infrared spectra and normal vibrations of N,N-dimethylformamide and N, N-dimethylthioformamide", *Bull. Chem. Soc. Jpn.* (1971), **44**, 316-322.

[97] Weng, X.; Cui, Y.; Shaikhutdinov, S.; Freund, H. J. "CO_2 Adsorption on CaO(001): Temperature-Programmed Desorption and Infrared Study", *J. Phys. Chem. C* (2018), **123**, 1880-1887.

[98] Solis, B. H.; Cui, Y.; Weng, X.; Seifert, J.; Schauermann, S.; Sauer, J.; Shaikhutdinov, S.; Freund, H. J. "Initial stages of CO_2 adsorption on CaO: a combined experimental and computational study", *Phys. Chem. Chem. Phys.* (2017), **19**, 4231-4242.

[99] Yazaydın, A. Ö.; Snurr, R. Q.; Park, T. H.; Koh, K.; Liu, J.; LeVan, M. D.; Benin, A. I.; Jakubczak, P.; Lanuza, M.; Galloway, D. B. "Screening of metal-organic frameworks for carbon dioxide capture from flue gas using a combined experimental and modeling approach", *J. Am. Chem. Soc.* (2009), **131**, 18198-18199.

[100] Thétiot, F.; Duhayon, C.; Venkatakrishnan, T. S.; Sutter, J. P. "Modular assembling of $[Zr(C_2O_4)_4]^{4-}$ and $[DabcoH_2]^{2+}$ units in supramolecular hybrid architectures including an open framework with reversible sorption properties (Dabco= 1,4-Diazabicyclo[2.2.2] octane)", *Cryst. Growth Des.* (2008), **8**, 1870-1877.

[101] Bao, Z.; Yu, L.; Ren, Q.; Lu, X.; Deng, S. "Adsorption of CO_2 and CH_4 on a Magnesium-Based Metal Organic Framework", *J. Colloid Interface Sci.* (2011), **353**, 549−556.

[102] (a) Krishna, R. "Adsorptive separation of CO_2/CH_4/CO gas mixtures at high pressures", *Microporous Mesoporous Mater.* (2012), **156**, 217-223. (b) Myers, A. L.; Monson, P. A. "Adsorption in porous materials at high pressure: theory and experiment", *Langmuir* (2002), **18**, 10261-10273.

[103] (a) Liang, Z.; Marshall, M.; Chaffee, A. L. "CO_2 adsorption-based separation by metal organic framework (Cu-BTC) versus zeolite (13X)", *Energy Fuels* (2009), **23**, 2785-2789. (b) Bourrelly, S.; Llewellyn, P. L.; Serre, C.; Millange, F.; Loiseau, T.; Férey, G. "Different adsorption behaviors of methane and carbon dioxide in the isotypic nanoporous metal terephthalates MIL-53 and MIL-47", *J. Am. Chem. Soc.* (2005), **127**, 13519-13521. (c) Llewellyn, P. L.; Bourrelly, S.; Serre, C.; Vimont, A.; Daturi, M.; Hamon, L.; De Weireld, G.; Chang, J. S.; Hong, D. Y.; Kyu Hwang, Y. "High uptakes of CO_2 and CH_4 in mesoporous metal-organic frameworks MIL-100 and MIL-101", *Langmuir* (2008), **24**, 7245-7250. (d) Mason, J. A.; Sumida, K.; Herm, Z. R.; Krishna, R.; Long, J. R. "Evaluating metal-organic frameworks for post-combustion carbon dioxide capture via temperature swing adsorption", *Energy Environ. Sci.* (2011), **4**, 3030-3040.

[104] Yang, Y.; Shukla, P.; Wang, S.; Rudolph, V.; Chen, X. M.; Zhu, Z. "Significant improvement of surface area and CO_2 adsorption of Cu–BTC via solvent exchange activation", *RSC Adv.* (2013), **3**, 17065-17072.

[105] Pajuelo-Corral, O.; Rodríguez-Diéguez, A.; Beobide, G.; Pérez-Yáñez, S.; García, J. A.; San Sebastian, E.; Seco, J. M.; Cepeda, J. "Alkaline-earth and aminonicotinate based coordination polymers with combined fluorescence/long-lasting phosphorescence and metal ion sensing response", *J. Mater. Chem. C* (2019), **7**, 6997-7012.

Chapter 4

Multifunctional Lanthanide-based Chiral Metal-Organic Frameworks

4.1. Introduction

Metal-organic frameworks (MOFs) have attracted an increasing interest of researchers working in the field of multifunctional materials due to their structural and topological diversity, as well as the properties that arise from their structural features.[1] This is a result of the endless combinations of metal centers and organic ligands, which provides MOFs with the possibility of being synthesized with the desired functionalities by following the foundations set by the reticular chemistry.[2] Though it is true that potential porosity has traditionally been the most sought property given its implication in processes such as gas adsorption and separation,[3] drug or biomolecule release,[4] heterogeneous catalysis,[5] ionic conductivity[6] and crystallization templates,[7] other functionalities including magnetism and photoluminescence (PL) have also caused an important scientific impact.[8] In particular, the study of magnetic properties has recently focused on single-molecule magnets (SMMs) since they are revolutionizing cutting-edge technologies with applications for magnetic information storage, magneto-optics and molecular spintronics.[9] On the other hand, the growth of MOFs showing PL has been launched during the last decade owing to their large applicability as enhanced solid-state photodevices (OLEDs and so on)[10] as well as molecular sensors.[11] In this context, the use of Ln(III) ions as metal centers yielding novel MOFs has been multiplied due to not only their large and flexible coordination geometry but also to their unique magnetic and luminescent properties derived from their shielded 4*f* electron shell.[12]

In the field of magnetism, materials with SMM behaviour are of particular interest since these molecular species contain properties which are characteristic of bulk magnetic materials; concretely, once magnetized with an external field and under a certain temperature, SMMs present a relaxation time in which this magnetization is maintained once the external magnetic field is removed. This aspect of SMMs enables their use as information storage systems, among others, because de slow relaxation of the magnetization allows developing a binary system similar to the current one that uses the bit with 0 and 1 states, but based on the projection of the molecular spin (-z, +z) and with higher storage capacity given that each molecule acts as a quantum bit (qubit).[13]

The aforementioned magnetic relaxation is a consequence of the energy barrier (U_{eff}) generated by the magnetic anisotropy (D) in paramagnetic molecules, being the U_{eff} barrier governed by two main factors: (1) the static electronic structure, and (2) the dynamic coupling of the molecule to its environment, known as spin-phonon coupling.[14] SMMs need a bistable ground state (S) with well-separated sublevels (m_s), where the large magnetic moment of S is co-linear to the

magnetic moments of m_s. Figure 4.1 is an example of this requirement, in which, S = 10 ground state is split in 21 sublevels ($m_s = 2S + 1$) differentiated as $m_s = \pm 10$. Substates give information about the projection of the spin, being $-m_s$ an indicative of spin-down (-z), and $+m_s$ of spin-up (+z). Population of both types of sublevels is in equilibrium until an external magnetic field is applied and all the spins are oriented in the same direction as consequence of the stabilization of one type of sublevel. By removing this external field, unlike traditional paramagnetic materials, SMMs can maintain the orientation of the spins because the return to the equilibrium involves a relaxation process in which all m_s substates must be passed; that is, an energy/thermal barrier called U_{eff} must be overcome. This fact makes the SMM behaviour dependent on temperature since the relaxation process is limited by the so-called block-temperature (T_b) that determines the necessary energy to return to the equilibrium. Therefore, systems above their T_b will show no resistance to relaxation processes, whereas materials bellow their T_b will have spins blocked in m_s = -10 states (according to the example in Figure 4.1), and maintain magnetization, assuming slower relaxation times.[15]

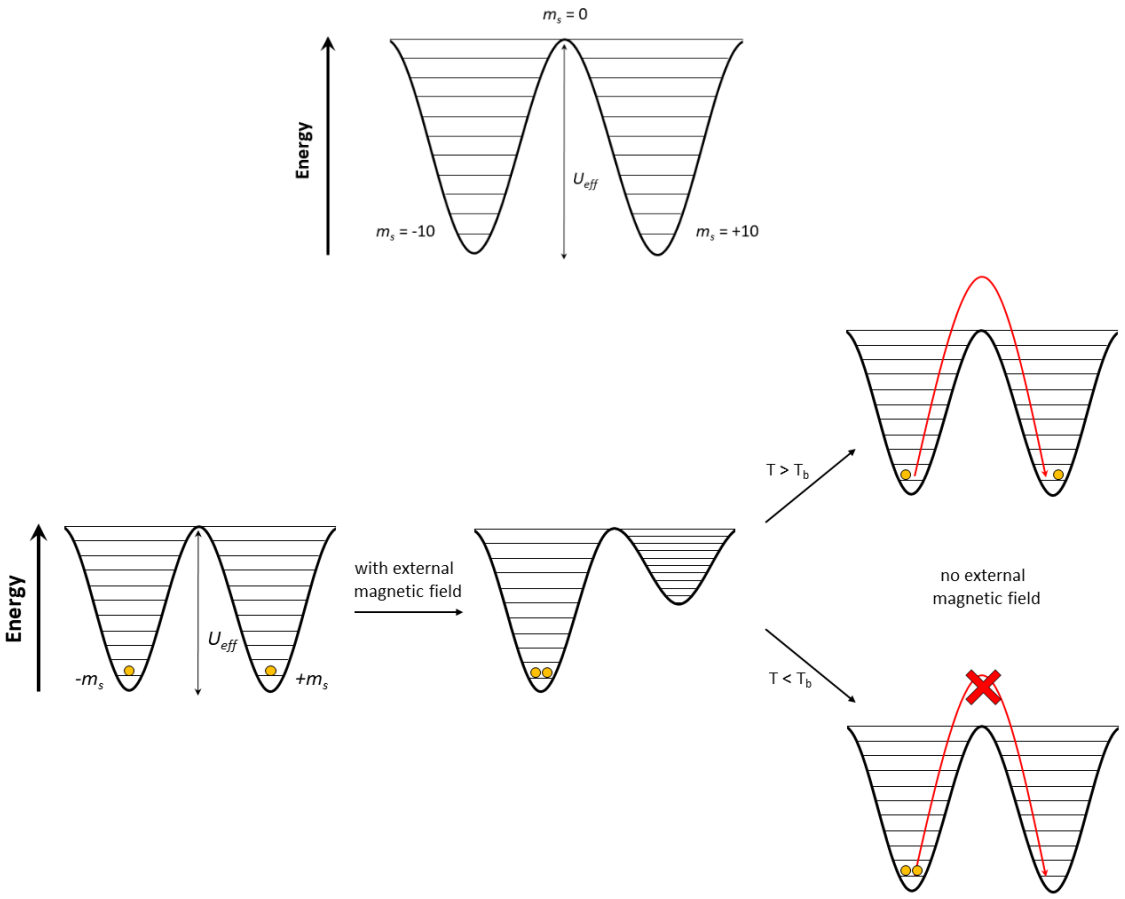

Figure 4.1. General description of SMMs. Upper section: Split of substates of S = 10 state as consequence of molecular anisotropy (D). Lower section: Description of a material with SMM behaviour.

As previously mentioned, this type of behaviour is largely determined by the magnetic anisotropy of the material, being lanthanide-based compounds the most promising in this field since they exhibit huge single-ion anisotropies. Due to their large spin-orbit coupling, magnetic properties of lanthanide ions are ruled by the quantum number (*J*); therefore, the number of unpaired electrons does not affect their magnetic moment, since it is determined by m_j values. These means that m_j sublevels determine the characteristic bistability of the ground state in lanthanide SMMs. In these materials, the split of m_j sublevels occurs in presence of a ligand field, and the U_{eff} barrier will depend on the changes in the lanthanide ion anisotropy by metal-ligand coordination.[16]

As shown in Figure 4.2, the electronic cloud of lanthanides are no perfect spheres and, depending on the metal, their shapes are described as oblate (for Ce(III), Pr(III), Nd(III), Tb(III), Dy(III) and Ho(III)), or prolate (for Pm(III), Sm(III), Er(III), Tm(III) and Yb(III)); so, the anisotropy could be encouraged by ligands with high electron concentration above and below the *xy* plane in oblate lanthanides, and by ligands with equatorial coordination geometry in the case of prolates.[17]

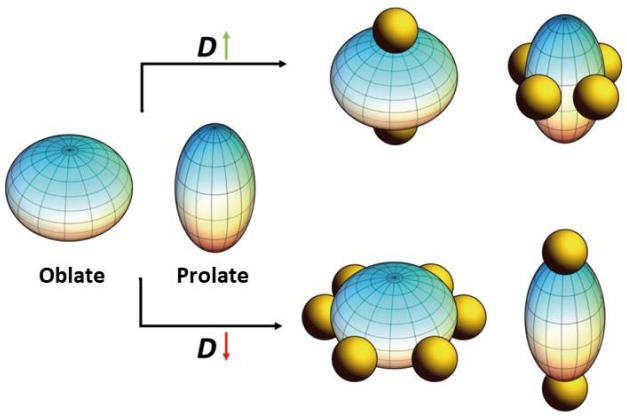

Figure 4.2. Single-ion anisotropy in lanthanides and influence of ligand field.

The assembly of SMMs into MOFs has become a topic of interest because it would make possible to obtain new types of molecular magnetic materials, since this combination allows to assemble the SMMs into the MOF nodes in an orderly way to build functional devices for information storage, among others. It also allows the development of dynamic magnetic coordination polymers for the sensing field, where the materials would change their magnetic properties due to guest-pore surface interactions. As corroborated in 2014 by Mínguez-Espallargas et al. with the first reported Ln(III)-based MOF showing SMM behavior,[18] these paramagnetic centers afford a large magnetic moment and significant single-ion anisotropy derived from spin−orbit coupling

(SOC),[19] which depending on their local environment, may lead to large barriers for the reversal of the magnetization.[20]

Regarding their luminescence performance, it should be pointed out that lanthanide-organic frameworks (LnOFs) present intense, narrow and long-lived emission bands covering the near-infrared and visible regions arising from the intraionic *f–f* transitions.[21] As stated in the "3.1. Introduction" section of Chapter 3, despite the low absorption coefficients associated to these transitions, lanthanide coordination to ligands may yield an efficient ligand-to-metal energy transfer and bring a bright emission by means of the well-known antenna effect (Figure 4.3).[22] Taking into account that this effect nurtures from the metal-ligand bond strength, ligands containing carboxylate linkers are appropriate given the large coordination capacity of those moieties.[23]

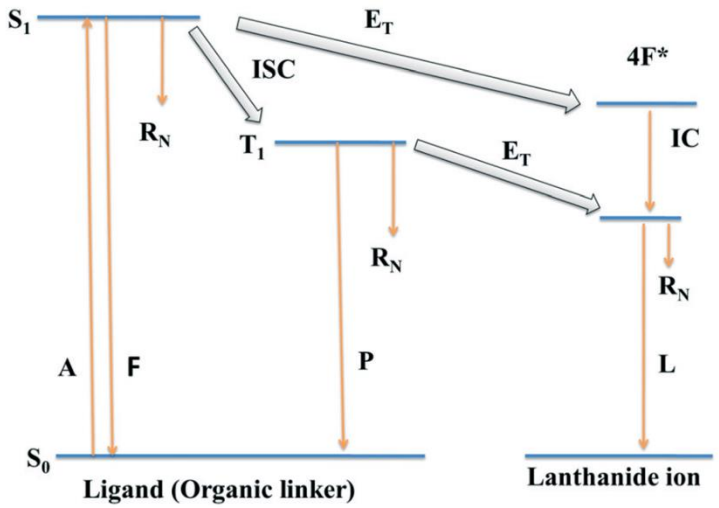

Figure 4.3. Schematic representation of energy absorption, migration, and emission in lanthanide MOFs. Abbreviations: S_0 = singlet ground state, S_1 = singlet first excited state, T_1 = triplet first excited state, A = absorption, F = fluorescence, P = phosphorescence, L = lanthanide centered luminescence, R_N = nonradiative transition, IC = internal conversion, ISC = intersystem crossing, and E_T = energy transfer. Plain arrows indicate radiative transitions.[24]

In addition to the previous considerations, the occurrence of a chiral crystal structure opens the way to other less explored physical phenomena related to the intriguing interaction of these solids with electromagnetic fields, where left- and right-handed structures tend to manifest opposed effects,[25] which are useful and applied in non-linear optics and magnetic materials.[26] In particular, circularly polarized luminescence (CPL) has intriguing applications in spintronics,[27] quantum computation,[28] and optical data storage.[29] Furthermore, it can be also used to induce exotic quantum phenomena such as the Floquet topological state,[30] as well as in other fields

such as chirality sensing[31] and enhanced image contrast for advanced medical imaging technologies.[32] In all cases, applicability of CPL demands a large value of the dissymmetry factor (g_{lum}), which is challenging since the mechanisms governing the chiroptical response are still somewhat obscure.[33]

It is interesting to note that most of the materials reported so far showing CPL properties are based on organic molecules, whereas the examples based on hybrid metal-organic materials are scarce.[34] Still, it seems that the latter hybrid materials can undoubtedly boost an enhanced performance by incorporating heavy atoms such as lanthanides(III).[35] Moreover, it is important to underline that studies on chiral MOFs showing SMM behaviour are rather scarce mainly because control of chirality is not an easy task.[36]

As indicated in Chapter 1, the second main objective of this thesis is focused on the design, synthesis, and structural and functional characterization of chiral MOFs, and to achieve this objective five isostructural enantiomeric pairs of 3D microporous MOFs based on Ln(III) ions and either L- or D-tartrate (L/D-tart) ligand have been synthesized and structurally, optically and magnetically characterized, in accordance with milestones 2.1, 2.2 and 2.2 indicated in page X of Chapter 1. Following, results obtained with this family of chiral MOFs are exposed, including their intriguing chiral luminescence and magnetic properties which are tuneable by thermal activation procedures.

4.2. Materials and methods

4.2.1. Compound synthesis

Five pairs of enantiomerically pure MOFs of general formula $[Ln_2(L/D\text{-}tart)_3(H_2O)_3]\cdot xH_2O\}_n$ (where Ln = Tb(III), Dy(III), Ho(III), Er(III) or Tm(III) and L/D-tart = L- or D-tartrate), which are detailed in Table 4.1, have been synthesized under hydrothermal conditions following the general procedure described below. The so-generated compounds have been obtained as single crystals and all crystal structures solved. It must be noticed that no racemization was observed during reaction despite what previously observed for other previous reports on chiral compounds.[37]

Table 4.1. Synthesized compounds.[a]

Formula	Compound	Code
{[Tb_2(μ_4-L/D-tart)$_2$(μ-L-tart)(H_2O)$_2$]·4H_2O}$_n$	Poly{[bis(mu4-L/D-tartrate-kO:k^{2}O',O'':k^{2}O''',O'''':kO''''')(mu-L/D-tartrate-k^{2}O,O':k^{2}O'',O''')diaquaditerbium(III)]tetrahydrate}	**Tb-L (7)** **Tb-D (8)**
{[Dy_2(μ_4-L/D-tart)$_2$(μ-L/D-tart)(H_2O)$_2$]·4H_2O}$_n$	Poly{[bis(mu4-L/D-tartrate-kO:k^{2}O',O'':k^{2}O''',O'''':kO''''')(mu-L/D-tartrate-k^{2}O,O':k^{2}O'',O''')diaquadidysprosium(III)]tetrahydrate}	**Dy-L (9)** **Dy-D (10)**
{[Ho_2(μ_4-L/D-tart)$_2$(μ-L/D-tart)(H_2O)$_2$]·xH_2O}$_n$	Poly{[bis(mu4-L/D-tartrate-kO:k^{2}O',O'':k2O''',O'''':kO''''')(mu-L/D-tartrate-k^{2}O,O':k^{2}O'',O''')diaquadiholmium(III)]hydrate} L enantiomer = 4 H_2O / D enantiomer = 3 H_2O	**Ho-L (11)** **Ho-D (12)**
{[Er_2(μ_4-L/D-tart)$_2$(μ-L/D-tart)(H_2O)$_2$]·xH_2O}$_n$	Poly{[bis(mu4-L/D-tartrate-kO:k^{2}O',O'':k^{2}O''',O'''':kO''''')(mu-L/D-tartrate-k^{2}O,O':k^{2}O'',O''')diaquadierbium(III)]hydrate} L enantiomer = 4 H_2O / D enantiomer = 3 H_2O	**Er-L (13)** **Er-D (14)**
{[Tm_2(μ_4-L/D-tart)$_2$(μ-L/D-tart)(H_2O)$_2$]·4H_2O}$_n$	Poly{[bis(mu4-L/D-tartrate-kO:k^{2}O',O'':k^{2}O''',O'''':kO''''')(mu-L/D-tartrate-*κ^{2}O,O′:κO″*)diaquadiyttrium(III)]tetrahydrate}	**Tm-L (15)** **Tm-D (16)**
{[Tb_2(μ_4-L-tart)$_2$(μ-L-tart)(H_2O)]·H_2O}$_n$	Poly{[bis(mu4-L-tartrate-kO:k^{2}O',O'':k^{2}O''',O'''':kO''''')(mu-L-tartrate-k^{2}O,O':k^{2}O'',O''')aquaditerbium(III)]hydrate}	**Tb-L' (17)**
[Tb_2(μ_4-L-tart)$_2$(μ-L-tart)(H_2O)]$_n$	Poly[bis(mu4-L-tartrate-kO:k^{2}O',O'':k^{2}O''',O'''':kO''''')(mu-L-tartrate-k^{2}O,O':k^{2}O'',O''')aquaditerbium(III)]	**Tb-L'' (18)**
[Tb_2(μ_4-L-tart)$_2$(μ-L-tart)]$_n$	Poly[bis(mu4-L-tartrate-kO:k^{2}O',O'':k^{2}O''',O'''':kO''''')(mu-L-tartrate-k^{2}O,O':k^{2}O'',O''')diterbium(III)]	**Tb-L''' (19)**
{[Dy_2(μ_4-L-tart)$_2$(μ-L-tart)(H_2O)]·H_2O}$_n$	Poly{[bis(mu4-L-tartrate-kO:k^{2}O',O'':k^{2}O''',O'''':kO''''')(mu-L-tartrate-k^{2}O,O':k^{2}O'',O''')aquadidysprosium(III)]hydrate}	**Dy-L' (20)**
[Dy_2(μ_4-L-tart)$_2$(μ-L-tart)(H_2O)]$_n$	Poly[bis(mu4-L-tartrate-kO:k^{2}O',O'':k^{2}O''',O'''':kO''''')(mu-L-tartrate-k^{2}O,O':k^{2}O'',O''')aquadidysprosium(III)]	**Dy-L'' (21)**
{[Dy_2(μ_4-L-tart)$_2$(μ-L-tart)]$_n$	Poly[bis(mu4-L-tartrate-kO:k^{2}O',O'':k^{2}O''',O'''':kO''''')(mu-L-tartrate-k^{2}O,O':k^{2}O'',O''')didysprosium(III)]	**Dy-L''' (22)**
{[TbY(μ_4-L-tart)$_2$(μ-L-tart)(H_2O)$_2$]·4H_2O}$_n$	Poly{[bis(mu4-L-tartrate-kO:k^{2}O',O'':k^{2}O''',O'''':kO''''')(mu-L-tartrate-k^{2}O,O':k^{2}O'',O''')diaquaterbium(III)yttrium(III)]tetrahydrate}	**TbY-L (23)**
{[DyY(μ_4-L-tart)$_2$(μ-L-tart)(H_2O)$_2$]·4H_2O}$_n$	Poly{[bis(mu4-L-tartrate-kO:k^{2}O',O'':k^{2}O''',O'''':kO''''')(mu-L-tartrate-k^{2}O,O':k^{2}O'',O''')diaquadysprosium(III)yttrium(III)]tetrahydrate}	**DyY-L (24)**
{[ErY(μ_4-L-tart)$_2$(μ-L-tart)(H_2O)$_2$]·4H_2O}$_n$	Poly{[bis(mu4-L-tartrate-kO:k^{2}O',O'':k^{2}O''',O'''':kO''''')(mu-L-tartrate-k^{2}O,O':k^{2}O'',O''')diaquaerbium(III)yttrium(III)]tetrahydrate}	**ErY-L (25)**
{[DyY(μ_4-L-tart)$_2$(μ-L-tart)(H_2O)]H_2O}$_n$	Poly{[bis(mu4-L-tartrate-kO:k^{2}O',O'':k^{2}O''',O'''':kO''''')(mu-L-tartrate-k^{2}O,O':k^{2}O'',O''')aquadysprosium(III)yttrium(III)]hydrate}	**DyY-L' (26)**
[DyY(μ_4-L-tart)$_2$(μ-L-tart)(H_2O)]$_n$	Poly[bis(mu4-L-tartrate-kO:k^{2}O',O'':k^{2}O''',O'''':kO''''')(mu-L-tartrate-k^{2}O,O':k^{2}O'',O''')aquadysprosium(III)yttrium(III)]	**DyY-L'' (27)**
[DyY(μ_4-L-tart)$_2$(μ-L-tart)]$_n$	Poly[bis(mu4-L-tartrate-kO:k^{2}O',O'':k^{2}O''',O'''':kO''''')(mu-L-tartrate-k^{2}O,O':k^{2}O'',O''')dysprosium(III)yttrium(III)]	**DyY-L''' (28)**

[a] L/D-tart = L/D-tartrate = $C_4H_4O_6^{2-}$

Crystalline Ln-L/D [where Ln = Tb(III), Dy(III), Ho(III), Er(III) or Tm(III)]. Single crystals of all compounds were obtained through a previously reported[38] hydrothermal procedure. Briefly, 5 mL of an aqueous solution containing 0.6 mmol of the corresponding Ln(III) nitrate were mixed

with an aqueous solution of the chiral tartaric acid (L- or D-H_2tar) (135.1 mg, 0.9 mmol) in 5 mL and sonicated. The resulting solution was heated in a Teflon liner at 140 °C for 48 h. After slow cooling to room temperature, prismatic single crystals were obtained, which were collected by filtration and washed several times with water. See Appendix III for more details.

4.2.2. Magnetic properties

Magnetic susceptibility measurements were performed on polycrystalline samples of the complexes with a Quantum Design SQUID MPMS-7T susceptometer at an applied magnetic field of 1000 G. The susceptibility data were corrected for the diamagnetism estimated from Pascal's Tables,[39] the temperature-independent paramagnetism, and the magnetization of the sample holder. *Ac* measurements were performed on a Physical Property Measurement System-Quantum Design model 6000 magnetometer under a 3.5 G *ac* field and frequencies ranging from 60 to 10 000 Hz. Magnetic *ac* measurements on the thermally activated Dy-L' (**20**) were performed with the standard setup since this sample is stable for some days before it spontaneously rehydrates to yield Dy-L (**9**). Instead, sample preparation of Tb-L''' (**19**) required an activation at 210 °C under vacuum and manipulation of the sample in a glove-box to preserve the sample against rehydration.

4.2.3. Photophysical properties

Fluorescence excitation and emission spectra recorded at room temperature were performed on a Varian Cary-Eclipse Fluorescence Spectrofluorimeter equipped with a xenon discharge lamp (peak power equivalent to 75 kW), Czerny–Turner monochromators, and an R-928 photomultiplier tube. For the fluorescence measurements, the photomultiplier detector voltage was fixed at 600 V while the excitation and emission slits were set at 5 and 2.5 nm.

PL measurements at 10 K as well as those conducted on thermally activated samples (Dy-L''' (**22**) was heated under vacuum at 483 K for 1 h and then cooled down to RT to collect the emission spectrum) were done using a close cycle helium cryostat enclosed in an Edinburgh Instruments FLS920 spectrometer, in such a way that the applied vacuum (10^{-7} bar) protected the samples from spontaneous rehydration. For steady state measurements in the UV-Vis range an IK3552R-G HeCd continuous laser (325 nm) was used as excitation source, whereas a Müller-Elektronik-Optik SVX1450 Xe lamp was employed to collect the excitation spectra. The emission measurements of the holmium (Ho-L/D (**11**/**12**)) and erbium (Er-L/D (**13**/**14**)) compounds in the NIR region were performed in a Hamamatsu NIR-PMT PicoQuant FluoTime 200 detector.

Photographs of crystalline samples were obtained in a micro-PL system included in an Olympus optical microscope illuminated with a HeCd laser or a Hg lamp.

4.2.4. Chiroptical properties

CD spectra were recorded at 25 °C on a Jasco J-815 or on an Olis DSM172 equipped with a Hamamatsu 150 W xenon arc lamp as light source. 1 cm path-length cuvettes and the following parameters were used for data acquisition on Jasco J-815: data pitch 0.5 nm; digital integration time (D.I.T.) 1 sec; scanning speed 200 nm/min; bandwidth 1 nm; accumulations 4. HT voltage was controlled (HT ≤ 800) to give reliable ellipticity values over the investigated wavelength range. CD raw data were processed with Jasco Spectra Manager 2 (Jasco) and Origin 9.5 (OriginLab Corp.).

Circularly polarized luminescence (CPL) measurements were performed on an Olis DSM172 spectrophotometer equipped with fixed wavelengths (355, 365 and 370 nm) LEDs as light source. A Hamamatsu photomultiplier tube was used as detector for ECD and a Hamamatsu photon counting detector for CPL measurements. Different settings and data processing were selected and carried out using the Olis GlobalWorks software. A fixed bandwidth of 1.0 nm and an integration time of 0.10 s were selected for ECD measurements, whilst for CPL experiments 1.00 s was selected as integration time.

4.2.5. Computational details

DFT calculations on the tartrate ligand were performed using the Gaussian 09 package,[40] using the Becke three parameter hybrid functional with the non-local correlation functional of Lee-Yang-Parr (B3LYP)[41] and the 6-311G++(d,p)[42] basis set. Further description of a suitable model can be found in the ESI. Molecular orbitals were plotted using GaussView 5.[43] On the other hand, a detailed description of the computational strategy adopted in this work to compute the magnetic coupling constant (J_{calc}) values has been described elsewhere.[44] One calculation was performed to determine the high-spin state and another to determine the low-spin broken symmetry state. The correctness of the latter state was ensured by means of its spin density distribution. Density functional theory was used to carry out two separate calculations to evaluate the coupling constant of each compound, employing the aforementioned hybrid B3LYP functional and Gaussian implemented 6-311G(d) basis set for all non-metallic atoms and the corresponding LANL2DZ pseudo-potentials for the metal atoms.[45]

4.3. Results and discussion

In this section we study the structure of the five pairs of chiral MOFs and their stability and reversibility in a dehydration process. In addition, data on luminescent and magnetic properties are provided along with some characteristics of chiral materials.

4.3.1. Crystallographic analysis

Summarized crystallographic data of Ln-L/D pairs are collected from Table 4.2 to Table 4.4 (see Appendix III for further details about refinement conditions).

Table 4.2. Crystallographic data of compounds (**7**)-(**10**).

Parameters	Tb-L (7)	Tb-D (8)	Dy-L (9)	Dy-D (10)
Empirical formula	$C_{12}H_{24}O_{24}Tb_2$	$C_{12}H_{24}O_{24}Tb_2$	$C_{12}H_{24}Dy_2O_{24}$	$C_{12}H_{24}Dy_2O_{24}$
M (g mol^{-1})	870.15	870.15	877.31	877.31
Cryst. System	Triclinic	Triclinic	Triclinic	Triclinic
Space group	*P1*	*P1*	*P1*	*P1*
a (Å)	6.0149(3)	6.0130(3)	5.9743(4)	5.9997(2)
b (Å)	7.3897(5)	7.3878(3)	7.3542(5)	7.3674(3)
c (Å)	13.2793(7)	13.2837(5)	13.1941(9)	13.2962(5)
α (º)	102.177(6)	102.251(4)	102.422(2)	102.281(4)
β (º)	101.709(5)	101.786(4)	101.664(2)	101.870(3)
γ (º)	90.413(5)	90.505(4)	90.613(2)	90.344(3)
V (Å^3)	564.18(6)	563.66(4)	553.55(7)	561.23(4)
Z	1	1	1	1

Table 4.3. Crystallographic data of compounds (**11**)-(**14**).

Parameters	Ho-L (11)	Ho-D (12)	Er-L (13)	Er-D (14)
Empirical formula	$C_{12}H_{24}Ho_2O_{24}$	$C_{12}H_{22}Ho_2O_{23}$	$C_{12}H_{24}Er_2O_{24}$	$C_{12}H_{22}Er_2O_{23}$
M (g mol^{-1})	882.17	864.15	886.83	868.81
Cryst. System	Triclinic	Triclinic	Triclinic	Triclinic
Space group	*P1*	*P1*	*P1*	*P1*
a (Å)	5.9870(4)	5.9693(2)	5.9743(4)	5.9614(5)
b (Å)	7.3670(5)	7.3865(2)	7.3542(5)	7.3515(6)
c (Å)	13.2590(9)	13.0842(5)	13.1941(9)	13.1229(11)
α (º)	102.346(2)	102.540(3)	102.422(2)	102.483(3)
β (º)	101.822(2)	101.363(3)	101.664(2)	101.551(3)
γ (º)	90.365(2)	90.912(2)	90.613(2)	90.767(3)
V (Å^3)	558.39(7)	551.07(3)	553.55(7)	549.18(8)
Z	1	1	1	1

Table 4.4. Crystallographic data of compounds (**15**)-(**16**).

Parameters	Tm-L (15)	Tm-D (16)
Empirical formula	$C_{12}H_{24}O_{24}Tm_2$	$C_{12}H_{24}O_{24}Tm_2$
M (g mol^{-1})	890.17	890.17
Cryst. System	Triclinic	Triclinic
Space group	*P1*	*P1*
a (Å)	5.9715(3)	5.9678(4)
b (Å)	7.3102(4)	7.3111(5)
c (Å)	13.3149(7)	13.3197(9)
α (º)	102.364(2)	102.352(2)
β (º)	102.224(2)	102.260(2)
γ (º)	90.276(2)	90.173(2)
V (Å^3)	554.11(5)	554.04(7)
Z	1	1

4.3.2. Structural characterization

Single crystal X-ray diffraction

The synthesized MOFs crystallize in the non-enantiogenic *P*1 space group in such a way that 3D open framework containing microchannels retains the chirality afforded by L-/D-tartrate ligands. The analysis of the X-ray diffraction data reveals the isostructural nature of all five pairs of compounds, with some expected slight differences (see below).

The asymmetric unit is comprised by two crystallographically independent Ln(III) ions [Ln(1) and Ln(2)], three tartrate ligands, two coordination water molecules and three/four lattice water molecules. Both Ln(III) atoms (Tb, Dy, Ho, Er) are nine coordinated species, with eight oxygen donor atoms from three tartrate dianionic ligands (six carboxylate and two hydroxyl oxygen atoms) and one additional oxygen donor atom provided by a coordinated water molecule [$Ln(O_{carb})_6(O_{hid})_2(O_w)_1$] (Figure 4.4). The crystal structure subtly adapts bond distances and coordination modes to the progressive decrease of the Ln(III) ion size, as previously observed for other lanthanide based families.[46] Remarkably, the decrease of the Ln(III) ion size brings clear-cut change for thulium(III), where Tm2 atoms are forced to drop their coordination number to eight in order to overcome the steric hindrance in the sphere (Figure 4.4).

Continuous shape measurements (CShMs, see Appendix III)[47] revealed that despite their equivalent coordination, Ln1 and Ln2 atoms build different polyhedra, resembling capped square antiprisms (CSAPR) and muffins (MFF), respectively, in Tb, Dy, Ho and Er-based compounds (Figure 4.4), whereas Tm2 builds an 8-vertices biaugmented trigonal prism (BTPR). It is worth noticing that moving from Tb(III) to Er(III), coordination polyhedra around Ln1 become

progressively less distorted and more similar to CSAPR whereas the opposed trend is observed for Ln2 environments (but Tm2).

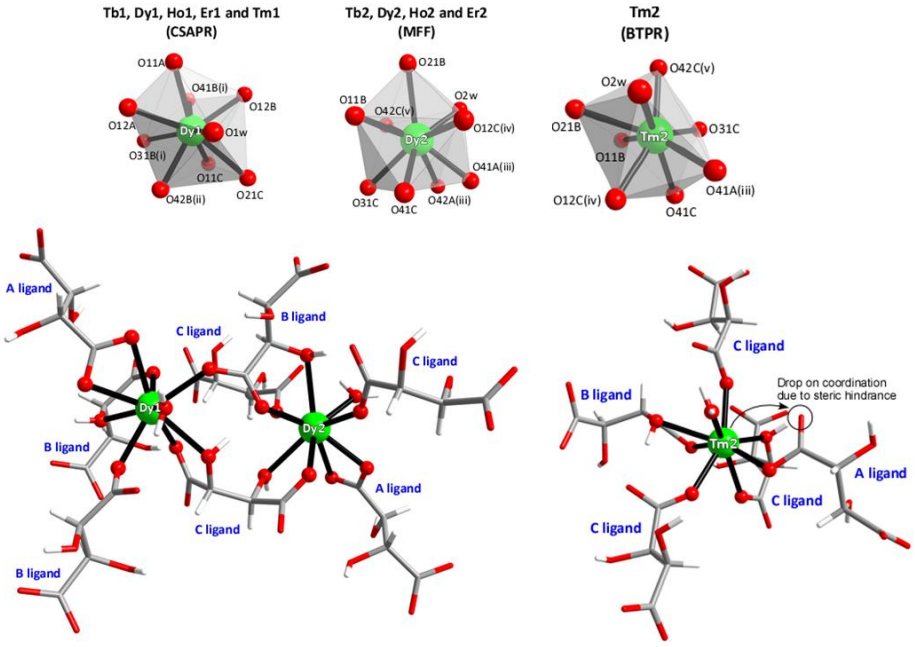

Figure 4.4. Excerpt of the crystal structure of compounds (**9**) and (**15**) showing the coordination polyhedra for Dy1 and Dy2, as well as the particular case of the coordination mode and polyhedron for Tm2. Symmetries: (i) x, 1 + y, z; (ii) – 1 + x, 1 + y, z; (iii) – 1 + x, – 1 + y, – 1 + z; (iv) x, – 1 + y, z; (v) 1 + x, y, z; (vi) x, – 1 + y, z.

As shown in

Table **4.5** and Table SIII.4, coordination bond lengths vary in the 2.29-2.80 Å range (shorter for Tm2), in agreement with data reported for other LnOFs,[2b,53,67b] where both limit distances correspond to the shell of Ln2 atoms in agreement with their aforementioned large distortion. In most of structures (compounds (**7**-**14**)), tartrate ligands show two different coordination modes. One of the tartrate ligands (A ligand) displays the bis(bidentate) μ-$\kappa^2O,O':\kappa^2O'',O'''$ mode, whereas two tartrate ligands (B and C) display a hexadentate μ_4-κO:$\kappa^2O',O'':\kappa^2O''',O'''':\kappa O'''''$ mode that exerts two five-member chelating rings involving a carboxylate and a hydroxyl oxygen atom. Instead, in Tm compounds, the A tartrate ligand is forced to acquire the bridging μ-$\kappa^2O,O':\kappa O''$ mode owing to the reduced coordination index shown by Tm2 atom (Figure 4.5).

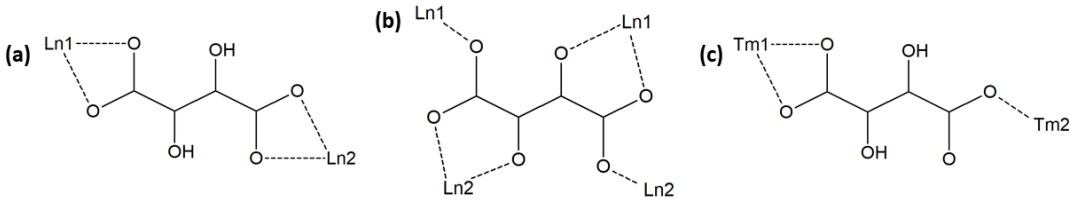

Figure 4.5. Coordination modes of tartrate ligands. **(a)** Bis(bidentate) μ-κ^{2}O,O':κ^{2}O'',O''' mode of A ligand in Tb-Er compounds. **(b)** Hexadentate μ_4-κO:κ^{2}O',O'':κ^{2}O''',O'''':κO''''' mode of B and C ligands in Tb-Tm compounds. **(c)** Bridging μ-κ^{2}O,O':κO'' mode of A ligand in Tm compounds.

Table 4.5. Selected bond lengths (Å) for Tb compounds.[a]

Tb-L (7)				**Tb-D (8)**			
Tb1–O11A	2.505(10)	Tb2–O11B	2.347(11)	Tb1–O11A	2.496(12)	Tb2–O11B	2.337(13)
Tb1–O12A	2.475(11)	Tb2–O21B	2.595(10)	Tb1–O12A	2.487(12)	Tb2–O21B	2.594(12)
Tb1–O12B	2.380(11)	Tb2–O31C	2.507(10)	Tb1–O12B	2.384(12)	Tb2–O31C	2.485(12)
Tb1–O11C	2.363(10)	Tb2–O41C	2.390(11)	Tb1–O11C	2.353(11)	Tb2–O41C	2.389(12)
Tb1–O21C	2.591(10)	Tb2–O2W	2.390(12)	Tb1–O21C	2.586(11)	Tb2–O2W	2.375(13)
Tb1–O1W	2.409(11)	Tb2–O41A(iii)	2.377(10)	Tb1–O1W	2.409(12)	Tb2–O41A(viii)	2.369(12)
Tb1–O31B(i)	2.492(11)	Tb2–O42A(iii)	2.796(11)	Tb1–O31B(vi)	2.499(12)	Tb2–O42A(viii)	2.767(13)
Tb1–O41B(i)	2.378(12)	Tb2–O12C(iv)	2.384(11)	Tb1–O41B(vi)	2.378(12)	Tb2–O12C(ix)	2.372(13)
Tb1–O42B(ii)	2.353(11)	Tb2–O42C(v)	2.324(11)	Tb1–O42B(vii)	2.354(12)	Tb2–O42C(x)	2.320(12)

[a] Symmetries: (i) x, 1 + y, z; (ii) – 1 + x, 1 + y, z; (iii) – 1 + x, – 1 + y, - 1 + z; (iv) x, - 1 + y, z; (v) 1 + x, y, z; (vi) x, - 1 + y, z; (vii) 1 + x, - 1 + y, z; (viii) 1 + x, 1 + y, 1 + z; (ix) x, 1 + y, z; (x) - 1 + x, y, z.

The porous nature of these flexible MOFs allows them to acquire a variable number of lattice water molecules, which brings small changes in the hydrogen bonding scheme. All the bridges imposed by tartrate ligands among neighboring Ln(III) atoms yields a 3D framework that may be described with the **fsx** topology since it possesses the $(4^2{\cdot}6^4)(4^2{\cdot}6^7{\cdot}8)$ point symbol, taking into account that Ln(III) and μ_4-tart ligands act as 5- and 4-connected nodes (Figure 4.6).[48] The growth of this structure leaves narrow microchannels along the crystallographic [001] direction that correspond to the ca. 13.5 % of the unit cell volume and are occupied by crystallization water molecules.[49] The latter are involved in a very intricate hydrogen bonding scheme in which they form infinite supramolecular chains that get anchored to the framework through hydrogen bonding interactions with hydroxyl groups and coordination water molecules (see Tables SIII.5-SIII.9 in Appendix III). In those cases where the content of lattice water molecules is lower (three water molecules per formula unit in Ho-D (**12**) and Er-D (**14**) the hydrogen bonding pattern is slightly modified (see Figure SIII.1 in Appendix III).

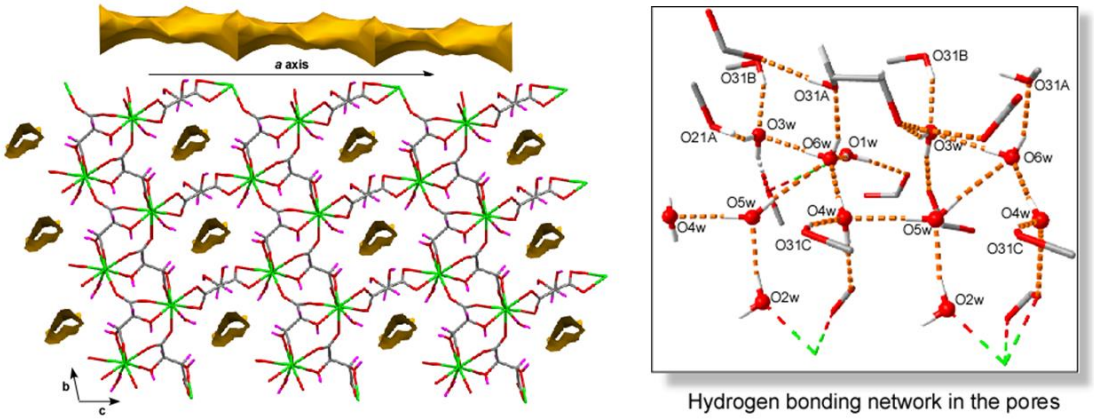

Figure 4.6. Packing of the 3D framework of Dy-L (**9**) MOF showing the voids and the hydrogen bonding network (including donor atoms names) of the lattice water molecules enclosed in within.

On another level, it must be mentioned that, as expected from the enantiomeric nature of these compounds, D-tartrate based MOFs show an equivalent arrangement which results from the application of an inversion center (see Figure SIII.2 in Appendix III).

Thermal evolution of the MOFs

The thermal behaviour of these MOFs entails an interesting feature because it involves several phase transitions accompanying the dehydration of the crystal structure which may be relevant for their properties. Considering that all compounds show a very similar temperature dependent behaviour (see Figures SIII.3-SIII.7 in Appendix III), compound Tb-L (**7**) was selected as a representative sample to conduct a thermodiffractometric study in order to follow plausible structural changes derived from sample heating. Starting from room temperature, the TG curve of the compound describes a small plateau up to 70 °C, which brings no remarkable change in the PXRD data but for a very slight expansion of the unit cell (which increases 1% in volume). Heating the Tb-L (**7**) phase above 90 °C causes shifts in most diffraction maxima (Figure 4.7) derived from a large shortening of the crystallographic *c* parameter (

Table 4.6, see also Figure SIII.13), compatible with a crushing of the microchannels upon dehydration, and accompanied by a significant cell volume drop (from 556 to 485 $Å^3$). This plausible loss of water molecules from the pores of this thermally activated phase (Tb-L' (**17**) hereafter) was confirmed by single crystal X-ray diffraction of a single crystal of Tb-L' (**17**), obtained upon heating a single crystal of the Tb-L (**7**) phase in the diffractometer at 110 °C and cooled down again to 100 K. The latter, revealed not only the loss of three water molecules from the channels to yield Tb-L' (**17**), a compound of $\{[Tb_2(\mu_4\text{-tart})_2(\mu\text{-tart})(H_2O)]\cdot H_2O\}_n$ formula, but

also that such dehydration provokes a subtle rearrangement of A tartrate ligands that force the loss of one coordination water molecule of Tb1 too.

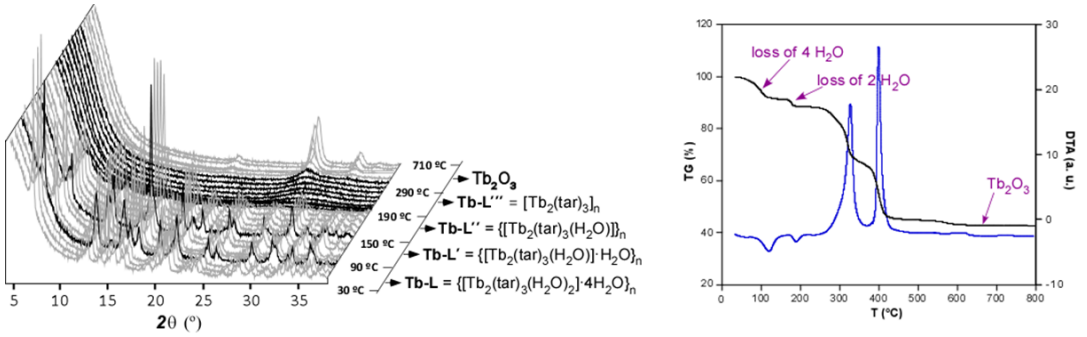

Figure 4.7. Analysis of the thermal behaviour of compound Tb-L (**7**). Note: diffractograms shown in black correspond to temperatures at which phase transition takes place.

Table 4.6. Unit cell parameters of the room and high temperature crystalline phases of compound Tb-L (**7**).[a]

Phase	a	b	c	α	β	γ	V
Tb-L	5.99	7.44	13.28	102.88	101.53	90.95	556
Tb-L'	5.92	7.41	11.97	107.83	103.32	89.94	485
Tb-L''	5.87	7.40	11.91	72.21	76.32	90.15	477
Tb-L'''	5.85	7.49	11.19	79.53	84.22	90.51	479

[a] Unit cell parameters correspond to fitting PXRD data. *a*, *b*, and *c*, α, β and γ, and *V*, are given in Å, degrees and Å^3, respectively.

The latter tartrate ligand passes from the carboxylate mediated and symmetric μ-$\kappa^2O,O':\kappa^2O'',O'''$ bridge to an asymmetric μ-$\kappa^3O,O',O'':\kappa^2O''',O''''$ mode in which carboxylate and hydroxyl oxygen atoms take part in the chelating moieties, respectively, for the coordination to Tb1 and Tb2 atoms (Figure 4.8). Consequently, Tb2 atom moves to a $(O_{carb})_5(O_{hid})_3(O_w)_1$ environment in which one of the originally coordinated carboxylate oxygen atoms (O42A) is now replaced by the hydroxyl O31A atom, in such a way that the CSAPR gets more idealized (S_{CSAPR} passes from 1.159 in Tb-L (**7**) to 0.973 in Tb-L' (**17**)). On its part, Tb1$(O_{carb})_6(O_{hid})_3$ chromophore is best described as a CSAPR once the coordination water molecule is lost. Such a reorganization of the tartrate A ligand brings a remarkable shortening of the Tb···Tb bridge (from 9.13 to 6.66 Å) and the crystallographic *c* parameter. In any case, this transformation brings no change in the framework topology, since Ln(III) atoms' connectivity is preserved. On another level, the crystallization water molecule remaining in the isolated pores is reoriented so as to get anchored to the framework through strong hydrogen bonding interactions, a fact that allows the resulting framework to maintain some potential porosity (5.4 % of the unit cell volume).

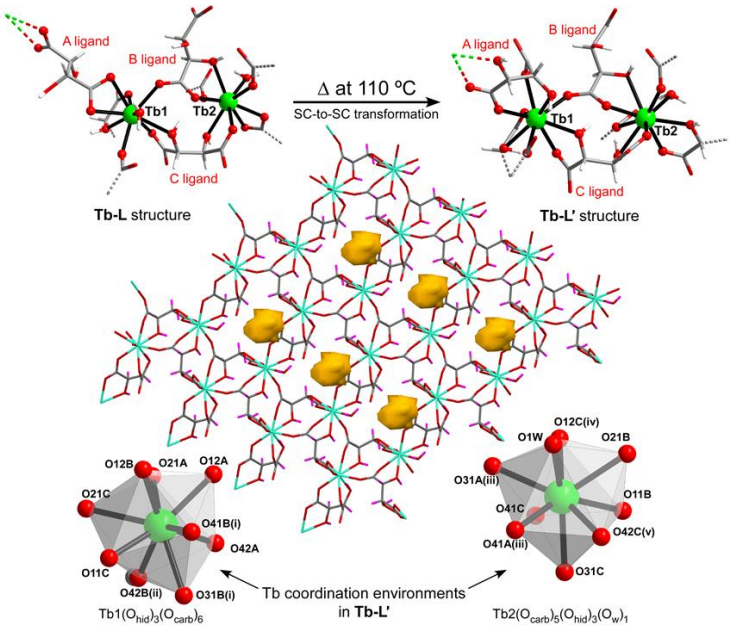

Figure 4.8. 3D framework of Tb-L' (**17**) displaying the isolated voids. Evolution of the coordination mode of A ligand according to the first dehydration-induced solid-state transformation is shown in the upper part. Tb polyhedra of Tb-L' (**17**) are shown in the lower part.

This first dehydration process is completed at ca. 120 °C and the obtained Tb-L' (**17**) phase is thermally stable up to 150 °C, as derived from the plateau in the TG curve (Figure 4.9). Interestingly, above 150 °C Tb-L' (**17**) undergoes a new phase transition associated with the loss of a lattice water molecule as confirmed by SCXR data collection on a single crystal of Tb-L (**7**) heated at 200 °C. This new thermally activated phase consists of a compound of $\{[Tb_2(\mu_4\text{-tart})_2(\mu\text{-tart})(H_2O)]\}_n$ formula (Tb-L'' (**18**) hereafter), where the loss of the lattice water molecule promotes a subtle compression of the flexible framework, as derived from the narrowed α and β angles of the unit cell (see

Table 4.6). Such transformations bring no changes in the connectivity of the framework, or its porosity (the geometrical porosity remains at 5.5 % of the actual unit cell volume, Figure 4.9). Despite this latter fact, tartrate A ligand, which exhibits the $\mu\text{-}\kappa^3O,O',O'':\kappa^2O''',O''''$ mode by joining to Tb1 and Tb2 atoms, is found to be disordered into two equivalent dispositions (each of which is refined with 50 % of occupation) that involve the alternation of different oxygen atoms (carboxylate/hydroxyl and carboxylate/water) occupying two positions of the O_9 donor set.

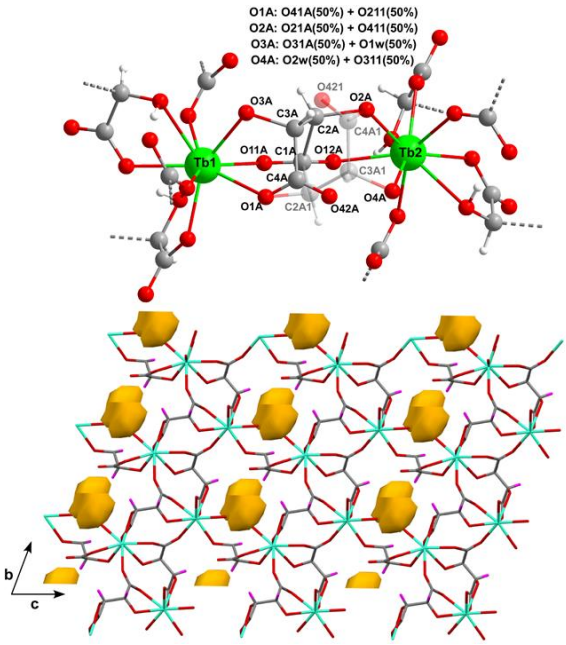

Figure 4.9. 3D framework of Tb-L'' (**18**). Top: Detail of the disordered tartrate A ligand in the coordination to terbium(III) atoms in Tb-L'' (**18**). Bottom: 3D framework of Tb-L'' (**18**) showing the isolated voids.

At this point, it is worth mentioning that the calculated PXRD diffractogram for Tb-L'' (**18**) fits well with those acquired in the 150-170 °C but it differs from those taken at the 210-290 °C range. Taking into account this fact and that the mass loss finishes at ca. 200 °C according to the TG curve, we can assume that this last crystalline phase (stable in the 210-290 °C range) corresponds to the anhydrous $[Tb_2(tart)_3]_n$ (Tb-L''' (**19**)) product, whose structure could not be determined due to the instability of single crystals at temperatures higher than 200 °C. The PXRD data acquired at 230 °C revealed that Tb-L''' (**19**) phase´s pattern fits well with a triclinic cell that is closely related to that of Tb-L'' (**18**) phase, thus suggesting the occurrence of a dense framework with no porosity in Tb-L''' (**19**). Finally, above 290 °C, two main exothermic processes provoke the decomposition of tartrate ligands into the final Tb_2O_3 residue.

On another level, the reversibility of the process could be confirmed by PXRD (Figure SIII.14). Following the activation of a sample of Tb-L (**7**) at 210 °C, it was found that Tb-L''' (**19**) phase is transformed back to Tb-L' (**17**) phase after some hours from the thermal activation. In this sequence, Tb-L'' (**18**) is not identified during the spontaneous rehydration (probably because it is less stable at standard conditions) although it should be formed in between. Finally, Tb-L' (**17**) remains stable for at least five days until it reverts back to Tb-L (**7**) when exposed to water saturated environments (see Appendix III for further details).

Once the structure of this family of MOFs has been described, the following magnetic measurements have been carried out in order to characterize their magnetic properties, as well as to know the influence of the changes in the structure derived from the dehydration process.

4.3.3. Magnetic properties

4.3.3.1. Static magnetic properties of hydrated phases

The temperature dependent magnetic susceptibility data were measured for polycrystalline samples of L-tartrate based enantiomeric MOFs (compounds Tb-L to Tm-L (**7-15**)) in the 5-300 K range under an applied magnetic field of 1000 Oe. The experimental $\chi_M T$ values at room temperature are close to those expected for the ground states with all Stark levels equally populated.[50] Cooling down the samples cause a progressive drop in the $\chi_M T$ product, as expected for the selective depopulation of the excited Stark sublevels (see Appendix III), although a significant contribution of antiferromagnetic exchange interactions could be also involved given the short ligand mediated Ln···Ln pathways present in the structure.[51] The χ_M^{-1} vs. T curves for these compounds followed the Curie-Weiss law almost in the whole temperature range, finding only small deviations for Ho-L (**11**) and Er-L (**13**) below 30 K (see Figure SIII.16). Given that there is no available expression to determine the magnetic susceptibilities of 3D systems with large anisotropy, $\chi_M T$ vs. T curves were fitted in the high temperature range (50-300 K) with expressions (Equations *(SIII.1)*, *(SIII.2)* and *(SIII.3)* in Appendix IIII) that assume only a splitting of the m_j energy levels ($H = \Delta J z^2$) in an axial crystal field (Table 4.7).[52]

Table 4.7. Best least-squares fits of the experimental magnetic data.[a]

Compound	g	Δ (cm^{-1})
Tb-L (7)	1.44	0.15
Dy-L (9)	1.32	0.31
Ho-L (11)	1.25	0.28
Er-L (13)	1.23	0.49
Tm-L (15)	1.15	0.53

[a] g is the gyromagnetic factor and Δ is the zero-field splitting parameter.

Inclusion of a zJ' parameter based on the molecular field approximation to account for the magnetic interaction between Ln(III) ions did not improve the fitting and brought almost negligible values (*ca.* -0.01 cm^{-1}). Additionally, DFT calculations were conducted on suitable gadolinium based dimeric models (which possess a spin-only $^8S_{7/2}$ ground state that allow a quantitative analysis of magnetic interactions)[53] to consider all the possible superexchange pathways: (i) Gd1···Gd2 through the carboxylate *syn-anti* and double chelating tartrate double

bridge; (ii) Gd1···Gd1 through the double carboxylate chelating ligand; (iii) Gd1···Gd2 through the chelating-monodentate tartrate ligand. These calculations support the existence of negligible exchange interactions of ferromagnetic nature ($J \approx 0.003$ cm^{-1}, see Figure SIII.17 in Appendix III), meaning that the 3D framework can be considered as an interconnected network of isolated Ln(III) centers from a magnetic point of view.

4.3.3.2. Dynamic magnetic properties of hydrated and dehydrated phases

As inferred from the crystal structure description (see CShMs in Tables SIII.10–SIII.12), the ligand field appears to be quite distorted and not especially suitable to stabilize high m_J ground states either for oblate or prolate ions. However, sample dehydration may tune the magnetic properties of these dehydrated phases derived from the reorganization of particularly the first but also the second coordination sphere of the metal. Due to the aforementioned distorted crystal field, only the most promising analogues (Tb-L (**7**), Dy-L (**9**) and Er-L (**13**)) were studied. Alternating current (*ac*) magnetic measurements revealed a lack of χ''_M signals under zero applied *dc* field (Figure SIII.18 in Appendix III) for all compounds. This could be attributed to the existence of quantum tunneling of the magnetization (QTM) and to the relatively short Ln···Ln distances (ca. 5.8 Å), which could provoke weak dipolar interactions that facilitate the fast relaxation of the magnetization hiding the SMM behavior.[54] It is well known that this effect might be partially or totally quenched by applying an external magnetic field (H_{dc}), and accordingly, under an H_{dc} = 1 kOe the three compounds show non-zero χ''_M signals. Tb-L (**7**) displays maxima at the highest frequencies (υ), whereas at lower frequencies only a small shoulder can be identified, confirming that QTM is still operating (Figure 4.10a). In the case of Dy-L (**9**), a small maximum could be identified only at the highest frequency and at the temperature limit of the device, suggesting a very small energy barrier for the reversal of the magnetization (Figure 4.10b). In contrast, Er-L (**13**) shows quite well-defined maxima below 4 K although QTM is shown to be still operative (Figure 4.10c). For Tb-L (**7**) and Er-L (**13**) the temperature dependence at each frequency was fitted to the generalized Debye model obtaining relaxation times for each temperature (Figures SIII.19b and SIII.21b). The noisy signals of the former allow to a poor fit of the data (inferred by the shape of χ''_M vs T curves), the high α values (around 0.5) obtained from the Cole-Cole plots suggest the presence of simultaneous relaxation processes. However, a reliable linear fit to the Orbach process affords an effective energy barrier of U_{eff} = 6.5 K and a pre-exponential factor $\tau_0 = 2.04 \cdot 10^{-6}$ s. The presence of SMM behavior in the Tb(III) analogue is worth mentioning. Actually, for non-Kramers ions a rigorous axial symmetry should be maintained in order to have a bi-stable ground state,[55] and this is not the case. In fact, apart from the CShMs measurements, the thermal evolution of the $\chi_M T$ product is indicative of a relatively

weak crystal field effect. Compounds with a well-defined axial ligand field usually display characteristic profiles where a very smooth decrease is observed in the whole temperature range with a sudden abrupt decrease at the lowest temperature (exhibiting magnetic blocking).[20,56] However, the presence of field induced SMM behavior is not novel for low symmetry systems, as in compound Tb-L (**7**) (see Table SIII.10 in Appendix III). In fact, this kind of systems can show quasi-degenerate ground states and consequently display slow relaxation of the magnetization.[57] In the case of Er-L (**13**), at the lowest temperatures, nearly temperature independent relaxation times were obtained (indicative of QTM), whereas at the highest temperatures the linear portion suggests the presence of the Orbach process. This is in good agreement with the high α values (0.49 at 2.0 K and 0.42 at 3.3 K) achieved from the Cole-Cole plots. Hence, the relaxation times were fitted to the simultaneous presence of Orbach and QTM processes (Equation *(4.1)(4.1)*) with the following set of parameters: U_{eff} = 33.8 K, τ_0 = 6.45x10^{-10} s and τ_{QTM} = 6.54x10^{-4} s. The dashed lines (Figure 4.10a and c, inset) indicate the contribution of each process at different temperatures.

$$\tau^{-1} = {\tau_{QTM}}^{-1} + {\tau_0}^{-1}\exp\left(-U_{eff}/k_BT\right) \qquad (4.1)$$

In view of the residual unquenched QTM occurring in the pure samples, the magnetic properties of equivalent but magnetically diluted samples (TbY-L (**23**), DyY-L (**24**) and ErY-L (**25**) hereafter) were analyzed, in which the contribution of possible weak dipolar interactions is avoided. The diluted samples were prepared by co-crystallizing the diamagnetic Y(III) counterpart along with the paramagnetic ions in a 9:1 Y(III):Ln(III) ratio. Similarly to what occurs with the non-diluted samples, under zero *dc* field no out-of-phase response was detected for TbY-L (**23**) and ErY-L (**25**). Interestingly, DyY-L (**24**) displays a weak χ''_M signal at low temperature, though no maximum is observed (Figure SIII.22). Once again, the measurements were repeated with H_{dc} =1 kOe and substantial differences were obtained. First of all, the peaks for TbY-L (**23**) are better defined and shifted to higher temperatures (Figure 4.10d). However, as observed for Er-L (**25**), the curves of TbY-L (**23**) still display the characteristic tail attributed to QTM below the maxima. Fitting of the χ''_M vs υ to obtain the relaxation times (Figure SIII.23b) turned to be more reliable in agreement with the better defined of χ''_M vs. *T* maxima. The relaxation times present the typical curvature suggesting the simultaneous presence of multiple relaxation pathways (Figure 4.10d, inset), in good agreement with the high α values extracted from the Cole-Cole plots (0.40 at 2.0 K and 0.11 at 4.4 K). The best fitting of the data was achieved with Equation (*4.2*), which accounts for Orbach, Raman and QTM relaxation processes (

Table **4.8**).

$$\tau^{-1} = {\tau_{QTM}}^{-1} + BT^n {\tau_0}^{-1} \exp\left(-U_{eff}/k_B T\right) \qquad (4.2)$$

The following set of parameters was obtained: U_{eff} = 52.0 K, τ_0 = 3.42x10^{-10} s, B = 177.9, n = 3.135 and τ_{QTM} = 8.33x10^{-4} s. Regarding the n parameter, for values between 1 and 6 can be considered reasonable[58] although a value of 7 might be expected for non Kramers ions.[59] An alternative fitting was attempted by fixing n = 7 without any successful result.

The Dy(III) analogue shows typical SMM behavior below 5 K with two sets of out-of-phase peaks in the 2.0-2.5 K and 3.5-4.5 K temperature ranges, attributed to fast (FR) and slow relaxation (SR), respectively (Figure 4.10e). In spite of the fact that they are clearly identified in the χ''_M vs. T plot, FR and SR appear to be somehow mixed complicating the analysis. Certainly, the Cole-Cole and χ''_M vs υ plots exhibit slightly mixed semicircles and broad maxima, respectively, despite of which the analysis with a simple Debye model gave quite reasonable results. In any case, in χ''_M vs. υ plots (Figure SIII.24b) the broad maximum observed at 2.0 K at around 1000 Hz is moved to higher frequencies as the temperature is increased, completely disappearing at 2.6 K. This is attributed to the FR. On the other hand, the maximum at high frequencies (around 10000 Hz) appears again at higher temperatures (4.0 K) but it rapidly disappears (at 4.4 K). The latter one corresponds to the SR, which was hidden by the larger intensity of the FR. This effect may be well illustrated by plotting the relaxation times extracted from the fit (Figure SIII.24c). The first low temperature points (2.0-2.8 K) display a quite linear trend that corresponds to the effective energy barrier associated to the FR. As the temperature is increased, the relaxation times become slower as the SR starts contributing, while another linear portion related to the barrier of SR is observed at the highest temperatures (4.0-4.4 K). The occurrence of two relaxation processes demands a fitting with the sum of two modified Debye functions to consider each relaxation independently, which was performed with the CCFIT Software[60] to obtain two sets of relaxation times. Thus, Arrhenius plots constructed for both relaxation processes (see inset of Figure 4.10e) afford effective energy barriers for the reversal of the magnetization and τ_0 values of 17.7 K with 1.78x10^{-8} s and 32.3 K with 1.83x10^{-8} s for FR and SR, respectively.

For ErY-L (**25**), the combination of the external magnetic field along with the dilution process is appropriate to completely quench the fast QTM, given the trend to zero observed for the χ''_M signals below the maxima as well as their well definition for the entire set of frequencies. Accordingly, the fitting of the relaxation times follows a linear trend in the whole temperature range, giving an effective energy barrier of U_{eff} = 33.9 K and τ_0 = 1.52x10^{-9} s, which are very similar values to the non-diluted samples.

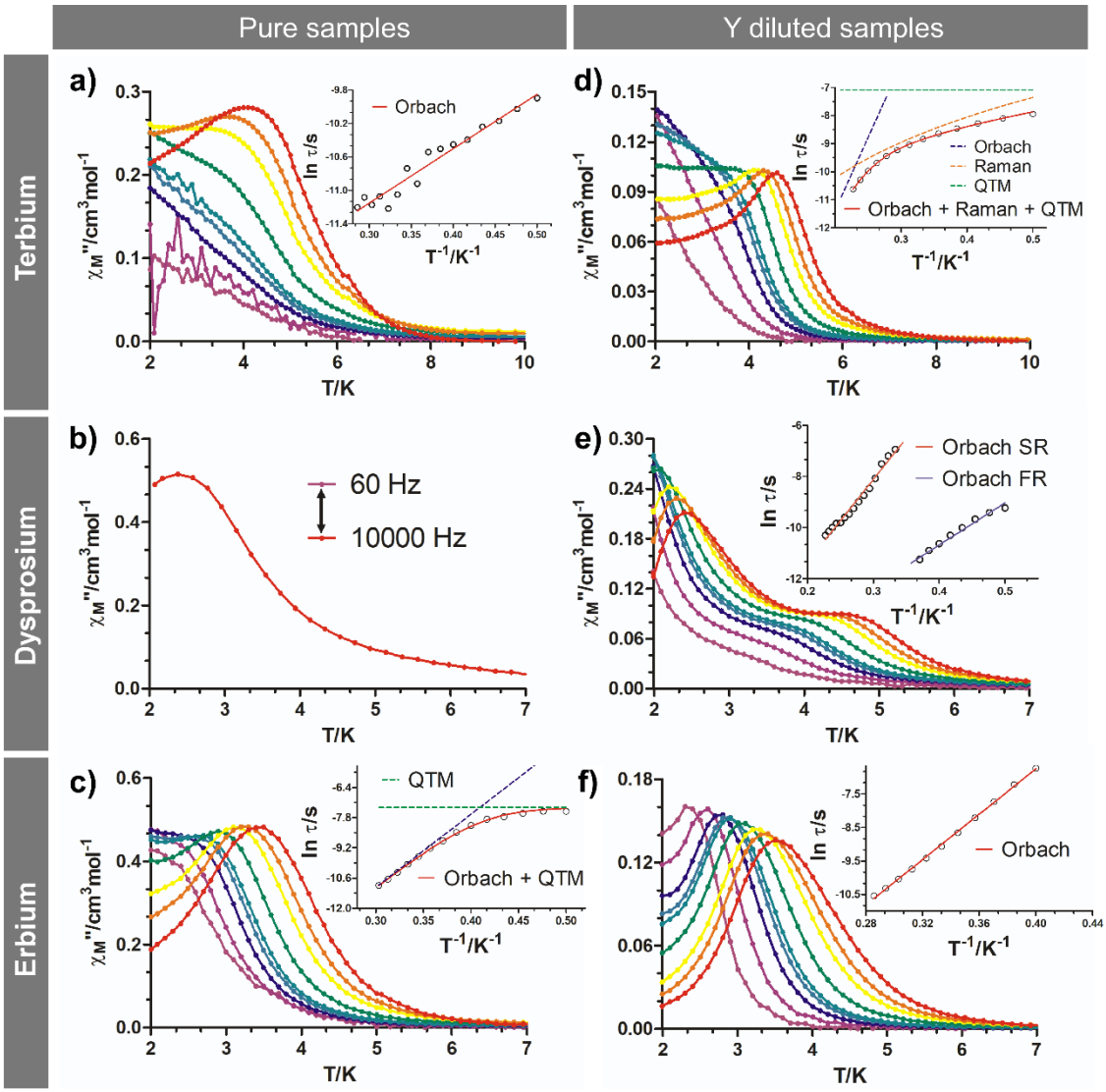

Figure 4.10. Temperature dependence of the out-of-phase *ac* susceptibility under Hdc = 1 kOe for the pure **a)** Tb-L (**7**), **b)** Dy-L (**9**) and **c)** Er-L (**13**) samples and diluted **d)** TbY-L (**23**), **e)** DyY-L (**24**) and **f)** ErY-L (**25**) samples. Insets: Temperature dependence for the relaxation times and the best fits of the data to different relaxation processes.

Table 4.8. Fitting parameters of the magnetic ac measurements.

Compound	U_{eff} (K)	τ_0 (s)
Tb-L (7)	6.5	2.04×10^{-6}
Dy-L (9)	–	–
Er-L (13)	33.8	6.45×10^{-10}
TbY-L (23)[a]	52.0	3.42×10^{-10}
DyY-L (24)[b]	17.7 / 32.3	1.78×10^{-8} / 1.83×10^{-8}
ErY-L (25)	33.9	1.52×10^{-9}

[a] These values are estimated from a fitting in which QTM and Raman relaxation mechanisms are considered. [b] The two values correspond to FR/SR processes.

The hydrothermal synthesis of these MOFs, based on, allows the coordination of water molecules to the oxophilic Ln(III) ions. As afore mentioned, the dynamic magnetic properties of SMMs are known to be directly correlated to the coordination environment, meaning that changes in the number of relaxation processes or the height of the effective energy barrier may be expected. Hence, we have studied three out of the four existing diluted dysprosium phases (as synthesized DyY-L (**24**) and thermally activated DyY-L' (**26**) and DyY-L''' (**28**)) to analyze how the loss of lattice/coordination water molecules modulate the dynamic magnetic properties of these materials. The Dy-based analogue was chosen due to two main reasons: (a) the non-activated (DyY-L (**24**)) phase shows two thermally activated relaxation processes in such a way that more significant differences in the data could be expected, and (b) the Dy(III) ion is, probably, the most promising Ln(III) ion when designing high performance SMMs.

Under an external zero dc field, DyY-L' (**26**) does not show any maximum in the χ''_M vs. *T* plot (Figure SIII.27) as it occurs for DyY-L (**24**). When applying a magnetic field of 1 kOe, the highest frequency curves (4000-10000 Hz) display well defined maxima in the 2.0-3.0 K range (Figure 4.11a). Interestingly, the second set of maxima in DyY-L (**24**) associated to the SR process has disappeared for the activated DyY-L' (**26**) analogue, suggesting that the reorganization of the tartrate ligands (which could affect the molecular vibrations and, possibly, the relaxation modes) as well as the loss of the coordinated and lattice water molecules have a considerable impact in the relaxation process. Note that this first dehydration involves a complete rearrangement of one of the Dy(III) centers in DyY-L' (**26**) (Dy1 loses the coordination water molecule) so no direct association can be established between Dy centers and relaxations (FR and SR) for different phases. The Cole-Cole plots of DyY-L' (**26**) suggest a wide distribution of relaxation mechanisms, showing α values in the range of 0.31-0.52 (for 2.0 and 3.0 K, respectively). Thus, the relaxation times were fitted using Equation *(4.1)* giving the following set of parameters: U_{eff} = 16.7 K, τ_0 = $6.87x10^{-8}$ s and τ_{QTM} = $1.91x10^{-4}$ s.

In order to focus on the most interesting switch of the magnetic properties through the thermal activation of the material, the completely dehydrated DyY-L''' (**28**) phase was studied (see "4.2.2. Magnetic properties section" for further details on sample preparation). Even though SCXR structure could not be solved for this compound, TDX and TG analysis confirm the absence of water molecules in the framework of DyY-L''' (**28**) (see Appendix III for further details on sample preparation), meaning that a new rearrangement of the ligand field must have occurred, which could promote a second switch in the magnetic relaxation behavior. Indeed, *ac* measurements on DyY-L''' (**28**) under H_{dc} =1 kOe (no maxima were observed under zero *dc* field, see Figure SIII.27) display a non-defined but clearly appreciable new set of maxima at temperatures as high

as 13 K (Figure 4.11b). This increase in the temperature may be originated from a new and more axially defined crystal field around Dy(III) ions, which would provoke a bigger splitting between the ground and excited states that in turn increases the value of the effective energy barrier. However, the fact that the absence of the molecular vibrations of lost water molecule or even the reorganization of the phonon-structure of the material cannot be discarded. The data was then analyzed in the 10.9-14 K temperature range, obtaining α values indicative of a quite wide distribution of relaxation processes (0.35 at 10.9 K and 0.30 at 14.0 K, Figure SIII.29c) although relaxation times extracted from the χ''_M vs υ curves describe a linear Arrhenius plot (Figure 4.11b, inset). This incoherence might be due to the small shoulder below the analyzed temperature (in the 6-8 K range), accordingly assuming that another relaxation process, responsible of enlarging the α value when lowering the temperature, is taking part. However, the tendency clearly indicates that the relaxation distribution is becoming narrower and therefore the data was fitted to a pure Orbach process with an effective energy barrier of U_{eff} = 58.7 K and $\tau_0 = 2.82 \times 10^{-7}$ s.

Finally, the reversibility of the magnetic properties was also studied by collecting a new *ac* curve at 10000 Hz on a sample after one entire activation/deactivation cycle. As depicted in Figure 4.11c, both *ac* curves at 10000 Hz almost overlap, confirming the reversible character of the material, in good agreement with the PXRD analysis conducted.

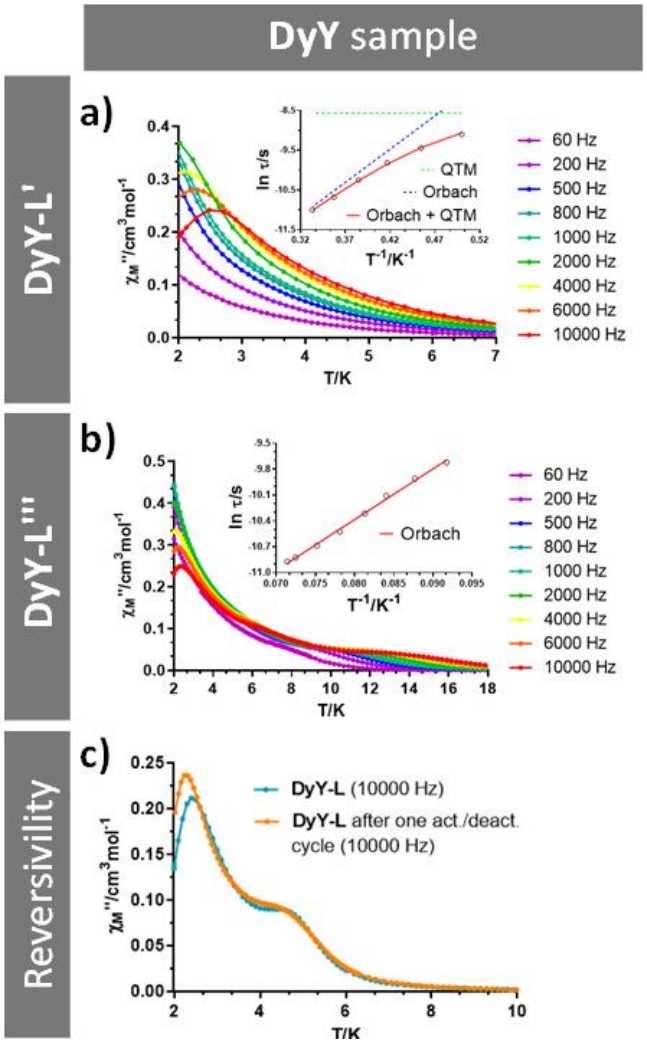

Figure 4.11. Temperature dependence of the out-of-phase *ac* susceptibility under an external magnetic field of 1 kOe for **a)** DyY-L' (**26**) and **b)** DyY-L''' (**28**) samples. Insets: temperature dependence for the relaxation times and best fits. **c)** *ac* curves at 10000 Hz for the non-activated and fully dehydrated/rehydrated sample.

In addition to magnetic properties, lanthanide-based MOFs may possess luminescent properties that can be influenced by coordinated/adsorbed solvent molecules; therefore, the following section details the data obtained from the photoluminescence study of this MOF family.

4.3.4. Photoluminescence

4.3.4.1. Luminescence properties of hydrated phases

Lanthanide centered emissions in coordination polymers (CPs) are known to be useful for developing solid-state photodevices[61] given their intense emissions in the visible spectra or in the near-infrared (NIR) region[62]. For this reason, photoluminescence measurements were carried out on polycrystalline samples of all L-enantiomeric compounds (Tb-L to Tm-L (**7**-**15**))

given that the measured luminescent properties are enantiomer independent, as observed for the Dy-L (**9**) and Dy-D (**10**) pair (Figure SIII.30 in Appendix III). Whereas compounds Ho-L (**11**) and Er-L (**13**) exposure to UV excitation yielded no characteristic Ho(III) and Er(III) based emissions these compounds provided an almost identical band in the 400-650 nm range (see Figures SIII.31 and SIII.32) attributable to the n ← π* emissions of the metal coordinated tartrate ligands. With regard to those compounds containing Ln(III) atoms potentially emitting in the visible range, non-radiative relaxation tends to be less important since, being more energetic than NIR emissions, it is comparatively less quenched by molecular vibrations, i.e. thermal deactivation.[22] Taking into account that these emissions arise from ligand-to-metal charge transfers (LMCT), and that they may change according to the temperature, the latter parameter was also studied. Such a LMCT in Ln(III)-organic systems is known to proceed from the first excited triplet state (T_1), so we made use of DFT calculations to estimate the energy and shape of that state. In T_1, the MO shows the lobes spread over the whole molecule but especially over the oxygen atoms (Figure SIII.45). Moreover, the calculation to estimate the vertical excitation energy between T_1 and the ground singlet state (S_0) with the same optimized geometry, which presents an almost identical shape of T_1, gives a value of 19639 cm^{-1} which can be considered as the energy of T_1. No Tm(III) based emissions were observed for compound Tm-L (**15**), which showed a similar spectrum to Ho-L (**11**) and Er-L (**13**). When compounds Tb-L (**7**) and Dy-L (**9**) are excited at room temperature under monochromatic 325 nm light, they present emission spectra composed of a minor wide band assigned to the ligand fluorescence (as it peaks at ca. 400 nm and resembles the emission shown by compounds Ho-L (**11**) and Er-L (**13**)) in addition to intraionic transitions associated with Ln(III) ions (Figure 4.12).

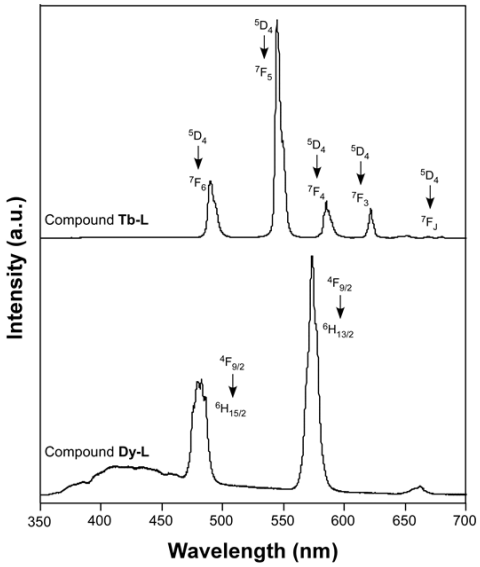

Figure 4.12. Emission spectra of compounds Tb-L (**7**) and Dy-L (**9**) recorded at room temperature under laser λ_{ex} = 325 nm.

In particular, compound Tb-L (**7**) displays four main groups of signals sited at 490 nm ($^7F_6 \leftarrow {}^5D_4$), 544 nm ($^7F_5 \leftarrow {}^5D_4$), 585 nm ($^7F_4 \leftarrow {}^5D_4$) and 622 nm ($^7F_3 \leftarrow {}^5D_4$) arising from intraionic transitions of Tb(III) ions. A comparatively weaker luminescence is observed for the Dy-L (**9**), since in addition to the characteristic multiplets centered at 481 nm ($^6H_{15/2} \leftarrow {}^4F_{9/2}$), 573 nm ($^6H_{13/2} \leftarrow {}^4F_{9/2}$) and at 662 nm ($^6H_{11/2} \leftarrow {}^4F_{9/2}$), the band assigned to tartrate ligand fluorescence (previously shown for Ho-L (**11**) and Er-L (**13**)) is significantly stronger. It is worth noticing the large intensity of the second band, which dominates the spectrum, and the fact that the third band is observed, conversely to most of reported lanthanide-organic complexes but habitually present on strongly emitting inorganic phosphors.[63] Indeed, these strong emissions are quite surprising considering that the tartrate ligand lacks strong absorbing chromophores. An inspection of the excitation spectra at the main line (λ_{em} = 544 for Tb-L (**7**) and 573 nm for Dy-L (**9**)) reveals the absence of any significant wide band in the spectra, thus indicating the lack of any ligand centered excitation. Instead, only narrow bands associated with the intraionic *f-f* transitions of the lanthanide are present, among which $^7F_6 \rightarrow {}^5L_9$ and $^6H_{15/2} \rightarrow {}^5P_{3/2}$,[64] one of the most intense bands respectively for Tb-L (**7**) and Dy-L (**9**) samples, fall within the employed excitation wavelength (λ_{ex} = 325 nm). The obtained results are in agreement with the micro-PL images taken on a microscope in which some selected excitation lines (λ_{ex} = 365, 435 and 536 nm) have been chosen. Under UV excitation, Tb-L (**7**) displays intense green emission according to the fact that the excitation band corresponding to the $^5D_4 \rightarrow {}^6L_{10}$ (at 364 nm) fits well with λ_{ex} = 365 nm. On the other hand, Dy-L (**9**) sample is not such effectively excited through any intraionic transition (see Appendix III).

The overall low energy transfer observed from tartrate ligands to Ln(III) centers may be explained according to the lower energy of T_1 state (calculated at ≈ 19639 cm^{-1} through DFT methodology) than those emitting levels of Ln(III) atoms ($^5D_4$ level for Tb(III) ≈ 20500 cm^{-1}, and $^4F_{9/2}$ level for Dy(III) ≈ 20800 cm^{-1}).[65] According to Latva's empirical rule,[66] the optimal ligand-to-metal energy transfer process for Ln(III) based complexes needs an energy gap in the 2500-4000 cm^{-1} range, which is surpassed in all cases. This rule also explains why Tm(III) atoms (with the emitting $^1G_4$ level at ca. 21600 cm^{-1}) do not show the characteristic emission in compound Tm-L (**15**).

To get deeper insights, the luminescence properties of Tb-L (**7**) and Dy-L (**9**) were measured at 10 K to avoid the vibrational quenching derived from the thermal energy of the bond electrons.[67] Upon laser excitation (λ_{exc} = 325 nm), emission spectra of samples revealed a significant enhancement of the emitted light, which allowed distinguishing many of the individual transitions grouped in each manifold (Figure SIII.38).[68] It must be noted that the enhancement comes from the increased efficient intraionic excitation and not from an improved antenna effect given the similar shape of the low temperature excitation spectra (see Appendix III). A common feature to all spectra is the occurrence of ligand-based fluorescence, though the intensity of these bands is comparatively low with those recorded at room temperature. In the spectrum of the Tb(III) compound (Tb-L (**7**)) seven multiplets corresponding to the ^7F_J (J = 0-6) ← $^5D_4$ transitions are observed, although the last three multiplets are relatively weak. Given the good emission capacity of the Tb-based compound, a detailed analysis of its emission was performed as a function of the temperature (measuring a spectra each 25 °C). As inferred from Figure SIII.39 (see Appendix III), the emission capacity in terms of integrated emission from room temperature to 10 K remains almost unchanged (covering the 350–700 nm range). On the other hand, the spectrum of Dy-L (**9**) displays the same three bands centered at 483, 578 and 664 nm, among which the second one (green emission) also exhibits the highest intensity. Nonetheless, it must be remarked that there is a change in the relative intensity of the bands with the temperature, passing from an intensity ratio of 2.13 to 1.4. The analysis of the emission lifetimes revealed monoexponential decays from both compounds in good agreement with the fact that although the crystal structure contains two independent Ln(III) centers, they have identical coordination shells which makes them equivalent from the spectroscopic viewpoint. The fitting of the curves with the exponential function [$I_t = A_0 + A_1 \cdot \exp(-t/\tau)$], gives a relatively large lifetime of ca. 1 ms, which is completely stable with the temperature. This fact supports, once again, that decreasing the temperature brings no enhancement of the radiative part, but it only implies a decrease of the non-radiative losses which translate in an overall improvement of the emission capacity. The fitting of the decay curve for Dy-L (**9**) gives homogenous lifetimes for the two main emission

maxima, with a value of ca. 30 μs. On its part, the low temperature also decreases the non-radiative quenching in Tm-L (**15**) up to the point that thulium(III) centered emissions can be traced in the emission spectrum recorded at 10 K (Figure SIII.33).

With the aim of getting deeper insights into the enhancement of the PL signal at low temperature, the DFT calculation to estimate the energy of the T_1 state is conducted by fixing 10 K as the temperature. The T_1-S_0 gap for the tartrate molecule at triplet geometry enlarges up to 23398 cm^{-1}, meaning that the energy gap regarding lanthanide's excited emissive levels could fit into the efficient region considered by Latva and that the more brilliant emissions of Tb-L (**7**) and Dy-L (**9**) (in addition to the Tm-based emission per se) are due to not only the lower vibrational quenching but also to a more efficient ligand-to-lanthanide energy transfer.

4.3.4.2. Luminescence properties of dehydrated phases

Considering the exciting transformations taking place when heating the synthesized samples, as shown before in the "Thermal evolution of the MOFs" section, we decided to explore the modulation of the PL signal with the loss of lattice/coordination water molecules, and we selected Dy-L (**9**) as an example. The emission spectrum recorded for Dy-L´ (**20**) at RT (thermally activated at 110 °C) displays a clear increase of the absolute emission (21 times) mainly due to the tartrate-centered fluorescence band, which gets of similar intensity compared to the Dy-based signals (see Figures SIII.40–SIII.42 in Appendix III for further details). This impressive rise may be attributed to the loss of O–H oscillators of water molecules in the coordination and outer spheres, which are known to act as efficient quenchers of the luminescence.[69] The second and third transformations that render Dy-L'' (**21**) and Dy-L''' (**22**) phases when heating the sample at 190 and 210 °C, respectively, exhibit an almost immediate rehydration back to Dy-L' (**20**), so their luminescent properties had to be performed directly under vacuum to ensure that rehydration is prevented. Dy-L'' (**21**) and Dy-L''' (**22**) phases exhibit an almost indistinguishable spectrum, dominated by the Dy-centered bands (peaking at λ_{ex} = 482 and 573 nm). The RT spectra collected for Dy-L' (**20**) and Dy-L''' (**22**) phases (after heating them under vacuum to 110 and 210 °C, respectively) are easily distinguished by the position and relative intensity of the tartrate-centered fluorescence band, which is dropped redshift from λ_{em} = 407 nm for Dy-L' (**20**) to 517 nm for Dy-L''' (**22**). All these modifications in the PL, though not too dramatic, could be enough as to employ these MOFs for sensing utilities.

The fact that these compounds are found as enantiomeric pairs makes it possible to study, in addition to the already mentioned magnetic and luminescent properties, certain characteristics

related to chirality such as Circular Dichroism (CD) and Circularly Polarized Luminescence (CPL). The results obtained are presented below.

4.3.5. Chiroptical properties of LnOFs

4.3.5.1. Circular dichroism experiments on hydrated phases

The chiral character of the prepared MOFs prompted us to explore their differential absorption properties of circularly polarized light. CD (and the corresponding UV-vis) spectra were acquired for water suspensions of each pair of enantiomeric MOFs, as well as for the water solutions of L- and D- tartaric acid samples. As observed in Figure 4.13, CD spectra of the MOFs are characterized by two well-defined regions: an intense band centered at 195 nm and a less intense one at 221 nm, with opposite Cotton effects, respectively. Bands at the same wavelengths are of course present in the corresponding UV-Vis spectra and can be assigned to n $\rightarrow \pi^*$ transitions according to TD-DFT calculations (see Appendix III). CD spectra of enantiomeric samples are mirror images, clearly indicating the enantiopurity of the samples. These results are in agreement with those reported by Tushari et al. for compounds Er-L (**13**) and Er-D (**14**).[70] Crucially, CD spectra of water solutions of L- and D-tartaric acids (free ligands) show two bands at 190 and 214 nm which are blue-shifted and inverted (+/- sign) compared to the ones observed for the MOFs samples.

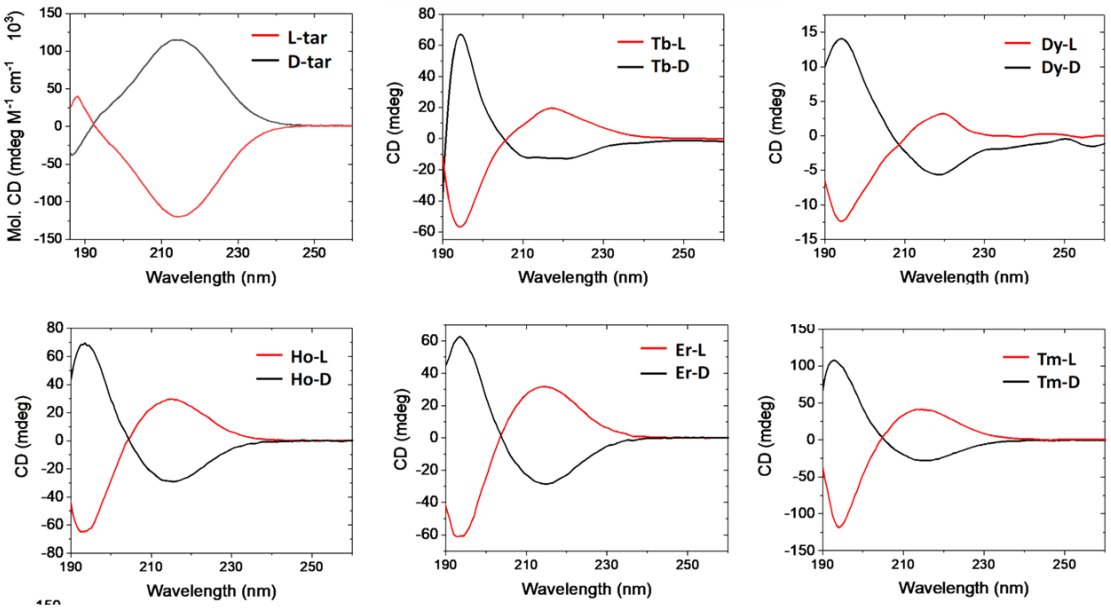

Figure 4.13. CD spectra recorded for all compounds.

Just as the five pairs of MOFs are capable of absorbing polarized light, and certain compounds (Tb-L (**7**) and Dy-L (**9**)) possess luminescent properties, the Circularly polarized luminescence (CPL) experiment described below has been conducted to determine the polarized light emission capacity of these compounds.

4.3.5.1. Circularly polarized luminescence experiments

CPL is a well-known property of lanthanide cations.[71] It comes from magnetic dipole allowed Ln centered *f-f* transitions, usually showing a large degree of circular polarization.[72] In this work, we were able to measure the circularly polarized emission of the Tb-based MOF, resulting, as far as we are aware, in the second example of this chiroptical property in chiral MOF.[34] The CPL spectra centered at the $^7F_5 \leftarrow {}^5D_4$ transition of Tb compounds are plotted in Figure 4.14. In a chiral environment, the degeneration of the sublevels of the band disappears, showing a complex pattern. The complexity derives from the different signs and magnitudes of the rotational strengths of the transitions, a fact that has been extensively reported.[73] In this particular, the spectra reveal the presence of two main bands (centered at 540 and 555 nm) while a third band sited at 560 nm may be also guessed. Interestingly, the two main CPL bands show symmetrically opposed signs with luminescence dissymmetry factor g_{lum} values around $4x10^{-3}$ and $1x10^{-3}$, respectively. This fact precludes the presence of any artefact in our measurements (see also Appendix III). These values are also in agreement with other previously reported data of chiral Tb CPs.[74] Although we could detect the emission of other fluorescent bands with low intensity, their weak chiroptical response avoided to extract reliable data for such bands. CPL experiments run on the rest of the samples did not yield measurable CPL signals.

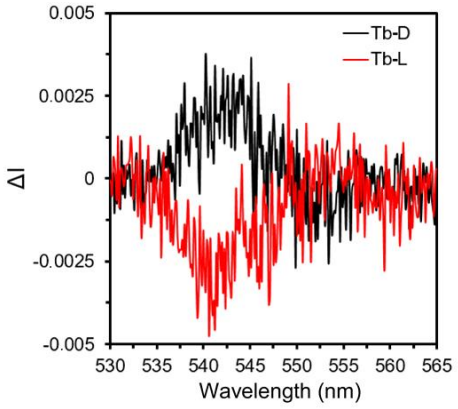

Figure 4.14. CPL spectra for the $^7F_5 \leftarrow {}^5D_4$ transition for Tb-L (**7**) and Tb-D (**8**) compounds.

4.5. References

[1] (a) V. Guillerm, D. Kim, J.F. Eubank, R. Luebke, X. Liu, K. Adil, M.S. Lah, M. Eddaoudi, *Chem. Soc. Rev.*, 2014, **43**, 6141. (b) M. Eddaoudi, D.F. Sava, J.F. Eubank, K. Adil and V. Guillerm, *Chem. Soc. Rev.*, 2015, **44**, 228. (c) M. O'Keeffe and O. M. Yaghi, *Chem. Rev.*, 2012, **112**, 675. (d) D. J. Tranchemontagne, J. L. Mendoza-Cortés and M. O'Keeffe, *Chem. Soc. Rev.*, 2009, **38**, 1257. (e) S. R. Batten, N. R. Champness, X.-M. Chen, J. Garcia-Martinez, S. Kitagawa, L. Öhrström, M. O'Keeffe, M. P. Suh and J. Reedijk, *Pure* Appl*. Chem.*, 2013, **85**, 1715.

[2] (a) M. D. Allendorf and V. Stavila, *CrystEngComm*, 2015, **17**, 229. (b) Y. B. Zhang, H. L. Zhou, R. B. Lin, C. Zhang, J. B. Lin, J. P. Zhang and X. M. Chen, *Nat. Commun.*, 2012, **3**, 642. (c) J. Cepeda, G. Beobide, O. Castillo, A. Luque and S. Pérez-Yáñez, *Coord. Chem. Rev.*, 2017, **352**, 83.

[3] (a) O. K. Farha, I. Eryazici, N. C. Jeong, B. G. Hauser, C. E. Wilmer, A. A. Sarjeant, R. Q. Snurr, S. T. Nguyen, A. O. Yazaydin and J. T. Hupp, *J. Am. Chem. Soc.*, 2012, **134**, 15016–16021. (b) H.-C. J. Zhou and S. Kitagawa, *Chem. Soc. Rev.*, 2014, **43**, 5415–5418. (c) J.-C. Tan and B. Civalleri, *CrystEngComm*, 2015, **17**, 197−198.

[4] (a) P. Horcajada, R. Gref, T. Baati, P. K. Allan, G. Maurin, G. Férey, R. Morris and C. Serre, *Chem. Rev.*, 2012, **112**, 1232. (b) I. Abánades Lázaro and R. S. Forgan, *Coord. Chem. Rev.*, 2019, **380**, 230.

[5] J. Liu, L. Chen, H. Cui, J. Zhang, L. Zhang and C. Y. Su, *Chem. Soc. Rev.*, 2014, **43**, 6011.

[6] (a) J. Cepeda, S. Pérez-Yáñez, G. Beobide, O. Castillo, E. Goikolea, F. Aguesse, L. Garrido, A. Luque and P. A. Wright, *Chem. Mater.*, 2016, **28**, 2519. (b) K. Fujie, R. Ikeda, K. Otsubo, T. Yamada and S. Kitagawa, *Chem. Mater.*, 2015, **27**, 7355.

[7] (a) Y. Inokuma, S. Yoshioka, J. Ariyoshi, T. Arai, Y. Hitora, K. Takada, S. Matsunaga, K. Rissanen and M. Fujita, *Nature*, 2013, **465**, 461. (b) C. Wang, D. Liu and W. Lin, *J. Am. Chem. Soc.*, 2013, **135**, 13222.

[8] (a) K. Binnemans, *Chem. Rev.*, 2009, **109**, 4283. (b) M. D. Allendorf, C. A. Bauer, R. K. Bhaktaa and R. J. T. Houk, *Chem. Soc. Rev.*, 2009, **38**, 1330. (c) G. Minguez Espallargas and E. Coronado, *Chem. Soc. Rev.*, 2018, **47**, 533. (d) M. Murrie, *Chem. Soc. Rev.*, 2010, **39**, 1986. (e) S. Gómez-Coca, D. Aravena, R. Morales and E. Ruiz, *Coord. Chem. Rev.*, 2015, **289**, 379.

[9] (a) R. Vincent, S. Klyatskaya, M. Ruben, W. Wernsdorfer and F. Balestro, *Nature*, 2012, **488**, 357. (b) M. Ganzhorn, S. Klyatskaya, M. Ruben and W. Wernsdorfer, Nat. *Nanotechnol.*, 2013, **8**, 165. (c) M. Prezioso, A. Riminucci, P. Graziosi, I. Bergenti, R. Rakshit, R. Cecchini, A. Vianelli, F. Borgatti, N. Haag, M. Willis, A. J. Drew, W. P. Gillin and V. A. Dediu, *Adv. Mater.*, 2013, **25**, 534. (d) R. Sessoli, M.-E. Boulon, A. Caneschi, M. Mannini, L. Poggini, F. Wilhelm and A. Rogalev, *Nat. Phys.*, 2015, **11**, 69.

[10] (a) E. San Sebastian, A. Rodríguez-Diéguez, J. M. Seco, J. Cepeda, *Eur. J. Inorg. Chem.*, 2018, 2155. (b) C. Murawski, K. Leo, M. C. Gather, *Adv. Mater.* **2013**, *25*, 6801. (c) M. Gutiérrez, C. Martin, K. Kennes, J. Hofkens, M. Van der Auweraer, F. Sánchez and A.Douhal, *Adv. Opt. Mater.*, 2018, **6**, 1870022.

[11] (a) F.-Y. Yi, D. Chen, M.-K. Wu, L. Han and H.-L. Jiang, *ChemPlusChem*, 2016, **81**, 675–690. (b) Z. Hu, B. J. Deibert and J. Li, *Chem. Soc. Rev.*, 2014, **43**, 5815.

[12] (a) N. N. Greenwood and A. Earnshaw, Chemistry of the elements (2nd ed.), Butterworth-Heinemann, 1997, pp. 1230. (b) R. A. Layfield, M. Murugesu (eds), *Lanthanides and Actinides in Molecular Magnetism*, Wiley-VCH, Weinheim, Germany, 2015. (c) B. W. Wang, S. Gao, *The Rare Earth Elements Fundamental and Applications,* D. A. Atwood, John Wiley and sons, 2012.

[13] Neese, F.; Pantazis, D. A. "What is not required to make a single molecule magnet", *Faraday Discuss.* (2011), **148**, 229-238.

[14] Ding, Y. S.; Yu, K. X.; Reta, D.; Ortu, F.; Winpenny, R. E. P.; Zheng, Y. Z.; Chilton, N. F. "Field-and temperature-dependent quantum tunnelling of the magnetisation in a large barrier single-molecule magnet", *Nature communications* (2018), **9**, 1-10.

[15] Ruiz, J.; Mota, A. J.; Rodríguez-Diéguez, A.; Oyarzabal, I.; Seco, J. M.; Colacio, E. "Rational design of ferromagnetic coupled diphenoxocarboxylate triply bridged dinuclear nickel (II) complexes: orbital countercomplementarity of the bridging ligands", *Dalton Transactions* (2012), **41**, 14265-14273.

[16] Piquer, L. R.; Sañudo, E. C. "Heterometallic 3d–4f single-molecule magnets", *Dalton Transactions* (2015), **44**, 8771-8780.

[17] Rinehart, J. D.; Long, J. R. "Exploiting single-ion anisotropy in the design of f-element single-molecule magnets", *Chem. Sci.* (2011), **2**, 2078-2085.

[18] Baldoví, J. J.; Coronado, E.; Gaita-Ariño, A.; Gamer, C.; Giménez-Marqués, M.; Minguez Espallargas, G. "A SIM-MOF: Three-Dimensional Organisation of Single-Ion Magnets with Anion-Exchange Capabilities", *Chemistry–A European Journal* (2014), **20**, 10695-10702.

[19] (a) D. N. Woodruff, R. E. P. Winpenny and R. A. Layfield, *Chem. Rev.*, 2013, **113**, 5110. (b) R. Sessoli and A. K. Powell, *Coord. Chem. Rev.*, 2009, **253**, 2328.

[20] F.-S. Guo, B. M. Day, Y.-C. Chen, M.-L. Tong, A. Mansikkamäki, R. A. Layfield, *Science*, 2018, **362**, 1400.

[21] (a) J. C. G. Bünzli, C. Piguet, *Chem. Soc. Rev*., 2005, **34**, 1048. (b) D. Parker, *Chem. Soc. Rev*., 2004, **33**, 156. (c) J. Heine, K. Müller-Buschbaum, *Chem. Soc. Rev*., 2013, **42**, 9232.

[22] (a) Y.-W. Yip, H. Wen, W.-T. Wong, P. A. Tanner and K.-L. Wong, *Inorg. Chem.*, 2012, **51**, 7013. (b) D. E. Barry, D. F. Caffrey and T. Gunnlaugsson, *Chem. Soc. Rev.*, 2016, **45**, 3244.

[23] J. M. Seco, I. Oyarzabal, S. Pérez-Yáñez, J. Cepeda, A. Rodríguez-Diéguez, *Inorg. Chem*., 2016, **55**, 11230.

[24] Subudhi, S.; Rath, D.; Parida, K. M. "A mechanistic approach towards the photocatalytic organic transformations over functionalised metal organic frameworks: a review", *Catal. Sci. Technol.* (2018), **8**, 679-696.

[25] W. Liu and X. Tang, *Struct. Bond*, 2015, **163**, 29.

[26] (a) B. Kesanli and W. Lin, *Coord. Chem. Rev.*, 2003, **246**, 305. (b) G. Ferey, *Chem. Soc. Rev.*, 2008, **37**, 191. (c) T. Verbiest, S. V. Elshocht, M. Kauranen, L. Hellemans, J. Snauwaert, C. Nuckolls, T. J. Katz and A. Persoons, *Science*, 1998, **282**, 913.

[27] (a) R. Farshchi, M. Ramsteiner, J. Herfort, A. Tahraoui, H. T. Grahn, *Appl. Phys. Lett.*, 2011, **98**, 162508. (b) I. Žutić, J. Fabian and S. Das Sarma, *Rev. Mod. Phys.*, 2004, **76**, 323.

[28] (a) C. Wagenknecht, C.-M. Li, A. Reingruber, X.-H. Bao, A. Goebel, Y.-A. Chen, Q. Zhang, K. Chen, J.-W. Pan, *Nat. Photon.*, 2010, **4**, 549. (b) J. F. Sherson, H. Krauter, R. K. Olsson, B. Julsgaard, K. Hammerer, I. Cirac and E. S. Polzik, *Nature*, 2006, **443**, 557.

[29] C. Wang, H. Fei, Y. Qiu, Y. Yang, Z. Wei, Y. Tian, Y. Chen, Y. Zhao, *Appl. Phys. Lett.*, 1999, **74**, 19.

[30] (a) T. Oka, H. Aoki, *Phys. Rev. B*, 2009, **79**, 081406. (b) Y. H. Wang, H. Steinberg, P. Jarillo-Herrero, N. Gedik, *Science*, 2013, **342**, 453.

[31] Y. Yang, R. C. da Costa, M. J. Fuchter and A. J. Campbell, *Nat. Photonics,* 2013, **7**, 634.

[32] T. Novikova, A. Pierangelo, A. De Martino, A. Benali and P. Validire, *Opt. Photonics News,* 2012, 26.

[33] (a) M. Wakabayashi, S. Yokojima, T. Fukaminato, K.-I. Shiino, M. Irie and S. Nakamura, *J. Phys. Chem. A*, 2014, **118**, 5046. (b) S. Abbate, F. Lebon, G. Longhi, M. Passarello and V. T. Liveri, *Chirality*, 2011, **23**, 910. (c) T. Mori, S. Grimme and Y. Innoue, *J. Org. Chem.*, 2007, **72**, 6998.

[34] S.-M. Chen, L.-M.Chang, X.-K. Yang, T. Luo, H. Xu, Z.-G. Gu, J. Zhang, *ACS Applied Materials & Interfaces*, 2019, **11**, 31421.

[35] (a) R. Carr, N. H. Evans and D. Parker, *Chem. Soc. Rev.*, 2012, **41**, 7673. (b) G. Bozoklu, C. Gateau, D. Imbert, J. Pécaut, K. Robeyns, Y. Filinchuk, F. Memon, G. Muller and M. Mazzanti, *J. Am. Chem. Soc.*, 2012, **134**, 8372.

[36] (a) L. H. G. Kalinke, C. Cangussu, M. Mon, R. Bruno, E. Tiburcio, F. Lloret, D. Armentano, E.Pardo and J. Ferrando-Soria, *Inorg. Chem.*, 2019, **58**, 14498. (b) Y. Guo, L. Zhang, N. Muhammad, Y. Xu, Y. Zhou,F. Tang and S. Yang, *Inorg. Chem.*, 2018, **57**, 995.

[37] E. Coronado, J. R. Galán-Mascarós, C. J. Gómez-García and A. Murcia-Martínez, *Chem.–Eur. J.*, 2006, **12**, 3484.

[38] (a) P. Yan, J. Xing, G. Li, W. Sun, J. Zhang and G. Hou, *J. Coord. Chem.*, 2009, **62**, 2095. While these (Yan et al.**[38]** and Thushari et al.[70]) described previously the structural properties of D enantiomers only for the Tb(III) and Dy(III) based MOFs, we herein provide a complete structural description (see SI) of 3D arrangement of both D- and L-enantiomers for all compounds (Tb-Tm).

[39] A. Earnshaw, *Introduction to Magnetochemistry*; Academic Press: London, 1968.

[40] M. J. Frisch, G. W. Trucks, H. B. Schlegel, G. E. Scuseria, M. A. Robb, J. R. Cheeseman, G. Scalmani, V. Barone, B. Mennucci, G. A. Petersson, H. Nakatsuji, M. Caricato, X. Li, H. P. Hratchian, A. F. Izmaylov, J. Bloino, G. Zheng, J. L. Sonnenberg, M. Hada, M. Ehara, K. Toyota, R. Fukuda, J. Hasegawa, M. Ishida, T. Nakajima, Y. Honda, O. Kitao, H. Nakai, T. Vreven, J. A. Montgomery Jr., J. E. Peralta, F. Ogliaro, M. Bearpark, J. J. Heyd, E. Brothers, K. N. Kudin, V. N. Staroverov, R. Kobayashi, J. Normand, K. Raghavachari,

A. Rendell, J. C. Burant, S. S. Iyengar, J. Tomasi, M. Cossi, N. Rega, J. M. Millam, M. Klene, J. E. Knox, J. B. Cross, V. Bakken, C. Adamo, J. Jaramillo, R. Gomperts, R. E. Stratmann, O. Yazyev, A. J. Austin, R. Cammi, C. Pomelli, J. W. Ochterski, R. L. Martin, K. Morokuma, V. G. Zakrzewski, G. A. Voth, P. Salvador, J. J. Dannenberg, S. Dapprich, A. D. Daniels, O. Farkas, J. B. Foresman, J. V. Ortiz, J. Cioslowski and D. J. Fox, Gaussian 09, revision A.02, Gaussian, Inc., Wallingford, CT, 2009.

[41] (a) A. D. Becke, *J.* Chem. *Phys.*, 1993, **98**, 5648. (b) B. Miehlich, A. Savin, H. Stoll and H. Preuss, *Chem. Phys. Lett.*, 1989, **157**, 200. (c) C. Lee, W. Yang, R. G. Parr, *Phys. Rev. B*, 1988, **37**, 785.

[42] (a) V. A. Rassolov, M. A. Ratner, J. A. Pople, P. C. Redfern, L. A. Curtiss, *J. Comput. Chem.*, 2001, **22**, 976. (b) M. M. Francl, W. J. Pietro, W. J. Hehre, J. S. Binkley, D. J. DeFrees, J. A. Pople and M. S. Gordon, *J. Chem. Phys.*, 1982, **77**, 3654. (c) P. C. Hariharan and J. A. Pople, *Mol. Phys.*, 1974, **27**, 209.

[43] *GaussView, Version 5, R. Dennington, T. Keith and J. Millam, Semichem Inc., Shawnee Mission: KS, 2009.*

[44] (a) E. Ruiz, A. Rodríguez-Fortea, J. Cano, S. Álvarez and P. Alemany, *J. Comput. Chem.*, 2003, **24**, 982. (b) E. Rudberg, P. Salek, Z. Rinkevicius and H. Agren, *J. Chem. Theory Comput.*, 2006, **2**, 981.

[45] (a) P. J. Hay and W. R. Wadt, *J. Chem. Phys.*, 1985, **82**, 270. (b) W. R. Wadt and P. J. Hay, *J. Chem. Phys.*, 1985, **82**, 284. (c) P. J. Hay and W. R. Wadt, *J. Chem. Phys.*, 1985, **82**, 299.

[46] (a) Shannon, R. D. *Acta Crystallogr.*, 1976, **A32**, 751. (b) E. A. Quadrelli, *Inorg. Chem.*, 2002, **41**, 167.

[47] M. Llunell, D. Casanova, J. Cirera, J. M. Bofill, P. Alemany, S. Alvarez, M. Pinsky, D. Avnir, SHAPE v1.1b, Barcelona (Spain), 2005.

[48] (a) TOPOS: http://www.topos.ssu.samara.ru. (b) V. A. Blatov, M. O'Keeffe and D. M. Proserpio, *CrystEngComm*, 2010, **12**, 44. (c) V. A. Blatov, A. P. Shevchenko and D. M. Proserpio, *Cryst. Growth Des.*, 2014, **14**, 3576.

[49] A. L. Spek, *Acta Cryst.*, 2009, **D65**, 148.

[50] (a) L. Sorace, C. Benelli and D. Gatteschi, *Chem. Soc. Rev.*, 2011, **40**, 3092. (b) P. Díaz-Gallifa, O. Fabelo, J. Pasán, L. Cañadillas-Delgado, F. Lloret, M. Julve and C. Ruiz-Pérez, *Inorg. Chem.* **2014**, *53*, 6299.

[51] (a) D. Aguilà, L. A. Barrios, V. Velasco, L. Arnedo, N. Aliaga-Alcalde, M. Menelaou, S. J. Teat, O. Roubeau, F. Luis and G. Aromí, *Chem.–Eur. J.* **2013**, *19*, 5881. (b) N. W. Waggoner, B. Saccoccia, I. A. Ibarra, V. M. Lynch, P. T. Wood and S. M. Humphrey, *Inorg. Chem.* **2014**, *53*, 12674.

[52] J. Cepeda, R. Balda, G. Beobide, O. Castillo, J. Fernández, A. Luque, S. Pérez-Yáñez, P. Román and D. Vallejo-Sánchez, *Inorg. Chem.*, 2011, **50**, 8437.

[53] (a) L. Cañadillas-Delgado, T. Martín, O. Fabelo, J. Pasán, F. S. Delgado, F. Lloret, M. Julve, C. Ruiz-Pérez, *Chem.–Eur. J.*, 2010, **16**, 4037. (b) L. Cañadillas-Delgado, O. Fabelo, J. Pasán, F. S. Delgado, F. Lloret, M. Julve, C. Ruiz-Pérez, *Dalton Trans.*, 2010, 7286.

[54] J. Ruiz, A.J. Mota, A. Rodríguez-Diéguez, S. Titos, J.M. Herrera, E. Ruiz, E. Cremades, J.P. Costes, E. Colacio, *Chem. Commun.*, 2012, **48**, 7916.

[55] N. Ishikawa, M. Sugita, T. Ishikawa, S.-y Koshihara, Y. Kaizu, *J. Am. Chem. Soc*., 2003, **125**, 8694.

[56] (a) F.-S. Guo, B. M. Day, Y.-C. Chen, M. Liang-Tong, A. Mansikkamäki, R. A. Layfield, *Angew. Chem. Int. Ed*., 2017, **56**, 11445. (b) C. A. P. Goodwin, F. Ortu, D. Reta, N. F. Chilton, D. P. Mills, *Nature*, 2017, **548**, 439. (c) S.-D. Jiang, B.-W. Wang, H.-L Sun, Z.-M. Wang, S. Gao, *J. Am. Chem. Soc*., 2011, **133**, 4730. (d) Y.-S. Ding, T. Han, Y.-Q. Zhai, D. Reta, N. F. Chilton, R. E. Winpenny, Y.-Z. Zheng, *Chem.-Eur. J*., 10.1002/chem.202000646

[57] P. Antal, B. Drahoš, R. Herchel, Z. Trávníček, *Dalton Trans*., 2016, **45**, 15114.

[58] A. Singh, K. N. Shrivastava, *Phys. Status Solidi*, 1979, **95**, 273.

[59] P. L. Scott and C. D. Jeffries, *Phys. Rev.*, 1962, **127**, 32.

[60] N. F. Chilton, CCFIT program, The Chilton Group, Manchester, U.K., 2014, http://www.nfchilton.com/software.html.

[61] (a) R. C. Evans, P. Douglas, C. J. Winscom, *Coord. Chem. Rev.,* 2006, **250**, 2093. (b) Q. -D. Liu, R. Wang, S. Wang, *Dalton Trans.*, 2004, 2073. (c) J. Rocha, C. D. S. Brites, L. D. Carlos, *Chem. Eur. J.*, 2016, **22**, 14782.

[62] (a) K. Binnemans, *Chem. Rev.*, 2009, **109**, 4283. (b) J. C. G. Bünzli, *Coord. Chem. Rev.*, 2015, **293-294**, 19.

[63] (a) B. C. Jamalaiah and Y. R. Babu, *Mat. Chem. Phys.*, 2018, **211**, 181. (b) Z. Y. Mao, Y. C. Zhu, L. Gan, Y. Zeng, F. F. Xu, Y. Wang, H. Tian, J. Li and D. J. Wang, *J. Lumin.*, 2013, **134**, 148. (c) B. Y. Huang, B. L. Feng, L. Luo, C. L. Han, Y. T. He and Z. R. Qiu, *Mater. Sci. Eng. B,* 2016, **212**, 71.

[64] W. M. Yen, S. Shionoya, H. Yamamoto, in Phosphor Handbook, CRC Press, Athens, 2007.

[65] (a) E. Echenique-Errandonea, I. Oyarzabal, J. Cepeda, E. San Sebastian, A. Rodríguez-Diéguez, J. M. Seco, *New J. Chem.*, 2017, **41**, 5467. (b) S. Biju, N. Gopakumar, J.-C. G. Bunzli, R. Scopelliti, H. K. Kim, M. L. P. Reddy, *Inorg. Chem*., 2013, **52**, 8750.

[66] M. Latva, H. Takalo, V. M. Mukkala, C. Matachescu, J. C. Rodriguez-Ubis, J. Kanakare, *J. Lumin.*, 1997, **75**, 149.

[67] (a) P. C. R. Soares-Santos, L. Cunha-Silva, F. A. Almeida-Paz, R. A. S. Ferreira, J. Rocha, L. D. Carlos, H. I. S. Nogueira, *Inorg. Chem.*, 2010, **49**, 3428. (b) J. Cepeda, S. Pérez-Yáñez, G. Beobide, O. Castillo, J. A. García, M. Lanchas, A. Luque, *Dalton Trans.*, 2015, **44**, 6972. (c) A. de Bettencourt-Dias, P. S. Barber, S. Viswanathan, D. T. de Lill, A. Rollett, G. Ling, S. Altun, *Inorg. Chem.*, 2010, **49**, 8848.

[68] Phosphor Handbook, ed. W. M. Yen, S. Shionoya, H. Yamamoto, CRC Press, Boca Raton, 2007.

[69] A. Beeby, I. M. Clarkson, R. S. Dickins, S. Faulkner, D. Parker, L. Royle, A. S. de Sousa, J. A. Gareth Williams and M. Woods, *J. Chem. Soc. Perkin Trans.*, 1999, **2**, 493.

[70] S. Thushari, J. A. K. Cha, H. H.-Y. Sung, S. S.-Y. Chui, A. L.-F. Leung, Y.-F. Yen and I. D. Williams, *Chem. Commun*., 2005, 5515.

[71] F. Zinna, and L. Di Bari, *Chirality*, 2015, **27**, 1.

[72] C. K. Luk and F. S. Richardson, *J. Am. Chem. Soc*., 1975**, 97**, 6666.

[73] (a) C. K. Luk and F. S. Richardson, *Chem Phys. Lett.*, 1974, **25**, 215. (b) M. Seitz, E. G. Moore, A. J. Ingram, G. Muller and K. N. Raymond, *J. Am. Chem. Soc.*, 2007, **129**, 15468. (c) A. P. S. Samuel, J. L. Lunkley, G. Muller and K. N. Raymond, *Eur. J. Inorg. Chem.*, 2010, 3343. (d) L. VandenElzen and T. A. Hopkins, *ACS Sustainable Chem. Eng.*, 2019, **7**, 16690.

[74] (a) M. Seitz, K. Do, A. J. Ingram, E. G. Moore, G. Muller and K. N. Raymond, *Inorg. Chem.*, 2009, **48**, 8469.

Chapter 5

Chiral Metal-Organic Framework with CISS Effect as Ideal Long-Range Spin Filtering Material

5.1. Introduction

The spin of an electron is, along with its charge, one of its two basic intrinsic properties. From a non-relativistic point of view, the spin of the electron is described as the property of the electron to rotate on an imaginary axis that crosses it. In the classical world, this is expressed as an electron rotating clockwise (CW) or counterclockwise (CCW). As it is an electrically charged and rotating body, it has an associated angular magnetic moment, called the spin magnetic moment (μ_s).[1]

In the quantum mechanical world, the projection of the spin angular momentum of an electron measured in a particular direction determined by an external magnetic field (B) can only result in the $\bar{h}/2$ or $-\bar{h}/2$ values, which, translated into the classical world, means that the spin magnetic moment can take two directions: spin up (1/2) or spin down (-1/2) (Figure 5.1). In absence of an external magnetic field, these two states are degenerate, that is, both states have the same energy; while, in the presence of magnetic interactions, this degeneration disappears, and the spin states split.[2]

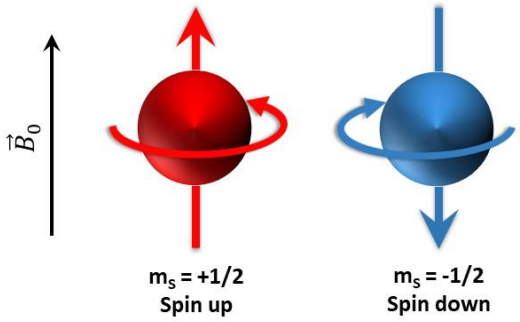

Figure 5.1. Two electrons in the presence of an external magnetic field ($\vec{B}_0$), rotating CCW (spin +1/2) and CW (spin -1/2) on an imaginary axis that cross them.

Thus, in an ordinary electric field, the electrons' spin is oriented arbitrarily without their orientation influencing the electric current generating a "non-polarized electronic current" (NPEC). However, in a spintronic field, the situation is quite different since the electron spins will be of a single type (up or down) of the two possible, that is, the electric field is constituted by a "spin-polarized electron current" (SPEC). Spin-polarized currents have a large part of their electrons with a defined spin state; therefore, in order to generate a polarized current, an electronic current must cross a material capable of acting as a spin filter (Figure 5.2), letting the electrons with "suitable" or "preferred" spin travel through the material, and scattering back or blocking electrons with the "non-suitable" or "non-preferred" spin.[3] The first reference to the

phenomenon of these types of currents and the field that studies them, called spintronics,[4] is from scarcely 30 years ago, and although the number and type of applications based on spin currents has increased exponentially since then, the variety in the type of materials capable of generating spintronic currents is alarmingly scarce.[5]

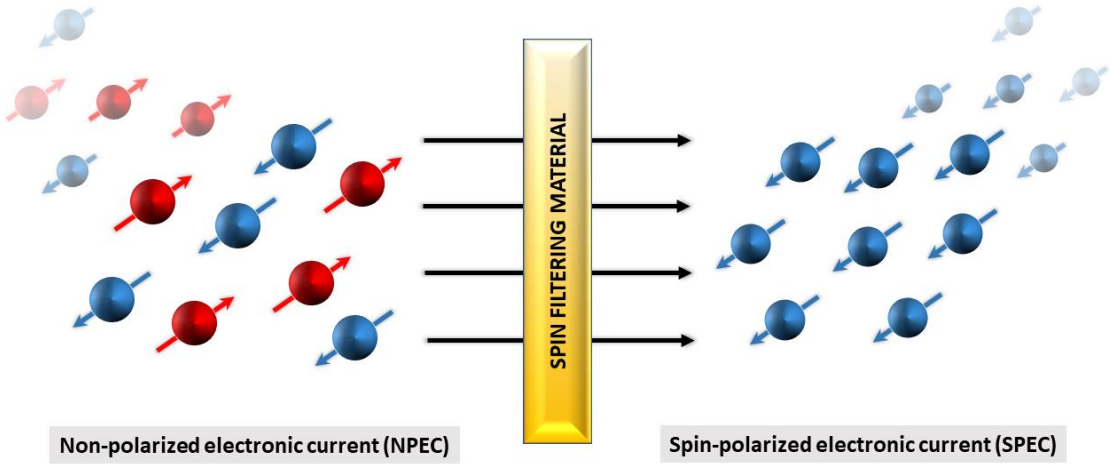

Figure 5.2. Schematic illustration of the generation of a spin-polarized electronic current.

The generation of spin currents was mainly limited to magnetically active materials and spin-active interfaces[6] until the discovery of the Chiral Induced Spin Selectivity (CISS) effect in 2012.[7] Although the special electrical and magnetic properties of chiral molecules are now well known, until 1999 the effect of their chirality on electron transmission had gone unnoticed. This fact opened the way to the study of new spin filters based on a phenomenon that, as indicated, years later would be described as the CISS effect.[8]

In nature, most of the processes based on electron transfer occur in saturated chiral proteins rather than in systems which, *a priori*, may have much better conductive properties, such as conjugated molecules or metals. This fact suggests that the answer to this natural choice lies in the efficiency of electron transport. The delocalization of the charges in the conjugated systems, and the electron scattering that occurs in metals, cause the electrons to circulate through the material in random directions, in addition to the collisions between charges that cause the loss of energy as heat. In the case of chiral systems, electrons "feel" as if an external magnetic field is acting on their spin, favouring the circulation of the "appropriate" spin and blocking the one that is not. This type of spin selection occurs in biological systems and, besides allowing the charge transport over long distances and in one direction by minimizing electron scattering, the efficiency of the process increases considerably and heat radiation by energy loss, which could damage the surrounding tissues, is avoided.[9]

The discovery and understanding of the CISS effect has been a great advance in the field of spin filters, although it is important to understand the theoretical basis and operation of this phenomenon in order to better understand the CISS effect and design new materials. The basics of this phenomenon, still in its infancy, is explained below.

5.1.1. Understanding the CISS effect

The CISS effect refers to the ability of chiral molecules to transfer electrons with one preferential spin orientation over the other; therefore, chirality is an indispensable requirement for a molecule to act as a spin filter based on CISS effect. In addition, helical structures help to improve this effect, as will be detailed in the paragraphs below.[10] Actually, the CISS effect could be renamed as HISS effect, from Helicity Induced Spin Selectivity.

When an electron passes through a chiral molecule, which has a chiral electrostatic potential due to its structure, a magnetic field $\vec{B}$ is generated, which is described by Equation *(5.1)*:

$$\vec{B} = \frac{\vec{v}}{c^2}\, x\, \vec{E}_{chiral} \qquad (5.1)$$

where $\vec{v}$ is the speed of the moving electron, c is the speed of light and $\vec{E}_{chiral}$ is the electrostatic field generated from the electrons and nuclei of the chiral molecule.It is worth noting that the $\vec{E}_{chiral}$ field maintains the property of chirality because its direction changes according to the direction of the electric current and the stereochemistry of the molecule. In the case of helical chiral molecules, which are constructed from atoms arranged in spirals, the direction of the spiral has a great influence on certain physical properties of a material.[7a] Spirals that turn clockwise generate a right-handed helical structure, while counterclockwise spirals give left-handed helical structures, and, according to Physic's laws, the direction of the $\vec{E}_{chiral}$ generated by the flow of an electric current through the material will be aligned parallel or antiparallel depending on the sense of the helix. Furthermore, the fact that $\vec{E}_{chiral}$ is a directional vector means that it can act as a dipole field, which can accumulate a positive partial charge (q^+) at one end of the helix and a negative partial charge (q^-) at the other end.[11] Figure 5.3 is a schematic illustration of this physical description of helical chiral molecules.

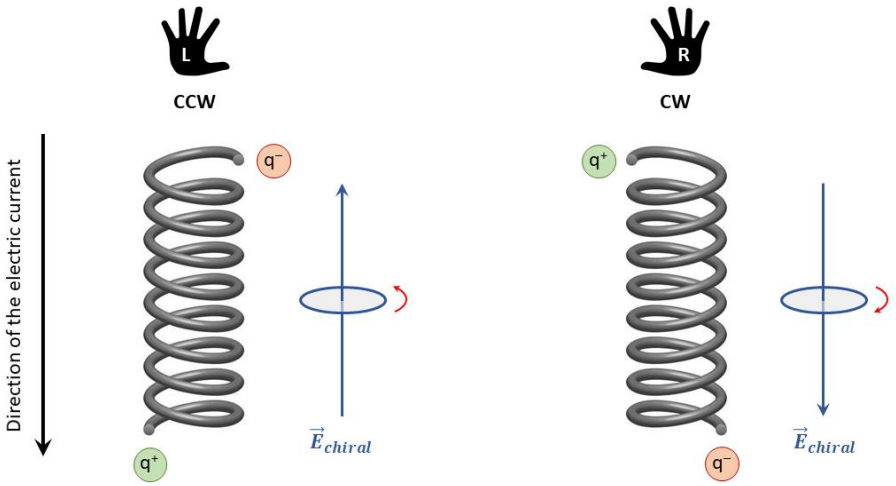

Figure 5.3. Scheme of the $\vec{E}_{chiral}$ formation according to the sense of each helix in a particular direction of the electron current.

As indicated by Equation *(5.1)*, due to the movement of charges through the helical molecule, the magnetic field $\vec{B}$ is generated, breaking the degenerated state of both types of spin and causing their splitting. In this context, $\vec{E}_{chiral}$ interacts with electrons according to their spin and interferes on the charge transport process: electrons with the spin aligned in parallel to $\vec{E}_{chiral}$ can cross the helix, while electrons with antiparallel spin are blocked. In this way, SPECs can be obtained through chiral molecules with 100 % efficiency. It is important to emphasize that, as shown in Figure 5.4, $\vec{E}_{chiral}$ depends on the direction of the electric current; therefore, the effect of spin choice changes according to the sense of the helix and the direction of the current.

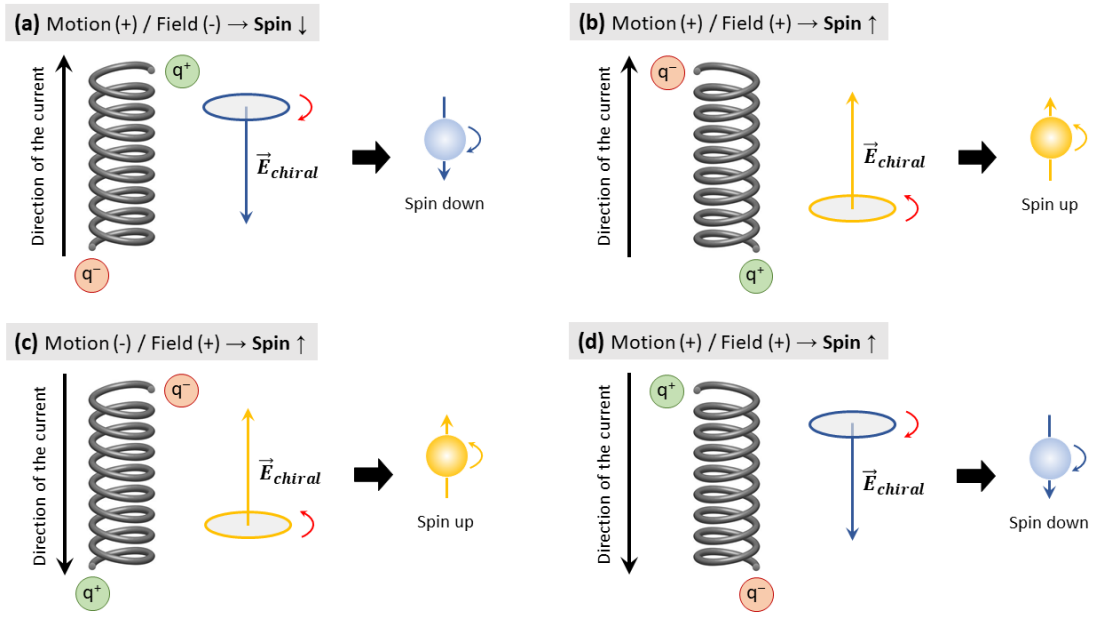

Figure 5.4. Simplified description of the four possible scenarios for the spin-polarization of a current with an electron moving within a chiral potential. The spin alignment flips with the handedness of the helix.

It is important to note that Figure 5.4 refers to chiral molecules being electronic spin filters, which is actually only a simplified explanation of the CISS effect phenomenom adopted for the shake of using the same terminology used in the literature. Actually, due to the model discussed by Aragonés et al.,[12] chiral molecules are considered helicity filters, rather than spin filters, since the helicity is defined as the projection of the spin, +/-, in the direction of electron propagation, k, which indicates that there are two states of positive helicity, labeled {|k,+>, |-k,+>}, and two states of negative helicity, {|k,->, |-k,->} (Figure 5.5). According to this model, each enantiomer ideally filters one of the two helicity components, depending on two experimental control variables: (1) the sign of the bias voltage, which determines the direction of the electron current, and (2) the spin of the electrons. This gives a total of four possible experiments for each enantiomer.

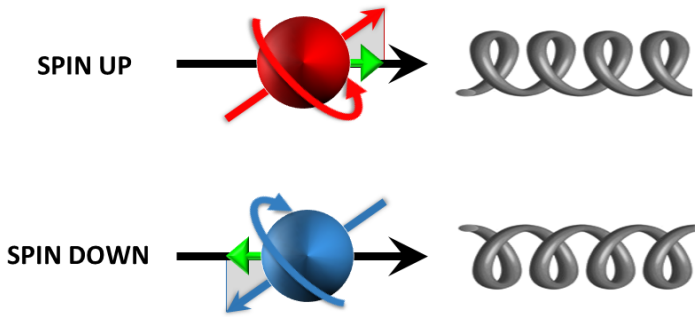

Figure 5.5. Definition of the helicity as the projection of the spin.

The CISS effect can be enhanced with an enhanced spin-orbit coupling (SOC) in the system, which involves the coupling between the magnetic moment associated with the spin and the linear moment of the electron by the interaction with electrostatic potential. Although the SOC is of very low intensity, in the presence of an electrostatic dipole field (as the one presented by the helical structures) it becomes important and can generate interactions with the spin of the moving electrons.[7a]

SOC value of each atomic element changes according to its atomic number (*Z*), but in the case of secondary structures such as helix, depending on their composition, the SOC value can be increased considerably. So, the SOC of these molecules will be considerable due to the sum of the different elements that can compose the structure. When electrons are introduced into a helix with a dipole field, both linear moment and spin are aligned with the $\vec{E}_{chiral}$ field due to the SOC influence, facilitating the transmission of electrons with the spin parallel to the field and avoiding the dispersion which would generate energy losses (and consequently efficiency losses) in the form of heat (Figure 5.6). This means that, depending on the direction of movement and

the direction of the helix, the stabilisation of one of the spines occurs through the SOC energy.[7a,13]

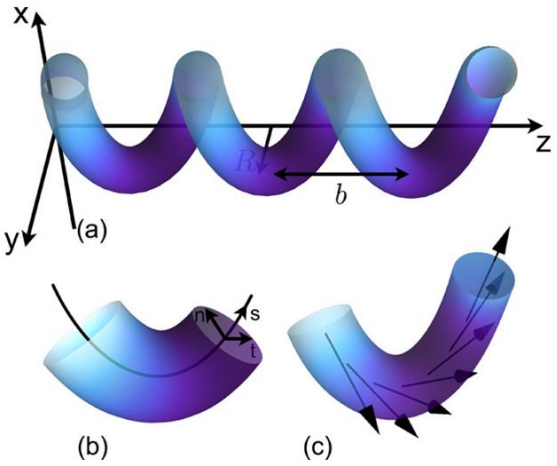

Figure 5.6. Helix-shaped tube and the corresponding coordinate system. **(a)** Electrons are confined within a helical tube of radius *R* and pitch *b*. **(b)** Helical coordinate system is defined by the position along the spiral axis *s* as well as *n* and *t* that span the perpendicular plane. **(c)** Spin-orbit coupling acts as an effective Zeeman field rotating as a function of position along the helix.[13]

According to these basic principles, in recent years different types of organic molecules capable of acting as spin filters have been studied, as well as establishing the basis for the design of new and more effective spin filters. The following section reviews the few materials with which the CISS effect has been studied.

5.1.2. Chiral materials with CISS effect

The spin polarization (SP) power of the former type of materials, such as transition metal ferromagnets and their alloys, is only moderate (up to 45%);[14] and alternative materials have been proposed as promising spin filters with varying performance.[15,16] Alternatively, after the discovery of the CISS effect in 2012,[7] it is now well established that chiral molecules can work as efficient filters[17,18,19,20] for electron spin, transmitting preferentially one spin component over the other in processes involving electron transfer, electron transport, and electron transmission. Such is the case of self-assembled chiral monolayers composed of helical DNA,[21,22,23] oligopeptides,[24,25] helicenes[26] and cysteine-capped-CdSe chiral quantum dots.[27] These non-magnetic chiral materials are being implemented in CISS-based spin devices[28,29,30,31] since they can show large room-temperature magnetoresistance. The SP power of such diamagnetic chiral conductive (bio)molecules has been measured using distinct types of experimental set-ups, which are usually designed to measure the differential current intensity transmitted through a

chiral system when either the direction of magnetization is reversed or, alternatively, when a polarized electron current flowing in one particular direction is injected through two enantiomers of the same system. Different enantiomers of the same chiral system have been reported to transmit preferentially one electron spin component over the other, with SP values ranging from 5 to up to 85%.[32] In the field of inorganic materials, a 2D lead-iodide based perovskite has recently been proven to transmit one preferred electronic spin over the other, to yield temperature-independent SP values as high as ca. 85%.[33]

In order to comply with milestone 2.4) related to the second main goal of this dissertation (see page X of Chapter 1), Chapter 5 reports on the performance of a 3D metal-organic framework (MOF) as a spin filtering material. MOFs are well-known potentially porous materials that have been intensely studied during the last decades for their unlimited and versatile structural architectures derived from their modular constituents: metal ions or clusters and organic ligands.[34,35] MOFs can inherit the properties of both components, *e.g.* metal and ligands, and benefit from their interplay to optimize their performance in applications in different fields.[36,37,38] In this regard, the use of MOFs in spintronic devices and as electrical conductors are two emerging fields that, though still in their infancy, offer the opportunity to develop materials with outstanding properties compared to their inorganic analogues. In addition to very large SP power, these examples exhibit a striking long-distance spin polarized charge transport that is measurable over ranges larger than 1 µm (see Appendix IV). In this regard, the results are equivalent to those obtained by Bullard et al.[39] for low resistance molecular wires.

Bearing those ideas in mind, the Dy-L (**9**) compound has been selected,[40] which consists of enantiomerically pure 3D microporous, water-insoluble, thermally stable, (chiro)luminescent and paramagnetic MOF, as described in Chapter 4. Interestingly, the CISS effect of this type of materials has been recently described[41] on a diamagnetic homologue, the Y(III) based isostructural enantiomeric pair (Y-L and Y-D). As described in that work, the CISS effect also provokes an enantiospecific Nuclear Magnetic Resonance (NMR) response under the conditions of a cross-polarization (CP) experiment. Briefly, ^{13}C intensity signals were consistently more intense for the D-enantiomer than for the L-enantiomer under such experimental conditions, an interesting phenomenon arising from changes of the nuclear spin relaxation times due to the electron spin spatial asymmetry induced by chemical bond polarization involving a chiral center. These experiments put forward on firm grounds that the CISS effect, which induces an asymmetric chemical bond polarization for the two spin channels in the J-coupling tensor, is the mechanism responsible for the enantiospecific response. The CISS effect inherent to this family of straightforwardly synthesized (and low-cost) MOFs is herein explored in the charge transport

scenario of producing spin polarization when a spin-polarized current is flown across this material. In particular, Dy-L (**9**) is here shown to be a semi-conductive MOF, in line with some lately described MOFs referred to as low band-gap materials,[42] and is also proved to display the limiting largest SP power reported so far, with an actual value of 100% (within the experimental uncertainty) at any applied bias in the ±12 V range. Dy-L (**9**) could be therefore considered as an ideal spin filter both in terms of stability and performance. The multidimensional character of the helicity of the MOF, in which the helices (chiral motifs) propagate in different crystallographic directions, may promote a multichannel electron transmission through the materials. This fact, together with the large spin-orbit coupling (SOC) of the lanthanide Dy(III) centers, which enhances the CISS effect, are likely to be responsible for the strikingly high SP values obtained.[17] The latter results were obtained by means of magnetically polarized conductive atomic force microscopy (CM-AFM) experiments designed to measure electron transmission through single crystals of Dy-L (**9**) deposited on indium tin oxide (ITO) substrates. By reversing the magnetic polarization of the injected electron spins, the limiting SP behaviour of Dy-L (**9**) was characterized.

5.2. Materials and methods

5.2.1. Studied compound

Table 5.1. Synthesized compounds.[a]

Formula	Compound	Code
$\{[Dy_2(\mu_4\text{-L-tart})_2(\mu\text{-L-tart})(H_2O)_2]\cdot 4H_2O\}_n$	Poly{[bis(mu4-L-tartrate-kO:k^{2}O',O'':k^{2}O''',O'''':kO''''')(mu-L-tartrate-k^{2}O,O':k^{2}O'',O''')diaquadidysprosium(III)]tetrahydrate}	**Dy-L (9)**

[a] L-tart = L-tartrate = $C_4H_4O_6^{2-}$

5.2.2. AFM and C-AFM measurements

Deposition of Dy-L single crystals on ITO substrate. Indium tin oxide (ITO) coated glass slides with surface resistivity 8-12 Ω/sq were purchased from Sigma Aldrich and used as substrate. The deposition of the MOF single crystals on the ITO substrates was carried out by drop-casting of water suspensions of the MOF (0.1 mg/mL). Subsequently, after complete solvent evaporation, the coating was characterized by atomic force microscopy (AFM).

Atomic force microscopy (AFM) operating in tapping mode was used to determine the morphology of Dy-L (**9**) single crystals coated on ITO substrate. The measurement was carried out at room temperature by ICON (Bruker) equipped with Nanoscope V controller using a TESP-

V2 tip (nominal tip radius 10 nm, cantilever thickness between 3.25-4.75 µm, resonance frequency of ~320 Hz and spring constant of ~42 N/m).

Conductive atomic force microscopy (C-AFM). The C-AFM was performed employing PeakForce TUNA mode using ICON (Bruker) equipped Nanoscope V as controller. The measurements were done with a MESP tip cover with Co/Cr (nominal tip radius 35 nm, cantilever thickness 2.75 µm, resonance frequency of ~72 Hz and spring constant of ~3 N/m) recommended for magnetic property investigations. As ensure by supplier, the MESP has a medium nominal coercivity of 400 Oe and a medium magnetic moment of 1e-13 EMU. To prepare the samples for C-AFM analysis silver paint was used to ensure conductive contact between AFM chuck and investigated MOFs.

The current-voltage (I/V) curves were collected in PeakForce spectroscopy mode. For each magnetization experiments, south and north orientation field, the MESP tip was kept 2 min before measurement. At least 50 I/V curves were recorded for non-magnetized, south-magnetized and north-magnetized MESP tip in different places of different Dy-L (**9**) single crystals (see Appendix IV). The I/V curves were acquired by ramping voltage back and forth in the range from -10 to +10 V.

5.3. Results and discussion

5.3.1. Morphological characterization of Dy-L (9)

As detailed in Chapter 4 of this work, the MOF family to which Dy-L (**9**) belongs crystallize in the non-enantiogenic triclinic *P1* space group and consist of a 3D open framework tailored by the coordination of tartrate ligands to Dy(III) atoms through two distinct coordination modes, which leaves microchannels filled by crystallization water molecules. Since the CISS effect is enhanced by electron propagation through extended helical paths,[21,22,23] the structural description provided in the following lines will mainly focus on such secondary structural motifs found in the reported materials. In this sense, Figure 5.7 shows the views of the crystal packing of Dy-L (**9**) through the crystallographic *a*, *b* and *c* axes, in which a helicoidal motif established by the sequential coordination of the bis-chelating tartrate ligand (with the κ^2O,O':κ^2O'',O''' pattern). This particular helix extends along the [010] direction, and crystallographically more complex helixes are also packed along the 3D building of the material, so that the crystal could be viewed as a highly anisotropic multi-helical system in which properties could depend on the direction analyzed.

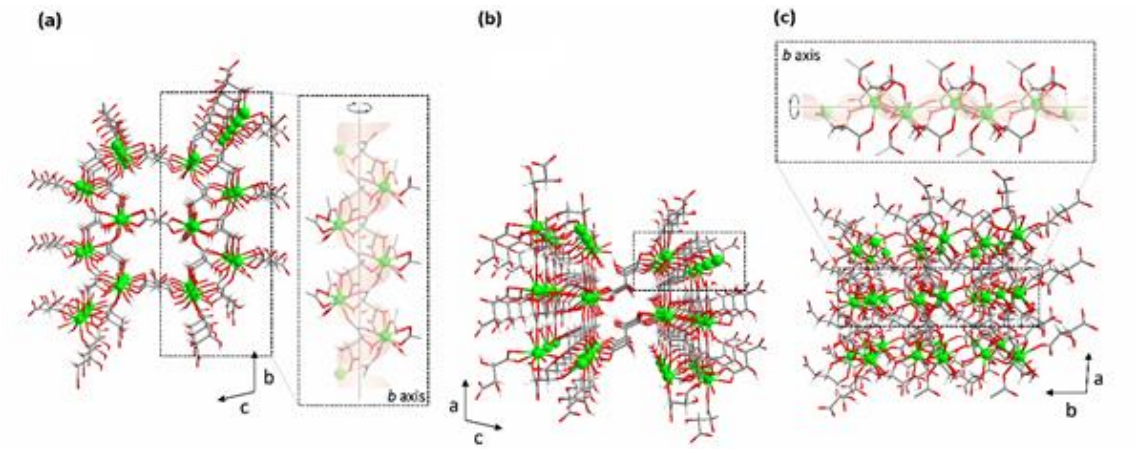

Figure 5.7. Perspective views of Dy-L (**9**) thought crystallographic axes **(a)** *a*, **(b)** *b* and **(c)** *c*, respectively, and the identified secondary structure helicoidal motives.

In view of the above mentioned helicity, that unfolds spatially in different directions, and based on previous reports[26] showing that spin selectivity depends on helicity and the number of chiral paths, and can be enhanced through multiple tunneling process, we expect a similar mechanism to occur in the MOFs described herein.

5.3.2. Morphological characterization of Dy-L (9) by atomic force microscopy (AFM)

The morphology and dimension of the single crystals of Dy-L (**9**) drop casted on ITO substrate were studied by AFM (Figure 5.8). According to the indexation of the crystal faces, based on the X-ray single-crystal diffraction data collection on Dy-L (**9**),[40] and the detailed analysis of AFM results, the uniform morphology of the single crystals was confirmed. Aided by the face indexation on the single crystal exposed X-rays, it could be unequivocally determined that single crystals are preferentially oriented through the crystallographic *c* axis, while they lie on *ab* plane, which stands parallel to the substrate surface (see Figure 5.8). Moreover, this disposition as well as crystal homogeneity was confirmed by AFM-height profiles of multiple single crystals (see Appendix IV). This could be the underlying explanation to the apparent lack of anisotropy of spin polarization. However, this does not necessarily imply that under some other orientation conditions the phenomenon could become anisotropic.

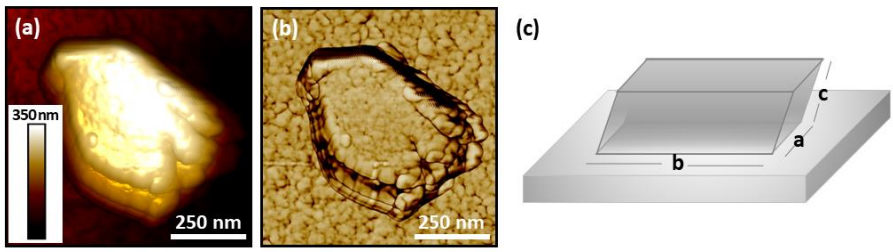

Figure 5.8. AFM images **(a)** height and **(b)** phase of Dy-L **(9)** single crystal deposited on the ITO substrate, and **(c)** representation of the most probable orientation of the single crystals on the ITO substrate.

5.3.3. Charge transport and optical activity measurements

Typical circular dichroism (CD) spectra of Dy-L **(9)**, showing the enantiopurity of the samples, were reported previously[40] and reproduced in the Chapter 4 of this manuscript. Briefly, CD spectra showed two high-energy CD signals (at 190 and 214 nm) arising from the induced optical activity of the ligand within the inorganic framework. In addition, diffuse reflectance experiments acquired on a pressed pellet of single crystals of the compounds in the 200-900 nm range (see Appendix IV) revealed that Dy-L (**9**) is a low band-gap material (< 1.53 eV).

For charge transport measurements, current-voltage (I-V) characteristics were measured at room temperature for Dy-L (**9**), using the set-up shown in Figure 5.9a, where a current of non-polarized electrons was injected via a non-magnetized (H=0) conducting Co/Cr tip (Tip_0). An electric bias potential was applied between the AFM tip and the ITO substrate, and the resulting current indicated electron transport from the tip to the substrate through the 3D MOF single crystal.

Figure 5.9b collects the I/V curves averaged over both ramping directions (n=50 each) obtained with the non-magnetized Tip_0 setup (black line) in the -2.0 to 2.0 range (see Appendix IV for the ±10 V bias range and non-averaged individual curves) using C-AFM in PeakForce spectroscopic mode. The curves reveal that crystals of Dy-L (**9**) behave as moderate electrical conductors, with conductivity values of ca. 0.00645 (± 0.00027) μS/cm in the linear region (see Appendix IV for additional details).

Subsequently, the samples were subjected to a study of spin-dependent electron conduction using the C-AFM. Spin selectivity studies were carried out by injecting spin polarized electrons via a magnetized conducting tip (Co/Cr) that controls the spin of the electrons injected to the MOF. The tip was magnetized for 2 minutes in a pre-defined orientation so that the magnetic dipoles either point arbitrarily north (Tip_+) or south (Tip_-) using an external permanent magnet.[33, 43,44] The magnetized tips were immediately loaded into the cantilever holder and I-V

spectroscopy measurements in the ±10 V range (see Appendix IV) were recorded in both ramping directions. The averaged (n=50) I-V traces are shown in Figure 5.9b both for Tip_+ and Tip_- magnetization conditions. As derived from the slope of the traces, the intensity of the current transmitted through the chiral MOF strongly depends on the direction of the spin polarization of the injected electrons.

In this respect, in the Tip_- set up, where electron spins were oriented arbitrarily south, the I-V average curve turns flat (high resistance) in the whole range, with conductivity values reduced to ca. 0.00022 μS/cm (±0.00001) (calculated in the ±1 V bias range). On the contrary, in the Tip_+ setup, where electrons with the opposite spin were preferentially injected, the curve shows a dramatic increase in the slope (low resistance), which eventually saturates the current amplifier at bias voltages beyond ±2 V. As a result, conductivity values (calculated in the ±1 V bias range were signal is not saturated), were more than three orders of magnitude larger as compared to the Tip_- experiments, with a value of ca. 0.28694 (±0.01020) μS/cm.

Despite saturation, there is a clear S-shape behavior as the one encountered in solar cells, whose presence points to the existence of charge transport bottlenecks of the same type associated with contact resistance.[45] This remarkable difference in transport properties of spin polarized electrons is at the heart of our findings for the family of materials we are considering here. It is also important to notice that, as expected, the values of currents measured with the unpolarized tip, lie in all cases between those for the respective magnetized tips. This is so because the native tip has a relatively small value of natural magnetization, and hence generates an initial spin polarization.

In an alternative form of data representation (Figure 5.9c and d, for the Tip_+ and Tip_0 set-ups, respectively), were results obtained in both ramping directions are not averaged, the I-V curves reveal that there is certain voltage hysteresis, which can be attributed to a well-known phenomenon in C-AMF, namely that of contact resistance,[46] which is generated by a capacitance building effect at the contacts. Another explanation for this kind of hysteresis is charge trapping in the MOF structure that creates an asymmetry in the two ramping directions. Any of these effects creates an asymmetry in the two ramping directions in all experimental set ups (Tip_- is omitted since current intensity was null, see Appendix IV). We are currently investigating this behavior using STM techniques.

As mentioned above, the central result of our work is the observation of large limiting values of SP. It should be stressed that the main effect of the heavy nuclei in the MOF structure is to increase the effective spin-orbit interaction, which translates into an enhanced CISS

effect.[17,18,19,20] This of course does not rule out the importance of hyperfine interactions in the magnetic response associated to the CISS effect, but the experimental demonstration the CISS effect can coexist with paramagnetism, is very revealing. [47]

An important aspect of our experimental results has to do with the relatively large dispersion in the I-V curves. This can be attributed to a large extent to a limitation of the C-AFM technique regarding the number of atoms involved in the contact, *i.e.* to the contact area.[45]

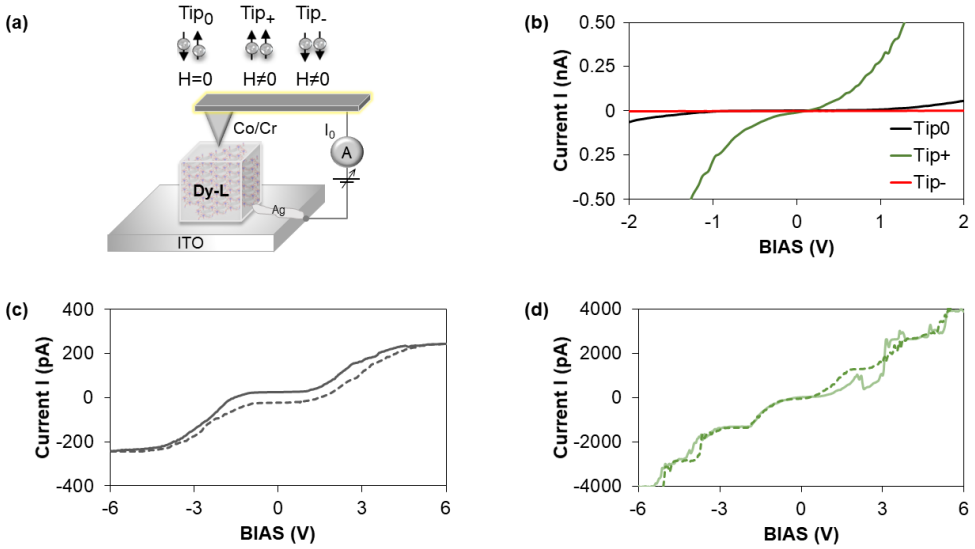

Figure 5.9. Experimental set-up and results for CM-AFM. **(a)** Set-up used to acquire the I/V curves and calculate the SP power of single crystals of Dy-L (**9**) deposited on ITO substrate, using a non-polarized electron current (H=0, Tip_0) or electron currents polarized (H≠0) in opposite directions (Tip_+ or Tip_-). **(b)** I/V curves averaged over both ramping directions as a function of applied bias in the ±2 range (see Appendix IV for I/V curves in the full bias range, *i.e.*, ±10 V) for the Tip_0 (black), Tip_+ (green) and Tip_- (red) experimental set-ups; **(c)** and **(d)** I/V curves as a function of applied bias in the ±6 V range, averaged over 50 measurements, but not over both ramping directions. Curves obtained in the – to + ramping direction are shown as solid lines, and curves obtained in the + to – ramping direction are shown as dashed line; **(c)** experiments run using the Tip_0 setup and d) experiments run using the Tip_+ experimental set-up (see Appendix IV for further details and statistics).

The spin polarization (SP) power of single crystals of Dy-L (**9**) was quantified as a function of applied bias (Figure 5.9c) using Equation *(5.2)(5.2)*, where I_+ and I_- are the currents measured in the Tip_+ and Tip_- experimental setups, respectively.

$$SP = 100\text{x}\,\frac{|I_+ - I_-|}{|I_+ + I_-|} \qquad (5.2)$$

The average SP values were calculated both in the negative (-10 V to 0 V) and positive (0 V to 10 V) bias ranges, which reached average values as high as ca. 100% for Dy-L (**9**) single crystals, independent of the bias, even considering that the current saturation for Tip_- case implies much higher currents flowing within these higher bias range (most of voltage range in Figure 5.9b). It is worth mentioning that in our case the SP power depends very weakly on the bias, as observed

in Figure 5.9c. For positive and negative bias values, which imply injection of electrons either from the tip to the ITO or vice versa, the SP powers are slightly different. It is the first time in the literature that such a large spin polarization ability, mainly due to the CISS effect, is reported at room temperature, being significantly larger than values measured for other (a)chiral systems. In this respect, a lead-iodide based perovskite with an SP value of 85% was the best filter reported so far,[28] whereas the majority of other known chiral systems stick to values in the range of 5 to 60%.[21-27] The largely improved spin selectivity may arise from the multiple electron transmission processes through chiral helical paths occurring in the system. The role of the metal centers, Dy(III) ions, is limited to enhancing the SOC, which in turn increases spin-polarization,[48] caused by the CISS effect, which selects one of the spin orientations by means of the coupling of the spin of the transmitted electrons with their linear momenta. This effect minimizes the backscattering of the electrons with the "preferred" spin and hampers the conduction of the electrons with magnetically unfavourable spins. It is important to mention here that Dy-L (**9**) is a paramagnetic material at room temperature,[34] so, no ferromagnetic coupling is expected to account for any fraction of the SP power observed; in consequence, the excellent performance of the material in the generation of pure spin currents can be ascribed to both the chirality and helicity of the system, as well as to the large SOC of the Dy(III) centers. It should be noted that the magnitude of both the conductivity and spin selectivity of the material may vary with the direction at which current transmission is measured; *i.e*, depending on the orientation of the crystals on the ITO surface (work in progress). An additional influence of the metal centers could enter through the inclusion of exchange interactions.[49] This topic is an open issue in the literature.

5.4. References

[1] Veltman, M. J. G. (2018). *Facts And Mysteries In Elementary Particle Physics*. World Scientific.

[2] Strange, P. (1998). *Relativistic Quantum Mechanics: With Applications in Condensed Matter and Atomic Physics*. Cambridge University Press.

[3] Sharma, P. "How to create a spin current", *Science* (2005), **307**, 531-533.

[4] Wolf, S. A.; Awschalom, D. D.; Buhrman, R. A.; Daughton, J. M.; Von Molnár, S.; Roukes, M. L.; Chtchelkanova, A. Y.; Treger, D. M. "Spintronics: a spin-based electronics vision for the future", *Science* (2001), **294**, 1499-1495.

[5] Cornia, A.; Seneor, P. "Spintronics: the molecular way", *Nature Materials* (2017), **16**, 505-506.

[6] Davidson, A.; Amin, V. P.; Aljuaid, W. S.; Haney, P. M.; Fan, X. "Perspectives of electrically generated spin currents in ferromagnetic materials", *Phys. Lett. A* (2020), **384**, 126228.

[7] (a) Naaman, R.; Waldeck, D. H. "Chiral-induced spin selectivity effect", *J. Phys. Chem. Lett.* (2012), **3**, 2178-2187. (b) Naaman, R.; Waldeck, D. H. "Spintronics and chirality: Spin selectivity in electron transport through chiral molecules", *Ann. Rev. Phys. Chem.* (2015), **66**, 263-281.

[8] Rikken, G. L. J. A.; Raupach, E. "Observation of magneto-chiral dichroism", *Nature* (1997), **390**, 493-494.

[9] Johnson, M. K. (1989). *Electron transfer in biology and the solid state: inorganic compounds with unusual properties*. Communication presented in the Inorganic Chemistry Symposium, Athens.

[10] Naaman, R.; Paltiel, Y.; Waldeck, D. H. "Chiral Molecules and the Spin Selectivity Effect", *J. Phys. Chem. Lett.* (2020), **11**, 3660-3666.

[11] Watson, George (1998). "PHYS345 Introduction to the Right Hand Rule". University of Delaware.

[12] Aragonés, A. C.; Medina, E.; Ferrer-Huerta, M.; Gimeno, N.; Teixidó, M.; Palma, J. L.; Tao, N.; Ugalde, J. M.; Giralt, E.; Díez-Pérez, I.; Mujica, V. "Measuring the spin-polarization power of a single chiral molecule", *Small* (2017), **13**, 1602519.

[13] Michaeli, K.; Naaman, R. "Origin of spin-dependent tunneling through chiral molecules*", J. Phys. Chem. C* (2019), **123**, 17043-17048.

[14] Tsymbal, E. Y.; Mryasov, O. N.; LeClair, P. R. "Spin-dependent tunnelling in magnetic tunnel junctions", *J. Phys. Condens. Matter* (2003), **15**, R109.

[15] Miao, G.-X.; Chang, J.; Assaf, B. A.; Heiman, D.; Moodera, J. S. "Spin regulation in composite spin-filter barrier devices", *Nat. Commun.* (2014), **5**, 3682.

[16] Dowben, P. A.; Skomski, R. "Are half-metallic ferromagnets half metals?", *J. Appl. Phys.* (2004), **95**, 7453.

[17] Naaman, R.; Paltiel, Y.; Waldeck, D. H. "Chiral Molecules and the Electron Spin", *Nat. Rev. Chem.* (2019), **3**, 250-260.

[18] Michaeli, K.; Kantor-Uriel, N.; Naaman, R.; Waldeck, D. H. "The electron's spin and molecular chirality – how are they related and how do they affect life processes?", *Chem. Soc. Rev.* (2016), **45**, 6478-6487.

[19] Zöllner, M. S.; Varela, S.; Medina, E.; Mujica, V.; Herrmann. C. "Insight into the origin of Chiral-Induced Spin Selectivity from a symmetry analysis of electronic transmission", *J. Chem. Theory Comput.* (2020), **16**, 2914-2929.

[20] Maslyuk, V. V.; Gutierrez, R.; Dianat, A.; Mujica, V.; Cuniberti, G. "Enhanced Magnetoresistance in Chiral Molecular Junctions", *JPC Letters* (2018), **9**, 5453-5459.

[21] Senthil Kumar, K.; Kantor-Uriel, N.; Mathew, S. P.; Guliamov, R.; Naaman, R. "A device for measuring spin selectivity in electron transfer", *Phys. Chem. Chem. Phys.* (2013), **15**, 18357-18362.

[22] Ray, S. G.; Daube, S. S.; Leitus, G.; Vager, Z.; Naaman, R. "Chirality-induced spin-selective properties of self-assembled monolayers of DNA on gold", *Phys. Rev. Lett.* (2006), **96**, 036101.

[23] Göhler, B.; Hamelbeck, V.; Markus, T. Z.; Kettner, M.; Hanne, G. F.; Vager, Z.; Naaman, R.; Zacharias H. "Spin selectivity in electron transmission through self-assembled monolayers of double-stranded DNA", *Science* (2011), **331**, 894-897.

[24] Wei, J. J.; Schafmeister, C.; Bird, G.; Paul, A.; Naaman, R.; Waldeck, D. H. "Molecular chirality and charge transfer through self-assembled scaffold monolayers", *J. Phys. Chem. B* (2006), **110**, 1301-1308.

[25] Carmeli, I.; Skakalova, V.; Naaman, R.; Vager, Z. "Magnetization of chiral monolayers of polypeptide: A possible source of magnetism in some biological membranes", *Angew. Chem. Int. Ed.* (2002), **41**, 761-764.

[26] Vankayala, K.; Mathew, S. P.; Cohen, S. R.; Hernández Delgado, I.; Lacour, J.; Naaman, R.; "Helicenes - A new class of organic spin filter", *Adv. Mater.* (2016), **28**, 1957-1962.

[27] Bloom, B. P.; Kiran, V.; Varade, V.; Naaman, R.; Waldeck, D. H. "Spin selective charge transport through cysteine capped CdSe quantum dots", *Nano Lett.* (2016), **16**, 4583-4589.

[28] Banerjee-Ghosh, K.; Ben Dor, O.; Tassinari, F.; Capua, E.; Yochelis, S.; Capua, A.; Yang, S. H.; Parkin, S. S.; Sarkar, S.; Kronik, L.; Baczewski, L. T.; Naaman, R.; Paltiel, Y. "Separation of enantiomers by their enantiospecific interaction with achiral magnetic substrates", *Science* (2018), **360**, 1331-1334.

[29] Kumar, A.; Capua, E.; Vankayala, K.; Fontanesi, C.; Naaman, R. "Magnetless device for conducting three-dimensional spin-specific electrochemistry", *Angew. Chem. Inter. Ed.* (2017), **56**, 14587-14590.

[30] Michaeli, K.; Varade, V.; Naaman, R.; Waldeck, D. H. "A New Approach Towards Spintronics-Spintronics With no Magnets", *J. Phys. Condens. Matter* (2017), **29**, 103002.

[31] Tassinari, F.; Banerjee-Ghosh, K.; Parenti, F.; Kiran, V.; Mucci, A.; Naaman, R. "Enhanced hydrogen production with chiral conductive polymer based electrodes", *J. Phys. Chem. C* (2017), **121**, 15777-15783.

[32] Kulkarni, C.; Mondal, A. K.; Das, T. K.; Grinbom, G.; Tassinari, F.; Mabesoone, M. F.; Meijer, E. W.; Naaman, R. "Highly efficient and tunable filtering of electrons' spin by supramolecular chirality of nanofiber-based materials", *Adv. Mater.* (2020), **32**, 1904965.

[33] Lu, H.; Wang, J.; Xiao, C.; Pan, X.; Chen, X.; Brunecky, R.; Berry, J. J.; Zhu, K.; Beard, M. C.; Vardeny, Z. V. "Spin-dependent charge transport through 2D chiral hybrid lead-iodide perovskites", *Sci. Adv.* (2019), **5**, eaay0571.

[34] Batten, S. R.; Champness, N. R.; Chen, X.-M.; Garcia-Martinez, J.; Kitagawa, S.; Öhrström, L.; O'Keeffe, M.; Suh, M. P.; Reedijk, J. "Terminology of metal-organic frameworks and coordination polymers (IUPAC Recommendations 2013)", *Pure Appl. Chem.* (2013), **85**, 1715-1724.

[35] Guillerm, V.; Kim, D.; Eubank, J. F.; Luebke, R.; Liu, X.; Adil, K.; Lah, M. S.; Eddaoudi, M. "A supermolecular building approach for the design and construction of metal-organic frameworks", *Chem. Soc. Rev.* (2014), **43**, 6141-6172.

[36] Jiao, L.; Seow, J. Y. R.; Skinner, W. S.; Wang, Z. U.; Jiang, H.-L. "Metal-organic frameworks: Structures and functional applications", *Mater. Today* (2019), **27**, 43-68.

[37] Stavila, V.; Talin, A. A.; Allendorf, M. D. "MOF-based electronic and opto-electronic devices*", Chem. Soc. Rev.* (2014), **43**, 5994-6010.

[38] Mínguez Espallargas, G.; Coronado, E. "Magnetic functionalities in MOFs: from the framework to the pore", *Chem. Soc. Rev.* (2018), **47**, 533-557.

[39] Bullard, G.; Tassinari, F.; Ko, C.H.; Mondal, A. K.; Wang, R.; Mishra, S.; Naaman, R. Therien, M. J. "Low-resistance molecular wires propagate spin-polarized currents", *J. Am. Chem. Soc.* (2019), **141**, 14707-14711.

[40] Huizi-Rayo, U.; Zabala-Lekuona, A.; Terenzi, A.; Cruz, C.M.; Cuerva, J. M.; Rodríguez-Diéguez, A.; García, J. A.; Seco, J. M.; San Sebastian, E.; Cepeda, J. "Influence of thermally-induced structural transformations over magnetic and luminiscence properties of tartrate-based chiral lanthanide organic-frameworks", *J. Mat. Chem. C* (2020), **8**, 8243-8256.

[41] San Sebastian, E.; Cepeda, J.; Huizi-Rayo, U.; Terenzi, A.; Santos, J.I.; Matxain, J.M.; Ugalde, J. M.; Mujica, V. "Enantiospecific Response in Cross-Polarization Solid-State Nuclear-Magnetic-Resonance of Optically Active Metal Organic Frameworks", *J. A.m. Chem. Soc.* (2020), **142**, 17989.

[42] Usman, M.; Mendiratta, S.; Lu, K.-L. "Semiconductor metal-organic frameworks: future low-bandgap materials", *Adv. Mater.* (2017), **29**, 1605071.

[43] Aragonès, A. C.; Aravena, D.; Cerdá, J. I.; Acís-Castillo, Z.; Li, H.; Real, J. A.; Sanz, F.; Hihath, J.; Ruiz, E.; Díez-Pérez; I. "Large conductance switching in a single-molecule device through room temperature spin-dependent transport", *Nano Lett.* (2016), **16**, 218-226.

[44] Bruker AFM probes (n.d). Retrieved November 31, 2020 from https://www.brukerafmprobes.com/

[45] Ionescu-Zanetti, C.; Mechler, A. "Applications of Conductive Atomic Force Microscopy", *Microsc. Microanal.* (2005), **19**, 9-11.

[46] Saive, R. "S-Shaped current-voltage characteristics in solar cells: A review", *IEEE J. Photovolt.* (2019), **9**, 1477-1484.

[47] Torres-Cavanillas, R.; Escorcia-Ariza, G.; Brotons-Alcázar, I.; Sanchis-Gual, R.; Mondal, P. C.; Rosaleny, L. E.; Giménez-Santamarina, S.; Sessolo, M.; Galbiati, M.; Tatay, S. "Reinforced room-temperature spin filtering in chiral paramagnetic metallopeptides", *J. Am. Chem. Soc.* (2020), **142**, 17572-17580.

[48] Medina, E.; González-Arraga, L. A.; Finkelstein-Shapiro, D.; Berche, B.; Mujica, V. "Continuum model for chiral induced spin selectivity in helical molecules", *J. Chem. Phys.* (2015), **142**, 194308.

[49] Dianat, A.; Gutierrez, R.; Alpern, H.; Mujica, V.; Ziv, A.; Yochelis, S.; Millo, O.; Paltiel, Y.; Cuniberti, G. "Role of exchange interactions in the magnetic response and inter-molecular recognition of chiral molecules", *Nano Lett.* (2020), **20**, 7077–7086.

Appendixes

Supplementary information

APPENDIX I – Supporting information of Chapter 2

S1. Materials and measurements

All chemicals were of reagent grade and were used as commercially obtained. Elemental analyses (C, H, N) were performed on an Euro EA Elemental Analyzer, whereas the metal content, determined by inductively coupled plasma (ICP-AES) was performed on a Horiba Yobin Yvon Activa spectrometer. Infrared (IR) spectra (400-4000 cm-1) were recorded on a Nicolet FT-IR 6700 spectrometer in KBr pellets. Thermal analysis (TGA) was performed on a METTLER TOLEDO TGA/SDTA851 thermal analyzer in synthetic air (80% N_2, 20% O_2) flux of 50 $cm^3 \cdot min^{-1}$, from room temperature to 800 °C with heating rate of 5 °C·min^{-1} and a sample size of about 10–20 mg per run.

S2. X-ray Data Collection and Structure Determination

X-ray data collection was performed on suitable single crystals of all compounds at 100(2) K. Diffraction intensities were collected on a Bruker VENTURE area detector equipped with graphite-monochromated Mo-Kα radiation (λ = 0.73073 Å) by applying the ω-scan method. The data reduction was performed with the CrysAlis Pro software package[1] or APEX2[2] software and corrected for absorption using SADABS,[3] depending on the diffractometer used. Crystal structures were solved by direct methods using the SIR97 program[4] and refined by full-matrix least squares on F^2 including all reflections using anisotropic displacement parameters by means of the WINGX crystallographic package.[5] The structure refinement converges with Flack parameters equal to -0.02(1). It is worth noticing that, given the microporous nature of the MOF, its crystal structure contains channels filled with two lattice water molecules in within. CCDC 1981571-1981583 contains the supplementary crystallographic data for this communication. These data can be obtained free of charge via http://www.ccdc.cam.ac.uk/conts/retrieving.html (or from the Cambridge Crystallographic Data Centre, 12, Union Road, Cambridge CB2 1EZ, UK; fax: +44 1223 336033). Crystallographic data is summarized in Table 2.5 in the manuscript.

The X-ray powder diffraction (XRPD) patterns were collected at 25 °C on a Phillips X'PERT powder diffractometer with Cu-K_α radiation (λ = 1.5418 Å) over the range 5° < 2θ < 50° with a step size of 0.02° and an acquisition time of 2.5 s per step. Indexation of the diffraction profiles were made by means of the FULLPROF program (pattern-matching analysis)[6] based on the space group and the cell parameters found by single crystal X-ray diffraction.

Table SI.1. Structure refinement details of compound (**1**).

Parameters	NaSc (1)
D_X (g cm^{-3})	1.707
Dimensions (mm)	0.12 x 0.12 x 0.12
Colour	Colourless
F(000)	3552
μ (mm^{-1})	0.427
Θ range	2.640 – 28.787°
hkl range	-21 ≤ h ≤ 25; -25 ≤ k ≤25; -23 ≤ l ≤ 25
Meas. / indep. refl.	28204 / 901
R eqv.	0.0448
Obs. refl. [I > 2σ(I)]	758
R, Rw	0.0745 / 0.2219
R, Rw(all)	0.0857 / 0.2371
GOF (S)	1.164
Parameters	54
Max. / mean Δ/σ	0.000 **/** 0.000
Weighting sch.	Shelxl (a=0.1123 / b=41.6264)
Max./min. Δρ (e Å^{-3})	1.320 / –0.722
Diffractometer	Bruker Venture
λ (Å)	0.71073
Temperature (K)	100(2)

S3. Reactant preparation

$ScCl_3$ 0.2 M solution in HCl. 137.7 mg (1.0 mmol) of Sc_2O_3 were dissolved with concentrated HCl in a 10 mL volumetric flask.

S4. Continuous Shape Measurements

Continuous shape measurements showed in Table SI.2 were calculated for the ML_4 and ML_8 coordination environments. The lowest SHAPE values for each ion are shown in bold blue, indicating best fits.

Table SI.2. CShMs for the ML_4 and ML_8 coordination environments.

CODES		
SP-4	*1 D4h*	*Square*
T-4	*2 Td*	*Tetrahedron*
SS-4	*3 C2v*	*Seesaw*
vTBPY-4	*4 C3v*	*Vacant trigonal bipyramid*

CODES		
OP-8	*1 D8h*	*Octagon*
HPY-8	*2 C7v*	*Heptagonal pyramid*
HBPY-8	*3 D6h*	*Hexagonal bipyramid*
CU-8	*4 Oh*	*Cube*
SAPR-8	*5 D4d*	*Square antiprism*
TDD-8	*6 D2d*	*Triangular dodecahedron*
JGBF-8	*7 D2d*	*Johnson gyrobifastigium J26*
JETBPY-8	*8 D3h*	*Johnson elongated triangular bipyramid J14*
JBTPR-8	*9 C2v*	*Biaugmented trigonal prism J50*
BTPR-8	*10 C2v*	*Biaugmented trigonal prism*
JSD-8	*11 D2d*	*Snub diphenoid J84*
TT-8	*12 Td*	*Triakis tetrahedron*
ETBPY-8	*13 D3h*	*Elongated trigonal bipyramid*

Structure [ML4]	Na	Structure [ML8]	Sc
SP-4	**0.239**	**OP-8**	34.870
T-4	33.493	**HPY-8**	25.321
SS-4	17.772	**HBPY-8**	14.917
vTBPY-4	34.384	**CU-8**	7.123
		SAPR-8	3.270
		TDD-8	**0.412**
		JGBF-8	17.760
		JETBPY-8	30.291
		JBTPR-8	4.719
		BTPR-8	3.471
		JSD-8	5.028
		TT-8	7.269
		ETBPY-8	25.346

S5. FT-IR spectroscopy

As shown in Figure SI.1, FTIR spectra of compounds (**2**) and (**3**) are identical. The broad band at high frequencies (3500 cm^{-1}) corresponds to vibrations of O-H bonds of crystallization water molecules, following by two weak shoulders at 3220 and 3100 cm^{-1} related to C-H

vibrations of the pyrimidinic ring of the ligand. Asymmetric stretching vibrations of carboxylate groups and aromatic C–C and C–N bonds give intense bands around 1690 and 1500 cm^{-1}, whereas bands of the rage of 1390-1200 cm^{-1} correspond to the symmetric stretching of carboxylates groups. Finally, vibration bands of the M–O and M–N bonds are observed around 530 cm^{-1}.

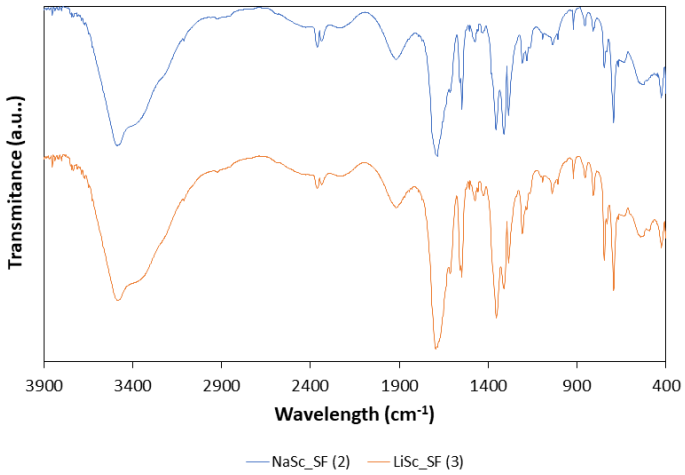

Figure SI.1. FTIR spectra of compounds (2) and (3).

S6. Photoluminescence

Photoluminescence spectra of NaSC_SF (**2**) at room temperature, in which no excitation bands are appreciated (Figure SI.2a) although emission band at 420 nm is also observed.

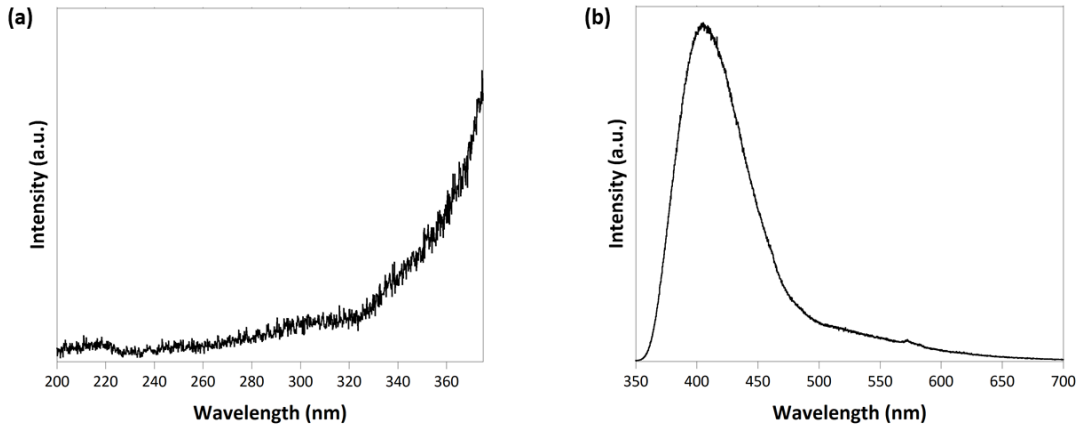

Figure SI.2. Photoluminescence measurements at RT of NaSC_SF (**2**). **(a)** Excitation and **(b)** emission spectra.

S7. References

[1] *CrysAlisPro Software System*, Agilent Technologies UK Ltd, Oxford, UK, 2019.

[2] Bruker Apex2, Bruker AXS Inc., Madison, Wisconsin, USA, 2004.

[3] G. M. Sheldrick, SADABS, Program for Empirical Adsorption Correction, Institute for Inorganic Chemistry, University of Göttingen, Göttingen, Germany, 1996.

[4] A. Altomare, M. C. Burla, M. Camilla, G. L. Cascarano, C. Giacovazzo, A. Guagliardi, A. G. G. Moliterni, G. Polidori, R. Spagna, *J. Appl. Crystallogr*., 1999, **32**, 115.

[5] (a) G. M. Sheldrick, SHELX-2014, Program for Crystal Structure Refinement, University of Göttingen, Göttingen, Germany, 2014. (b) L. J. Farrugia, *J. Appl. Cryst*., 1999, **32**, 837.

[6] J. Rodriguez-Carvajal, *Physica B*., 1993, **192**, 55.

APPENDIX II – Supporting information of Chapter 3

S1. Materials and measurements

All chemicals were of reagent grade and were used as commercially obtained. Elemental analyses (C, H, N) were performed on an Euro EA Elemental Analyzer. Infrared (IR) spectra (400-4000 cm-1) were recorded on a Nicolet FT-IR 6700 spectrometer in KBr pellets. Thermal analysis (TGA) was performed on a METTLER TOLEDO TGA/SDTA851 thermal analyzer in synthetic air (80% N_2, 20% O_2) flux of 50 $cm^3 \cdot min^{-1}$, from room temperature to 800 °C with heating rate of 5 $°C \cdot min^{-1}$ and a sample size of about 10–20 mg per run.

S2. X-ray Data Collection and Structure Determination

X-ray data collection was performed on suitable single crystals of all compounds at 100(2) K. Diffraction intensities were collected on a Bruker VENTURE area detector equipped with graphite-monochromated Mo-Kα radiation (λ = 0.73073 Å) by applying the ω-scan method. The data reduction was performed with the CrysAlis Pro software package[1] or APEX2[2] software and corrected for absorption using SADABS,[3] depending on the diffractometer used. Crystal structures were solved by direct methods using the SIR97 program[4] and refined by full-matrix least squares on F^2 including all reflections using anisotropic displacement parameters by means of the WINGX crystallographic package.[5] The structure refinement converges with Flack parameters equal to -0.02(1). It is worth noticing that, given the microporous nature of the MOF, its crystal structure contains channels filled with two lattice water molecules in within. CCDC 1981571-1981583 contains the supplementary crystallographic data for this communication. These data can be obtained free of charge via http://www.ccdc.cam.ac.uk/conts/retrieving.html (or from the Cambridge Crystallographic Data Centre, 12, Union Road, Cambridge CB2 1EZ, UK; fax: +44 1223 336033). Crystallographic data is summarized in Table 3.2 in the manuscript.

The X-ray powder diffraction (XRPD) patterns were collected at 25 °C on a Phillips X'PERT powder diffractometer with Cu-K_α radiation (λ = 1.5418 Å) over the range 5° < 2θ < 50° with a step size of 0.02° and an acquisition time of 2.5 s per step, and on a Empyream PANALYTICAL diffractometer with a Cu-K_α radiation (λ = 1.5418 Å) PIXcel3D detector which operated in continuous mode at 45 kV and 40 mA over the range 5° < 2θ < 35° with a step size of 0.013° and an acquisition time of 39.525 s per step. Indexation of the diffraction profiles were made by means of the FULLPROF program (pattern-matching analysis)[6] based on the space group and the cell parameters found by single crystal X-ray diffraction.

X-ray diffractograms collected at different temperatures were acquired using a Bruker D8 advanced with Cu radiation $K_{\alpha 1}$ (λ = 1.54056 Å) operating in continuous mode at 45 kV and 40 mA from 5 to 35° (2θ) using a step size of 0.01° and 0.1 s per step. The heating program followed was 5 ºC/min and with measurements every 10 °C at different temperatures (30-550 °C) under vacuum.

Table SII.1. Structure refinement details of compound (**4**).

Parameters	CaZn (4)
D_X (g cm^{-3})	1.480
Dimensions (mm)	0.14 x 0.09 x 0.06
Colour	Colourless
F(000)	6156
μ (mm^{-1})	1.058
Θ range	2.249 – 23.308°
hkl range	-31 ≤ h ≤ 29; -31 ≤ k ≤ 31; -21 ≤ l ≤ 21
Meas. / indep. refl.	64272 / 2171
R eqv.	0.0501
Obs. refl. [I > 2σ(I)]	1969
R, Rw	0.0445 / 0.1273
R, Rw(all)	0.0503 / 0.1352
GOF (S)	1.077
Parameters	223
Max. / mean Δ/σ	0.001 **/** 0.000
Weighting sch.	Shelxl (a=0.080100 / b=95.853203)
Max./min. Δρ (e Å^{-3})	1.124 / -0.878
Diffractometer	Bruker Venture
λ (Å)	0.71073
Temperature (K)	100(2)

S3. Continuous Shape Measurements

Continuous shape measurements showed in Table SII.2 were calculated for the ML_6 and ML_4 coordination environment for Tb-Tm and activated Tb compounds. The lowest SHAPE values for each ion are shown in bold blue, indicating best fits.

Table SII.2. CShM for the ML_6 and ML_8 coordination environment.

CODES		
HP-6	*1 D6h*	*Hexagon*
PPY-6	*2 C5v*	*Pentagonal pyramid*
OC-6	*3 Oh*	*Trigonal prism*
TPR-6	*4 D3h*	*Vacant trigonal bipyramid*
JPPY-6	*5 C5v*	*Johnson pentagonal pyramid J2*

CODES		
SP-4	*1 D4h*	*Square*
T-4	*2 Td*	*Tetrahedron*
SS-4	*3 C2v*	*Seesaw*
vTBPY-4	*4 C3v*	*Vacant trigonal bipyramid*

Structure [ML6]	Ca	Structure [ML4]	Zn
HP-6	28.938	**SP-4**	30.000
PPY-6	25.245	**T-4**	**1.723**
OC-6	**1.672**	**SS-4**	5.692
TPR-6	10.967	**vTBPY-4**	2.745
JPPY-6	28.135		

S4. FT-IR spectroscopy

Although FTIR spectra of compounds (4), (5) and (6) are very similar (Figure SII.1), some differences can be appreciate due to the different composition of the materials. Broad bands around 3500 cm^{-1} corresponds to O-H vibrations of water molecules or MeOH, whereas bands at 3100 and 2900 cm^{-1} are consequence of the asymmetric stretching of -CH_3 groups of DMF molecules. The narrow and intense band at 2200 cm^{-1} corresponds to -CN vibrations of the nitrile, and the region between 1700 and 1250 cm^{-1} covers the vibrations related to asymmetric stretching vibrations of carboxylate groups, -CO group of DMF and aromatic C–C bonds, and symmetric stretching of carboxylates groups. The bands located around 1100-740 cm^{-1} are related to vibration modes of DMF molecules, concretely the asymmetric and symmetric stretching of C-N bond, C-N-C and C-N-O bending and C-N-C twist, and last vibration band at 510 cm^{-1} corresponds to M-O bond. It should be noted that the DMF-related bands are less intense in compounds (5) and (6) due to their relatively low proportion in the composition of the materials (see Tables 3.5, 3.6 and 3.7 for further information).

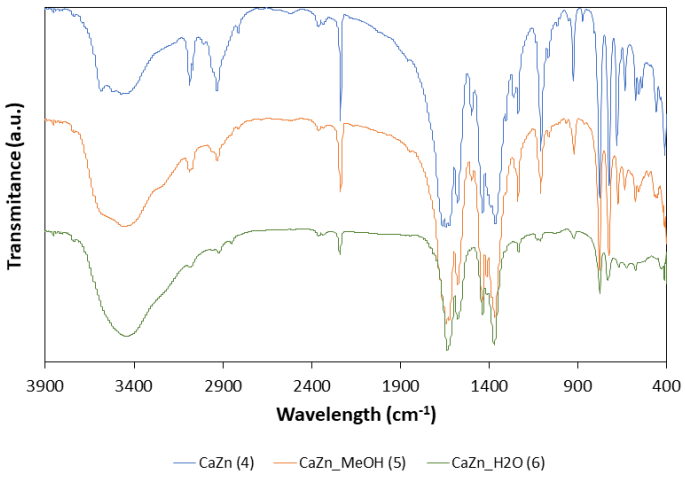

Figure SII.1. FTIR spectra of compounds (**4**-**6**).

S5. Photocatalytic CO_2 reduction

Sample preparation

For photocatalysis experiments, 60 mg of previously activated CaZn (**4**) (150 °C, 12 h) were suspended in water during 2-5 minutes and deposited on a glass fiber.

Photocatalysis: formation of other products

As mentioned in the main text, in the photocatalytic cycle performed under Ar and H_2O flow without CO_2, H_2 production has not been detected. This can be indicative of the formation of hydrocarbons since the H^+ generated in the water splitting could have reacted to give new products. But, as Figure SII.2 shows, only traces of CH_4 and MeOH have been achieved, confirming that CaZN (4) can photocatalyze water splitting only in presence of CO_2.

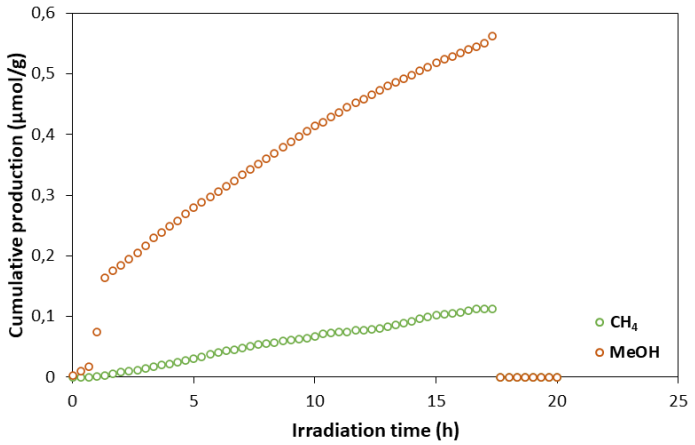

Figure SII.2. Evolution of the formation of other products in the photocatalytic CO_2 reduction under Ar and H_2O flow at variable times of visible light irradiation.

S6. References

[1] *CrysAlisPro Software System*, Agilent Technologies UK Ltd, Oxford, UK, 2019.

[2] Bruker Apex2, Bruker AXS Inc., Madison, Wisconsin, USA, 2004.

[3] G. M. Sheldrick, SADABS, Program for Empirical Adsorption Correction, Institute for Inorganic Chemistry, University of Göttingen, Göttingen, Germany, 1996.

[4] A. Altomare, M. C. Burla, M. Camilla, G. L. Cascarano, C. Giacovazzo, A. Guagliardi, A. G. G. Moliterni, G. Polidori, R. Spagna, *J. Appl. Crystallogr*., 1999, **32**, 115.

[5] (a) G. M. Sheldrick, SHELX-2014, Program for Crystal Structure Refinement, University of Göttingen, Göttingen, Germany, 2014. (b) L. J. Farrugia, *J. Appl. Cryst*., 1999, **32**, 837.

[6] J. Rodriguez-Carvajal, *Physica B*., 1993, **192**, 55.

APPENDIX III – Supporting information of Chapter 4

S1. Materials and measurements

All chemicals were of reagent grade and were used as commercially obtained. Elemental analyses (C, H, N) were performed on an Euro EA Elemental Analyzer, whereas the metal content, determined by inductively coupled plasma (ICP-AES) was performed on a Horiba Yobin Yvon Activa spectrometer. Infrared (IR) spectra (400-4000 cm-1) were recorded on a Nicolet FT-IR 6700 spectrometer in KBr pellets. Thermal analysis (TGA) was performed on a METTLER TOLEDO TGA/SDTA851 thermal analyzer in synthetic air (80% N_2, 20% O_2) flux of 50 $cm^3 \cdot min^{-1}$, from room temperature to 800 °C with heating rate of 5 °C·min^{-1} and a sample size of about 10–20 mg per run.

S2. X-ray Data Collection and Structure Determination

X-ray data collection was performed on suitable single crystals of all compounds at 100(2) K. Diffraction intensities of compounds Tb-L (**7**), Tb-D (**8**), Dy-L (**9**), Dy-D (**10**) and Ho-D (**12**) were collected on an Agilent Technologies Super-Nova diffractometer, which was equipped with monochromated Cu Kα radiation (λ = 1.54184 Å) and an Atlas CCD detector. The intensity data for compounds Tm-L (**15**) and Tm-D (**16**) were collected on an Agilent Technologies Super-Nova diffractometer but equipped with monochromated Mo Kα radiation (λ = 0.71073 Å) and an Eos CCD detector. Instead, data collection of compounds Ho-L (**11**), Er-L (**13**) and Er-D (**14**) was done on a Bruker VENTURE area detector equipped with graphite-monochromated Mo-Kα radiation (λ = 0.73073 Å) by applying the ω-scan method. The data reduction was performed with the CrysAlis Pro software package[1] or APEX2[2] software and corrected for absorption using SADABS,[3] depending on the diffractometer used. Crystal structures were solved by direct methods using the SIR97 program[4] and refined by full-matrix least squares on F^2 including all reflections using anisotropic displacement parameters by means of the WINGX crystallographic package.[5] During the data integration, it was observed that unit cell only indexed about half of the reflections, suggesting the occurrence of twinned specimens in both cases. Unusually large ADPs observed for many atoms as well as large R_1 and wR^2 agreement factors during the refinement stage further confirmed the latter. Accordingly, all structures were refined with the general twin law [(-1 0 0 / -0.02 0.96 -0.07 / 0.01 -0.98 -0.96) including the two crystallographic domains (all reflections) in such a way that final percentages for the minor domain were estimated to be of 40, 42, 30, 35, 25, 28, 10 and 15 % for Tb-L (**7**)**,** Tb-D (**8**)**,** Dy-L (**9**)**,** Dy-D (**10**)**,** Ho-L (**11**), Ho-D (**12**), Er-L (**13**), Er-D (**14**), Tm-L (**15**) and Tm-D (**16**). Hydrogen atoms belonging to the tartrate ligands

were located in the difference Fourier map and included with riding models as fixed contributions with isotropic thermal displacement parameters 1.2 and 1.5 times those of their parent carbon (C–H) and oxygen (O–H) atoms, respectively. Note that those hydrogen atoms belonging to O–H groups (hydroxyl or water molecules) were refined according to the optimized hydrogen bonding interaction. The structure refinement converges with Flack parameters equal to -0.02(1), 0.01(2), 0.02(1), -0.03(1), 0.02(2), 0.03(1), 0.02(1) and 0.02(1) respectively for Tb-L (**7**)**,** Tb-D (**8**)**,** Dy-L (**9**)**,** Dy-D (**10**)**,** Ho-L (**11**), Ho-D (**12**), Er-L (**13**), Er-D (**14**), Tm-L (**15**) and Tm-D (**16**), which confirms the chiral purity of all specimens. It is worth noticing that, given the microporous nature of the MOFs, their crystal structure contains channels filled with a variable number of lattice water molecules in within, which may slightly oscillate depending on the atmospheric conditions. CCDC 1981571-1981583 contains the supplementary crystallographic data for this communication. These data can be obtained free of charge via http://www.ccdc.cam.ac.uk/conts/retrieving.html (or from the Cambridge Crystallographic Data Centre, 12, Union Road, Cambridge CB2 1EZ, UK; fax: +44 1223 336033). Crystallographic data are summarized in Tables 4.2-4.4 in the manuscript.

Thermally activated crystals of Tb(III) specimens were measured at high- and low-temperature (Tb-L' (**17**) was measured at 383 directly heated in the diffractometer using a heating rate of 5 °C min^{-1} and 100 K so that not only the transformed phase could be solved but high-resolution data could be acquired). Instead, Tb-L'' (**18**) could only be measured at 100 K after pre-heating the single crystal at 473 K in the diffractometer to avoid single crystals get cracked. These data collections were taken on an Agilent Technologies Super-Nova diffractometer using the above-mentioned experimental setup. Despite the fact that specimens selected were twinned, no twin law was applied during the data reduction, otherwise it led to worse hkl files. During the refinement, a strong pseudosymmetry was observed, which causes PLATON program to suggest a transformation to monoclinic I-centered cell.[6] However, this suggestion is based on the fact that both lanthanide environments are equivalent, which is not, and brings an associated disorder that cannot be accurately handled. The rest of afore mentioned refinement strategy was followed for these crystal structures.

The X-ray powder diffraction (XRPD) patterns were collected at 25 °C on a Phillips X'PERT powder diffractometer with Cu-K_α radiation (λ = 1.5418 Å) over the range 5° < 2θ < 50° with a step size of 0.02° and an acquisition time of 2.5 s per step. Indexation of the diffraction profiles were made by means of the FULLPROF program (pattern-matching analysis)[7] based on the space group and the cell parameters found by single crystal X-ray diffraction.

Variable-temperature powder X-ray diffraction measurements were conducted on polycrystalline sample of compound Tb-L (**7**) under ambient atmosphere with heating rate of 5 °C·min^{-1} and measuring a complete diffractogram every 20 °C up to 510 °C, and every 50 °C from 510 °C up to 710 °C.

Table SIII.1. Structure refinement details of compounds (**7**)-(**10**).

Parameters	Tb-L (7)	Tb-D (8)	Dy-L (9)	Dy-D (10)
D_X (g cm^{-3})	2.561	2.563	2.632	2.596
Dimensions (mm)	0.33 x 0.21 x 0.06	0.11 x 0.08 x 0.03	0.23 x 0.19 x 0.12	0.23 x 0.19 x 0.12
Colour	Colourless	Colourless	Colourless	Colourless
F(000)	418	418	420	420
μ (mm^{-1})	6.334	6.339	36.815	36.311
θ range	2.824 - 25.346°	1.650 - 25.540°	3.508 - 74.244°	3.481 - 74.501°
hkl range	-7 ≤ h ≤ 7; -8 ≤ k ≤ 8; -15 ≤ l ≤ 15	-7 ≤ h ≤ 7; -8 ≤ k ≤ 8; -16 ≤ l ≤ 16	-7 ≤ h ≤ 7; -9 ≤ k ≤ 9; -16 ≤ l ≤ 16	-7 ≤ h ≤ 6; -9 ≤ k ≤ 9; -16 ≤ l ≤ 16
Meas. / indep. refl.	4840 / 4840	9724 / 3938	18899 / 4449	9372 / 4072
R eqv.	0.0282	0.0384	0.2225	0.1918
Obs. refl. [I > 2σ(I)]	4732	3838	4279	3927
R[a], Rw[b]	0.0391 / 0.1011	0.0434 / 0.1094	0.0842 / 0.2090	0.1017 / 0.2579
R, Rw (all)	0.0397 / 0.1015	0.0443 / 0.1100	0.0871 / 0.2110	0.1030 / 0.2600
GOF (S)[c]	1.041	1.044	1.061	1.172
Parameters	324	343	343	343
Max. / mean Δ/σ	0.006 / 0.000	0.005 / 0.000	0.004 / 0.000	0.003 / 0.000
Weighting sch.	Shelxl (a=0.0822 / b=0.3288)	Shelxl (a= 0.0776 / b=4.2738)	Shelxl (a=0.1352 / b=9.5716)	Shelxl (a=0.2000 / b=0.0000)
Max./min. Δρ (e Å^{-3})	2.786 / -0.914	2.909 / -1.163	4.363 / -1.722	4.235 / -2.382
Diffractometer	SuperNova, Single source at offset/far, Eos	SuperNova, Single source at offset/far, Eos	SuperNova, Single source at offset, Atlas	SuperNova, Single source at offset, Atlas
λ (Å)	0.71073	0.71073	1.54184	1.54184
Temperature (K)	100(2)	100(2)	100(2)	100(2)

[a] $S = [\sum w(F_0^2 - F_c^2)^2 / (N_{obs} - N_{param})]^{1/2}$. [b] $R_1 = \sum ||F_0| - |F_c|| / \sum |F_0|$. [c] $wR_2 = [\sum w(F_0^2 - F_c^2)^2 / \sum wF_0^2]^{1/2}$; $w = 1/[\sigma^2(F_0^2) + (aP)^2]$ where $P = (\max(F_0^2,0) + 2F_c^2)/3$ with a = 5.9161.

Table SIII.2. Structure refinement details of compounds (**11**)-(**14**).

Parameters	Ho-L (11)	Ho-D (12)	Er-L (13)	Er-D (14)
D_X (g cm^{-3})	2.623	2.604	2.660	2.627
Dimensions (mm)	0.13 x 0.10 x 0.06	0.16 x 0.13 x 0.06	0.07 x 0.05 x 0.04	0.13 x 0.10 x 0.05
Colour	Pinkish	Pinkish	Pinkish	Pinkish
F(000)	422	412	424	414
μ (mm^{-1})	7.151	14.061	7.648	7.702
θ range	2.834 - 28.789°	3.536 - 74.424°	3.234 - 31.924°	2.843 - 24.739°
hkl range	-8 ≤ h ≤ 8; -9 ≤ k ≤ 9; -17 ≤ l ≤ 17	-7 ≤ h ≤ 7; -9 ≤ k ≤ 9; -16 ≤ l ≤ 16	-8 ≤ h ≤ 8; -10 ≤ k ≤ 10; -17 ≤ l ≤ 19	-7 ≤ h ≤ 6; -7 ≤ k ≤ 8; -15 ≤ l ≤ 15
Meas. / indep. refl.	16950 / 5458	8596 / 3976	10693 / 4935	6474 / 3239
R eqv.	0.0434	0.0484	0.0271	0.0242
Obs. refl. [I > 2σ(I)]	5191	3921	4464	3151
R[a], Rw[b]	0.0356 / 0.0956	0.0464 / 0.1236	0.0393 / 0.1056	0.0245 / 0.0582
R, Rw (all)	0.0384 / 0.0969	0.0471 / 0.1243	0.0432 / 0.1115	0.0263 / 0.0588
GOF (S)[c]	1.230	1.109	1.094	1.093
Parameters	344	334	344	335
Max. / mean Δ/σ	0.004 **/** 0.000	0.003 **/** 0.000	0.003 **/** 0.000	0.004 **/** 0.000
Weighting sch.	Shelxl (a=0.0000 / b=12.8478)	Shelxl (a=0.0905 / b=1.8724)	Shelxl (a=0.0788 / b=1.1225)	Shelxl (a=0.0082 / b=2.2342)
Max./min. Δρ (e Å^{-3})	3.055 / -3.207	4.247 / -1.391	2.999 / -2.444	2.934 / -1.078
Diffractometer	Bruker Venture	SuperNova, Single source at offset, Atlas	Bruker Venture	Bruker Venture
λ (Å)	0.71073	1.54184	0.71073	0.71073
Temperature (K)	100(2)	100(2)	100(2)	100(2)

[a] $S = [\sum w(F_0^2 - F_c^2)^2 / (N_{obs} - N_{param})]^{1/2}$. [b] $R_1 = \sum ||F_0| - |F_c|| / \sum |F_0|$. [c] $wR_2 = [\sum w(F_0^2 - F_c^2)^2 / \sum wF_0^2]^{1/2}$; $w = 1/[\sigma^2(F_0^2) + (aP)^2]$, where $P = (\max(F_0^2,0) + 2F_c^2)/3$ with a = 5.9161.

Table SIII.3. Structure refinement details of compounds (**15**)-(**16**).

Parameters	Tm-L (15)	Tm-D (16)
D_X (g cm^{-3})	2.668	2.668
Dimensions (mm)	0.11 x 0.08 x 0.05	0.10 x 0.08 x 0.05
Colour	Colourless	Colourless
F(000)	426	426
μ (mm^{-1})	8.073	8.074
θ range	2.857 - 28.831°	2.856 - 26.472°
hkl range	-8 ≤ h ≤ 8; -9 ≤ k ≤ 9; -17 ≤ l ≤ 17	-7 ≤ h ≤ 7; -9 ≤ k ≤ 9; -16 ≤ l ≤ 16
Meas. / indep. refl.	20350 / 5641	15245 / 4511
R eqv.	0.0305	0.0374
Obs. refl. [I > 2σ(I)]	5494	4344
R[a], Rw[b]	0.0219 / 0.0611	0.0251 / 0.0671
R, Rw (all)	0.0233 / 0.0614	0.0265 / 0.0678
GOF (S)[c]	1.236	1.143
Parameters	344	344
Max. / mean Δ/σ	0.005 / 0.000	0.006 / 0.000
Weighting sch.	Shelxl (a=0.0000 / b=4.2682)	Shelxl (a=0.0000 / b=6.2275)
Max./min. Δρ (e Å^{-3})	2.088 / -2.079	1.560 / -1.527
Diffractometer	Bruker Venture	Bruker Venture
λ (Å)	0.71073	0.71073
Temperature (K)	100(2)	100(2)

[a] $S = [\sum w(F_0^2 - F_c^2)^2 / (N_{obs} - N_{param})]^{1/2}$. [b] $R_1 = \sum ||F_0| - |F_c|| / \sum |F_0|$. [c] $wR_2 = [\sum w(F_0^2 - F_c^2)^2 / \sum wF_0^2]^{1/2}$; $w = 1/[\sigma^2(F_0^2) + (aP)^2]$ where $P = (\max(F_0^2,0) + 2F_c^2)/3$ with a = 5.9161.

S3. Structural details

Table SIII.4. Selected bond lengths (Å) for Tb-Tm compounds.[a]

Tb-L (7)				**Tb-D (8)**			
Tb1–O11A	2.505(10)	Tb2–O11B	2.347(11)	Tb1–O11A	2.496(12)	Tb2–O11B	2.337(13)
Tb1–O12A	2.475(11)	Tb2–O21B	2.595(10)	Tb1–O12A	2.487(12)	Tb2–O21B	2.594(12)
Tb1–O12B	2.380(11)	Tb2–O31C	2.507(10)	Tb1–O12B	2.384(12)	Tb2–O31C	2.485(12)
Tb1–O11C	2.363(10)	Tb2–O41C	2.390(11)	Tb1–O11C	2.353(11)	Tb2–O41C	2.389(12)
Tb1–O21C	2.591(10)	Tb2–O2W	2.390(12)	Tb1–O21C	2.586(11)	Tb2–O2W	2.375(13)
Tb1–O1W	2.409(11)	Tb2–O41A(iii)	2.377(10)	Tb1–O1W	2.409(12)	Tb2–O41A(viii)	2.369(12)
Tb1–O31B(i)	2.492(11)	Tb2–O42A(iii)	2.796(11)	Tb1–O31B(vi)	2.499(12)	Tb2–O42A(viii)	2.767(13)
Tb1–O41B(i)	2.378(12)	Tb2–O12C(iv)	2.384(11)	Tb1–O41B(vi)	2.378(12)	Tb2–O12C(ix)	2.372(13)
Tb1–O42B(ii)	2.353(11)	Tb2–O42C(v)	2.324(11)	Tb1–O42B(vii)	2.354(12)	Tb2–O42C(x)	2.320(12)
Dy-L (9)				**Dy-D (10)**			
Dy1–O11A	2.483(18)	Dy2–O11B	2.310(16)	Dy1–O11A	2.512(19)	Dy2–O11B	2.329(17)
Dy1–O12A	2.445(16)	Dy2–O21B	2.568(15)	Dy1–O12A	2.476(19)	Dy2–O21B	2.568(17)

Dy1–O12B	2.345(16)	Dy2–O31C	2.475(15)	Dy1–O12B	2.33(2)	Dy2–O31C	2.473(17)
Dy1–O11C	2.330(15)	Dy2–O41C	2.356(16)	Dy1–O11C	2.343(17)	Dy2–O41C	2.37(2)
Dy1–O21C	2.551(16)	Dy2–O2W	2.348(16)	Dy1–O21C	2.568(16)	Dy2–O2W	2.360(19)
Dy1–O1W	2.370(17)	Dy2–O41A(iii)	2.325(17)	Dy1–O1W	2.394(19)	Dy2–O41A(viii)	2.38(2)
Dy1–O31B(i)	2.477(15)	Dy2–O42A(iii)	2.780(19)	Dy1–O31B(vi)	2.508(16)	Dy2–O42A(viii)	2.84(2)
Dy1–O41B(i)	2.370(18)	Dy2–O12C(iv)	2.328(15)	Dy1–O41B(vi)	2.39(2)	Dy2–O12C(ix)	2.358(17)
Dy1–O42B(ii)	2.339(17)	Dy2–O42C(v)	2.294(17)	Dy1–O42B(vii)	2.30(2)	Dy2–O42C(x)	2.315(18)
Ho-L (11)				**Ho-D (12)**			
Ho1–O11A	2.482(11)	Ho2–O11B	2.322(12)	Ho1–O11A	2.462(8)	Ho2–O11B	2.320(8)
Ho1–O12A	2.451(10)	Ho2–O21B	2.571(11)	Ho1–O12A	2.462(8)	Ho2–O21B	2.578(8)
Ho1–O12B	2.352(11)	Ho2–O31C	2.465(11)	Ho1–O12B	2.355(8)	Ho2–O31C	2.425(8)
Ho1–O11C	2.335(10)	Ho2–O41C	2.366(11)	Ho1–O11C	2.325(8)	Ho2–O41C	2.342(9)
Ho1–O21C	2.571(10)	Ho2–O2W	2.346(11)	Ho1–O21C	2.567(8)	Ho2–O2W	2.387(8)
Ho1–O1W	2.370(17)	Ho2–O41A(iii)	2.347(11)	Ho1–O1W	2.373(9)	Ho2–O41A(viii)	2.382(8)
Ho1–O31B(i)	2.491(11)	Ho2–O42A(iii)	2.800(12)	Ho1–O31B(vi)	2.487(8)	Ho2–O42A(viii)	2.631(8)
Ho1–O41B(i)	2.365(12)	Ho2–O12C(iv)	2.348(11)	Ho1–O41B(vi)	2.354(8)	Ho2–O12C(ix)	2.338(8)
Ho1–O42B(ii)	2.340(10)	Ho2–O42C(v)	2.297(11)	Ho1–O42B(vii)	2.335(8)	Ho2–O42C(x)	2.317(8)
Er-L (13)				**Er-D (14)**			
Er1–O11A	2.481(10)	Er2–O11B	2.288(11)	Er1–O11A	2.466(7)	Er2–O11B	2.314(8)
Er1–O12A	2.433(10)	Er2–O21B	2.565(10)	Er1–O12A	2.451(8)	Er2–O21B	2.558(8)
Er1–O12B	2.346(10)	Er2–O31C	2.434(11)	Er1–O12B	2.356(8)	Er2–O31C	2.419(9)
Er1–O11C	2.305(9)	Er2–O41C	2.354(11)	Er1–O11C	2.310(8)	Er2–O41C	2.343(9)
Er1–O21C	2.560(10)	Er2–O2W	2.336(10)	Er1–O21C	2.560(8)	Er2–O2W	2.360(8)
Er1–O1W	2.343(11)	Er2–O41A(iii)	2.338(11)	Er1–O1W	2.357(8)	Er2–O41A(viii)	2.374(9)
Er1–O31B(i)	2.470(11)	Er2–O42A(iii)	2.772(12)	Er1–O31B(vi)	2.462(9)	Er2–O42A(viii)	2.665(9)
Er1–O41B(i)	2.351(11)	Er2–O12C(iv)	2.356(10)	Er1–O41B(vi)	2.353(8)	Er2–O12C(ix)	2.349(9)
Er1–O42B(ii)	2.318(10)	Er2–O42C(v)	2.276(11)	Er1–O42B(vii)	2.317(8)	Er2–O42C(x)	2.297(9)
Tm-L (15)				**Tm-D (16)**			
Tm1–O11A	2.475(7)	Tm2–O11B	2.285(7)	Tm1–O11A	2.476(9)	Tm2–O11B	2.290(9)
Tm1–O12A	2.432(7)	Tm2–O21B	2.541(7)	Tm1–O12A	2.432(9)	Tm2–O21B	2.534(9)
Tm1–O12B	2.323(7)	Tm2–O31C	2.450(7)	Tm1–O12B	2.322(9)	Tm2–O31C	2.451(8)
Tm1–O11C	2.316(6)	Tm2–O41C	2.346(7)	Tm1–O11C	2.302(8)	Tm2–O41C	2.353(9)
Tm1–O21C	2.589(6)	Tm2–O2W	2.316(7)	Tm1–O21C	2.596(8)	Tm2–O2W	2.311(9)
Tm1–O1W	2.337(7)	Tm2–O41A(iii)	2.301(7)	Tm1–O1W	2.345(9)	Tm2–O41A(viii)	2.294(9)
Tm1–O31B(i)	2.453(6)	Tm2–O42A(iii)	2.800(12)	Tm1–O31B(vi)	2.455(8)	Tm2–O12C(ix)	2.307(9)
Tm1–O41B(i)	2.341(7)	Tm2–O12C(iv)	2.308(7)	Tm1–O41B(vi)	2.340(9)	Tm2–O42C(x)	2.271(9)
Tm1–O42B(ii)	2.306(6)	Tm2–O42C(v)	2.271(7)	Tm1–O42B(vii)	2.307(9)		

[a] Symmetries: (i) x, 1 + y, z; (ii) – 1 + x, 1 + y, z; (iii) – 1 + x, – 1 + y, - 1 + z; (iv) x, - 1 + y, z; (v) 1 + x, y, z; (vi) x, - 1 + y, z; (vii) 1 + x, - 1 + y, z; (viii) 1 + x, 1 + y, 1 + z; (ix) x, 1 + y, z; (x) - 1 + x, y, z.

Table SIII.5. Hydrogen bonding interactions (Å, °) of compounds Tb-L and Tb-D.[a]

D–H...A[b]	D–H	H...A	D...A	D–H...A	D–H...A[b]	D–H	H...A	D...A	D–H...A
Tb-L (1)					**Tb-D (8)**				
O21A–H21A···O42A(i)	0.84	1.99	2.815(17)	171.4	O21A–H21A···O42A(x)	0.83	2.00	2.825(17)	171.9
O31A–H31A···O12A(ii)	0.86	1.88	2.717(17)	166.1	O31A–H31A···O12A(xi)	0.87	1.87	2.726(18)	167.0
O21B–H21B···O11C(iii)	0.88	1.72	2.582(15)	166.7	O21B–H21B···O11C(xii)	0.89	1.73	2.597(16)	166.4
O31B–H31B···O3W	0.85	1.90	2.726(15)	163.2	O31B–H31B···O3W	0.84	1.94	2.75(2)	163.1
O21C–H21C···O11B	0.84	1.74	2.573(16)	167.2	O21C–H21C···O11B	0.85	1.75	2.586(18)	167.0
O31C–H31C···O4W	0.83	1.97	2.725(17)	150.5	O31C–H31C···O4W	0.85	1.97	2.76(2)	152.6

O1W–H11W···O6W	0.80	2.04	2.823(15)	168.5	O1W–H11W···O6W	0.80	2.06	2.847(17)	167.8
O1W–H12W···O41B(iv)	0.85	1.89	2.725(17)	169.3	O1W–H12W···O41B(xiii)	0.85	1.89	2.728(18)	169.0
O2W–H21W···O5W	0.82	1.91	2.720(17)	166.6	O2W–H21W···O5W	0.84	1.90	2.73(2)	165.9
O2W–H22W···O41C(ii)	0.85	1.91	2.729(15)	159.4	O2W–H22W···O41C(xi)	0.85	1.93	2.735(18)	158.1
O3W–H31W···O21A(iii)	0.84	2.07	2.862(16)	156.3	O3W–H31W···O21A(xii)	0.84	2.08	2.876(19)	159.3
O3W–H32W···O11A	0.88	1.97	2.824(16)	161.6	O3W–H32W···O11A	0.85	1.98	2.79(2)	161.9
O4W–H41W···O41A(v)	0.89	1.85	2.737(18)	175.6	O4W–H41W···O41A(xiv)	0.88	1.83	2.70(2)	174.3
O4W–H42W···O6W(vi)	0.83	1.94	2.765(17)	172.3	O4W–H42W···O6W(xv)	0.83	1.94	2.76(2)	173.7
O5W–H51W···O4W(vii)	0.83	2.02	2.848(19)	172.1	O5W–H51W···O4W(xvi)	0.84	2.04	2.88(3)	172.5
O5W–H52W···O6W(viii)	0.87	2.46	3.321(17)	171.2	O5W–H52W···O6W(xvii)	0.86	2.43	3.28(2)	172.0
O6W–H61W···O31A(ix)	0.84	1.99	2.805(16)	162.5	O6W–H61W···O31A(xviii)	0.84	1.97	2.777(18)	160.1
O6W–H62W···O3W	0.87	1.95	2.808(18)	174.8	O6W–H62W···O3W	0.83	1.94	2.77(2)	176.7

[a] Symmetry codes: (i) – 1 + x, y, z; (ii) 1 + x, y, z; (iii) x, - 1 + y, z; (iv) – 1 + x, 1 + y, z; (v) – 1 + x, y, - 1 + z; (vi) x, y, - 1 + z; (vii) 1 + x, - 1 + y, z; (viii) x, - 1 + y, - 1 + z; (ix) – 1 + x, - 1 + y, z; (x) 1 + x, y, z; (xi) - 1 + x, y, z; (xii) x, 1 + y, z; (xiii) 1 + x, - 1 + y, z; (xiv) 1 + x, y, 1 + z; (xv) x, y, 1 + z; (xvi) - 1 + x, 1 + y, z; (xvii) x, 1 + y, 1 + z; (xviii) 1 + x, 1 + y, z. [b] D: donor. A: acceptor.

Table SIII.6. Hydrogen bonding interactions (Å, °) of compounds Dy-L and Dy-D.[a]

D–H...A[b]	D–H	H...A	D...A	D–H...A	D–H...A[b]	D–H	H...A	D...A	D–H...A
Dy-L (9)					**Dy-D (10)**				
O21A–H21A...O42A(i)	0.85	1.98	2.82(2)	173.8	O21A–H21A...O42A(x)	0.87	1.96	2.82(3)	172.6
O31A–H31A...O12A(ii)	0.85	1.87	2.70(2)	166.0	O31A–H31A...O12A(xi)	0.85	1.87	2.71(3)	164.9
O21B–H21B...O11C(iii)	0.87	1.73	2.59(2)	167.0	O21B–H21B...O11C(xii)	0.87	1.73	2.59(3)	166.7
O31B–H31B...O3W	0.85	1.91	2.73(2)	162.0	O31B–H31B...O3W	0.83	1.89	2.70(2)	162.9
O21C–H21C...O11B	0.85	1.74	2.57(2)	166.8	O21C–H21C...O11B	0.85	1.71	2.55(3)	166.3
O31C–H31C...O4W	0.85	1.98	2.76(3)	151.6	O31C–H31C...O4W	0.84	1.99	2.76(3)	151.7
O1W–H11W...O6W	0.82	2.02	2.83(2)	167.0	O1W–H11W...O6W	0.83	2.04	2.86(3)	168.4
O1W–H12W...O41B(iv)	0.85	1.86	2.70(3)	167.2	O1W–H12W...O41B(xiii)	0.85	1.86	2.69(3)	166.8
O2W–H21W...O5W	0.85	1.89	2.72(3)	165.1	O2W–H21W...O5W	0.84	1.85	2.67(3)	164.1
O2W–H22W...O41C(ii)	0.86	1.90	2.71(2)	158.2	O2W–H22W...O41C(xi)	0.87	1.91	2.74(3)	158.8
O3W–H31W...O21A(iii)	0.83	2.05	2.84(3)	158.7	O3W–H31W...O21A(xii)	0.86	2.07	2.88(3)	157.4
O3W–H32W...O11A	0.86	1.96	2.79(3)	162.0	O3W–H32W...O11A	0.86	1.99	2.82(3)	161.3
O4W–H41W...O41A(v)	0.87	1.86	2.73(3)	175.9	O4W–H41W...O41A(xiv)	0.89	1.88	2.77(3)	176.2
O4W–H42W...O6W(vi)	0.83	1.92	2.75(3)	173.7	O4W–H42W...O6W(xv)	0.83	1.91	2.74(3)	171.6
O5W–H51W...O4W(vii)	0.85	2.00	2.84(4)	170.0	O5W–H51W...O4W(xvi)	0.86	1.99	2.84(3)	169.6
O5W–H52W...O6W(viii)	0.84	2.41	3.24(3)	168.8	O5W–H52W...O6W(xvii)	0.88	2.44	3.30(3)	167.6
O6W–H61W...O31A(ix)	0.87	1.96	2.80(3)	160.9	O6W–H61W...O31A(xviii)	0.86	1.96	2.80(3)	163.6
O6W–H62W...O3W	0.84	1.93	2.76(3)	175.0	O6W–H62W...O3W	0.88	1.96	2.84(3)	174.6

[a] Symmetry codes: (i) – 1 + x, y, z; (ii) 1 + x, y, z; (iii) x, - 1 + y, z; (iv) – 1 + x, 1 + y, z; (v) – 1 + x, y, - 1 + z; (vi) x, y, - 1 + z; (vii) 1 + x, - 1 + y, z; (viii) x, - 1 + y, - 1 + z; (ix) – 1 + x, - 1 + y, z; (x) 1 + x, y, z; (xi) - 1 + x, y, z; (xii) x, 1 + y, z; (xiii) 1 + x, - 1 + y, z; (xiv) 1 + x, y, 1 + z; (xv) x, y, 1 + z; (xvi) - 1 + x, 1 + y, z; (xvii) x, 1 + y, 1 + z; (xviii) 1 + x, 1 + y, z. [b] D: donor. A: acceptor.

Table SIII.7. Hydrogen bonding interactions (Å, °) of compounds Ho-L and Ho-D.[a]

D–H...A[b]	D–H	H...A	D...A	D–H...A	D–H...A[b]	D–H	H...A	D...A	D–H...A
Ho-L (11)					**Ho-D (12)**				
O21A–H21A···O42A(i)	0.85	1.95	2.799(15)	173.5	O21A–H21A···O42A(x)	0.86	1.96	2.809(12)	166.2

O31A–H31A···O12A(ii)	0.86	1.87	2.717(16)	169.6	O31A–H31A···O12A(xi)	0.85	1.88	2.706(12)	167.0
O21B–H21B···O11C(iii)	0.85	1.76	2.606(15)	171.8	O21B–H21B···O11C(xii)	0.85	1.74	2.582(11)	171.3
O31B–H31B···O3W	0.86	2.02	2.745(18)	141.9	O31B–H31B···O3W	0.92	1.91	2.748(11)	150.8
O21C–H21C···O11B	0.84	1.74	2.575(17)	169.3	O21C–H21C···O11B	0.86	1.74	2.589(12)	169.5
O31C–H31C···O4W	0.84	1.93	2.71(2)	152.8	O31C–H31C···O4W	0.84	1.80	2.635(13)	171.3
O1W–H11W···O6W	0.85	2.03	2.841(17)	158.4	O1W–H11W···O5W	0.86	2.05	2.871(12)	159.8
O1W–H12W···O41B(iv)	0.85	1.92	2.706(17)	153.1	O1W–H12W···O41B(xiii)	0.84	1.88	2.710(12)	169.7
O2W–H21W···O5W	0.85	1.95	2.699(19)	146.4	O2W–H21W···O4W(xii)	0.78	2.37	2.804(14)	116.5
O2W–H22W···O41C(ii)	0.85	1.95	2.730(15)	152.2	O2W–H22W···O41C(xi)	0.85	1.91	2.722(12)	158.7
O3W–H31W···O21A(iii)	0.86	2.03	2.857(18)	160.1	O3W–H31W···O21A(xii)	0.87	2.00	2.814(11)	154.0
O3W–H32W···O11A	0.87	1.97	2.796(17)	157.7	O3W–H32W···O11A	0.87	1.97	2.802(12)	159.5
O4W–H41W···O41A(v)	0.85	2.02	2.76(2)	145.2	O4W–H41W···O41A(xiv)	0.86	1.91	2.751(14)	166.2
O4W–H42W···O6W(vi)	0.85	1.95	2.75(2)	158.8	O4W–H42W···O5W(xv)	0.87	2.03	2.873(13)	164.1
O5W–H51W···O4W(vii)	0.85	2.06	2.89(2)	165.1	O5W–H51W···O31A(xvi)	0.85	1.97	2.807(13)	168.6
O5W–H52W···O6W(viii)	0.85	2.49	3.26(2)	151.2	O5W–H52W···O3W	0.85	1.93	2.771(14)	173.5
O6W–H61W···O31A(ix)	0.85	2.15	2.802(16)	132.6					
O6W–H62W···O3W	0.85	2.03	2.768(19)	145.0					

[a] Symmetry codes: (i) – 1 + x, y, z; (ii) 1 + x, y, z; (iii) x, - 1 + y, z; (iv) – 1 + x, 1 + y, z; (v) – 1 + x, y, - 1 + z; (vi) x, y, - 1 + z; (vii) 1 + x, - 1 + y, z; (viii) x, - 1 + y, - 1 + z; (ix) – 1 + x, - 1 + y, z; (x) 1 + x, y, z; (xi) - 1 + x, y, z; (xii) x, 1 + y, z; (xiii) 1 + x, - 1 + y, z; (xiv) 1 + x, y, 1 + z; (xv) x, y, 1 + z; (xvi) - 1 + x, 1 + y, z. [b] D: donor. A: acceptor.

Table SIII.8. Hydrogen bonding interactions (Å, °) of compounds Er-L and Er-D.[a]

D–H...A[b]	**D–H**	**H...A**	**D...A**	**D–H...A**	**D–H...A[b]**	**D–H**	**H...A**	**D...A**	**D–H...A**
Er-L (13)					**Er-D (14)**				
O21A–H21A···O42A(i)	0.85	1.97	.816(15)	174.6	O21A–H21A···O42A(x)	0.85	1.97	2.810(12)	170.7
O31A–H31A···O12A(ii)	0.85	1.88	2.721(15)	169.4	O31A–H31A···O12A(xi)	0.85	1.88	2.723(11)	167.0
O21B–H21B···O11C(iii)	0.86	1.76	2.609(14)	172.3	O21B–H21B···O11C(xii)	0.85	1.75	2.598(12)	168.7
O31B–H31B···O3W	0.84	2.01	2.726(18)	142.9	O31B–H31B···O3W	0.87	1.91	2.734(12)	158.4
O21C–H21C···O11B	0.85	1.74	2.572(15)	168.0	O21C–H21C···O11B	0.85	1.74	2.576(11)	166.6
O31C–H31C···O4W	0.87	1.90	2.71(3)	153.8	O31C–H31C···O4W	0.85	1.78	2.624(15)	170.5
O1W–H11W···O6W	0.87	2.04	2.874(15)	159.4	O1W–H11W···O5W	0.88	2.10	2.872(13)	146.1
O1W–H12W···O41B(iv)	0.84	1.91	2.689(15)	152.2	O1W–H12W···O41B(xiii)	0.86	1.87	2.702(12)	164.0
O2W–H21W···O5W	0.86	1.95	2.705(19)	145.9	O2W–H21W···O4W(xii)	0.85	2.09	2.811(16)	141.9
O2W–H22W···O41C(ii)	0.85	1.93	2.713(15)	151.9	O2W–H22W···O41C(xi)	0.85	1.88	2.707(13)	163.9
O3W–H31W···O21A(iii)	0.84	2.03	2.838(17)	160.6	O3W–H31W···O21A(xii)	0.86	1.96	2.795(13)	163.5
O3W–H32W···O11A	0.88	1.93	2.768(17)	158.3	O3W–H32W···O11A	0.85	1.96	2.785(13)	164.8
O4W–H41W···O41A(v)	0.87	2.02	2.79(3)	146.4	O4W–H41W···O41A(xiv)	0.86	1.93	2.763(15)	162.2
O4W–H42W···O6W(vi)	0.85	1.93	2.728(19)	156.5	O4W–H42W···O5W(xv)	0.86	2.06	2.899(15)	165.2
O5W–H51W···O4W(vii)	0.86	2.07	2.91(3)	165.3	O5W–H51W···O31A(xvi)	0.85	1.99	2.819(14)	163.6
O5W–H52W···O6W(viii)	0.84	2.43	3.20(2)	151.1	O5W–H52W···O3W	0.85	1.97	2.807(12)	165.7
O6W–H61W···O31A(ix)	0.89	2.15	2.819(16)	131.0	O21A–H21A···O42A(x)	0.85	1.97	2.810(12)	170.7
O6W–H62W···O3W	0.83	2.02	2.744(17)	144.8	O31A–H31A···O12A(xi)	0.85	1.88	2.723(11)	167.0

[a] Symmetry codes: (i) – 1 + x, y, z; (ii) 1 + x, y, z; (iii) x, - 1 + y, z; (iv) – 1 + x, 1 + y, z; (v) – 1 + x, y, - 1 + z; (vi) x, y, - 1 + z; (vii) 1 + x, - 1 + y, z; (viii) x, - 1 + y, - 1 + z; (ix) – 1 + x, - 1 + y, z; (x) 1 + x, y, z; (xi) - 1 + x, y, z; (xii) x, 1 + y, z; (xiii) 1 + x, - 1 + y, z; (xiv) 1 + x, y, 1 + z; (xv) x, y, 1 + z; (xvi) - 1 + x, 1 + y, z. [b] D: donor. A: acceptor.

Table SIII.9. Hydrogen bonding interactions (Å, °) of compounds Tm-L and Tm-D.[a]

D–H...A[b]	D–H	H...A	D...A	D–H...A	D–H...A[b]	D–H	H...A	D...A	D–H...A
Tm-L (15)					**Tm-D (16)**				
O21A–H21A···O42A(i)	0.85	1.91	2.751(10)	168.6	O21A–H21A···O42A(x)	0.85	1.91	2.751(13)	167.5
O31A–H31A···O12A(ii)	0.85	1.88	2.722(10)	167.0	O31A–H31A···O12A(xi)	0.86	1.88	2.729(13)	167.1
O21B–H21B···O11C(iii)	0.85	1.75	2.595(9)	175.9	O21B–H21B···O11C(xii)	0.85	1.77	2.610(12)	169.3
O31B–H31B···O3W	0.86	1.91	2.724(11)	157.0	O31B–H31B···O3W	0.88	1.89	2.729(14)	158.3
O21C–H21C···O11B	0.85	1.73	2.575(9)	171.8	O21C–H21C···O11B	0.85	1.73	2.574(12)	172.4
O31C–H31C···O4W	0.90	2.00	2.775(11)	143.7	O31C–H31C···O4W	0.85	2.00	2.763(14)	149.7
O1W–H11W···O6W	0.85	2.03	2.864(11)	167.2	O1W–H11W···O6W	0.85	2.10	2.859(14)	148.7
O1W–H12W···O41B(iv)	0.85	1.87	2.704(10)	164.8	O1W–H12W···O41B(xiii)	0.85	1.87	2.700(13)	164.0
O2W–H21W···O5W	0.84	1.90	2.722(11)	166.7	O2W–H21W···O5W	0.85	1.93	2.718(14)	153.1
O2W–H22W···O41C(ii)	0.86	1.88	2.706(10)	159.1	O2W–H22W···O41C(xi)	0.86	1.87	2.700(13)	160.8
O3W–H31W···O21A(iii)	0.86	2.02	2.835(11)	158.4	O3W–H31W···O21A(xii)	0.87	2.02	2.841(14)	156.7
O3W–H32W···O11A	0.86	1.97	2.787(10)	158.5	O3W–H32W···O11A	0.87	1.95	2.775(13)	158.4
O4W–H41W···O41A(v)	0.85	1.96	2.800(11)	171.9	O4W–H41W···O41A(xiv)	0.85	1.96	2.804(14)	171.6
O4W–H42W···O6W(vi)	0.85	1.96	2.799(11)	169.3	O4W–H42W···O6W(xv)	0.86	1.97	2.818(15)	170.3
O5W–H51W···O4W(vii)	0.86	2.02	2.844(13)	160.1	O5W–H51W···O4W(xvi)	0.87	2.01	2.835(17)	159.3
O5W–H52W···O6W(viii)	0.86	2.43	3.251(12)	160.8	O5W–H52W···O6W(xvii)	0.86	2.43	3.263(14)	161.0
O6W–H61W···O31A(ix)	0.88	2.00	2.804(10)	151.1	O6W–H61W···O31A(xviii)	0.86	1.97	2.800(13)	162.0
O6W–H62W···O3W	0.87	1.97	2.802(12)	161.8	O6W–H62W···O3W	0.86	1.96	2.798(15)	163.6

[a] Symmetry codes: (i) – 1 + x, y, z; (ii) 1 + x, y, z; (iii) x, - 1 + y, z; (iv) – 1 + x, 1 + y, z; (v) – 1 + x, y, - 1 + z; (vi) x, y, - 1 + z; (vii) 1 + x, - 1 + y, z; (viii) x, - 1 + y, - 1 + z; (ix) – 1 + x, - 1 + y, z; (x) 1 + x, y, z; (xi) - 1 + x, y, z; (xii) x, 1 + y, z; (xiii) 1 + x, - 1 + y, z; (xiv) 1 + x, y, 1 + z; (xv) x, y, 1 + z; (xvi) - 1 + x, 1 + y, z; (xvii) x, 1 + y, 1 + z; (xviii) 1 + x, 1 + y, z. [b] D: donor. A: acceptor.

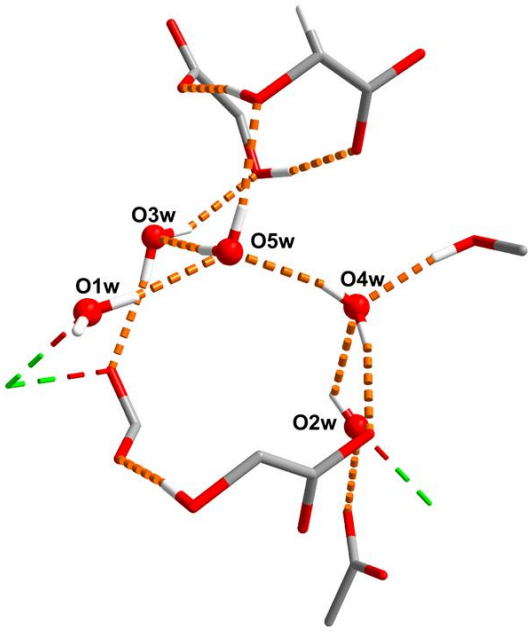

Figure SIII.1. Hydrogen bonding scheme on compound Ho-D (**12**).

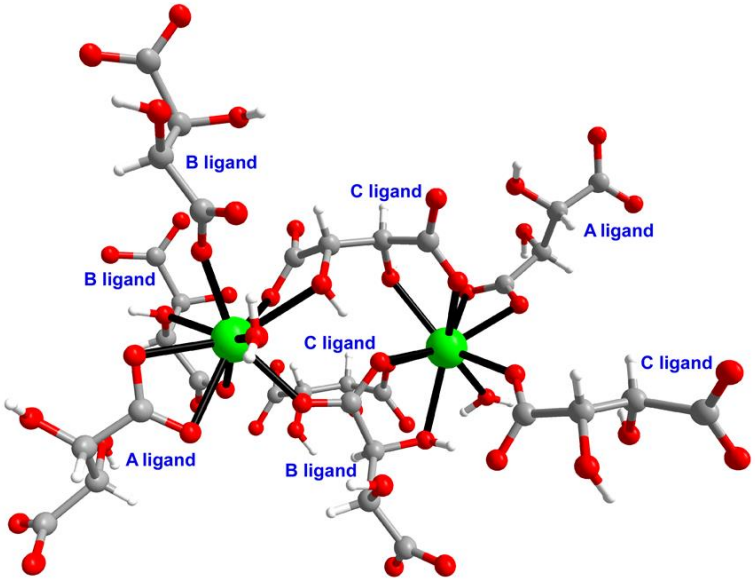

Figure SIII.2. Fragment of the structure of compound Dy-D (**10**) showing the ligands forming the coordination polyhedra.

S4. Synthesis of chiral MOFs

Compound Tb-L (7): 5 mL of an aqueous solution containing 0.6 mmol of $Tb(NO_3)_3 \cdot 6H_2O$ (271.8 mg) were mixed with an aqueous solution of L-tartaric acid ($_L$-H_2TTA) (135.1 mg, 0.9 mmol) in 5 mL and sonicated. The resulting solution was heated in a Teflon liner at 140 °C for 48 h. After slow cooling to room temperature, colourless prismatic single crystals Tb-L (**7**) were obtained, which were collected by filtration and washed several times with water. Elemental analysis for

$C_{12}H_{24}O_{24}Tb_2$ (877.3 g mol^{-1}). Calcd.: C, 16.43; H, 2.76; Tb, 37.05. Found: C, 16.69; H, 2.48; Tb, 37.09.

Compound Tb-D (8): Compound Tb-D (**8**) was synthesized by the same method used with compound Tb-L (**7**) using 0.9 mmol (135.1 mg) of D-tartaric acid ($_D$-H_2TTA), obtaining colourless prismatic single crystals. Elemental analysis for $C_{12}H_{24}O_{24}Tb_2$ (877.3 g mol^{-1}). Calcd.: C, 16.43; H, 2.76; Tb, 37.05. Found: C, 16.64; H, 2.55; Tb, 37.12.

Compound Dy-L (9): Compound Dy-L (**9**) was synthesized by the same method used with compound Tb-L (**7**) using 0.6 mmol (263.2 mg) of $Dy(NO_3)_3{\cdot}5H_2O$, obtaining colourless prismatic single crystals. Elemental analysis for $C_{12}H_{24}Dy_2O_{24}$ (877.3 g mol^{-1}). Calcd.: C, 16.43; H, 2.76; Dy, 37.05. Found: C, 16.69; H, 2.48; Dy, 37.09.

Compound Dy-D (10): Compound Dy-D (**10**) was synthesized by the same method used with compound Dy-L (**9**) using 0.9 mmol (135.1 mg) of D-tartaric acid ($_D$-H_2TTA), obtaining colourless prismatic single crystals. Elemental analysis for $C_{12}H_{24}Dy_2O_{24}$ (877.3 g mol^{-1}). Calcd.: C, 16.43; H, 2.76; Dy, 37.05. Found: C, 16.64; H, 2.55; Dy, 37.12.

Compound Ho-L (11): Compound Ho-L (**11**) was synthesized by the same method used with compound Dy-L (**9**) using 0.6 mmol (264.7 mg) of $Ho(NO_3)_3{\cdot}6H_2O$, obtaining pinkish prismatic single crystals. Elemental analysis for $C_{12}H_{24}Ho_2O_{24}$ (882.2 g mol^{-1}). Calcd.: C, 16.34; H, 2.74; Ho, 37.39. Found: C, 16.32; H, 2.84; Ho, 37.23.

Compound Ho-D (12): Compound Ho-D (**12**) was synthesized by the same method used with compound Ho-L (**11**) using 0.9 mmol (135.1 mg) of D-tartaric acid ($_D$-H_2TTA), obtaining pinkish prismatic single crystals. Elemental analysis for $C_{12}H_{22}Ho_2O_{23}$ (864.2 g mol^{-1}). Calcd.: C, 16.68; H, 2.57; Ho, 38.17. Found: C, 16.48; H, 2.65; Ho, 38.11.

Compound Er-L (13): Compound Er-L (**13**) was synthesized by the same method used with compound Ho-L (**11**) using 0.6 mmol (266.0 mg) of $Er(NO_3)_3{\cdot}5_2O$, obtaining pinkish prismatic single crystals. Elemental analysis for $C_{12}H_{24}Er_2O_{24}$ (886.8 g mol^{-1}). Calcd.: C, 16.25; H, 2.73; Ho, 37.72. Found: C, 16.22; H, 2.64; Er, 37.83.

Compound Er-D (14): Compound Er-D (**14**) was synthesized by the same method used with compound Er-L (**13**) using 0.9 mmol (135.1 mg) of D-tartaric acid ($_D$-H_2TTA), obtaining pinkish prismatic single crystals. Elemental analysis for $C_{12}H_{22}Er_2O_{23}$ (868.8 g mol^{-1}). Calcd.: C, 16.59; H, 2.55; Ho, 38.50. Found: C, 16.37; H, 2.46; Er, 38.39.

Compound Tm-L (15): Compound Tm-L (**15**) was synthesized by the same method used with compound Er-L (**13**) using 0.6 mmol (277.8 mg) of $Tm(NO_3)_3{\cdot}6H_2O$, obtaining colourless prismatic single crystals. Elemental analysis for $C_{12}H_{24}O_{24}Tm_2$ (890.2 g mol^{-1}). Calcd.: C, 16.19; H, 2.72; Tm, 37.95. Found: C, 16.25; H, 2.64; Tm, 38.03.

Compound Tm-D (16): Compound Tm-D (**16**) was synthesized by the same method used with compound Tm-L (**15**) using 0.9 mmol (135.1 mg) of D-tartaric acid ($_D$-H_2TTA), obtaining colourless prismatic single crystals. Elemental analysis for $C_{12}H_{24}O_{24}Tm_2$ (890.2 g mol^{-1}). Calcd.: C, 16.19; H, 2.72; Tm, 37.95. Found: C, 16.12; H, 2.58; Tm, 37.82.

S5. Continuous Shape Measurements

Continuous shape measurements showed in Table SIII.10-Table SIII**.12** were calculated for the LnO_9 and LnO_8 coordination environment for Tb-Tm and activated Tb compounds. The lowest SHAPE values for each ion are shown in bold blue, indicating best fits.

Table SIII.10. CShMs for the LnO_9 coordination environment.

CODES		
EP-9	*1 D9h*	*Enneagon*
OPY-9	*2 C8v*	*Octagonal pyramid*
HBPY-9	*3 D7h*	*Heptagonal bipyramid*
JTC-9	*4 C3v*	*Johnson triangular cupola J3*
JCCU-9	*5 C4v*	*Capped cube J8*
CCU-9	*6 C4v*	*Spherical-relaxed capped cube*
JCSAPR-9	*7 C4v*	*Capped square antiprism J10*
CSAPR-9	*8 C4v*	*Spherical capped square antiprism*
JTCTPR-9	*9 D3h*	*Tricapped trigonal prism J51*
TCTPR-9	*10 D3h*	*Spherical tricapped trigonal prism*
JTDIC-9	*11 C3v*	*Tridiminished icosahedron J63*
HH-9	*12 C2v*	*Hula-hoop*
MFF-9	*13 Cs*	*Muffin*

Structure [ML9]	**Tb-L (7)**		**Dy-L (9)**		**Ho-L (11)**		**Er-L (13)**		**Tm-L (15)**
	Tb1	**Tb2**	**Dy1**	**Dy2**	**Ho1**	**Ho2**	**Er1**	**Er2**	**Tm1**
EP-9	34.907	35.216	34.879	35.285	35.088	35.656	34.887	35.485	35.066
OPY-9	23.136	22.499	23.167	22.644	23.005	22.577	22.906	22.621	23.180
HBPY-9	18.128	17.538	18.126	17.812	18.179	17.792	18.027	17.915	18.456
JTC-9	15.360	15.275	15.339	15.391	15.339	15.400	15.169	15.469	15.358
JCCU-9	10.279	10.194	10.304	10.193	10.358	10.300	10.289	10.406	10.482
CCU-9	9.076	8.610	9.083	8.583	9.176	8.804	9.108	8.764	9.336
JCSAPR-9	1.929	2.094	1.868	2.064	1.817	2.025	1.763	2.041	2.041
CSAPR-9	**1.159**	1.423	**1.116**	1.446	**1.088**	1.389	**1.085**	1.412	**1.116**

JTCTPR-9	3.433	3.554	3.360	3.497	3.315	3.407	3.207	3.422	3.250
TCTPR-9	2.159	2.620	2.123	2.684	2.076	2.593	2.093	2.627	2.134
JTDIC-9	11.722	12.043	11.686	12.047	11.699	12.237	11.662	12.211	11.713
HH-9	10.344	10.196	10.374	10.054	10.456	10.324	10.418	10.187	10.485
MFF-9	1.343	**1.345**	1.328	**1.371**	1.329	**1.374**	1.354	**1.404**	1.421

Table SIII.11. CShMs for the LnO_8 coordination environment of Tm2 in Tm-compounds.

CODES		
EP-9	*1 D9h*	*Enneagon*
OPY-9	*2 C8v*	*Octagonal pyramid*
HBPY-9	*3 D7h*	*Heptagonal bipyramid*
JTC-9	*4 C3v*	*Johnson triangular cupola J3*
JCCU-9	*5 C4v*	*Capped cube J8*
CCU-9	*6 C4v*	*Spherical-relaxed capped cube*
JCSAPR-9	*7 C4v*	*Capped square antiprism J10*
CSAPR-9	*8 C4v*	*Spherical capped square antiprism*
JTCTPR-9	*9 D3h*	*Tricapped trigonal prism J51*
TCTPR-9	*10 D3h*	*Spherical tricapped trigonal prism*
JTDIC-9	*11 C3v*	*Tridiminished icosahedron J63*
HH-9	*12 C2v*	*Hula-hoop*
MFF-9	*13 Cs*	*Muffin*

Structure [ML8]	**Tm-L (15)**
	Tm2
OP-8	27.245
HPY-8	23.434
HBPY-8	15.240
CU-8	11.186
SAPR-8	2.198
TDD-8	2.590
JGBF-8	10.779
JETBPY-8	27.145
JBTPR-8	1.875
BTPR-8	**1.267**
JSD-8	3.351
TT-8	11.780
ETBPY-8	22.003

Table SIII.12. CShMs for the LnO_9 coordination environment for the thermally activated Tb compounds.

CODES		
EP-9	*1 D9h*	*Enneagon*
OPY-9	*2 C8v*	*Octagonal pyramid*
HBPY-9	*3 D7h*	*Heptagonal bipyramid*
JTC-9	*4 C3v*	*Johnson triangular cupola J3*
JCCU-9	*5 C4v*	*Capped cube J8*
CCU-9	*6 C4v*	*Spherical-relaxed capped cube*
JCSAPR-9	*7 C4v*	*Capped square antiprism J10*
CSAPR-9	*8 C4v*	*Spherical capped square antiprism*
JTCTPR-9	*9 D3h*	*Tricapped trigonal prism J51*
TCTPR-9	*10 D3h*	*Spherical tricapped trigonal prism*
JTDIC-9	*11 C3v*	*Tridiminished icosahedron J63*
HH-9	*12 C2v*	*Hula-hoop*
MFF-9	*13 Cs*	*Muffin*

Structure [ML9]	**Tb-L' (17)**		**Tb-L'' (18)**	
	Tb1	**Tb2**	**Tb1**	**Tb2**
EP-9	34.294	34.229	34.271	34.287
OPY-9	21.543	21.784	21.647	21.800
HBPY-9	19.997	19.543	19.984	19.623

JTC-9	14.114	13.890	14.115	13.919
JCCU-9	10.155	10.086	9.989	9.898
CCU-9	8.898	8.892	8.803	8.747
JCSAPR-9	1.572	1.632	1.503	1.591
CSAPR-9	**0.973**	**1.060**	**0.971**	**1.014**
JTCTPR-9	2.318	2.318	2.141	2.213
TCTPR-9	1.873	1.957	1.779	1.829
JTDIC-9	10.595	10.343	10.878	10.639
HH-9	10.013	9.956	10.074	9.978
MFF-9	1.640	1.687	1.629	1.640

S6. Thermogravimetric analysis

The thermogravimetric behaviour of all compounds is very similar given their isostructural nature. The general behaviour accounting for the most common $\{[Ln_2(\mu_4\text{-tart})_2(\mu\text{-tart})(H_2O)_2]\cdot 4H_2O\}_n$ formula is described, although some counterparts (Ho-D (**12**) and Er-D (**14**)) possess only three lattice water molecules in agreement with the SCXR data. Heating of the sample starts with a short plateau in the TG curve from room temperature up to ca. 70 °C, after which three lattice water molecules present in the channels as well as one coordination water molecule are lost. This first dehydration finishes at ca. 120 °C. Then, after a small plateau of ca. 30 °C, materials experiment the loss of one lattice and one coordination water molecules, which finishes at ca. 210 °C and yields a dehydrated phase of the compound that shows no mass loss up to ca. 260 °C. Above the latter temperature, all compounds present two main exothermic processes which involve to the decomposition of tartrate ligands, leading to the corresponding Ln_2O_3 as a final residue.

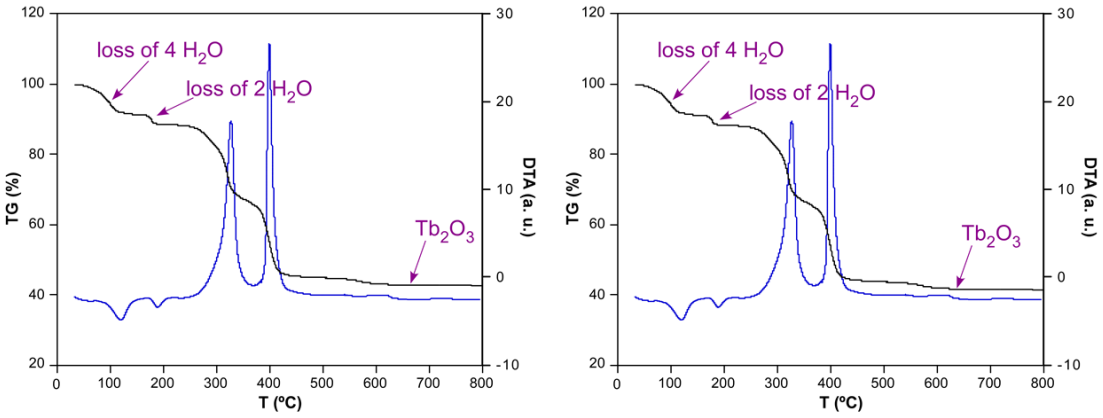

Figure SIII.3. TG/DTA analysis for compounds Tb-L (**7**) and Tb-D (**8**).

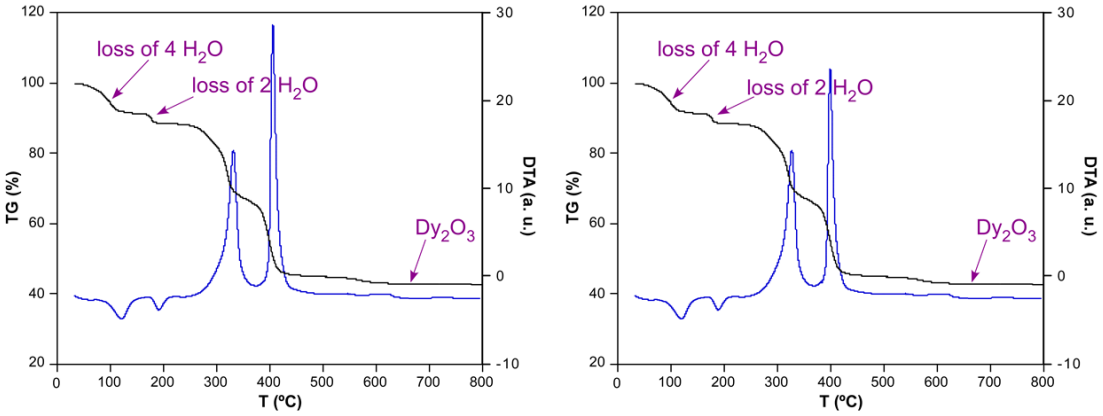

Figure SIII.4. TG/DTA analysis for compounds Dy-L (**9**) and Dy-D (**10**).

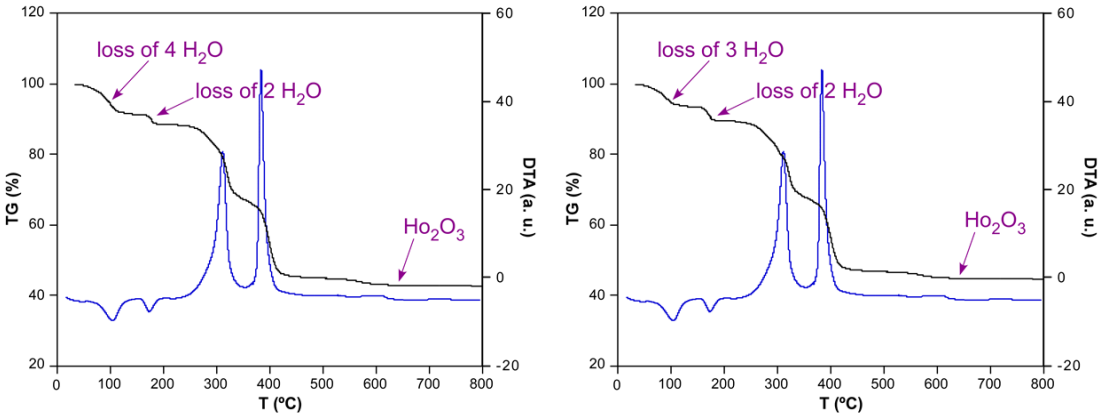

Figure SIII.5. TG/DTA analysis for compounds Ho-L (**11**) and Ho-D (**12**).

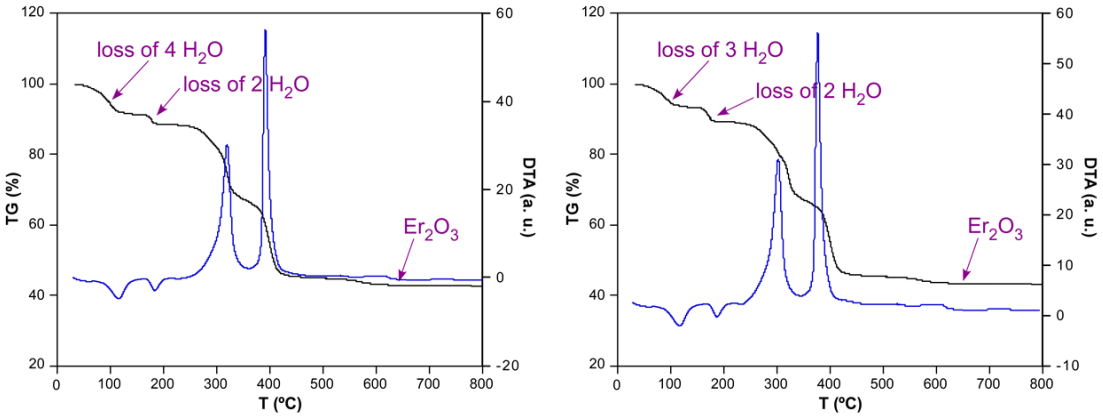

Figure SIII.6. TG/DTA analysis for compounds Er-L (**13**) and Er-D (**14**).

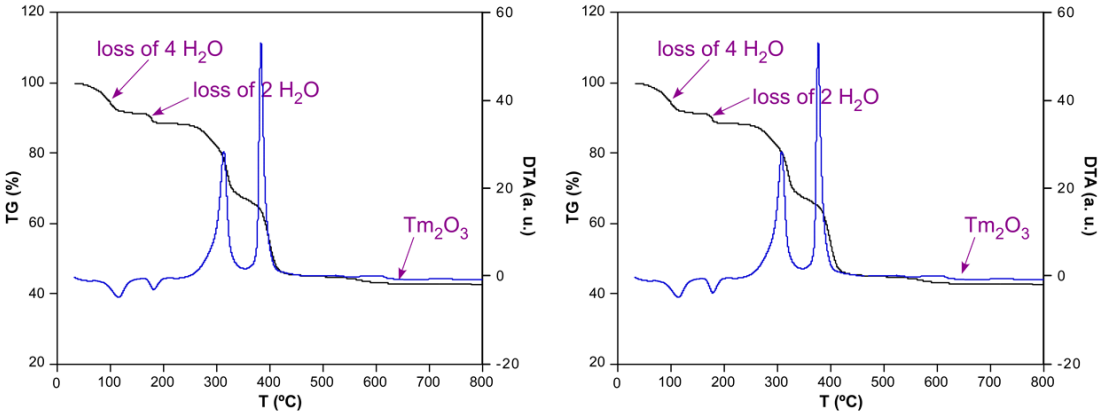

Figure SIII.7. TG/DTA analysis for compounds Tm-L (**15**) and Tm-D (**16**).

S7. Powder X-ray diffraction analysis

Pattern-matching analysis confirms the purity of the polycrystalline samples of all compounds.

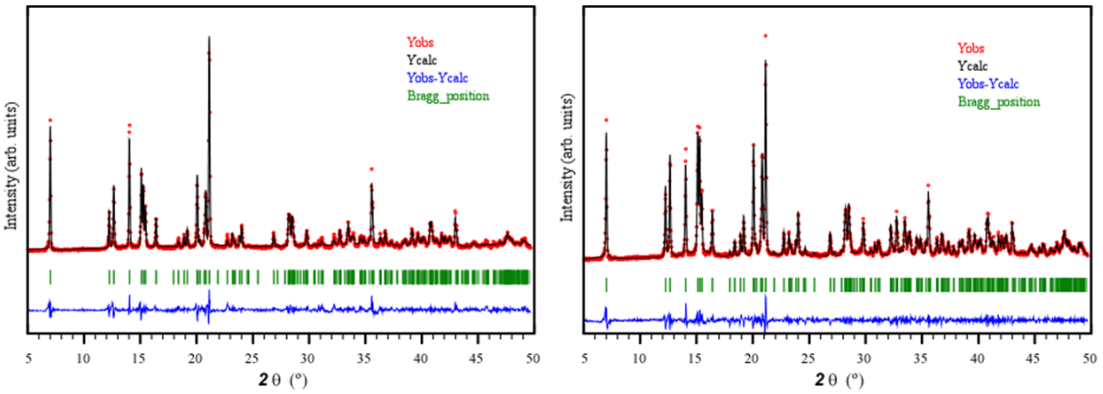

Figure SIII.8. Pattern-matching analysis of polycrystalline sample of compounds Tb-L (**7**) and Tb-D (**8**).

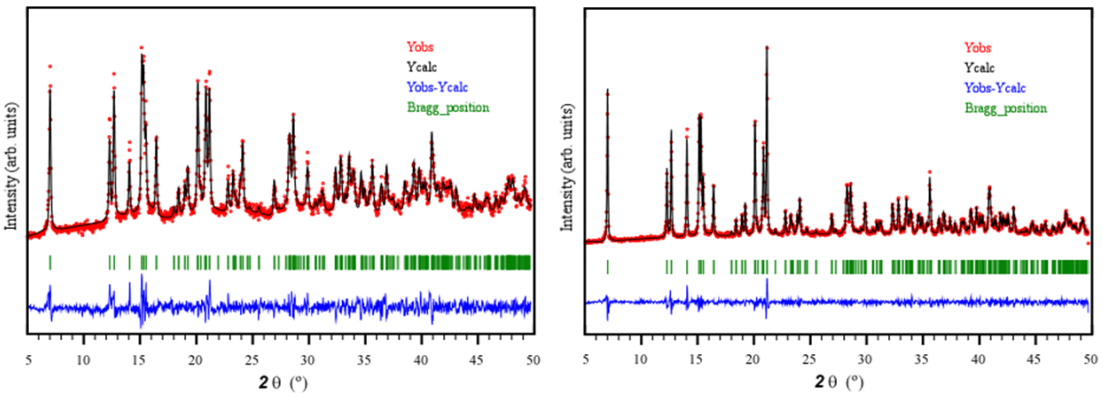

Figure SIII.9. Pattern-matching analysis of polycrystalline sample of compounds Dy-L (**9**) and Dy-D (**10**).

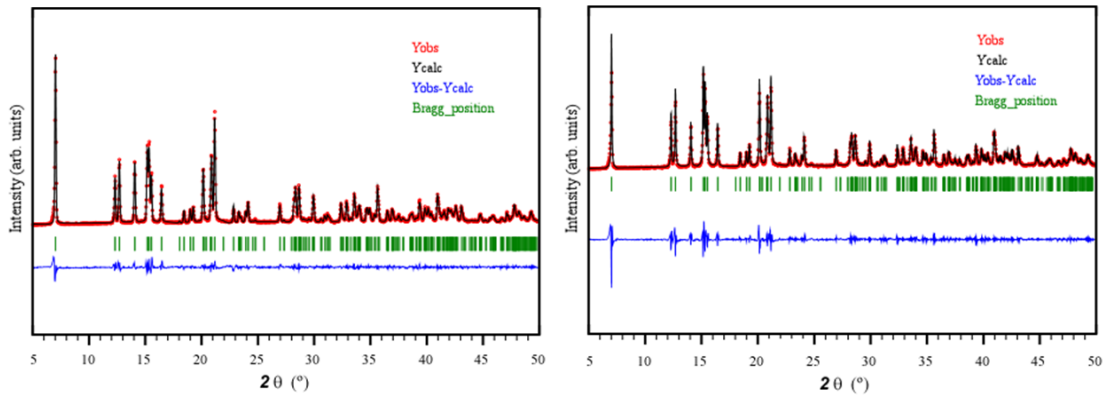

Figure SIII.10. Pattern-matching analysis of polycrystalline sample of compounds Ho-L (**11**) and Ho-D (**12**).

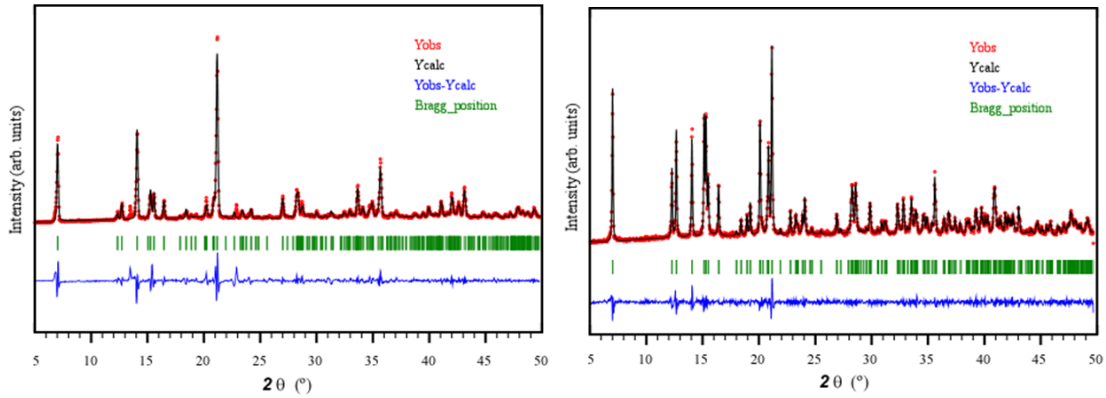

Figure SIII.11. Pattern-matching analysis of polycrystalline sample of compounds Er-L (**13**) and Er-D (**14**).

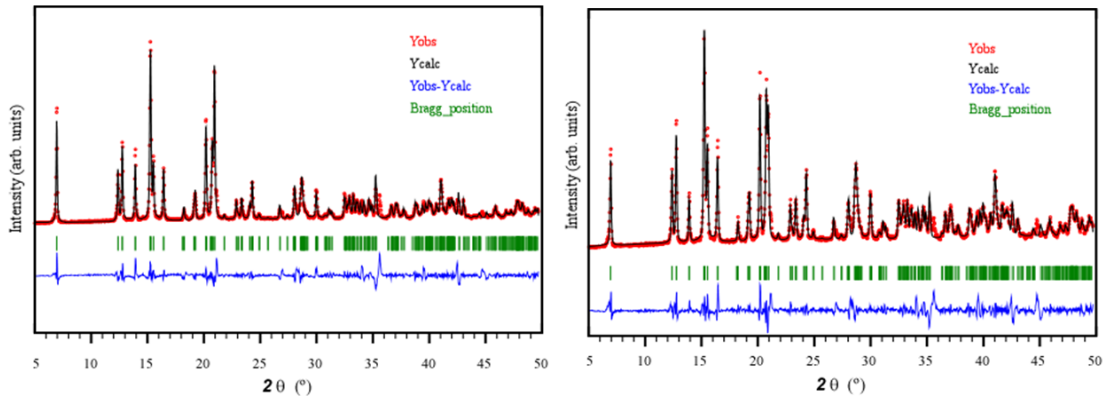

Figure SIII.12. Pattern-matching analysis of polycrystalline sample of compounds Tm-L (**15**) and Tm-D (**16**).

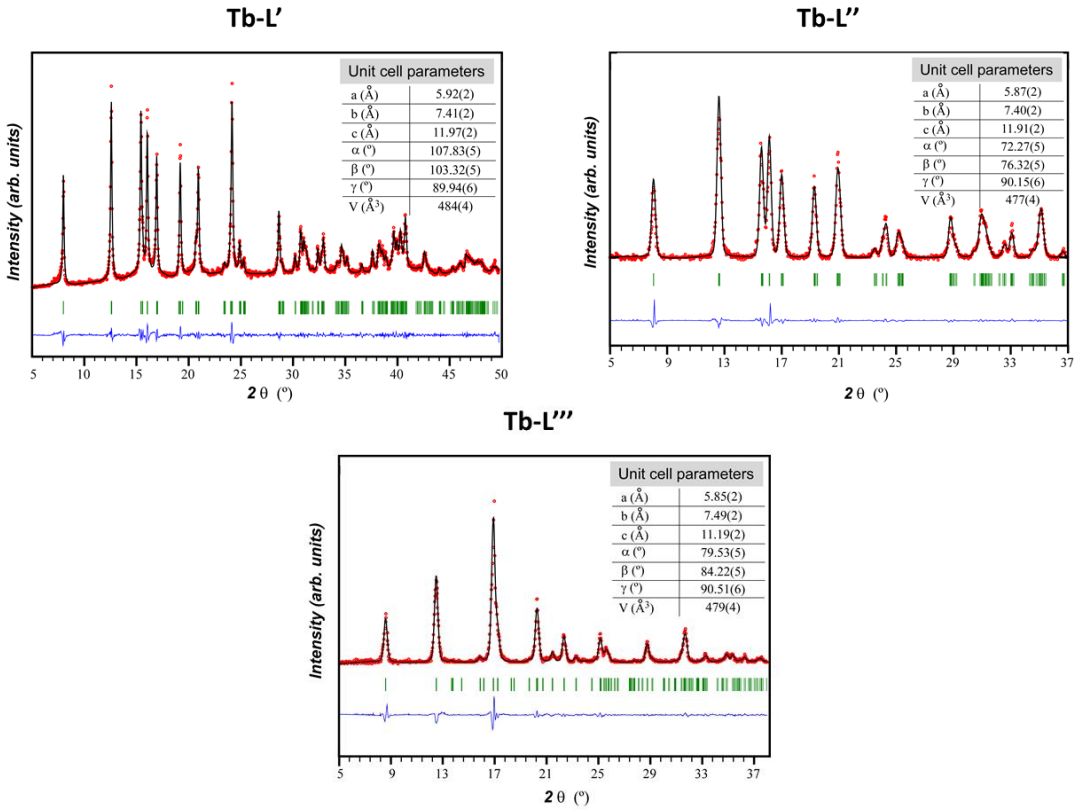

Figure SIII.13. Pattern-matching analysis of the activated polycrystalline sample of compounds Tb-L' (**17**), Tb-L'' (**18**) and Tb-L''' (**19**).

In view of the interesting behaviour shown by these MOFs upon dehydration, a polycrystalline sample of Tb-L (**7**) was selected to study the reversibility of the rehydration process. To that end, the sample was heated up to 210 °C for 4 hours (yielding Tb-L''' (**19**)) in an oven and a diffractogram was collected at open atmosphere (shown in orange in Figure SIII.14). The sample was then left at STP conditions and a diffractogram was collected at some selected times. As shown in Figure SIII.14, the material is rapidly rehydrated to give Tb-L' (**17**), which corresponds to a partially rehydrated phase. This phase shows a relatively large stability at these conditions and, actually, it needs to be exposed to humid conditions as to be completely rehydrated and give the initial Tb-L (**7**). Although no further studies could be performed to exactly know the conditions (relative humidity and temperature) at which the Tb-L' (**17**) → Tb-L (**7**) rehydration takes place (it was observed to occur but could not be measured), a simple experiment confirmed the reversibility. In particular, a solid sample of Tb-L' (**17**) was soaked in water and kept stirring for 2 hours. The sample was filtered, dried and characterized by PXRD, observing that it corresponds to Tb-L (**7**) compound. Therefore, it may be concluded that the Tb-L' (**17**) → Tb-L (**7**) is not dependent on the time elapsed but it needs a high water concentration in the medium that forces the coordination of water molecules and rearrangement of the tartrate ligands.

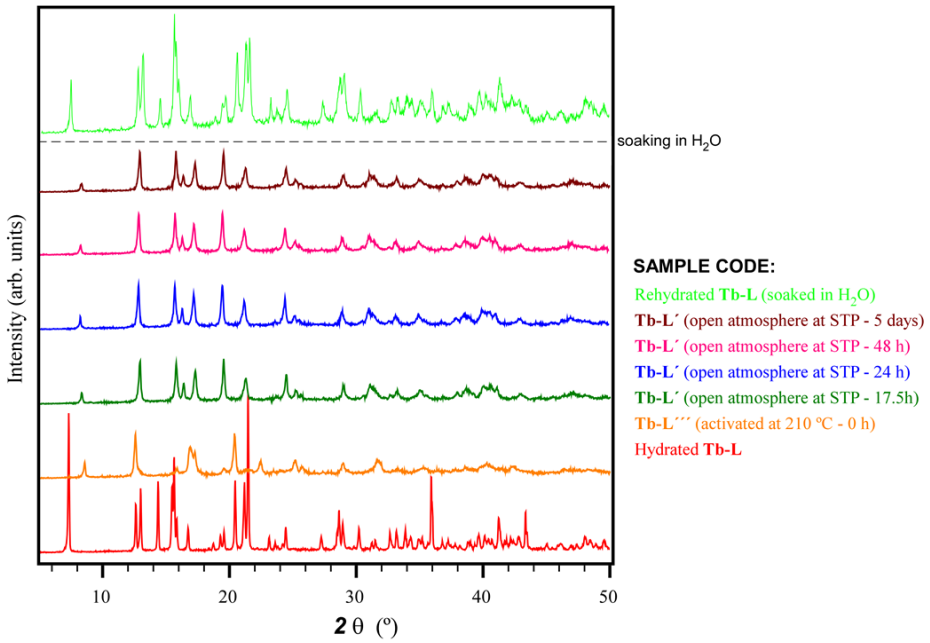

Figure SIII.14. PXRD sequence of Tb-L (**7**) to follow the reversible dehydration/rehydration process.

S8. FT-IR spectroscopy

At high frequencies of FTIR spectrum, all compounds exhibit an intense band around 3600 cm^{-1} that corresponds to the vibration of O-H bond of water. Between 3500 and 2900 cm^{-1} stretching bands of the alcoholic O–H bond are appeared. Weak shoulders between 2850 and 2400 cm^{-1} are attributed to C–H stretching vibrations of the tartrate ligand. The intense vibrations around 1610 cm^{-1} correspond to the asymmetric stretching of the carboxylate groups, while the symmetric stretching and bending of the same group occur in the lower range of 1500-1400 cm^{-1}. Bending bands of the C-H bonds are observed around 1320 cm^{-1}, followed by bending bands of the alcoholic O-H between 1300 and 1200 cm^{-1}. Stretching of C-O bond of the secondary alcohols occurs in the range of 1150-1000 cm^{-1}. Different bands at the range of 950-800 cm^{-1} are attributed to trisubstituted C–H bending vibrations. The vibration bands of the M–O bonds (M = Tb, Dy, Ho, Er, Tm) are observed around the range of 605-400 cm^{-1}.

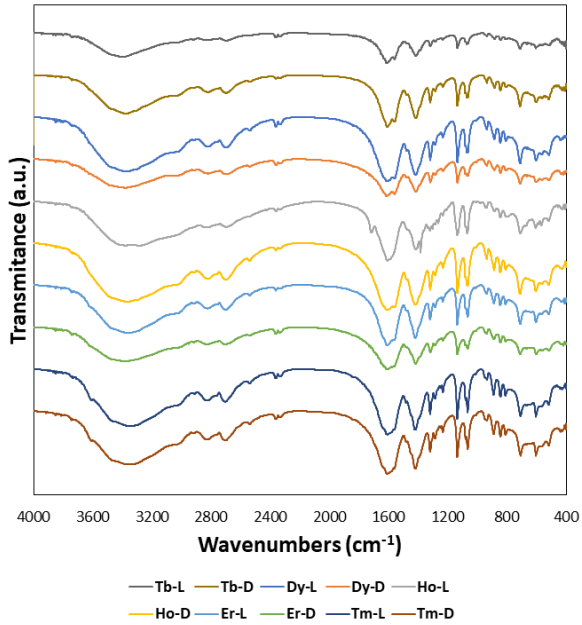

Figure SIII.15. FTIR spectra of (**7**-**16**) compounds.

S9. DC susceptibility measurements

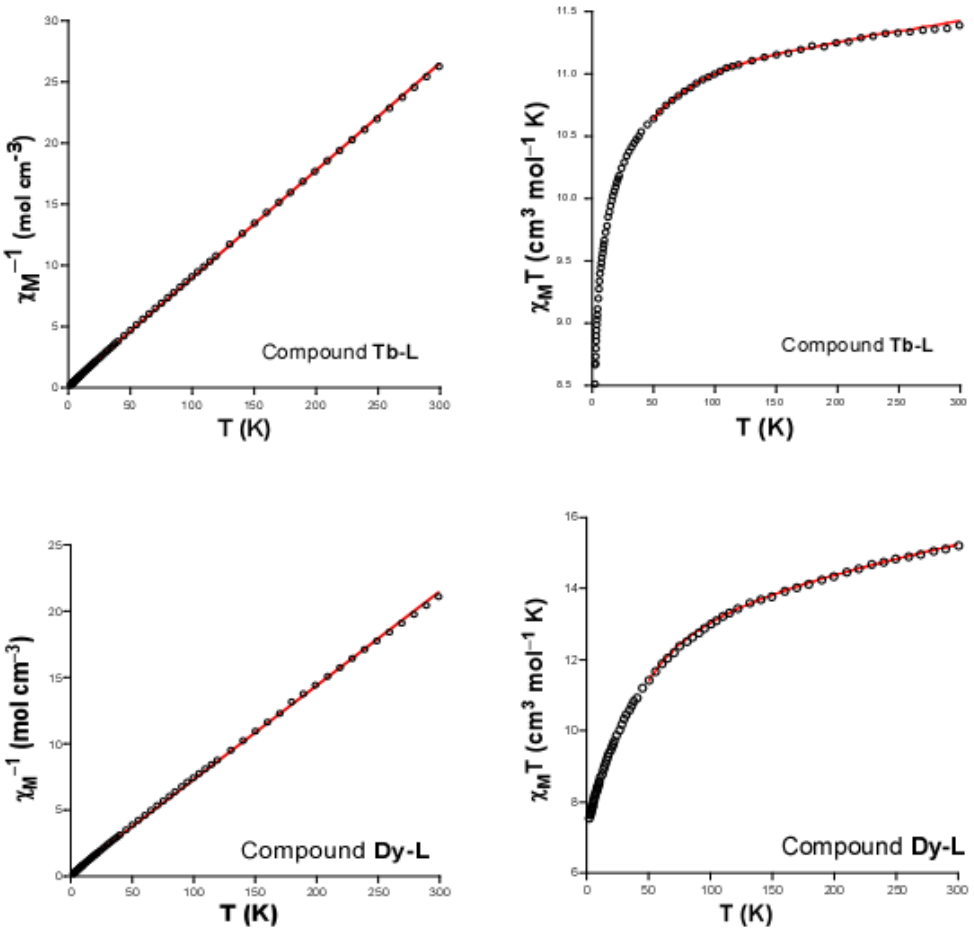

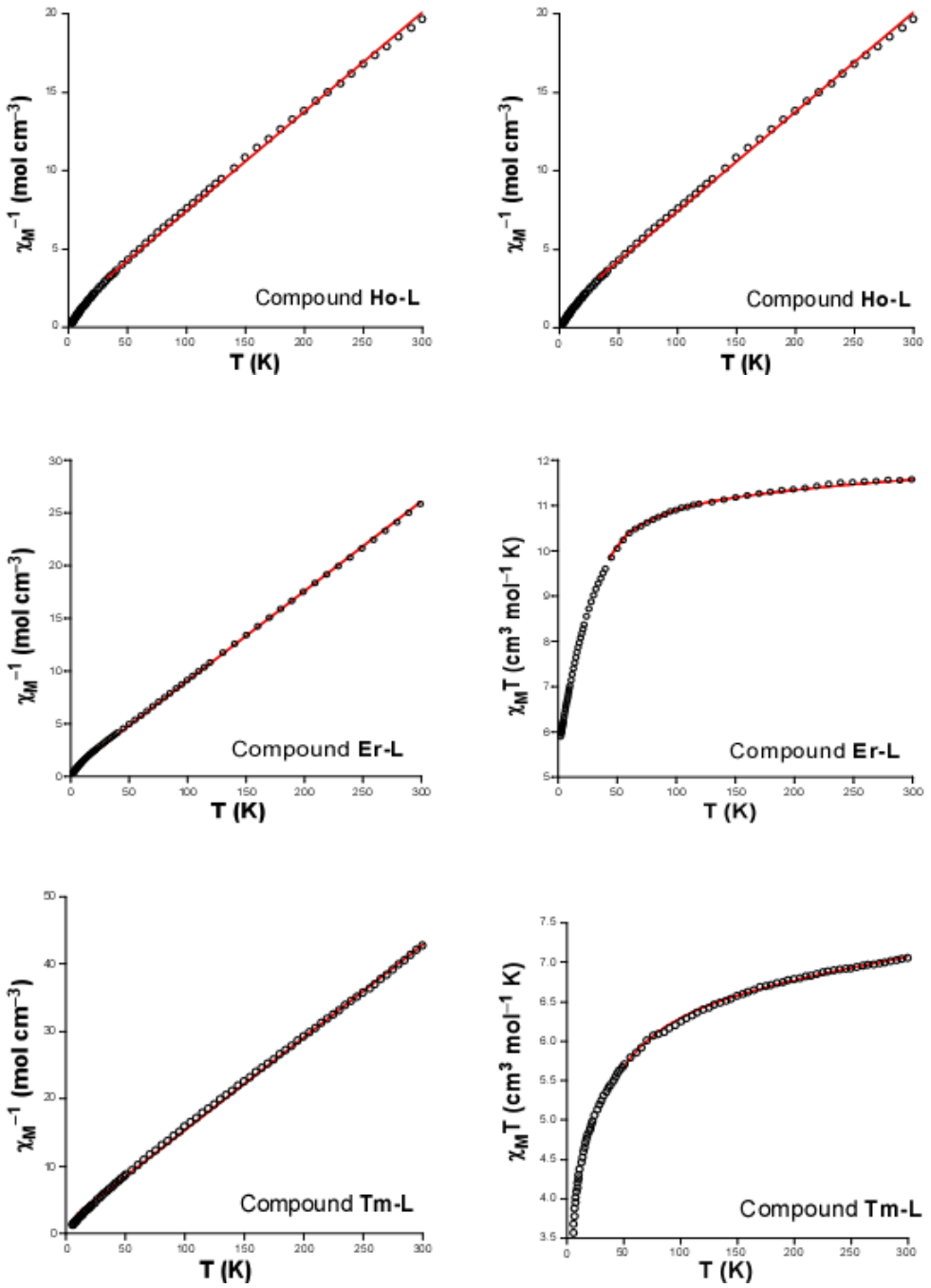

Figure SIII.16. χ_M^{-1} vs T and χ_MT vs T plots of all left-handed MOFs showing best theoretical fits (red line).

$$\chi_{Tb} = \frac{Ng^2\beta^2}{kT}\frac{2e^{-\Delta/kT}+4e^{-2\Delta/kT}+18e^{-9\Delta/kT}+32e^{-16\Delta/kT}+50e^{-25\Delta/kT}+72e^{-36\Delta/kT}}{1+2e^{-\Delta/kT}+2e^{-2\Delta/kT}+2e^{-9\Delta/kT}+2e^{-16\Delta/kT}+2e^{-25\Delta/kT}+2e^{-36\Delta/kT}} \quad \textit{(SIII.1)}$$

$$\chi_{Dy} = \frac{Ng^2\beta^2}{kT}\left(\frac{0.5e^{-0.25\Delta/kT}+4.5e^{-2.25\Delta/kT}+12.5e^{-6.25\Delta/kT}+24.5e^{-12.25\Delta/kT}}{1+2e^{-\Delta/kT}+2e^{-2\Delta/kT}+2e^{-9\Delta/kT}+2e^{-16\Delta/kT}+2e^{-25\Delta/kT}+2e^{-36\Delta/kT}}+\right.$$
$$\left.\frac{40.5e^{-20.25\Delta/kT}+60.5e^{-30.25\Delta/kT}+84.5e^{-42.25\Delta/kT}+112.5e^{-56.25\Delta/kT}}{1+2e^{-\Delta/kT}+2e^{-2\Delta/kT}+2e^{-9\Delta/kT}+2e^{-16\Delta/kT}+2e^{-25\Delta/kT}+2e^{-36\Delta/kT}}\right) \quad \textit{(SIII.2)}$$

$$\chi_{Er} = \frac{Ng^2\beta^2}{kT}\left(\frac{0.5e^{-0.25\Delta/kT} + 4.5e^{-2.25\Delta/kT} + 12.5e^{-6.25\Delta/kT} + 24.5e^{-12.25\Delta/kT}}{1 + 2e^{-\Delta/kT} + 2e^{-2\Delta/kT} + 2e^{-9\Delta/kT} + 2e^{-16\Delta/kT} + 2e^{-25\Delta/kT} + 2e^{-36\Delta/kT}} + \frac{40.5e^{-20.25\Delta/kT} + 60.5e^{-30.25\Delta/kT} + 84.5e^{-42.25\Delta/kT} + 112.5e^{-56.25\Delta/kT}}{1 + 2e^{-\Delta/kT} + 2e^{-2\Delta/kT} + 2e^{-9\Delta/kT} + 2e^{-16\Delta/kT} + 2e^{-25\Delta/kT} + 2e^{-36\Delta/kT}}\right) \quad \textit{(SIII.3)}$$

S10. DFT based calculation of the magnetic exchange constant

The coupling constant of the magnetic exchange was calculated through the three non-equivalent superexchange pathways that cross tartrate ligands showing different coordination modes, which imposes three different distances between lanthanide(III) atoms. The calculations were carried out on a gadolinium(III)-based dimeric models due to the quenched angular orbital momentum in the states of this ion (ground term is $^8S_{7/2}$). DFT based broken symmetry strategy has been calculated to achieve the value of J for the three superexchange pathways.

Superexchange path	1	2	3
J (cm^{-1})	0.003	0	0.003

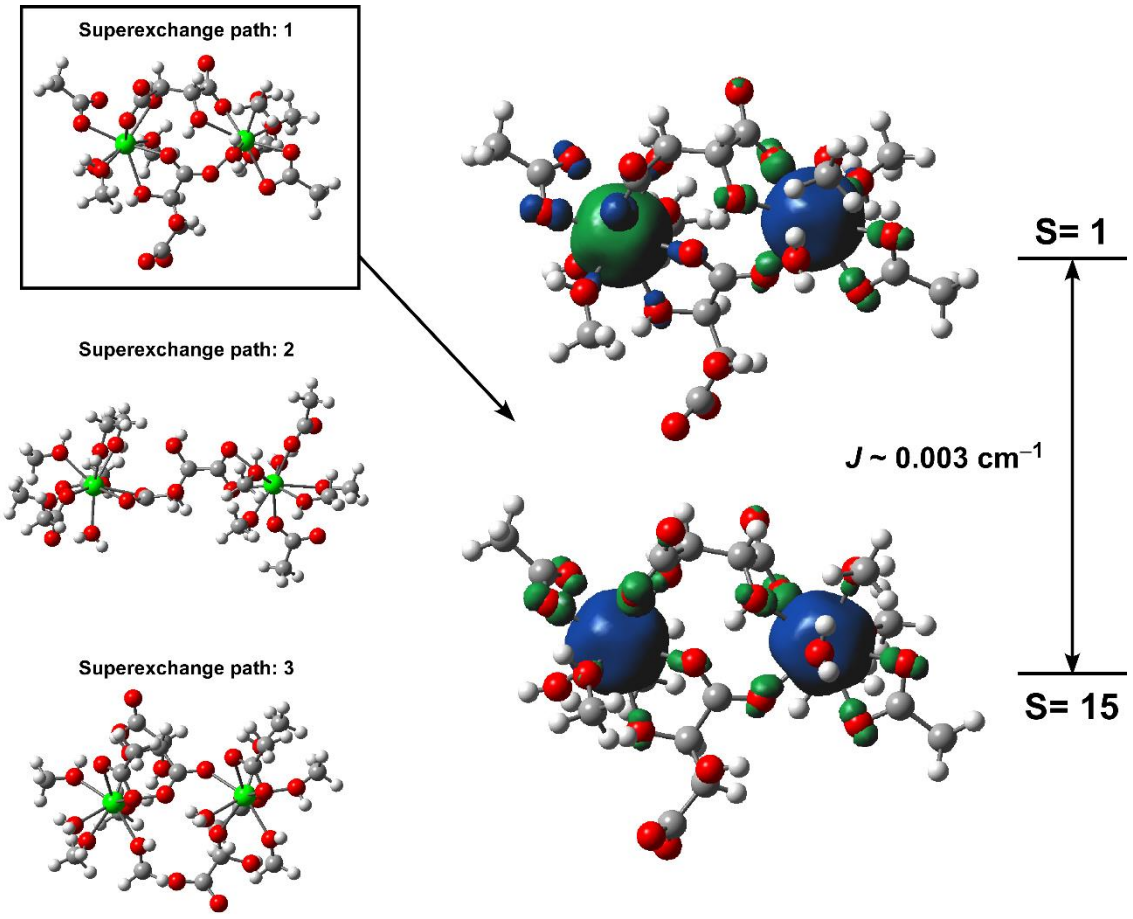

Figure SIII.17. View of the superexchange pathways on dimeric models of a gadolinium(III) based MOF showing the spin density distribution on the pathway number 1.

S11. Magnetic *ac* measurements

Under zero *dc* field

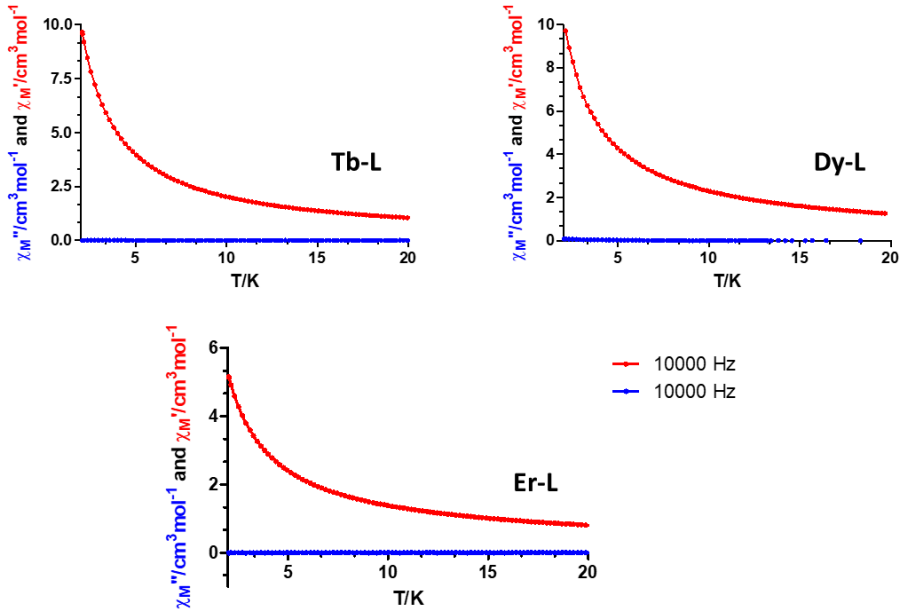

Figure SIII.18. Temperature dependence of in-phase (red) and out-of-phase (blue) components of the *ac* susceptibility in a zero applied *dc* field for Tb-L (**7**), Dy-L (**9**) and Er-L (**13**).

H_{dc} = 1000 Oe for Tb-L (7)

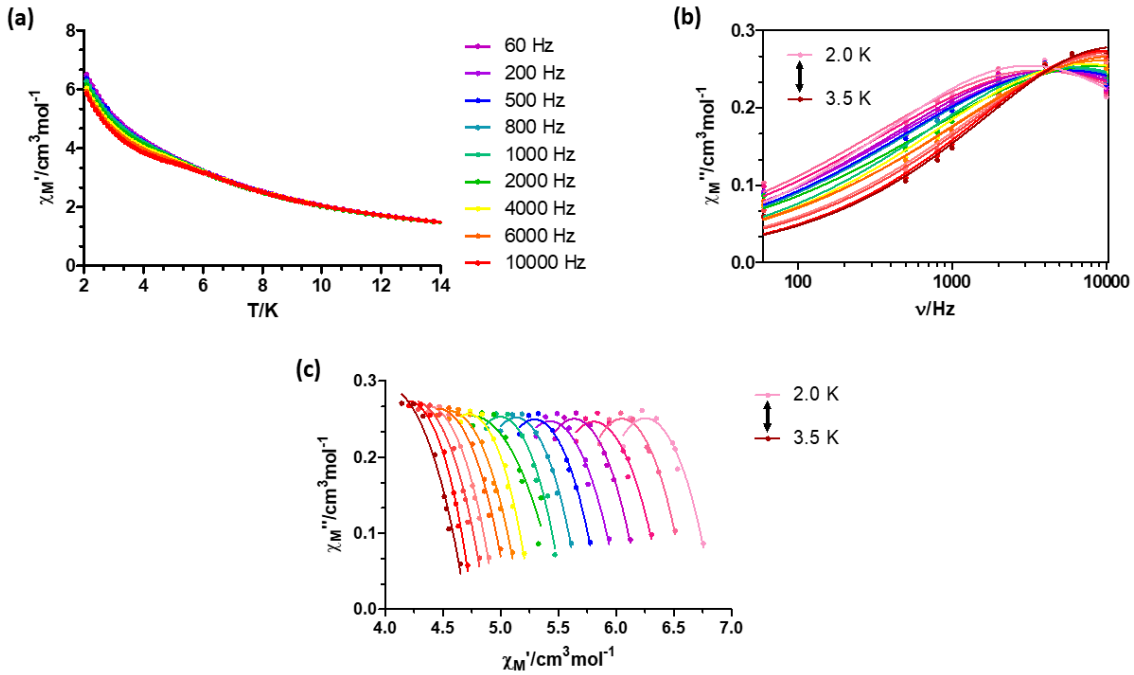

Figure SIII.19. (a) Temperature dependence of in-phase component of the *ac* susceptibility in a *dc* applied field of 1 kOe for Tb-L (**7**). **(b)** Variable-temperature frequency dependence of the χ_M'' signal under 1 kOe applied field for Tb-L (**7**). Solid lines represent the best fitting of the experimental data to the Debye model. **(c)** Cole-Cole plots under 1 kOe field for Tb-L (**7**). Solid lines represent the best fit to the generalized Debye model.

H_{dc} = 1000 Oe for Dy-L (9)

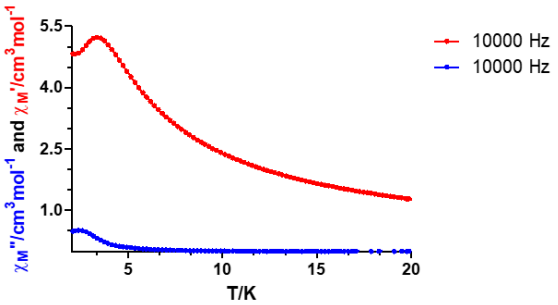

Figure SIII.20. Temperature dependence of in-phase (red) and out-of-phase (blue) components of the *ac* susceptibility in a *dc* applied field of 1 kOe for Dy-L (**9**).

H_{dc} = 1000 Oe for Er-L (13)

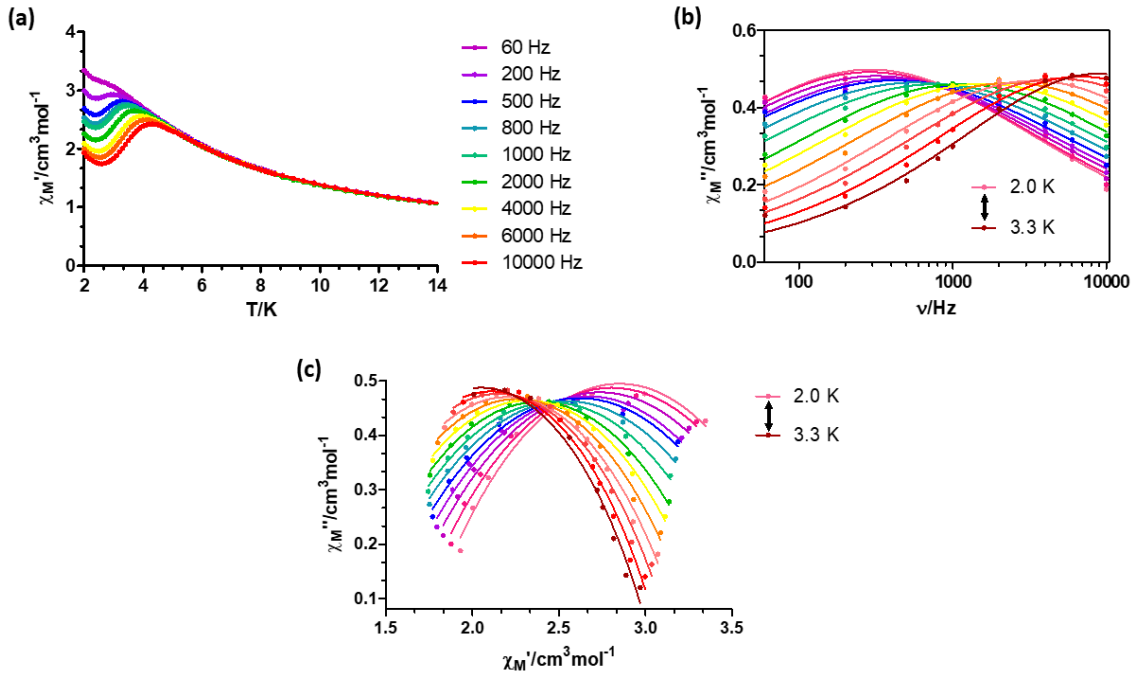

Figure SIII.21. (a) Temperature dependence of in-phase component of the *ac* susceptibility in a *dc* applied field of 1 kOe for Er-L (**13**). **(b)** Variable-temperature frequency dependence of the χ_M'' signal under 1 kOe applied field for Er-L (**13**). Solid lines represent the best fitting of the experimental data to the Debye model. **(c)** Cole-Cole plots under 1 kOe field for Er-L (**13**). Solid lines represent the best fit to the generalized Debye model.

Under zero *dc* field measurements for diluted samples

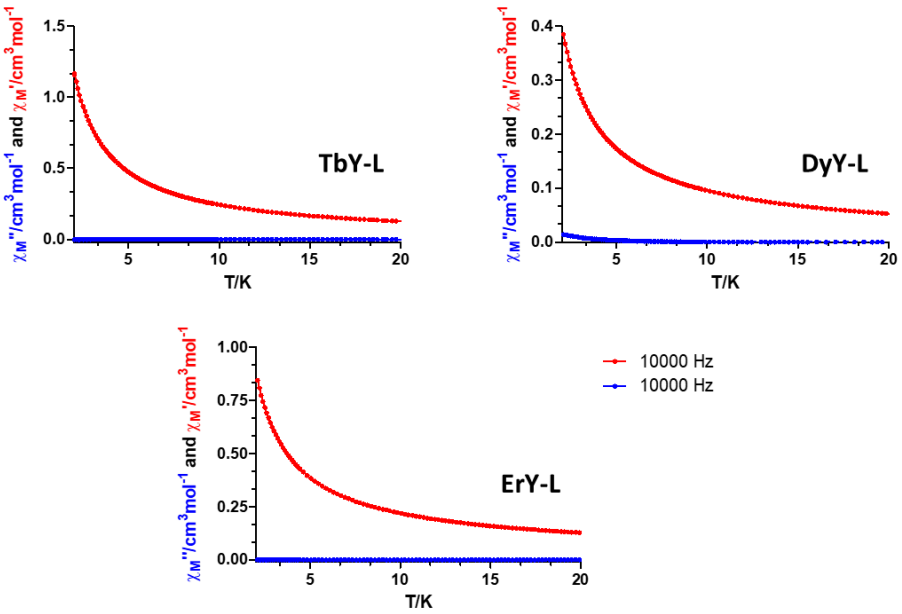

Figure SIII.22. Temperature dependence of in-phase (red) and out-of-phase (blue) components of the *ac* susceptibility in a zero applied *dc* field for TbY-L (**23**), DyY-L (**24**) and ErY-L (**25**).

H_{dc} = 1000 Oe for TbY-L (23)

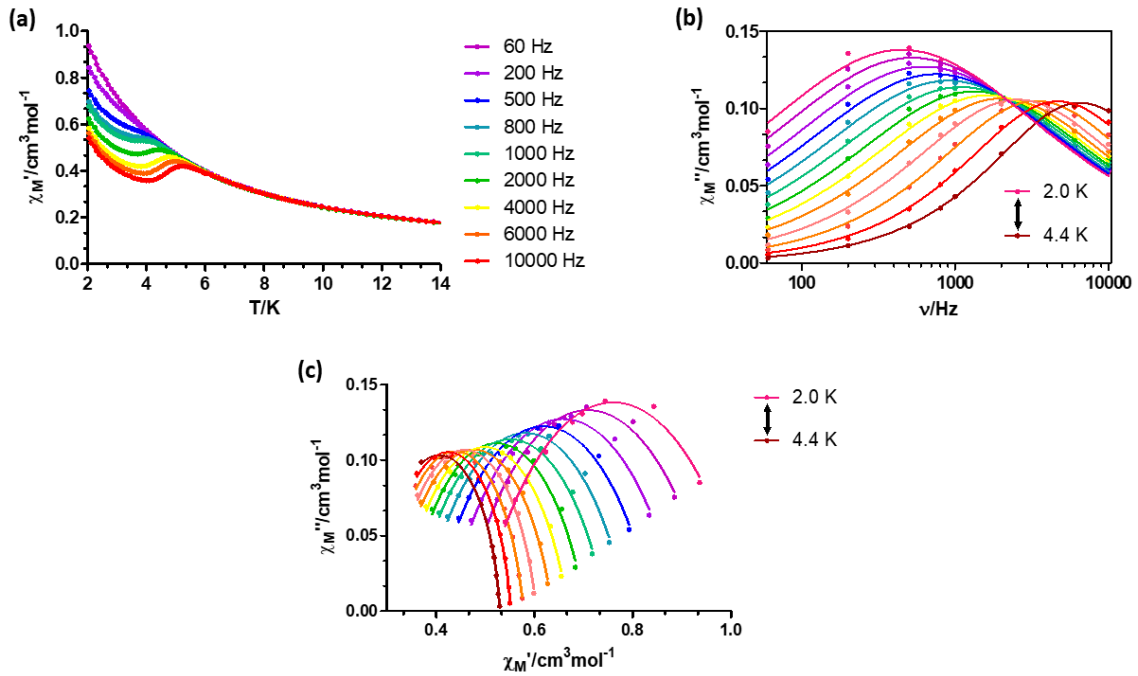

Figure SIII. 23. **(a)** Temperature dependence of in-phase component of the *ac* susceptibility in a *dc* applied field of 1 kOe for TbY-L (**23**). **(b)** Variable-temperature frequency dependence of the χ_M'' signal under 1 kOe applied field for TbY-L (**23**). Solid lines represent the best fitting of the experimental data to the Debye model. **(c)** Cole-Cole plots under 1 kOe field for TbY-L (**23**). Solid lines represent the best fit to the generalized Debye model.

H_{dc} = 1000 Oe for DyY-L (24)

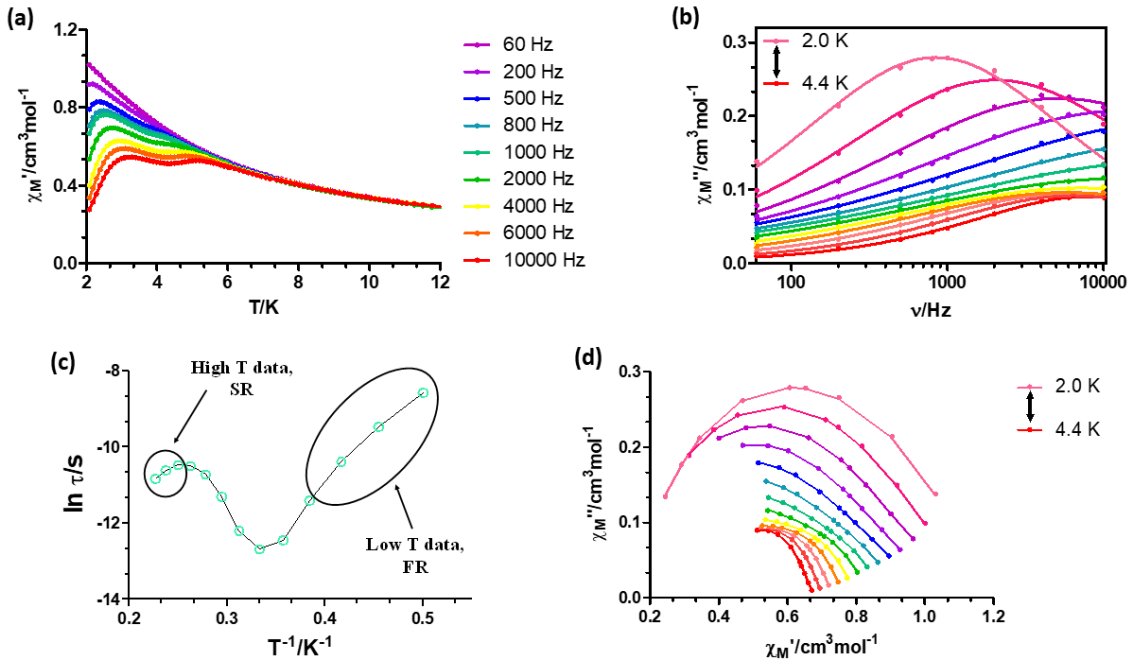

Figure SIII.24. (a) Temperature dependence of in-phase component of the *ac* susceptibility in a *dc* applied field of 1 kOe for DyY-L (**24**). **(b)** Variable-temperature frequency dependence of the χ_M'' signal under 1 kOe applied field for DyY-L (**24**). Solid lines represent the best fitting of the experimental data to the Debye model. **(c)** Arrhenius plot for the relaxation times of DyY-L (**24**) fitting the data to a single process. The solid line is a guide for the eye. **(d)** Cole-Cole plots under 1 kOe field for DyY-L (**24**). Solid lines represent the best fit to the generalized Debye model.

Table SIII.13. Relaxation fitting parameters from least-squares fitting of χ(ϕ) data for compound DyY-L (**24**).

T (K)	FR		SR	
	α_1	τ_1	α_2	τ_2
2.0	0.22	9.81E-05	-	-
2.1	0.28	8.16E-05	-	-
2.2	0.31	6.34E-05	-	-
2.3	0.32	4.51E-05	-	-
2.4	0.38	3.37E-05	-	-
2.5	0.35	2.42E-05	-	-
2.6	0.38	1.86E-05	-	-
2.7	0.39	1.31E-05	-	-
2.8	0.40	9.77E-06	-	-
2.9	0.47	6.48E-06	-	-
3.0	-	-	0.34	9.70E-04
3.1	-	-	0.15	7.48E-04
3.2	-	-	0.22	5.52E-04
3.3	-	-	0.31	3.12E-04
3.4	-	-	0.33	2.11E-04
3.5	-	-	0.34	1.60E-04
3.6	-	-	0.35	1.25E-04
3.7	-	-	0.36	9.62E-05
3.8	-	-	0.36	7.67E-05
3.9	-	-	0.33	6.76E-05

4.0	-	-	0.32	5.46E-05
4.1	-	-	0.22	5.36E-05
4.2	-	-	0.20	4.58E-05
4.3	-	-	0.15	3.92E-05
4.4	-	-	0.11	3.38E-05

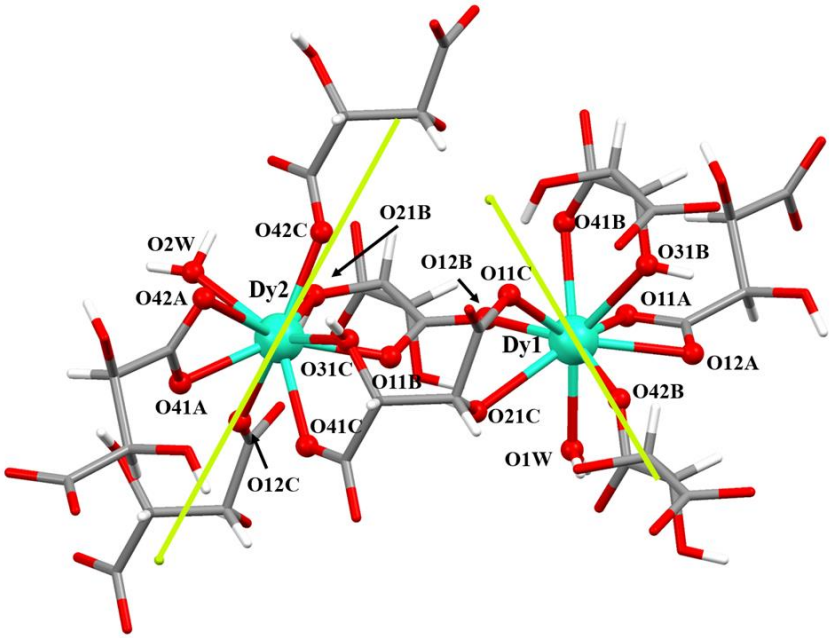

Figure SIII.25. Magnetic axes of the Dy(III) ions calculated with the Magellan software. Both independent Dy1 and Dy2 ions along with the eight coordinated L-tartrate molecules were included in the calculation. Crystallization water molecules were omitted.

H_{dc} = 1000 Oe for ErY-L (25)

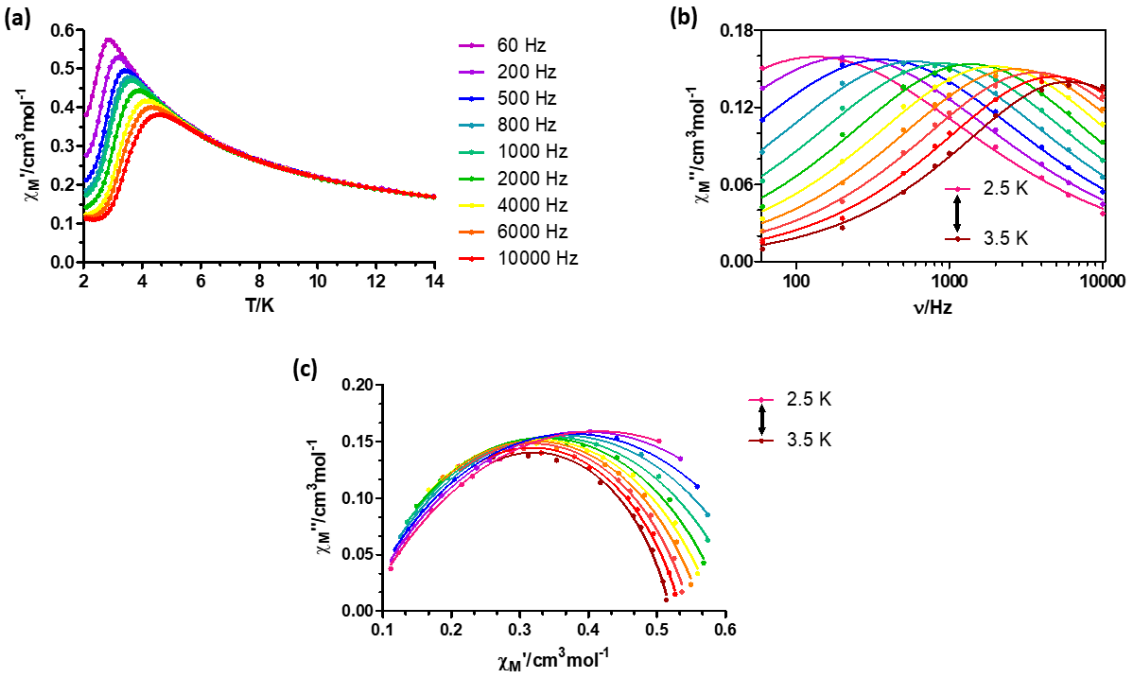

Figure SIII.26. (a) Temperature dependence of in-phase component of the *ac* susceptibility in a *dc* applied field of 1 kOe for ErY-L (**25**). **(b)** Variable-temperature frequency dependence of the χ_M'' signal under 1 kOe applied field for ErY-L (**25**). Solid lines represent the best fitting of the experimental data to the Debye model. **(c)** Cole-Cole plots under 1 kOe field for ErY-L (**25**). Solid lines represent the best fit to the generalized Debye model.

Under zero *dc* field measurements for thermally activated DyY-L samples

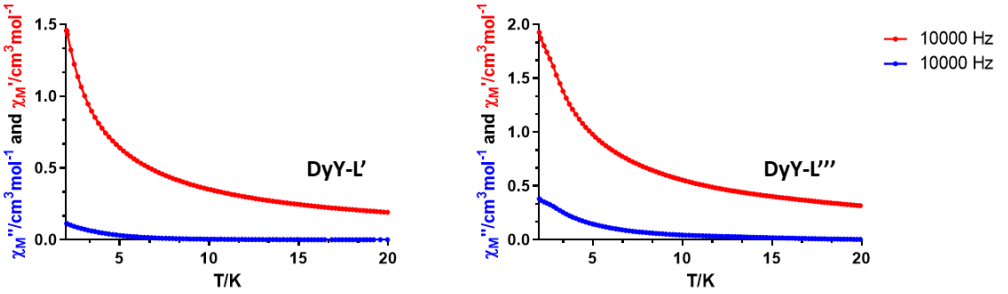

Figure SIII.27. Temperature dependence of in-phase (red) and out-of-phase (blue) components of the *ac* susceptibility in a zero applied *dc* field for DyY-L' (**26**) and DyY-L''' (**28**).

H_{dc} = 1000 Oe for DyY-L' (26)

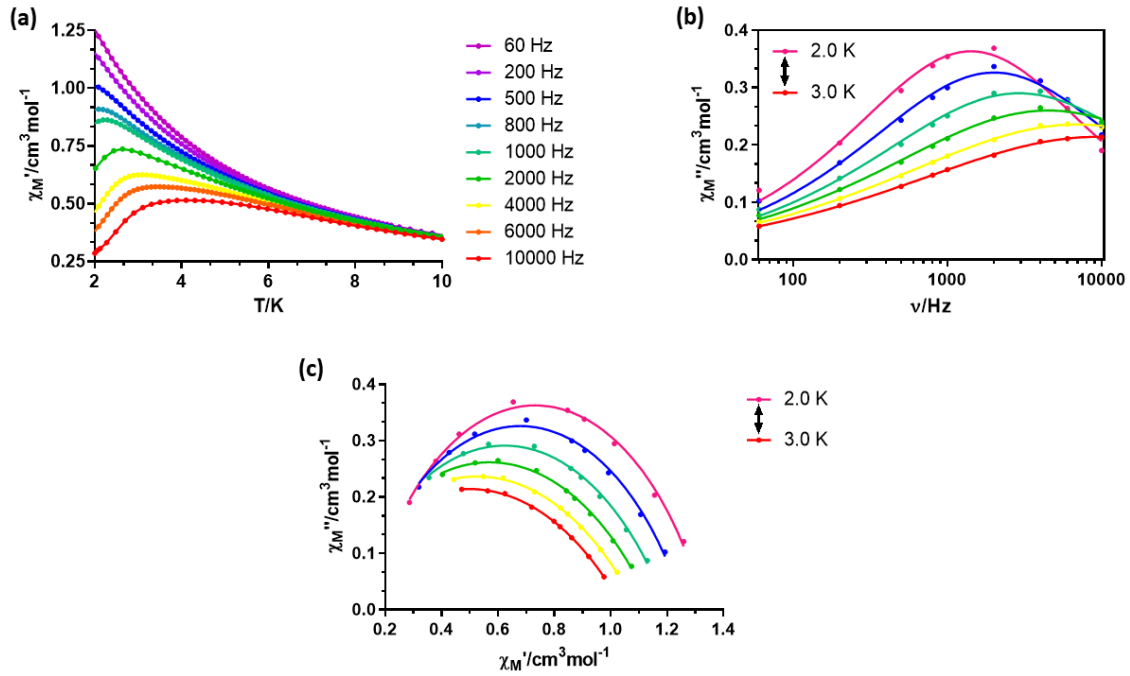

Figure SIII.28. **(a)** Temperature dependence of in-phase component of the *ac* susceptibility in a *dc* applied field of 1 kOe for DyY-L' (**26**). **(b)** Variable-temperature frequency dependence of the χ_M" signal under 1 kOe applied field for DyY-L' (**26**). Solid lines represent the best fitting of the experimental data to the Debye model. **(c)** Cole-Cole plots under 1 kOe field for DyY-L' (**26**). Solid lines represent the best fit to the generalized Debye model.

H_{dc} = 1000 Oe for DyY-L''' (28)

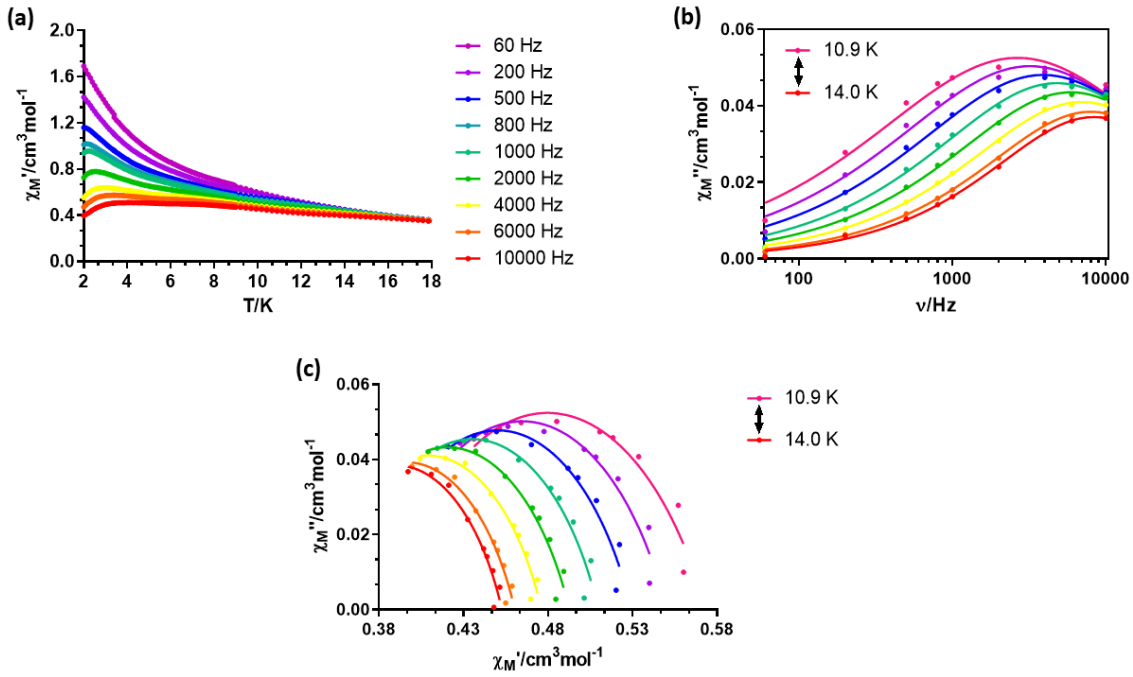

Figure SIII.29. (a) Temperature dependence of in-phase component of the *ac* susceptibility in a *dc* applied field of 1 kOe for DyY-L''' (**28**). **(b)** Variable-temperature frequency dependence of the χ_M" signal under 1 kOe applied field

for DyY-L''' (**28**). Solid lines represent the best fitting of the experimental data to the Debye model. **(c)** Cole-Cole plots under 1 kOe field for DyY-L''' (**28**). Solid lines represent the best fit to the generalized Debye model.

S12. Photoluminescence measurements

The following figure shows a comparative view of the visible spectra collected for the dysprosium based enantiomeric MOFs (compounds Dy-L (**9**) and Dy-D (**10**)) under the same experimental conditions to corroborate their equality.

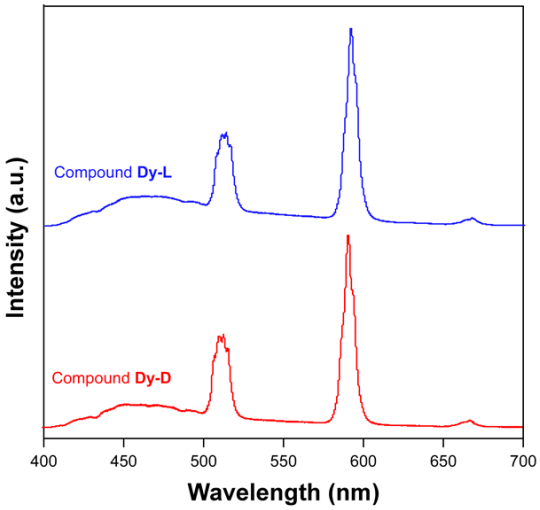

Figure SIII.30. Emission spectra of Dy-based compounds (Dy-L (**9**) and Dy-D (**10**)) under λ_{ex} = 325 nm taken at room temperature.

When compounds Ho-L (**11**) and Er-L (**13**) are exposed to UV excitation, they only display emission bands in the visible spectrum (see Figure SIII.31 and Figure SIII.32). The whole emission band corresponds to a unique excitation pathway given that all excitation spectra recorded under different emission lines show almost the same pattern, except for the intensity which changes according to the emission wavelength.

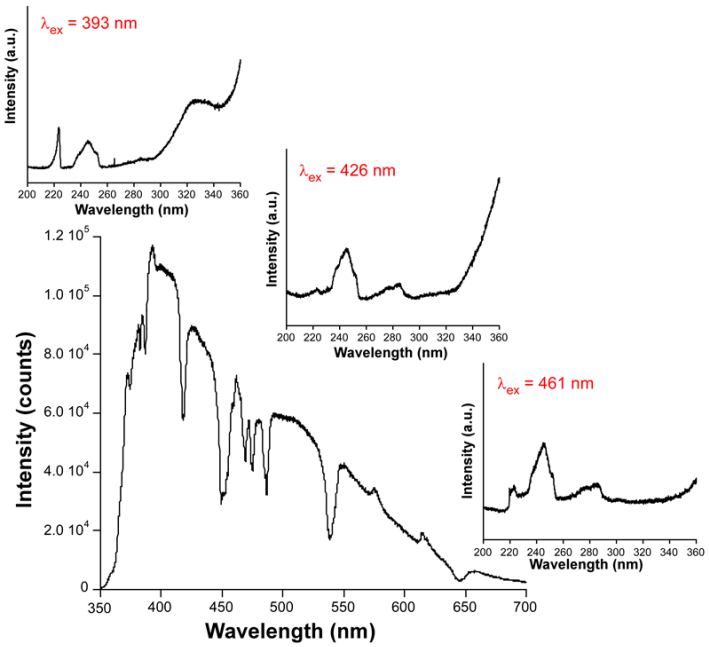

Figure SIII.31. Emission (λ_{ex} = 325 nm) and excitation (on main emissions) spectra of compounds Ho-L (**11**).

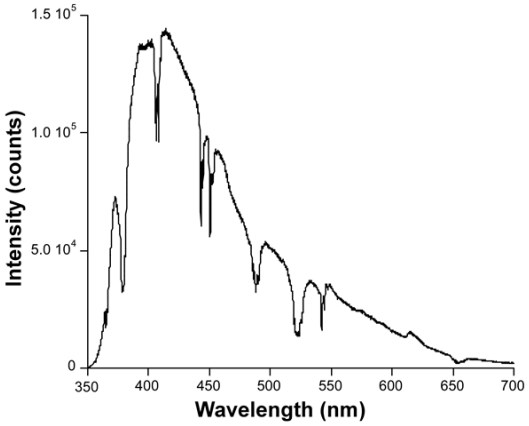

Figure SIII.32. Emission (λ_{ex} = 325 nm) spectrum of compound Er-L (**13**).

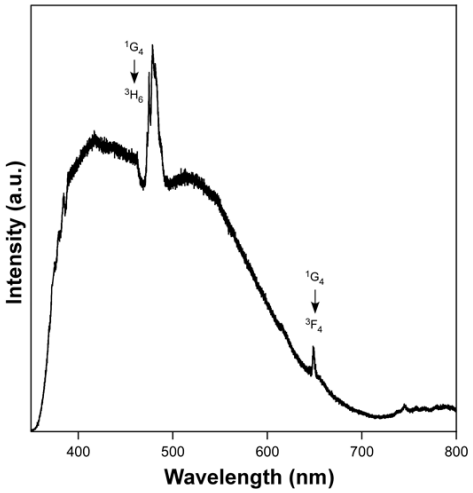

Figure SIII.33. Emission (λ_{ex} = 325 nm) spectrum of compound Tm-L (**15**) recorded at 10 K.

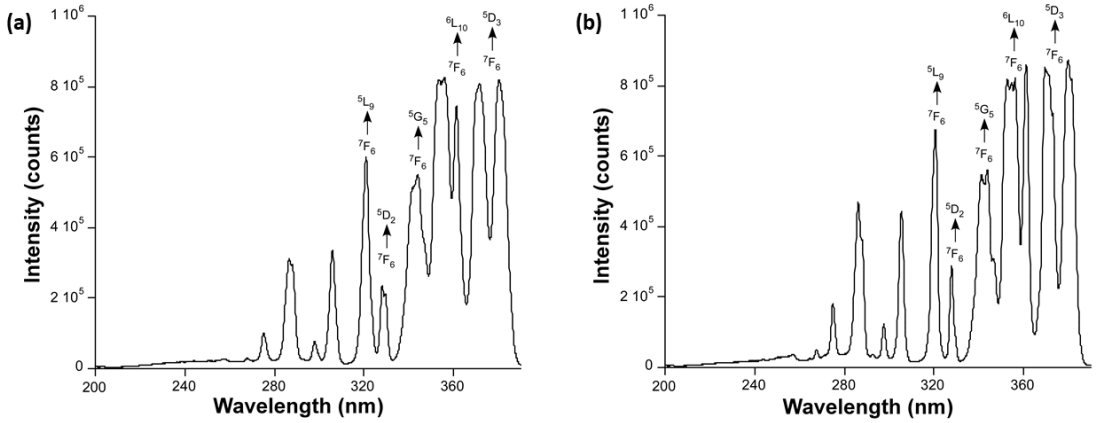

Figure SIII.34. Excitation spectra recorded at the main emission line at 544 nm for compound Tb-L (**7**) **(a)** at room temperature and **(b)** 10 K.

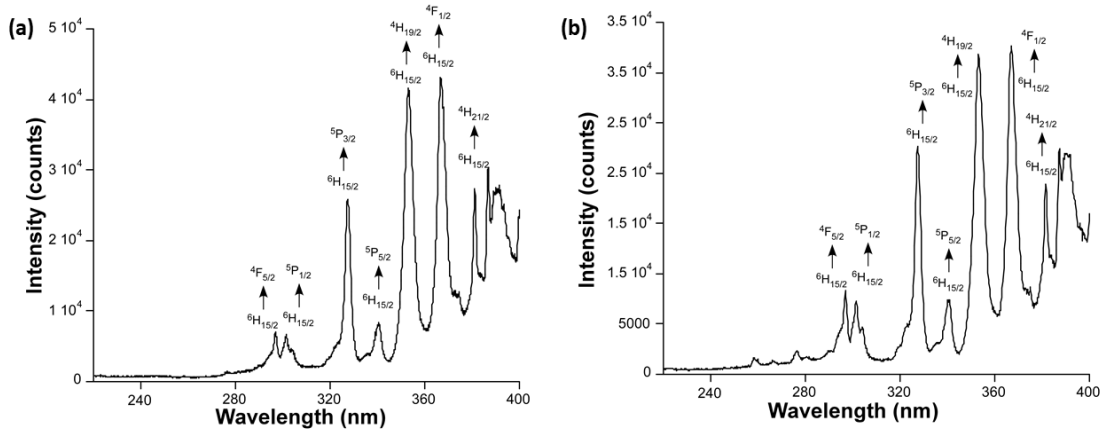

Figure SIII.35. Excitation spectra recorded at the main emission line at 573 nm for compounds **(a)** Dy-L (**9**) and **(b)** Dy-D (**10**) acquired at room temperature.

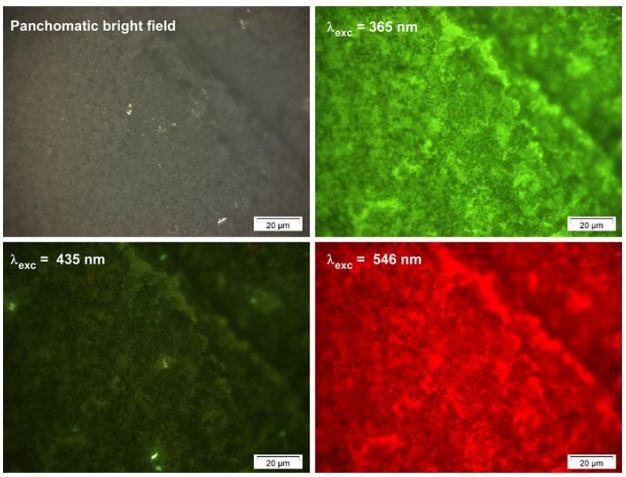

Figure SIII.36. Micro-PL images taken on polycrystalline sample of compound Tb-L (**7**) under different excitation beams.

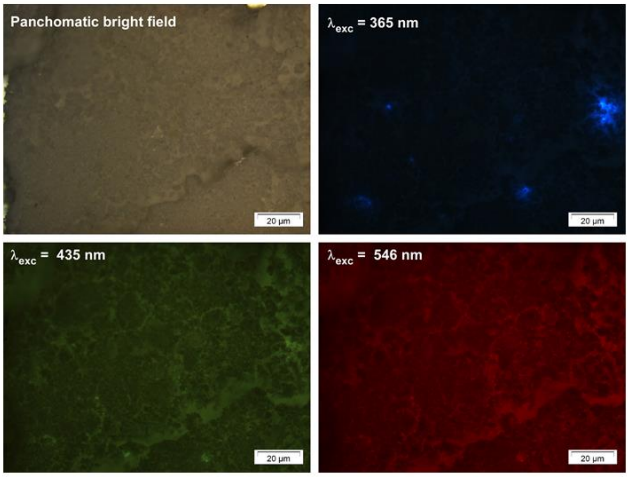

Figure SIII.37. Micro-PL images taken on polycrystalline sample of compound Dy-L (**9**) under different excitation beams.

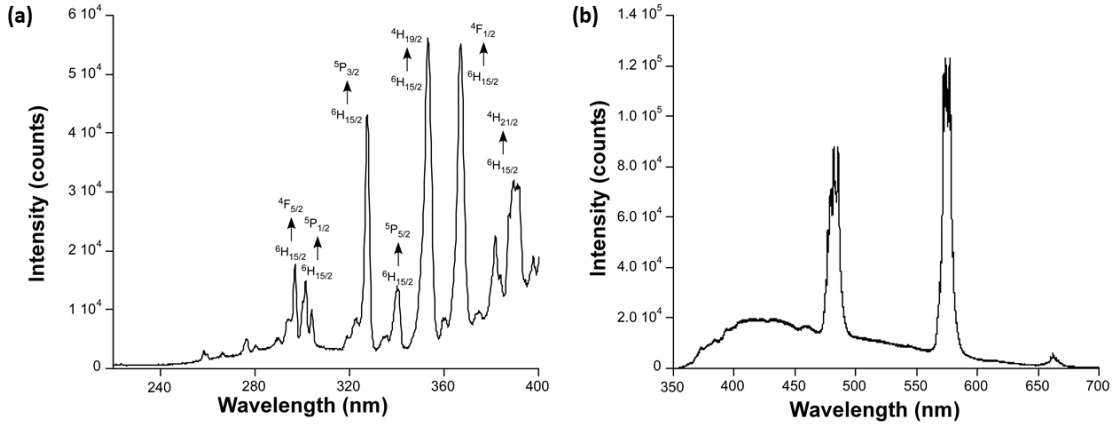

Figure SIII.38. Low temperature (10 K) **(a)** excitation and **(b)** emission spectra recorded at the main emission line of compound Dy-L (**9**).

Emission spectra of compound Tb-L (**7**) were performed at different temperatures in order to check whether it shows thermochromic behaviour. However, as inferred from Figure SIII.39, the emission of the compound is almost unchanged with the temperature, showing almost no change in the integrated intensity in the whole 10-300 K range.

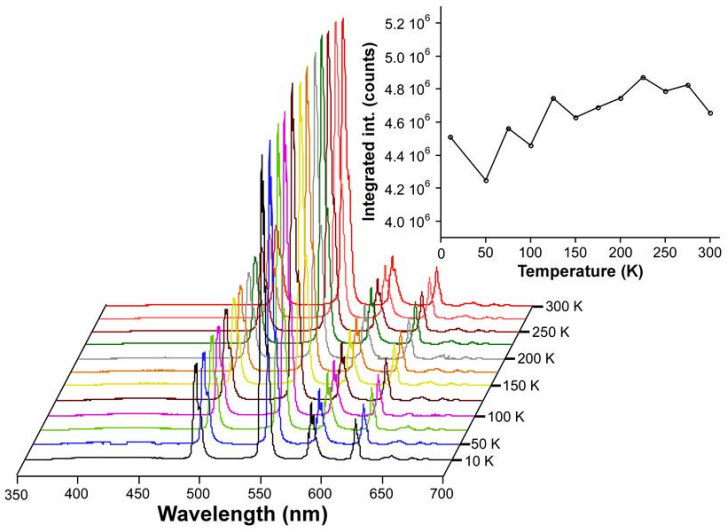

Figure SIII.39. Variable temperature emission spectra recorded at 325 nm excitation for compounds Tb-L (**7**). Inset plot represents the change in the integrated intensity.

As shown in the thermal behaviour of these MOFs, they show two phase transformations according to the heating of the sample. In particular, when Dy-L (**9**) sample is heated at 110 °C it losses three lattice and one coordination water molecules to render Dy-L' (**20**), which possesses the $\{[Dy_2(\mu_4\text{-tart})_2(\mu\text{-tart})(H_2O)]\cdot H_2O\}_n$ formula. This fact changes a bit the photoluminescent properties of the compound.

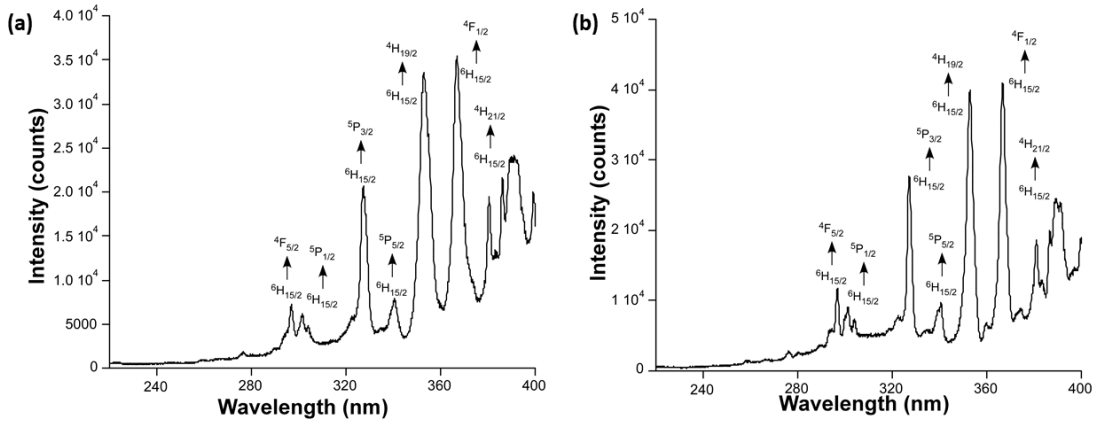

Figure SIII.40. Excitation spectra recorded at the main emission line at 573 nm for the thermally activated Dy-L' (**20**) **(a)** at room temperature and **(b)** at 10 K.

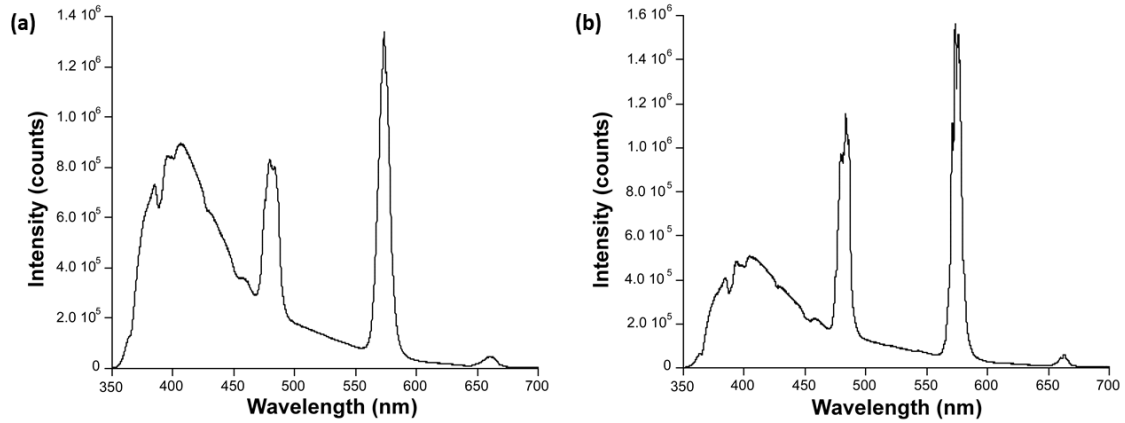

Figure SIII.41. Emission spectra recorded at 325 nm excitation the thermally activated Dy-L' (**20**) **(a)** at room temperature and **(b)** at 10 K.

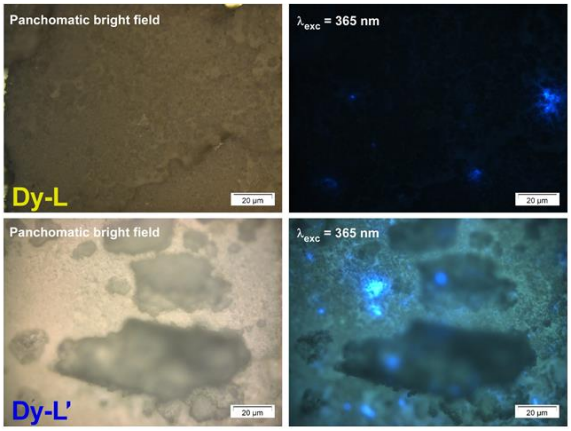

Figure SIII.42. Comparative micro-PL images taken under λ_{ex} = 365 nm on polycrystalline samples of Dy-L (**9**) and Dy-L' (**20**).

As mentioned in the manuscript and S5 section, Dy-L' (**20**) can be further dehydrated to achieve Dy-L'' (**21**) and Dy-L''' (**22**) crystalline phases, with $[Dy_2(tart)_3(H_2O)]_n$ and $[Dy_2(tart)_3)]_n$ formulae, respectively, which are easily rehydrated back to Dy-L' (**20**), a fact that does not permit measuring their PL spectra at open ambient conditions. Nonetheless, with the aim of getting deeper insight into the evolution of the PL signal with increasing temperature, and subsequent dehydration of the material, emission spectra have been recorded at those temperatures where Dy-L (**9**) (294 K), Dy-L'' (**21**) (463 K) and Dy-L''' (**22**) (483 K) phases are achieved. Figure SIII.43a and b show the emission and excitation spectra of these latter phases collected at the corresponding temperature.

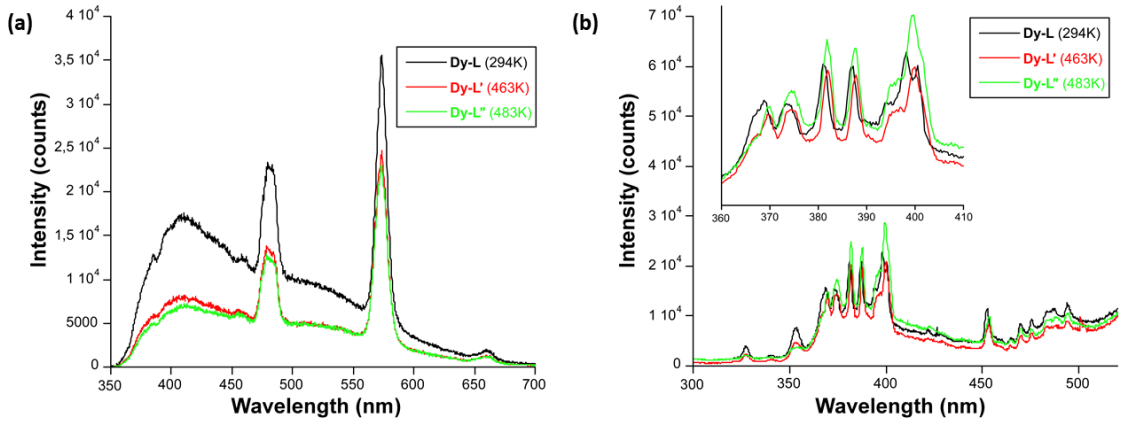

Figure SIII.43. (a) Emission spectra of Dy-L (**7**) and thermally activated Dy-L'' (**21**) and Dy-L''' (**22**) phases recorded at 325 nm excitation at selected temperatures. **(b)** Excitation spectra of the Dy-L'' (**21)** and Dy-L''' (**22**) phases recorded at 574 nm emission line.

As observed in Figure SIII.43a, there is no significant change in the relative emission of the compound (nor shift in the main bands), in such a way that the unique change according to temperature corresponds to the general drop of the absolute emission. Focusing on the excitation spectra recorded at λ_{em} = 573 nm (main emission band) and the same temperatures, a very small shifts of the intraionic excitation lines can be observed. In particular, the most intense excitation line moves from 398.2 nm (at 294 K) to 399.6 nm (at 483 K). This shift corresponds to an energy of 0.011 eV, which may be attributed to the thermal energy absorbed by the electronic structure absorbed by the system in view of the similar value estimated for κT (of 0.016 eV) for the temperature change (of 189 K = 483 - 294 K).

For comparative purposes, the emission spectra of the Dy-based material were also measured at RT just after the heating at 483 K (preserving the vacuum applied), in such a way that the RT emission spectrum of the dehydrated Dy-L''' (**22**) phase could be collected. Step by step, the first dehydration (from Dy-L (**9**) to Dy-L' (**20**) phase) clearly brings the most drastic changes to PL emission because: i) the tartrate based fluorescence is largely enhanced (the band sited in the 350-450 nm range) and ii) the relative intensity between the Dy-centered bands (ratio of λ_{em} = 573 nm / 481 nm) passes from 2.17 to 1.64. Upon further dehydration, Dy-L'' (**21**) and Dy-L''' (**22**) display an equivalent emission spectra, so only Dy-L''' (**22**) is used for the comparison. The complete dehydration to Dy-L''' (**22**) phase does not involve any ratiometric change with regard to Dy-centered bands in Dy-L' (**20**) but it promotes a drop of the first band (tartrate centered emission) intensity as well as an important shift of 110 nm (the band is sited at λ_{em} = 407 nm for Dy-L' (**20**) and at λ_{em} = 517 nm for Dy-L''' (**22**)). The three emission spectra are shown in Figure SIII.44.

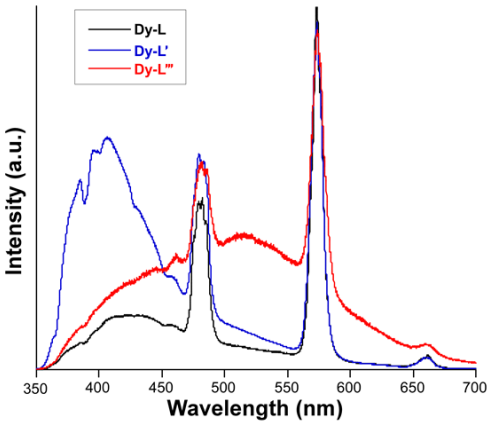

Figure SIII.44. Comparison of the emission spectra of various phases of Dy-L (**9**) compound.

S13. Calculation of the triplet state energy of tartrate ligand

The energy of the triplet state was calculated with Gaussian 09 package, using the Becke three parameter hybrid functional with the non-local correlation functional of Lee-Yang-Parr (B3LYP) with the 6-311G++(d,p) basis set. Firstly, the geometry of the singlet state taken from X-ray crystal structure was optimized, a model that was then employed to optimize the triplet state geometry. Finally, the T_1-S_0 energy difference was estimated on the basis of the vertical energy between those states with triplet state geometry. The calculation was both performed at room temperature and low temperature (10 K). As observed in Figure SIII.45, MOs show a similar shape.

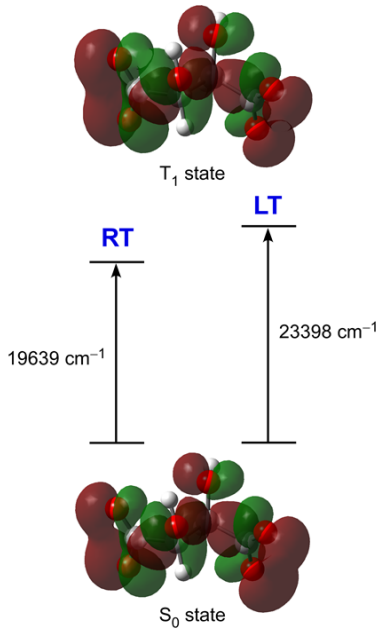

Figure SIII.45. View of the molecular orbitals of triplet state (T_1) and singlet (S_0) states on an optimized tartrate molecule. T_1-S_0 energy difference is calculated both at room and low temperature.

S14. Lifetime measurements

Lifetime measurements were performed at 10 K over polycrystalline samples under excitation at the maximum (325 nm) for the main emission wavelengths arising from intraionic lanthanide transitions. The decay curves were recorded employing different exposure times in order to achieve 10^4 counts in the pulse of reference. The decay curves were analyzed by tail fitting. All decay curves are characterized by two distinguishable regions: (1) the first rapid decrease at very short times which are associated with the pulse of the lamp and (2) the following slower decrease corresponding to the lifetime of the sample. Accordingly, the fittings show these two contributions.

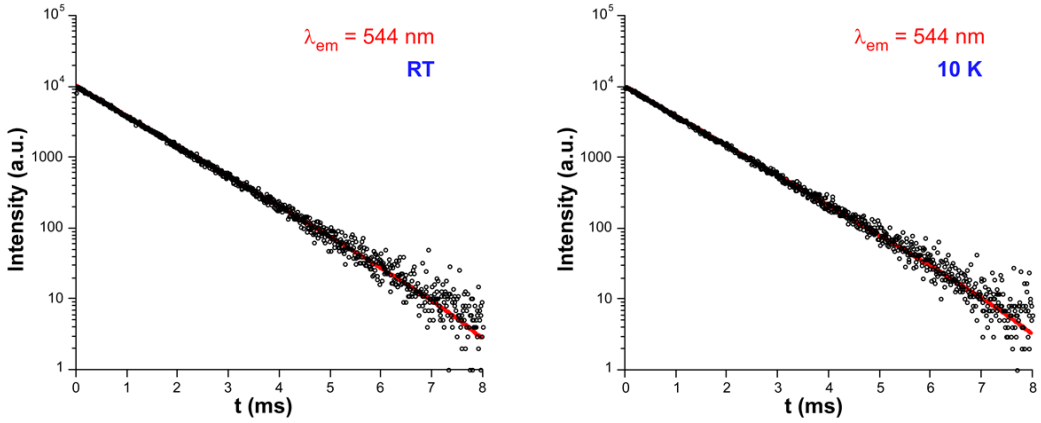

Figure SIII.46. Emission decay curves showing the best fitting for compound Tb-L (**7**).

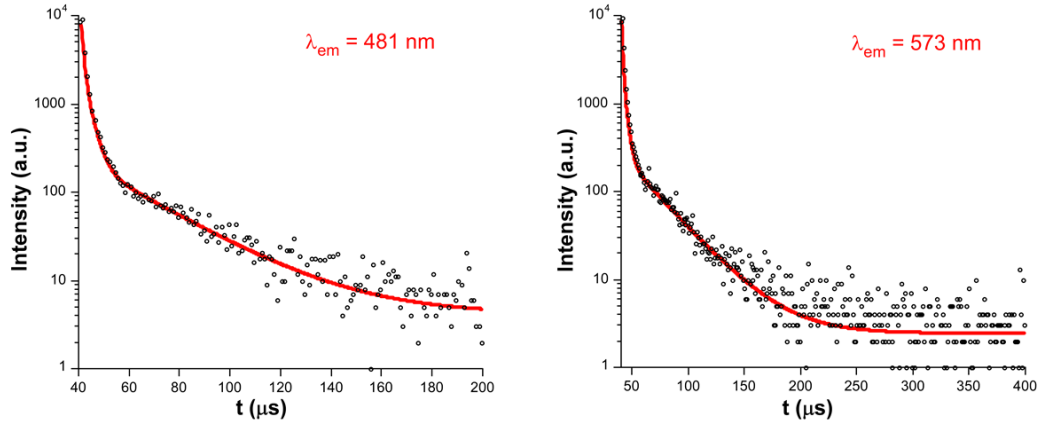

Figure SIII.47. Emission decay curves showing the best fitting for compound Dy-L (**9**).

Table SIII.14. Best fit results of decay curves performed at variable temperature monitoring different emission wavelengths.

Wavelength (nm)	τ_1 (µs)	τ_2 (µs)	Chi Sq.	T (K)
Compound Tb-L (7)				
544	1020.4(5) / 100%	–	1.239	10
544	1032.6(5) / 100%	–	1.198	298
Compound Dy-L (9)				
481	2.84(7) / 27%	26.6(4) / 73%	1.218	10
573	2.96(7) / 15%	31.0(3) / 85%	1.252	10

S15. Circular Dichroism and Circularly Polarized Luminescence measurements

Samples for CD measurements were prepared as follows: a precision weighted amount of material (2 mg) was suspended in mili-Q H_2O (4 mL) and sonicated over 1 h.

In case of CPL measurements, 10 mg of Tb-L (**7**) or Tb-D (**8**) were suspended Mili-Q H_2O (2 mL) and sonicated during 1 hour. The obtained suspension was used directly for CPL measurements. The resulting g_{lum} and ΔI spectra are an average spectra obtained after 10 scans. Circularly polarization was confirmed by looking at the signal at a frequency of 2 × the frequency of the PEM acting as an oscillating quarter-wave plate.[8] Figure SIII.48 shows the total fluorescence intensity ($I^L + I^R$) for Tb-D and Tb-L samples. The g_{lum} values were calculated following the expression:

$$g_{lum} = \frac{\Delta I}{\frac{1}{2}I} = \frac{I^L - I^R}{\frac{1}{2}(I^L + I^R)} \qquad (SIII.4)$$

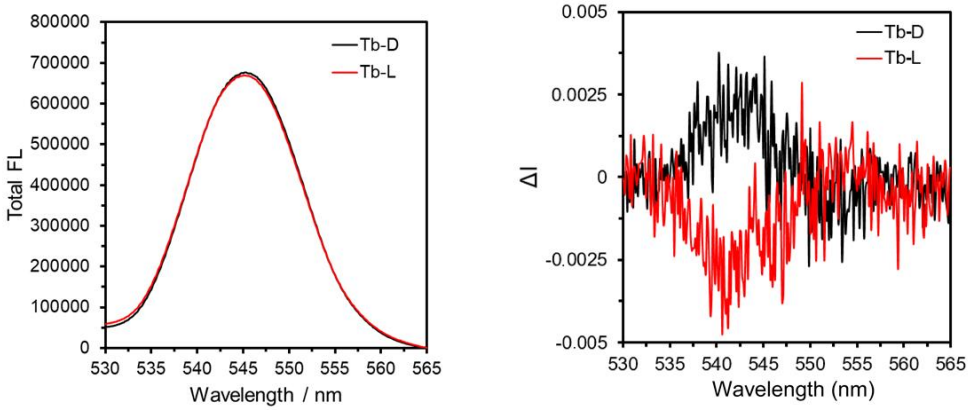

Figure SIII.48. Left: total fluorescence spectra used for the CPL measurements of the samples Tb-L (**7**) and Tb-D (**8**). Right: g_{lum} values of the CPL bands found between 530 and 565 nm.

S16. References

[1] *CrysAlisPro Software System*, Agilent Technologies UK Ltd, Oxford, UK, 2019.

[2] Bruker Apex2, Bruker AXS Inc., Madison, Wisconsin, USA, 2004.

[3] G. M. Sheldrick, SADABS, Program for Empirical Adsorption Correction, Institute for Inorganic Chemistry, University of Göttingen, Göttingen, Germany, 1996.

[4] A. Altomare, M. C. Burla, M. Camilla, G. L. Cascarano, C. Giacovazzo, A. Guagliardi, A. G. G. Moliterni, G. Polidori, R. Spagna, *J. Appl. Crystallogr*., 1999, **32**, 115.

[5] (a) G. M. Sheldrick, SHELX-2014, Program for Crystal Structure Refinement, University of Göttingen, Göttingen, Germany, 2014. (b) L. J. Farrugia, *J. Appl. Cryst*., 1999, **32**, 837.

[6] A. L. Spek, *Acta Cryst.*, 2009, **D65**, 148.

[7] J. Rodriguez-Carvajal, *Physica B*., 1993, **192**, 55.

[8] (a) H. P. J. M. Dekkers, P. F. Moraal, J. M. Timper and J. P. Riehl, *Appl. Spectrosc.*, 1985, **39**, 818. (b) J. P. Riehl and F. S. Richardson, *Chem. Rev.*, 1986, **86**, 1.

APPENDIX IV – Supporting information of Chapter 5

S1. Diffuse reflectance experiments and band-gap estimation

Diffuse reflectance spectrum on a pressed pellet of single crystals of Dy-L (**9**) was acquired with a Shimadzu UV-2600 spectrometer in the 190-900 nm at room temperature, using barium sulphate as reflectance standard (Figure SIV.1). The spectrum revealed the expected electronic transitions of different nature, the least energetic $f \longrightarrow f$ transition being located in the NIR region, at ca. 808 nm (1.53 eV). According to the literature,[1] less energetic transitions are generally found at ca. 1488 nm, which confirms that Dy-L (**9**) are low band gap materials with an estimated value of 0.77 eV, which falls below the range of typical semiconductor materials such as GaAs 1.4 ev), Si (1.2 eV) and Ge(1.7 eV).[2]

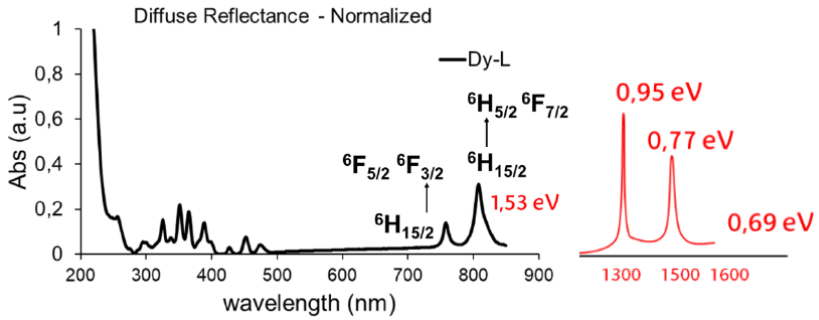

Figure SIV.1. Normalized diffuse reflectance spectrum of pressed pellets of Dy-L (**9**) single crystals (black). Additional transitions reported.[3]

S2. Dimensional analysis of Dy-L (9) single crystals by AFM

As shown in the Figure SIV 2, AFM height image confirmed the dimensional characteristics of analyzed Dy-L (**9**) single crystals. AFM height image profiles showed that the height of these analyzed single crystals was ~200 nm while the relation of 2D dimensions was equal to 0.8 µm/1 µm.

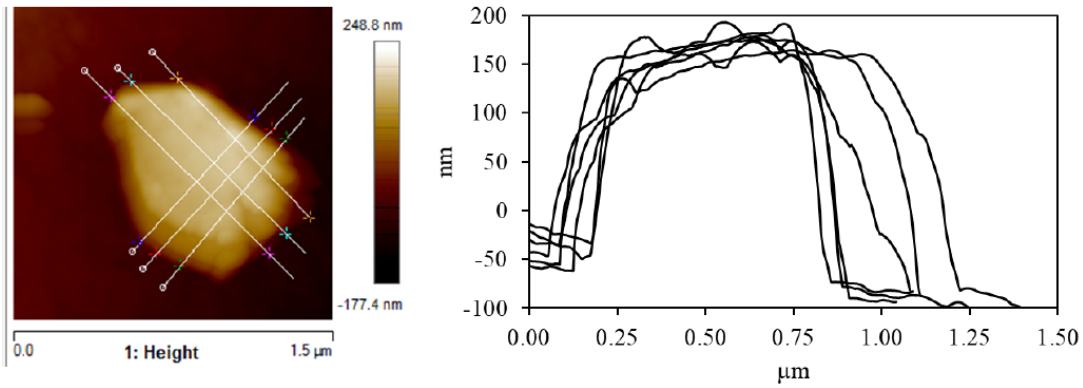

Figure SIV 2. AFM dimensional analysis of Dy-L (**9**) single crystal and corresponding profiles.

S3. Optical characterization of Dy-L (9) single crystals

Optical micrographs proved the presence of single crystals over ITO surface. Although the diversity in size is notable, the prismatic shape is quite defined and homogeneous (Figure SIV.3a and b), in addition to the fact that all the samples have the transparency and brightness that characterize single crystals. It should be noted that, as seen in Figure SIV.3c and d, among the largest crystals, others of nanometric dimensions can be seen that may be more suitable for AFM measurements.

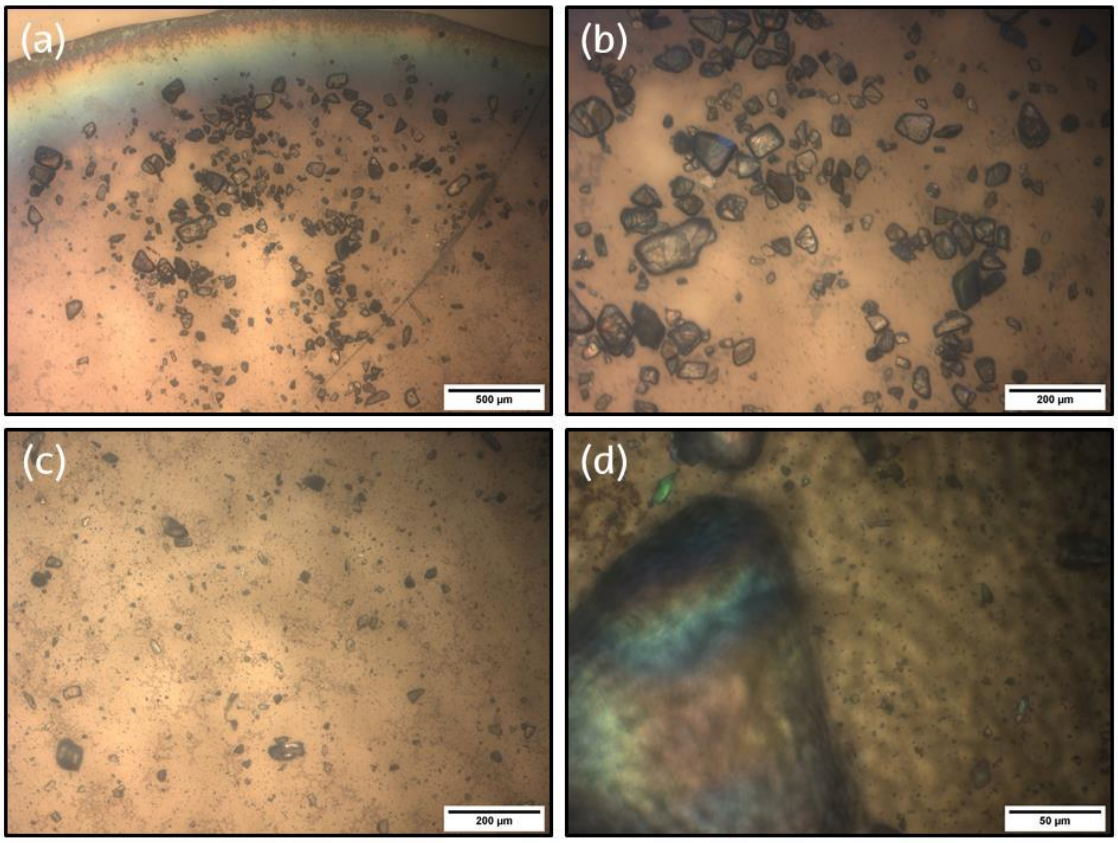

Figure SIV.3. Observation of single crystals by optical microscope. **(a)** Single crystals of different sizes over ITO surface. **(b)** Amplification in the observed area that shows the homogeneity of crystals. **(c)** Observation of a different area with smaller crystals. **(d)** Amplification of a new observed area that shows the smallest single crystals.

S4. Indexation of the faces of the single crystals

Indexation of the faces of the single crystals was done according to the analogy of their shape using the crystal exposed to X-ray as a reference. As observed in the photographs in Figure SIV.4 crystal exhibits a main (quite planar) face that corresponds to (0 0 1) Miller index (shown in the front view). Axis containing the latter reflection (index) is displayed in the second image, taken by turning the crystal 90º to the right. Last image shows the first view but incorporating (–1 0 0) index. This fact allows us concluding that crystallographic *c* axis crosses the main face of the crystal, whereas *a* and *b* axes are almost perpendicular to it.

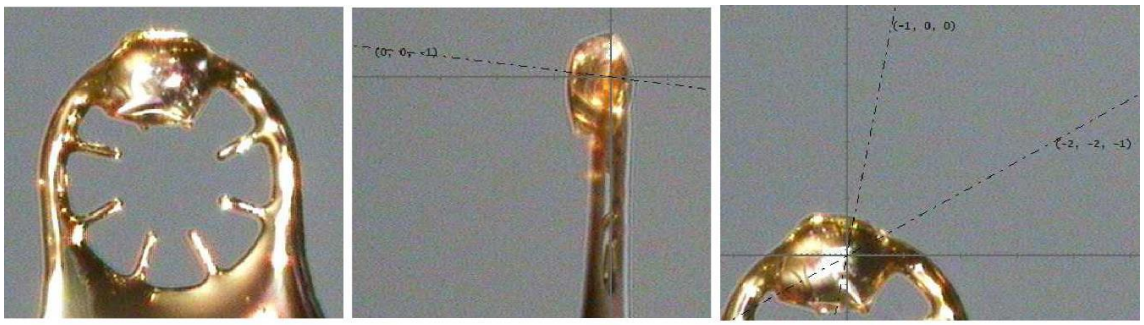

Figure SIV.4. Photographs of single crystals taken on the diffractometer, showing detail of the crystal faces (h k l).

S5. Charge transport measurements

For charge transport measurements, current-voltage (I/V) curves were measured for Dy-L (**9**) at room temperature. Through statistical analysis, the averages of Tip_0, Tip_+ and Tip_- curves were obtained, including the standard deviation for each case. I/V curves for Dy-L (**9**) single crystals deposited on ITO substrate were recorded in the full ±10 V bias range for the Tip_0, Tip_- and Tip_+ tip magnetic polarizations. Experiments were run in both ramping directions, *i.e.* from – to + bias values and from + to – bias values, respectively; experiments in each ramping direction was run 50 times (n=50). In these cases, electrical hysteresis is observed, derived from the electrical polarization of the charges in the Dy-L (**9**) single crystals upon current transmission, which was still present upon the two minutes gap left before running the experiment in the second voltage ramping direction. Also, were indicated, n=100 I/V curves (n=50 in each ramping directions) were averaged over both ramping directions, thus, neglecting the hysteresis effect.

Experiments were run, were indicated (Tip_+ set-up), with two alternative amplifiers with the aim of getting not saturated I/V curves. The sharp signal saturation initially observed in the case of Tip_+ magnetizations of the AFM probe was alleviated within a fairly large voltage range of ±2 V, where the current could be measured and the I/V characteristics displayed the expected linear behaviour flanked by two exponential (non-linear) branches, *i.e.*, I/V curves that exhibit the *S*-shape behaviour characteristic of molecular junctions and solar cells, as opposed to the abrupt jump in current in Figure SIV.5 and Figure SIV.6 (c) and (d). Still, due to the high current levels flowing across the MOF crystal in this particular magnetization direction, our current amplifiers saturated again beyond this voltage range, but, whereas Figure SIV.5 and Figure SIV.6 (c) and (d) show Tip_+ signals saturated at ca. 200pA, Figure SIV.5 and Figure SIV.6 (c´) and (d´) now saturate at ca. 1-2 nA, *i.e.* it seems that large current crossing our single crystals in the Tip_+ experiments, exceeds the limits of our amplifier again.

Figure SIV.6 is nearly the same as Figure SIV.5 but with I/V curves as a function of applied bias in the ±6 V range averaged over 50 measurements, and obtained either in the – to + ramping direction (solid lines) or + to – ramping direction (dashed lines), where hysteresis is observed; (a) and (b) results obtained in the Tip_0 setup, (c) and (d) and (e) and (f), as in (a) and (b) but magnetizing the Tip either in the + or – arbitrary directions, respectively. (c´) and (d´), as in (c) and (d) but with an alternative amplifier that permitted the measurement of higher currents.

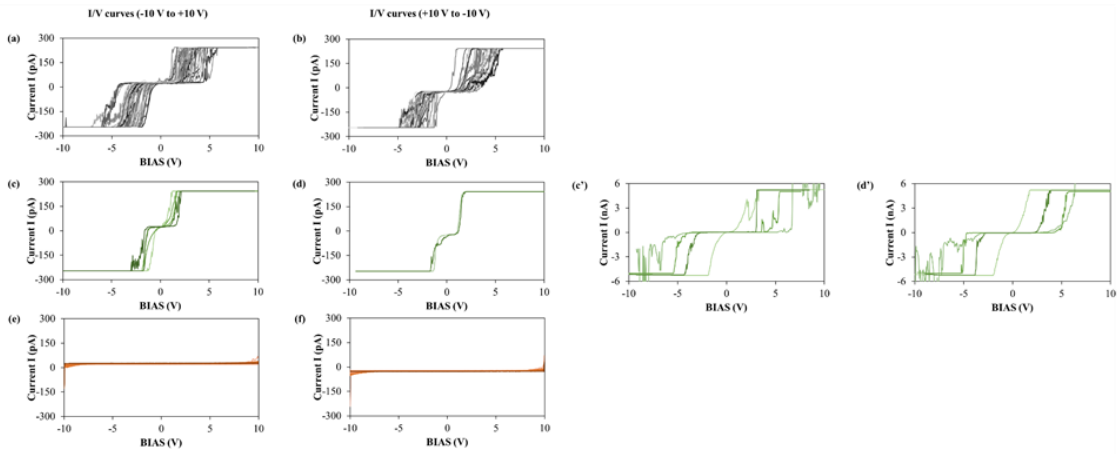

Figure SIV.5. I/V curves recorded in the full ±10 V bias range for Dy-L (**9**) single crystals deposited on ITO substrate. **(a)** and **(b)** are results from the Tip_0 experimental set-up with no AFM tip magnetization: **(a)** Individual (n=50) experiments with voltage ramping from negative to positive values; **(b)** Individual experiments (n=50) with voltage ramping from positive to negative values. **(c)** and **(d)**, as in **(a)** and **(b)**, respectively, but with tip magnetization arbitrarily north (Tip_+ experimental set up); **(c´)** and **(d´)**, as in **(c)** and (d) but with an alternative amplifier that permitted the measurement of higher currents (n=4). **(e)** and **(f)**, as in **(a)** and **(b)**, respectively, but with tip magnetization arbitrarily south (Tip_- experimental set up).

For charge transport measurements, current-voltage (I/V) curves were measured for Dy-L (**9**) at room temperature. Through statistical analysis, the averages of Tip_0, Tip_+ and Tip_- curves were obtained, including the standard deviation (SD) for each case (shown as grey bars in Figure SIV.6).

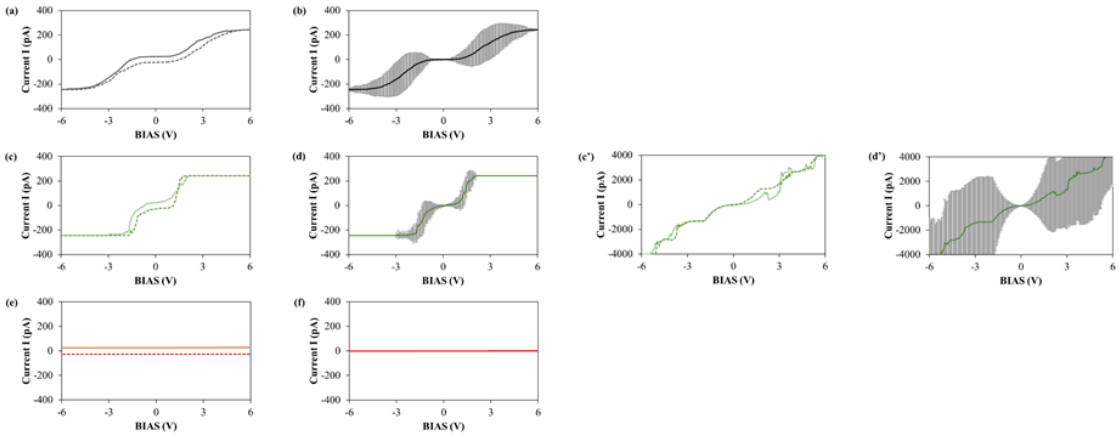

Figure SIV.6. Same as Figure SIV.5 but with I/V curves as a function of applied bias in the ±6 V range averaged over 50 measurements, and obtained either in the – to + ramping direction (solid lines) or + to – ramping direction (dashed lines), where hysteresis is observed; **(a)** and **(b)** results obtained in the Tip_0 setup, **(c)** and **(d)** and **(e)** and

(f), as in **(a)** and **(b)** but magnetizing the tip either in the + or – arbitrary directions, respectively. **(c´)** and **(d´)**, as in **(c)** and **(d)** but with an alternative amplifier that permitted the measurement of higher currents. Grey bars represent SD values.

S7. Conductivity estimations

As it is a non-ohmic material (relationship between the applied voltage and the resulting electric current is not linear), the method of static resistance was applied to estimate conductivity in arbitrary linear regions using Equations *(SIV.1)*, *(SIV.2)* and *(SIV.3)*, where X, R, ρ, A, L and σ represent the slope of the curve, the resistance of the material, the resistivity of the material, the cross-sectional area of a crystal, the length of the crystal and the conductivity of the material, respectively.

$$R = \frac{1}{X} \qquad (SIV.1)$$

$$\rho = R\frac{A}{L} \qquad (SIV.2)$$

$$\sigma = \frac{1}{\rho} \qquad (SIV.3)$$

Homogeneity of single crystals was confirmed by AFM morphology images. As Figure SIV.7 shows, A and L were calculated according to the height and dimensions given by AFM height image profiles (see Figure SIV 2), obtaining values of 10^{-8} cm^2 and $2x10^{-5}$ cm, respectively.

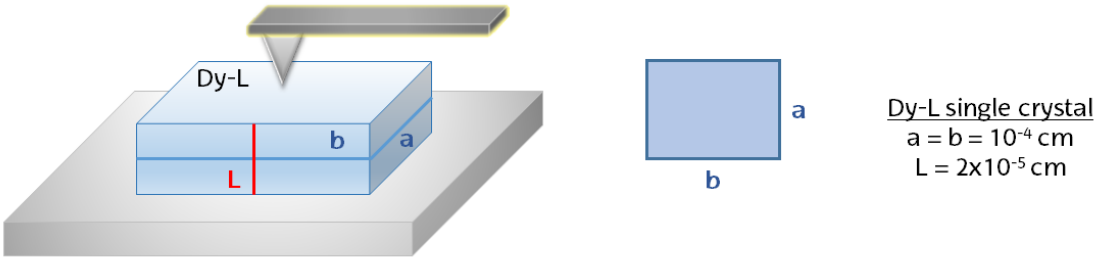

Figure SIV.7. Set-up of conductivity measurements in single crystals deposited on ITO substrate, and single crystal dimensions: Section A = a*b and height L.

In

Table SIV.**1**, conductance values for distinct linear regions in the I/V curves of the Tip_0, Tip_+ and Tip_- experimental setups are shown.

Table SIV.1. Conductivity values (μS/cm) obtained for single crystals of Dy-L (**9**) in the three distinct experimental conditions; SD = Standard Deviation

Set up	Bias Range	σ (μS/cm)	SD
Tip $_0$	-1.0 V to 1.0 V	0.00645	± 0.00027
Tip $_+$	-1.0 V to 1.0 V	0.28694	± 0.01020
Tip $_-$	-1.0 V to 1.0 V	0.00022	±0.00001

S6. References

[1] Huizi-Rayo, U.; Zabala-Lekuona, A.; Terenzi, A.; Cruz, C.M.; Cuerva, J. M.; Rodríguez-Diéguez, A.; García, J. A.; Seco, J. M.; San Sebastian, E.; Cepeda, J. "Influence of Thermally-Induced Structural Transformations over Magnetic and Luminescence Properties of Tartrate-based Chiral Lanthanide Organic-Frameworks", *J. Mat. Chem. C* (2020), **8**, 8243-8256.

[2] Thushari, S.; Cha, J. A. K.; Sung, H. H.-Y.; Chui, S. S.-Y.; Leung, A. L.-F.; Yen, Y.-F.; Williams, I. D. "Microporous chiral metal coordination polymers: hydrothermal synthesis, channel engineering and stability of lanthanide tartrates", *Chem. Commun.* (2005), 5515-5517.

[3] Volkovich, V. A.; Ivanov, A. B.; Yakimov, S. M.; Tsarevskii, D. V.; Golovanova, O. A.; Sukhikh, V. V.; Griffiths, T. R. "Electronic Absorption Spectra of Rare Earth (III) Species in NaCl–2CsCl Eutectic Based Melts", Physics, Technologies and Innovation (PTI-2016). *AIP Conf. Proc.* **1767**, 020023-1–020023-11.

List of publications

First publication

Autors	
Uxua Huizi-Rayo, Andoni Zabala-Lekuona, Alessio Terenzi, Carlos M. Cruz, Juan M. Cuerva, Antonio Rodríguez-Diéguez, Jose Angel García, José M. Seco, Eider San Sebastian, and Javier Cepeda	
Title	
Influence of thermally induced structural transformations on the magnetic and luminescence properties of tartrate-based chiral lanthanide organic-frameworks	
Journal, specify year, volume, pages	
Journal of Materials Chemistry C (2020), **8**, 8243-8256	
Impact factor (JCR)	**Year**
7.059	2019
H-index ***Scimago Journal & Country Rank (SJR)***	
108	

Second publication

Autors	
Eider San Sebastian, Javier Cepeda, Uxua Huizi-Rayo, Alessio Terenzi, Daniel Finkelstein-Shapiro, Daniel Padro, Jose Ignacio Santos, Jon M. Matxain, Jesus M. Ugalde, and Vladimiro Mujica	
Title	
Enantiospecific Response in Cross-Polarization Solid-State Nuclear Magnetic-Resonance of Optically Active Metal Organic Frameworks	
Journal, year, volume, pages	
Journal of American Chemical Society (2020), **142**, 42, 17989–17996	
Impact factor (JCR)	**Year**
14.612	2019
H-index ***Scimago Journal & Country Rank (SJR)***	
582	

Last publication

Autors	
Uxua Huizi-Rayo, Junkal Gutierrez, Jose Manuel Seco, Vladimiro Mujica, Ismael Diez-Perez, Jesus M. Ugalde, Agnieszka Tercjak, Javier Cepeda, and Eider San Sebastian	
Title	
An Ideal Spin Filter: Long-Range, High-Spin Selectivity in Chiral Helicoidal 3-Dimensional Metal Organic Frameworks	
Journal, year, volume, pages	
Nano Letters (2020), Just Accepted. https://doi.org/10.1021/acs.nanolett.0c02349	
Impact factor (JCR)	**Year**
11.238	2019
H-index **Scimago Journal & Country Rank (SJR)**	
461	

Acknowledgements

This work has been funded by:

- Red Guipuzcoana de Ciencia, Tecnologı´a e Innovación (OF218/2018)
- University of the Basque Country (GIU 17/13),
- Gobierno Vasco/Eusko Jaurlaritza (IT1005-16),
- Junta de Andalucía (FQM-394)
- Spanish Ministry of Economy and Competitiveness (MCIU/AEI/FEDER, UE) (PGC2018-102052-A-C22, PGC2018-102052-B-C21).
- Spanish Ministry of Science, Innovation and Universities and European Union (MICINN/FEDER and UE) in the frame of PGC2018-097699-B-I00, PGC2018-102052-A-C22 and PGC2018-102052-B-C21 projects)

Authors also thanks the technical and human support provided by SGIker of UPV/EHU, collaborators of the Institute IMDEA Energy and European funding (ERDF and ESF).